Development of Electrospray Ionization of Biomolecules on a Magnetic Sector Mass Spectrometer

by

YiBing Zhang

A thesis submitted for the degree of

Doctor of Philosophy

Department of Chemistry

University of Warwick

2002

Numerous Originals in Colour

Best Copy
Available

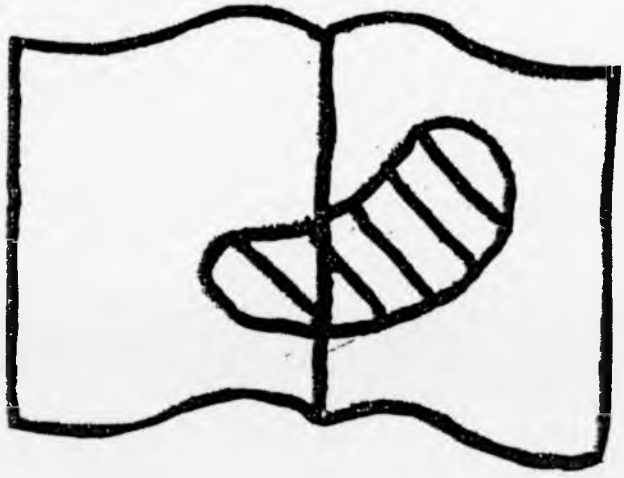

Abstract

The initial part of this study involves developments made on an electrospray ionization (ESI) source installed on a large-scale double-focusing reverse-geometry two-sector mass spectrometer. The practical considerations and some basic theory have been given in this thesis for each of the improvements made to the ESI source[3-1]. The process of partial re-designing the ion optical system showed that the ion beam was affected by both gas dynamics and by the field penetration from the lenses of the ion optical system in the region immediately after second skimmer. More than one order magnitude stronger ion signal intensities at the mass spectrometer final detector and easier ESI source operation conditions and stable ion signals has been achieved.

Mass-analyzed ion kinetic energy spectroscopy (MIKES) of different charge-states of relatively small peptides (substance P and bradykinin) for collision-induced dissociation (CID) and the metastable dissociation was carried out successfully. The translational energy losses caused shifts in the fragment ion peaks in the CID spectra, compared with fragment ion peaks in the metastable dissociation spectra.

A major part of the study concerned effects of ESI source condition on the charge state distributions of mass spectra. It has been shown that the ion optical effect of the potential difference(V_{HCT-S}) between the heated stainless steel capillary (HCT) and the first skimmer in the intermediate-pressure region (capillary-skimmer region or orifice-skimmer region) of the ESI source was the main factor in determining the charge state distribution of the ESI mass spectra. The temperature of the HCT and the potential difference between the first skimmer and the second skimmer has been shown to be also important factors. The collision-induced dissociation (or so-called capillary-

skimmer dissociation) effect of V_{HCT-S} has been shown to be relatively low in this sector-mass spectrometer ESI source.

Declaration

I hereby declare that this thesis is my own work and that, to the best of my knowledge and belief, it contains no material previously published or written by another person, nor material which to a substantial extent has been accepted for the award of any other degree or diploma of a university or institute of higher education, except where due acknowledgment is made in the text.

Yibing Zhang

Acknowledgments

Many thanks to Professor Peter J. Derrick for his patience, valuable advice, and kind help with my studies and life in the UK.

Thanks to Mr. Alex W. Colburn, without whose help the improvements to the ESI source of the MMM instrument could not have been carried out. He has also been a most reliable help with respect to solving problems with the MMM instrument. Thanks to Dr. Anastassios E. Giannakopulos for his suggestions, encouragement and help during my studies.

Dr. Mark P. Barrow and the current student Mr.Ganesh Pathmanayagam who could always be reached for help.

The rest of the members in Professor Peter J. Derrick's research group such as Dr. Benjamin Thomas, Dr. Andrew R. Bottrill, Mr. Philip Green, Mr. Liam A. McDonnell, and Mr. Sajid Bashir for invaluable discussions and for being my friends during my studies.

Thanks to Mr. Ken Westwood, Mr. Lee Butcher and Mr. Marcus Grant of the mechanical workshop for their help with all the mechanical jobs related to MMM instrument. Mr. Philip M. Roskelly of the electronic workshop for the rapid repairs of electronic equipment.

I also acknowledge the Committee of Vice-Chancellors and Principals of the Universities of the United Kingdom for the Overseas Research Students Awards (ORS) and the Graduate School of the Warwick University for funding me, covering the home student fee.

Last but no means least thanks to my wife Hong Liu, my son Yuxuan Zhang, my parents and rest of family for their love, support and encouragement.

Contents

List of Figures

Chapter 1 Introduction

1.1 General introduction

Following the first experiences of J. J. Thomson[1-1] in the early years of the last century, mass spectrometry has undergone countless improvements. We can say simply that the history of mass spectrometry was begun by J. J. Thomson's work, but the ideas and theories that J. J. Thomson's experiments were based on came from earlier studies. When in 1886, E. Goldstein discovered positive ions[1-2], the first light of the history of mass spectrometry was shown. In 1898, W. Wien analyzed the positive ions by magnetic deflection methods[1-3]. In 1912, J. J. Thomson[1-4] invented the first mass spectrograph and measured the mass spectra of O_2, N_2, CO, CO_2 and $COCl_2$. He also observed negative and multiply charged ions and metastable ions. In this work, he founded the basic principles underlying mass spectrometry.

In Thomson's experiments, the positively charged ions were accelerated and collimated by a cathode electrode and passed into a flight tube across which an electric-magnetic field was applied. The combination of the magnetic and electrical field separated the ions into beams corresponding to the mass to charge ratio of the ions present. Detection was made by allowing the ions to strike a photographic plate which was later removed and developed. The position of the blackened traces and the intensity of the blackening were used to calculate the masses and abundances of the ions present.

The first true mass spectrometer with a sector shape magnet (180^0) and direction focusing was constructed by A. J. Dempster in 1918[1-5]. In his instrument, the ions were detected by measuring their ion currents with sensitive electrometers and electroscopes. This meant that spectra could be acquired in real time and relative abundances were obtained more quickly and accurately than that with Thomson's

instrument. In 1919 F. W. Aston developed Thomson's first mass spectrograph with velocity focusing[1-6].

Since that time, the mass spectrometry has developed into a very large multidisciplinary field especially in the biological, chemical and physical sciences. There have been four Nobel Prizes awarded linked directly to mass spectrometry: 1906 to J. J. Thomson; 1922 to F. W. Aston; 1989 to W. Paul (for his contribution to quadrupole analyzer and ion trap analyzer[1-7, 1-8]) and 1992 to R. A. Marcus (for his theoretical contribution[1-9]). Many different ion sources, analyzers and detectors have been developed[1-10].

Native molecules with molecular masses above a thousand Daltons are usually not volatile and they are thermally labile. Therefore they cannot be volatilised without modification of the sample. The discovery of the fast atom bombardment (FAB) source[1-11] broke this blockage and allowed the non-volatile and thermally liable molecules to be analyzed by mass spectrometers. This increased the range of application of mass spectrometry to the samples whose molecular masses are a few thousand Daltons. The discovery of electrospray ionization (ESI)[1-12, 1-13] by Fenn et al. in 1984 and the matrix-assisted laser desorption/ionization (MALDI)[1-14] by Hillenkamp in 1985 were a few years later to change the history of mass spectrometry and now mass spectrometry can be used over much larger mass ranges than ever before. The multiple charging of the ESI ions and coupling of the MALDI source with the time-of-flight (TOF)[1-15] analyzer were the basic reasons that both ionization methods could analyze very large biomolecules and polymer samples.

Mass spectrometers mainly consist of three parts: ion sources, mass analyzers and detectors corresponding to the three steps in mass spectrometry: 1) the generation of

ions in the gaseous state after the introduction of the sample into the ion source; 2) the analysis of these ions by the mass analyzers: separation according to their mass to charge ratio, further fragmentation of ions to get more structural information by analysis of their offspring ions; 3) the separated ions and their offspring ions are detected by the detectors and both their mass to charge ratios and their intensities are recorded. In the following part of this chapter, a little detailed information will be given to some of them.

1.2 Ionization methods (ion sources)

Initially the sample must be introduced into the gas phase and ionized. This happens in the ion source. The process of vaporization and ionization may be distinct events such as for the electron impact (EI) [1-16, 1-17] and chemical ionization (CI) [1-18] techniques, or more concerted such as for the desorption and spray ionization methods. As the sample moves from the neutral to the charged state, there is usually a corresponding changing in the internal energy of the newly formed ions. Any highly exited species may undergo unimolecular dissociation or react with the other in the source. As a result the ion beam may consists of intact sample ions, fragment ions and gas-reaction product ions.

There are many kinds of ion sources such as: (1) the electron impact source (EI) [1-16, 1-17]; (2) the chemical ionization source (CI) [1-18]; (3) the desorption chemical ionization source (DCI) [1-19] ;(4) the fast ion or atom bombardment ionization source — liquid second ion mass spectrometry source (LSIMS) [1-20, 1-21] and the fast atom bombardment ionization source (FAB) [1-11]; (5) the field desorption (FD) source [1-22] ; (6) the laser desorption source (LD) [1-14] and the matrix assisted

ions in the gaseous state after the introduction of the sample into the ion source; 2) the analysis of these ions by the mass analyzers: separation according to their mass to charge ratio, further fragmentation of ions to get more structural information by analysis of their offspring ions; 3) the separated ions and their offspring ions are detected by the detectors and both their mass to charge ratios and their intensities are recorded. In the following part of this chapter, a little detailed information will be given to some of them.

1.2 Ionization methods (ion sources)

Initially the sample must be introduced into the gas phase and ionized. This happens in the ion source. The process of vaporization and ionization may be distinct events such as for the electron impact (EI) [1-16, 1-17] and chemical ionization (CI) [1-18] techniques, or more concerted such as for the desorption and spray ionization methods. As the sample moves from the neutral to the charged state, there is usually a corresponding changing in the internal energy of the newly formed ions. Any highly exited species may undergo unimolecular dissociation or react with the other in the source. As a result the ion beam may consists of intact sample ions, fragment ions and gas-reaction product ions.

There are many kinds of ion sources such as: (1) the electron impact source (EI) [1-16, 1-17]; (2) the chemical ionization source (CI) [1-18]; (3) the desorption chemical ionization source (DCI) [1-19] ;(4) the fast ion or atom bombardment ionization source — liquid second ion mass spectrometry source (LSIMS) [1-20, 1-21] and the fast atom bombardment ionization source (FAB) [1-11]; (5) the field desorption (FD) source [1-22] ; (6) the laser desorption source (LD) [1-14] and the matrix assisted

laser desorption ionization (MALDI)[1-14]; (7) the plasma desorption source (PD)[1-23]; (8) the thermospray source (TSP)[1-24] ; (9) the electrospray ionization source (ESI)[1-12, 1-13, 1-25, 1-26].

1.2.1 Electrospray ionization (ESI)

Electrospray ionization (ESI) was first reported by Fenn et al.[1-15, 1-16] and Aleksandrov et al.[1-25, 1-26] (independently) in 1984. But Dole et al.[1-27] had recognized the possibility of generating gas-phase ions of macromolecules by spraying a solution from the tip of an electrically charged capillary. In this early work[1-27], an ion-drift spectrometer was used for the ion analysis.

The typical ESI source consists of the following parts along with the ion flight path: the spray needle, the counter electrode, the end-metal-coated glass capillary (or heated stainless steel capillary or sample cone or metal orifice), the skimmers and lenses systems, finally the source slit. The spray needle, the counter electrode and the entrance of the capillary (or the outside side of the sample cone) are in the atmosphere pressure. The exit end of the capillary (or the inside side of the sample cone) are in the intermediate-pressure region. After one or two skimmers, the pressure will have come down to the background pressure for the normal working vacuum of the mass spectrometer.

Comparing with other ionization methods, the electrospray is not an ionization process in the sense that applies in electron ionization (EI) source, where the bombardment of the neutral molecules in the gaseous state with high-energy electron beam **ionizes** the sample molecules. The sample molecules are not **converted** to become ions but actually extra charges (positive or negative) are attached by this method, and it

is also possible that some sample ions are already present in the solution and are **transferred** to the gaseous phase. Except for the possible so-called nozzle-skimmer dissociation when suitable pressure and potential difference applied in the intermediate pressure region, there are no high-energy excitation steps in the whole process. So the ions produced by the ESI process have very low internal energy, which is the reason that the ESI mass spectrometer can be used to study the delicate non-covalent complexes of large bio-molecules.

The whole ESI process can be described as follows: the analyte sample is dissolved in a solution which is delivered (at a rate perhaps of 1 - 10 μL/min) by a syringe pump to the tip of the electrospray needle where high electric field is applied between the needle tip and the aperture to the mass spectrometer. In the positive working mode, the tip is at a high positive potential. Positive ions in the solution will accumulate at the solution surface facing the low-potential direction of the counter electrode and the aperture to the mass spectrometer (capillary or sample cone). The solution surface is thus drawn out in a down-field direction to establish a "Taylor cone". At high enough electric field, the cone is drawn to a point where the applied electric force exceeds the surface tension of the solution. The thin filament of solution cone extends until it breaks into droplets with extra positive charges. The droplets then drift under the field towards the entrance (the entrance of the capillary or the entrance sample cone) of the mass spectrometer, while at the same time spraying out through coulombic repulsion. The droplets reduce in the size due to solvent evaporation, which can be mainly caused by a counter current drying gas before entering the capillary[1-28] (or the entrance of the sample cone) in one source arrangement or mainly from the heat of the wall of the heated capillary[1-29] and the pressure gradient toward the mass

analyzer in another source arrangement. Droplets shrinkage leads to high surface charge densities. Further shrinking of the droplets, to the point where the electrostatic charge repulsion force overcomes the droplets surface tension (Rayleigh limit)[1-30], leads to fission to form the daughter droplets. Here uneven droplet subdivision leads to offspring droplets carrying unequal fractions of the excess charge and the mass from the parent droplet (about 15 % of charge and 2 % of mass)[1-30]. Consequently the chemical composition of each generation of offspring droplets will be different from those of the precursor and residue droplets. If the material is inhomogeneously distributed within the precursor droplets, sampling bias may result. The process will continue down to form the final ions (analyte molecules with extra positive charge attached, singly or multiply charged). Anything which could affect the above process would show its effects on the final spectra in one way or another.

The ions formed then pass through the capillary or the sampling cone and enter the so-called the intermediate-pressure region of the ESI source (this region is usually the capillary-skimmer or cone-skimmer region). The reason for using the capillary and the skimmers (or the sample cone and the skimmers) is to restrict the pumping load for the mass spectrometer pumps and at same time to allow ions produced in the high pressure region of the atmosphere region or the heated capillary to be transmitted to the high vacuum region of the mass spectrometer main (mass analyzers and detector). Ions in this region are very sensitive to the potential difference applied and the vacuum they experience. Due to the large pressure difference between the two ends of the capillary or the two sides of the sampling cone, the ions will experience so-called free jet expansion (adiabatic free expansion)[1-31] at the exit end of the capillary. Ions may undergo collision-induced dissociation under suitable pressure and potential difference in the

region, which is called capillary-skimmer (or nozzle-skimmer) dissociation. After passing the above region, ions will fly though the skimmer and other lenses and will enter the high vacuum part of the mass spectrometer, in which they are analyzed by the mass analyzers and recorded by the detector of the mass spectrometer.

The above process seems quite simple, but there are a lot of effects which can affect the final spectra. The potential difference applied to maintain the spray can cause electrochemical reaction in the spray needle which acts as a reaction cell. Oxidation of the solvent and / or the electrode itself have been seen in the positive ESI mode[1-32]. The stability of the spray itself is affected by parameters such as the conductivity of the spray needle and needle tip, the diameter and shape of the needle tip, the surface tension, the flow rate and the composition of the analyte solution and finally the potential difference applied between the spray needle tip and counter electrode (and the entrance end of the capillary).

Today ESI is one of the most widely used of ionization methods. It has been developed and improved very quickly to match the practical needs. The relatively new nanospray and microspray sources[1-33, 1-34] which use very lower flow rate have been found to be more sensitive than the normal electrospray[1-35] source. The difference between the nanospray or microspray and normal electrospray is only that the former uses a spray needle with finer tip which can produce smaller droplets. Smaller droplets need shorter flight times and distances in the heated counter current gas flow before ions are formed, and so the needle tip can be put much nearer the sampling orifice of the capillary. Because of this short distance between the spray needle tip and the sampling orifice, a much higher portion of the ions or offspring droplets can be caught by the sampling gas flow (which is caused by the pressure gradient and is only effective very

near sampling orifice region). For normal electrospray, only a small percentage of ions travel sufficiently near the sampling orifice region to be transferred into the source. With electrospray, most of the ions or droplets are neutralized and lost when, under the control of the electrostatic field they hit the counter electrode and the surface of the entrance end of the capillary. The shorter distance and lower potential difference applied with nanospray or microspray cause less coulombic expansion among the droplet /ion mixture and lessen the defocusing effect of the electric field between the end of the capillary and the spray needle tip. This latter effect is important in a normal ESI source(see 3.2 of Chapter 3 in this thesis).

Another development in ESI has been the so-called Z-Spray[1-36, 1-37]. The skimmer orifice axis is at a 90 degree angle with the ESI spray needle axis, and the following extracting cone axis is at a -90 degree angle with the skimmer orifice axis, so the ions fly in a Z-shape path, from the ESI needle tip, through the skimmer orifice and then the extracting orifice before they enter the mass spectrometer. It has been claimed[1-36] that the design is more efficient than a standard ESI source for the generation and separation of analyte ions from solvent and buffer agents.

The multi-ESI-sprayer, multi-atmospheric-prssure-inlet (designed and constructed by Moini et al.[1-38]) connected with a time-of-flight (TOF) mass spectrometer is another approach to the development of ESI. This new source has provided reference peaks on every acquisition without significant interaction between the reference standard and the analyte of interest. Exceptional mass accuracy has been claimed under dual-ESI-spray, dual-nozzle conditions.

One of the newest ESI source designs has been made by Smith et al.[1-39, 1-40, 1-41]. An electrodynamic ion funnel was installed directly after the capillary, followed by an

octapole ion guide before the entrance of the quadrupole mass spectrometer. As there was no other conductance-limiting apertures (skimmers), they claimed that the transmitted ion currents were a factor of 30-56 greater than those of the standard ESI interface for peptides and 18-22 greater for protein samples. Somewhat lower gain in sensitivity were found at the mass spectrometer detector which they believed was due to space charge effects in the octapole ion beam guide. The magnitude of the rf-amplitude of the ion funnel electrodes controlled the final ESI spectra acquired. A low-rf-amplitude operating mode allowed fragile non-covalent complexes (as well as generally undesired adducts) to be transmitted, and a high-rf-amplitude operating mode provided greater collisional activation and more effective adduct remove.

Another of the newest ESI source designs has been made by Williams et al.[1-42], and has called impact desolvation of electrosprayed microdroplets (IDEM). They claimed that the analytes were dissolved in an electrolyte solution which was electrosprayed in the vacuum, producing highly charged micron and sub-micron droplets (microdroplets). The microdroplets then were accelerated by a potential difference of about 5 - 10 kV to velocities of several km/s and impacted on a target surface. The impact vaporized the droplets and released the desolvated gas-phase analyte molecules ions largely free of adducts from solutions of high ionic strength. It was found that this IDEM source had substantial immunity to solution impurities and could electrospray 100 % aqueous solution. This IDEM source also produced ions with less multiple charging than a normal ESI source. All the above special points made IDEM source a good choice both to be linked directly with liquid separation techniques and to analyze samples taken directly from biological materials without extensive cleanup.

1.2.2 Matrix-assisted laser desorption/ionization (MALDI)[1-14, 1-43, 1-44]

Matrix-assisted laser desorption/ionization (MALDI)was first reported by Hillenkamp et al[1-14] in 1985. The principle of MALDI is to deposit energy by photoirradiation into a matrix. Put simply, it is an energy-sudden desorption and ionization method. In a MALDI experiment, the analyte is embedded in an excess of a suitable organic molecule (the matrix) which absorbs strongly at the laser wavelength used. The matrix absorbs the energy from the laser and is responsible for the break up of the condensed phase assisting the analyte molecules into the gaseous phase. The large excess of matrix is used to disrupt intermolecular forces between analyte molecules. In the dense cloud or plume above the sample surface, chemical reactions would occur giving a charge to the analyte molecule, and allowing their detection by the time-of-flight (TOF) mass spectrometry. The mechanism of the ion formation in MALDI is not well understood and is an active research area.

1.3 Mass analyzer

Once the ions have been produced from the ion source, they need to be separated according to their mass (m) to charge (z) ratio (m/z). They can be mass analyzed by one, or a combination of more then one, of the five types of mass analyzers. The five options are electric and magnetic sectors[1-45, 1-46], quadrupole[1-47, 1-48], time of flight[1-49, 1-50], ion trap[1-7, 1-51] and the ion cyclotron resonance[1-52, 1-53, 1-54] of these, the sector analyzers are the oldest type. The most recent development in mass analyzers is the Fourier transform ion cyclotron resonance mass spectrometer.

1.3.1 Sector analyzers

Ions formed in the source of a sector analyzer are accelerated through a voltage V_{acc} towards the source slit which is usually at earth potential. The fall in potential energy for the ions is equal to their gain in kinetic energy, that is :

$$E_o = qV_{acc} = ZeV_{acc} = \frac{(mv^2)}{2} \qquad (1\text{-}1)$$

Where E_O is the kinetic energy (J), **e** is the charge of an electron (1.6×10^{-19} C), **q** is the charge on the ion (C), **Z** is the number of charges on the ion, **m** is the mass of the ion (kg), V_{acc} is the accelerating voltage (volts), and **v** is the velocity of the ion (m/s).

All particles with the same charge acquire the same amount of kinetic energy, $E_O = ZeV_{acc}$, during this acceleration step. As the result, heavier ions will attain a lower final velocity than lighter ions of the same charge.

1.3.2 Magnetic sector

When ions (mass **m**, charge **q** and velocity **v**) enter a homogeneous magnetic field { field strength **B,** (tesla, T)} in the perpendicular direction, they will travel in a circular path of radius **R** (m), so that the centrifugal force equilibrates the magnetic force:

$$qvB = \frac{mv^2}{R} \qquad (1\text{-}2)$$

$$mv = qBR \qquad (1\text{-}3)$$

$$R = \frac{mv}{qB} \qquad (1\text{-}4)$$

Ions are dispersed according to their momentum-to-charge ratio. As the radius (R) of the arc of the magnetic sector is constant, only ions with a given momentum can follow the path through the flight tube for a given magnetic field, B. Thus the magnetic analyzer is a momentum analyzer (1-4). If the ions entering the field do not have the same kinetic energy, they will follow different trajectories through the field. This is called energy dispersion. If the ions entering the field follow different initial directions, and their divergence may increase during the trip through the field. This is called angular divergence.

1.3.3 Electric sector

Electric sectors use an electric field to separate ions with different kinetic energies. An electric field is applied across two parallel cylindrical plates of mean radius **r** (m). An ion beam diverging from a source slit passes between these plates. The radical electric field **E** (V/m) produced by the plates will deflect the ions. The ions of greater or lesser energies will follow paths of greater or lesser radii through the electric sector. The centrifugal force equilibrates the electrostatic force:

$$qE = \frac{mv^2}{r} \qquad (1\text{-}5)$$

Introducing the entrance kinetic energy (1-1) :

$$r = \frac{2E_c}{qE} \quad \text{or} \quad Er = \frac{2E_c}{q} \qquad (1\text{-}6)$$

Here the trajectory being independent to the mass, the electric sector is not a mass analyzer, but rather a kinetic energy analyzer.

1.3.4 The double focusing principle

By choosing correctly the geometry of the magnetic field (sector field) the magnetic sector can achieve direction focusing of the ion beam, and the electric sector can do likewise when its geometry is suitably chosen. This means that the angular divergence of the ions can be solved by a single sector. With a beam of ions with different kinetic energies, both sectors can produce an energy dispersion and a direction focusing. If two sectors with the same energy dispersion are arranged in such a way that the energy dispersion of the electric sector is contradictory to that of the magnetic sector, the energy dispersion effects of the two sectors can cancel each other out when the sectors are combined. This gives the term double focusing which means focusing of both the ions' direction (or spatial focusing) and the ions' energy (or velocity focusing).

1.4 Detectors

After the ion beam passes through the mass analyzers, it is then detected and transformed into a usable signal by a detector. There are several kinds of mass detectors: the photographic plates, the faraday cylinders, the electron multipliers, the array detectors and the photon multipliers. The oldest two kinds of detectors: photographic plate and faraday cylinder, directly measure the charges that reach them. The electron or photomutiplier detectors will increase the intensities of the signal. The method of detection employed by FT-ICR mass spectrometer uses a totally different principle to all of the above detectors, in which the movement of charge past a detection plate induces a current to counteract the effect of the proximity of the charge. This non-destructive detection method is one of the advantages of FT-ICR mass spectrometry.

1.4.1 Electron multipliers

One of the most commonly used types of detector is the electron multiplier. Electron multipliers dynodes have been discrete connected in series via a chain of resistors. A high voltage, called the multiplier's working potential, is applied to the system, and nearly equal potential drops will be set up between the adjacent dynodes. When detecting positive ions, the incoming ion strikes the negative high-voltage conversion dynode (conversion dynode or the first dynode) and causes the emission of secondary particles which can include the positive ions, negative ions, electrons and the neutrals. The negative ions and electrons are accelerated to strike the next dynode causing more emission of particles, and so on down the dynode chain. The resulting cascade of negative ions and electrons will result in a measurable current which can then be amplified. The final signal may be taken as a measure for determination of the relative intensity of the given ion. The gain of a multiplier may reach 10^7 to 10^8. One disadvantage of this kind of detector is that it may become saturated when the ion intensity is too strong. This may limit the sensitivity of the system.

The continuous dynode electron multiplier uses a cylinder or funnel-shaped tube dynode. The secondary negative ions and electrons from the high negative-potential conversion dynode (for positive ion detection) will strike the inner surface of the continuous dynode starting cascade processes.

1.4.2 Microchannel plates

Microchannel plates (MCP's) can be thought of as millions of cylindrical continuous dynode electron multipliers put together, with the channel diameter of each ranging from 4 to 25 μm and center-to-center distance between adjacent channels of 6

to 32 μm. A typical 1 kV potential difference will be applied between the sides of the plate. With the gain of a single plate being 10^5, the combination of several plates allows the amplification to reach 10^8. At every channel exit, a metal anode gathers the stream of the secondary electrons and the signal is transferred to a processor. Simultaneously recording the ion signal at different spots on the plate is possible.

1.4.3 Photomultipliers

A photomultiplier detector[1-55] usually consists of two conversion dynodes (MCP's), a phosphorescent screen and a photomultiplier. These detectors can be used in detection of both positive and negative ions. In the positive mode, the secondary electrons produced by the MCP's in the first stage will be accelerated towards and then strike the phosphor screen producing photons. The photons are transferred via a fiber optic coupling to a charge coupled device (CCD). The photons are changed to charge, integrated and stored. As this detection system uses discrete channels, it is possible to distinguish the signals from ions which strike different spots on the MCP's. Installing this type of detector on a sector instrument can increase the detection sensitivities of the instrument.

1.5 Ion dissociations

The determination of molecular structure by the mass spectrometry requires the target molecule to be ionized and to undergo the structural fragmentation. The fragmentation can happen in the ion source during ionization processes or subsequently by special methods such as collision-induced dissociation (CID) in a collision cell.

The ions produced in the ion source will undergo heavy fragmentation to form large numbers of different fragments if the imparted energy is high enough, as is the situation in an electron ionization (EI) source with high-energy electron beam bombardment. There may also be nearly no fragmentation as can be the case in an ESI source. Fragmentation in the source is important in EI mass spectrometry for the small molecules. To examine fragmentation of a specific ion, the parent ions are selected with a mass spectrometer (MS1). They are allowed to collide with the collision gas introduced for the purpose into a collision cell. As only the chosen parent ions can reach the collision cell, the fragment spectra obtained from a second mass spectrometer (MS2) will give direct information on the parent ions. The process could be repeated in the same way for the chosen daughter ions from the MS2. Multiple-stage experiments can be done in a quadrupole ion trap mass spectrometer or one fourier transform Ion cyclotron resonance mass spectrometer. In a trop, the experiment is performed in a different way. After choosing the parent ions, introducing the collision gas to induce the CID process and scanning the spectra, all the ions except the chosen daughter ions are ejected and the CID and the scanning again. For these two type instruments, many stages of CID are possible.

1.5.1 Metastable dissociation and collision-induced dissociation (CID) in mass-analyzed ion kinetic energy spectroscopy (MIKES)[1-56] experiments

There is a specific experiment called mass-analyzed ion kinetic energy spectroscopy (MIKES) which can only be performed with sector mass spectrometers in which the magnetic sector is positioned before the electric sector. In MIKES experiments, the electrostatic sector scan is recorded, while the magnetic field and the

accelerating potential are kept constant. CID experiments are performed in this way by choosing the parent ions according to momentum with the magnetic sector. The chosen ions then undergo the CID process in the collision cell which normally is put in the common focusing-point of a double focusing instrument between the two sectors. The fragmentation spectra then are acquired by the electric sector scans. As the electric sector is a kinetic energy analyzer, the ions are separated according to heir different kinetic energies. For the metastable dissociation experiments by MIKES, everything is the same as in the CID experiments excepting that there is no collision gas in the collision cell. The recorded spectra represent the fragments of the parent ions which have been undergone unimolecular dissociation in the second free-flight region between the two sectors.

It should be noted that during any fragmentation process, energy is released and converted into translational energy so that the fragment ion may be given an addition velocity component in any direction, opposing or supplementing the original velocity of the ion. The energy range then require a range of electrostatic analyzer voltages for transmission, so the MIKES spectrum is a relatively low-resolution spectrum.

1.5.2 Collision-induced dissociation (CID) in the capillary-skimmer region of an electrospray ionization source

The so-called capillary-skimmer dissociation (or nozzle-skimmer dissociation/ or orifice-skimmer dissociation) represents a special phenomenon in electrospray ionization (ESI). Fragments peaks can be recorded by the mass spectrometer when a suitable pressure and electric potential difference are applied in the so-called intermediate-pressure region between the capillary and skimmer in the ESI source. It

had been thought that the fragmentation energies came from multiple collisions between the ions and their ambient neutral particles when ions were accelerated by the potential difference applied in the region. The detailed process is more complicated than the above simple description[1-57]. This phenomenon gives the user of a one-stage mass spectrometer (on which an ESI source is installed) a very welcome tool to study the structure of sample molecules, as otherwise there are very few fragments peaks in an ESI spectrum. Quite a lot of effects are involved in the CID process in this region[1-58, 1-59]

1.5.3 The internal energy taken up during collision-induced dissociation

The maximum energy available to an ion in collision with a target gas is limited by their relative translational energy, called the center-of-mass collision energy E_{CM}. When the translation energy of the target gas is considered to be zero, E_{CM} is given by the following equation:

$$E_{CM} = \frac{m_g}{m_i + m_g} E_i \qquad (1\text{-}7)$$

the E_i is the translational energy of the incident (parent) ion, which depends on the ion's acceleration potential V_{acc} relative to the potential V_C of the collision cell:

$$E_i = q(V_{acc} - V_C) = ze(V_{acc} - V_C) \qquad (1\text{-}8)$$

From equation (1-7), when the incident mass m_i is increased the available center-of-mass energy drops accordingly. This is one of the basic reasons why large-mass ions will undergo the CID process less readily than the small ion. There are three ways to increase the available collision energy: 1) increase the mass of the target (or collision) gas $\mathbf{m_g}$, for example by using argon or krypton to change the helium; 2)

increase the accelerating potential of the source V_{acc}, (this is the advantage of the sector mass spectrometers as their ion sources must running at kilo-volts potentials); 3) increase the charge of the incident ion q, using higher charge states as the incident ion. All of the above three factors provide reasons to study the CID of large ions on sector instruments equipped with an ESI source.

It has been found that with low-energy and low molecular mass incident ions, a relatively large fraction of E_{CM} can be converted into internal energy, although this fraction decreases on increasing of the collision energy[1-60]. Using heavier target gases at low energies gives more fragmentation.

There are some limitations in high-energy CID. Using heavier target gases can cause significant scattering. The scattered fragment ions are lost and do not reach the detector when the scattering angle is too large. The heavier is the target gas, the larger it will be and loss by charge exchange during the CID process become important. Helium has a high ionization energy which can suppress charge exchange, and, as the lightest member of the inert gas family, the scattering effect is the smallest. Helium also appears to be most efficient inert gas for energy transfer via direct electronic excitation[1-61]

1.5.4 Translational energy loss during collision-induced dissociation

In a CID process, following the collision, an ion can have lost a fraction of its translational energy. If an electric sector is used to scan the fragment ion spectra of the parent (or incident) ion (MIKES experiment), this energy loss (which is also called a "Derrick shift")[1-62] will affect the positions of the fragments peaks. It is obvious that different fragments may have different energy shifts as they may formed via different pathways which require different energies. A study[1-63] has shown that the translational

energy loss can have a magnitude of tens of electronvolts for ions of m/z 1000 at incident ion energies of several kiloelectronvolts.

1.5.5 The pressure in the collisional cell and the collision times

The fragmentation efficiency in a CID process typically increases with increasing collision gas pressure. But at very higher gas pressures, collisional scattering begins to predominate so the overall efficiency falls again. As the direct measurement of the pressure in the collision cell is normally impossible, a useful technique is to use the observed pressure that attenuates the main beam of the ions by a given percentage. The higher is the collision gas pressure, the larger will be the chance of multiple collisions. It has been found that for an ion with a collision cross section of 5×10^{-16} cm^2 traversing a 1-cm collision region, a 30 % attenuation of the main beam on introduction of the collision gas will give the maximum overall efficiency and will represent 95 % of single, 5 % of double and 0 % of triple collisions[1-64].

1.6 The aim

The main focus of this doctoral project was to improve the performance of the electrospray ionization (ESI) source on the large scale double-focusing magnetic-sector mass spectrometer (MMM), all of which were home-made. The intention was to improve and modify the ESI source components and design and to redesign partially the ion optical system. The objective of the study was to investigate the effects of the potential difference between the heated stainless steel capillary (HCT) and the first skimmer in the so-called intermediate-pressure region on the characteristics of the ESI source. The original aim at the very beginning of this project was to study the collision-

induced dissociation (CID) of multiply charged peptides and small proteins with different charging states and different collision gases by MIKES on the above instrument. It became clear that CID in the collision cell was dependent upon the events in the ESI source.

1.7 References:

[1-1] I. W. Griffiths

Rapid Commun. Mass Spectrom. **11**, 2 (1997)

[1-2] E. Goldstein,

Eerl. Ber., **39**, 691(1886).

[1-3] W. Wien

Verhanal. Phys. Ges., **17**, (1898).

[1-4] J. J. Thomson

Rays of Positive Electricity and Their Application to Chemical Analysis,

Longmas Green, London, 1913.

[1-5] A. J. Dempster

Phys. Rev., **11**, 316 (1918).

[1-6] F. W. Aston,

Philos. Mag. VI, **38**, 707 (1919).

[1-7] W. Paul and H. S. Steinwedel

Z. Naturforsch., 8a, 448 (1953)

[1-8] W. Paul, H. P. Reinhard and U. von Zahn,

Z. Phys., **152**, 143 (1958)

[1-9] R. A. Marcus

J. Chem. Phys., **20**, 359 (1952).

[1-10] E. De Hoffmann, J. Charette and V. Stroobant

MASS SPECTROMETRY Principles and Applications,

translated by Julie TROTTIER and the authors,

published by JOHN WILEY & SONS.

[1-11] M. Barber, R. S. Bardoli, R. D. Sedgwick and A. H. Tyler

J. Chem. Soc., Chem. Commun., 325 (1981)

[1-12] M. Yamashita and J. B. Fenn

J. Phys. Chem., **88,** 4451 (1984)

[1-13] M. Yamashita and J. B. Fenn

J. Phys. Chem., **88,** 4671 (1984)

[1-14] M. Karas, D. Buchman and F. H. Hillenkamp

Anal. Chem., **57**, 2935 (1985)

[1-15] M. Yamashita and J. B. Fenn

J. Phys. Chem., **88,** 4671 (1984)

[1-16] A. J. Dempster,

Phys. Rev., **18**, 415 (1921)

[1-17] A. O. Nier,

Rev. Sci. Instrum., **18**, 398 (1947)

[1-18] M. S. B. Munson and F. H. Field

J. Am. Chem. Soc., **88**, 2681 (1966)

[1-19] M. A. Baldwin and F. W. Mclafferty

Org. Mass Spectrom., **7**, 1353 (1973)

[1-20] W. Aberth, K. M. Straub and A. L. Barligame,

Anal. Chem., **54**, 2029 (1982)

[1-21] A. M. Falick, G. H. Wang and F. C. Walls;

Anal Chem., **58,** 1308. (1986)

[1-22] H. D. Beckey

Principles of Field Ionization and Field Desorption in Mass Spectrometry,

Pergamon Press Oxford, 1977.

[1-23] R. D. Macfarlane

Anal. Chem., **55**, 1247A (1983)

[1-24] C. R. Blakney and M. L. Vestal

Anal. Chem., **55**, 750 (1983)

[1-25] M. L. Aleksandrov, L. N. Gall, V. N. Kransnov, V. L. Nikolaev, V. a. Pavlenko, and V. A. Shkurov

Dokl. Akad. Nauk. SSSR **277** 379 (1984)

[1-26] M. L. Aleksandrov, L. N. Gall, V. N. Kransnov, V. L. Nikolaev, V. A. Pavlenko, V. A. Shkurov, G. I. Baram, M. A. Gracher, V. D. Knorre, and Y. S. Kusner

Bioorg. Kim. **10**, 710 (1984)

[1-27] M. Dole, R. L. Hines, R. C. Mack, R. C. Mobley, L. D. Ferguson and M. B. Alice

J. Chem. Phys. **49**, 2240 (1968)

[1-28] J. B. Fenn, M. Mann, C. K. Meng, S. F. Wong, and C. M. Whitehouse

Mass Spectrom. Rev., **9**, 37 (1990)

[1-29] S. K. Chowdhury, V. Katta, and B. T. Chait,

Rapid Commun. Mass Spectrom., **4**, 81 (1990)

[1-30] P. Kebarle and L. Tang

Anal. Chem. **65**, 972 (1993)

[1-31] John B. Fenn

Int. J. Mass Spectrom. **200**, 459, (2000)

[1-32] A. T. Blades, M. G. Ikonomou and P. Kebarle

Ana. Chem. **63**, 2109 (1991)

[1-33] M. Wilm and M. Mann

Anal. Chem. **68**, 1 (1996)

[1-34] M. Wilm and M. Mann

Int. J. Mass Spectrom. Ion Proc. **136**, 167 (1994)

[1-35] M. R. Emmet and R. M. Caprioli

J. Am. Soc. Mass Spectrom., **5**, 605 (1994)

[1-36] Micromass company home Internet address:

Z-Spray Combined Inlet/Ion Source

http://www.micromass.co.uk/basics/Zspbtb.2.html

[1-37] B. Stevan

Patent: US 5756994 (1998-05-26)

[1-38] L. Jian and M. Moini

Ana. Chem. **72**, 20 (2000)

[1-39] S. A. Shaffer, D. C. Prior, G. A. Anderson, H. R. Udseth and R. D. Smith*

Anal. Chem. **70**, 4111 (1998)

[1-40] S. A. Shaffer, A. Tolmachev, D. C. Prior, G. A. Anderson, H. R. Udseth and R. D. Smith

Anal. Chem. **71**, 2957 (1999)

[1-41] T. Kim, A. V. Tolmachev, R. Harkewicz, D. C. Prior, G. Anderson, H. R. Udseth and R. D. Smith; H. Bailey, S. Rakov and J. H. Futrell

Anal. Chem. **72**, 2247 (2000)

[1-42] S. A. Aksyonov and P. Williams

Rapid Commun. Mass Spectrom. **15**, 2001 (2001)

[1-43] M. Karas and F. Hillenkamp

Anal. Chem., **60**, 2299 (1988)

[1-44] K. Tanaka, H. Waki, Y. Ido, S. Akita, Y. Yoshid and T. Yoshida

Rapid Commun. Mass Spectrom. **2**, 151 (1988)

[1-45] A. D. Nier;

Rev. Sci. Instrum., **11**, 212 (1940)

[1-46] A. D. Nier and T. R. Roberts;

Phys., Rev., **81**, 507 (1951)

[1-47] R. E. Ferguson, K. E. McKulloh and H.M. Rosenstock

J. Chem. Phys., **42**, 100 (1965).

[1-48] H. Kienitz

Massenspektrometrie, Verlag Chemie, Weinhein, 1968.

[1-49] A. E. Cameron and D. F. Eggers

Rev. Sci. Instrum., **19**, 605 (1948)

[1-50] W. C. Wiley and J. B. Mclaren

Rev. Sci. Instrum., **26**, 1150 (1955)

[1-51] G. C. Stafford, P. E. Kelley, J. E. Syka, W. E. Reynolds and J. F. J. Todd

Int. J. Mass Spectrom, Ion Process. **60**, 85 (1984)

[1-52] H. Sommer, H.A. Thomas and J. A. Hipple;

Phys. Rev., , **76**, 1877 (1949)

[1-53] H. Sommer, H.A. Thomas and J. A. Hipple;

Phys. Rev., , **82**, 697. (1951)

[1-54] C. L. Holliman, D. L. M. Rempel and M. L. Gross

Mass Spectrom. Rev., **13**, 105 (1994).

[1-55] J. H. Beynon, R. G. Cooks, J. W. Amy, W. E. Baitinger and T. Y. Ridley

Anal. Chem., **45**, 1023A (1973)

[1-56] J. R. Chapman

Practical Organic Mass Spectrometry: A Guide for Chemical and Biochemical Analysis

2nd edition, John Wiley and Sons Ltd.: Chichester, (1993)

[1-57] C. Collette, L. Drahos, E. De. Pauw and K. Vékey

Rapid Commun. Mass Spectrom. **12,** 1673 (1998)

[1-58] B. B. Schneider, D. J. Douglas and D. D. Y. Chen

J. Am. Soc. Mass Spectrom. **12,** 772 (2001)

[1-59] B. B. Schneider, D. J. Douglas and D. D. Y. Chen

Rapid Commun. Mass Spectrom. **15,** 249 (2001)

[1-60] K. L. Busch, G. L. Barinaga and S. A. McLuckey

Mass Spectrometry/Mass Spectrometry: Techniques and Applications of Tandem Mass Spectrometry

VCH, New York, (1988)

[1-61] C. D. Ouwerkerk, S. A. McLuckey, P. G. kistemaker and A. J. Boerboom

Int. J. Mass Spectrom. Ion Processes, **56,** 11 (1984)

[1-62] G. M. Neumann and P. J. Derrick

Org. Mass Spectrom. **19,** 165 (1984)

[1-63] H. J. Cooper and P. J. Derrick

Mass Spectrometry in Biomolecular Science, 201-259

R. M. Caprioli, A. Malorni and G. Sindona (eds.)

Kluwer Academic Publishers. Printed in the Netherlands. (1996)

[1-64] J. L. Holmes

Org. Mass Spectrom. **20,** 169 (1985)

Chapter 2: **Instrumentation**

2.1 The grand-scale reverse-geometry two-sector mass spectrometer with electrospray ionization source

The main instrument used in this thesis was a grand-scale reverse-geometry double-focusing two-sector mass spectrometer with electrospray ionization source (ESI). It was called the MMM instrument in the laboratory which referred with a sense of irony to the "Magnificent Mass Machine". The "reverse-geometry" referred to the fact that the magnetic sector was positioned in front of the electric sector in the instrument. The double-focusing principle was mentioned in Chapter 1 in this thesis. This instrument was constructed in part at La Trobe University, Australia, from 1976 to 1981 and moved to the University of New South Wales, Australia, in 1981. It was then transferred to the University of Warwick, U. K. in 1987. It was equipped originally with a field desorption (FD) source[2-1] and an electron ionization (EI) source. Then a matrix-assisted laser desorption/ionization (MALDI) source[2-2, 2-3] was designed and made. Its original electrospray ionization source was designed and fabricated between 1994 to 1997[2-4].

In this chapter, the MMM instrument itself will be described. Its original ESI source, the original ion optics system and the developments made on them during my study will be described in Chapter 3. The hybrid double focusing two-sector/time-of-flight (MAG-TOF) instrument with a MALDI source and the Fourier transform ion cyclotron resonance (FT-ICR) instrument with an ESI ion source will also be simply described here, as some samples were run on them. The intention of these experiments was to compare the results with those obtained from the MMM instrument with ESI

source, as the original doctoral project was to study the high-energy collisional-induced dissociation (CID) of peptides and the proteins.

2.1.1 The whole MMM instrument and the safety devices

The schematic diagram of the instrument is shown in the Figure 2 -1 and its photograph shown in Figure 2 - 2. Its unusually large scale gave a total 6.5 m ion flight path from the source slit (α-slit) to the last detector slit (γ-slit). With its strong magnetic field, a singly charged ion with mass 8000 Da could be transmitted at 8 kV accelerating voltage from the ion source to the detector.

The average pressure within this "C" shaped two-sector instrument was 10^{-7} mbar maintained by seven Edward *700 L/s* oil diffusion pumps[2-5]. Seven ionization gauges[2-6] had been put at different positions above or near each diffusion pumps to

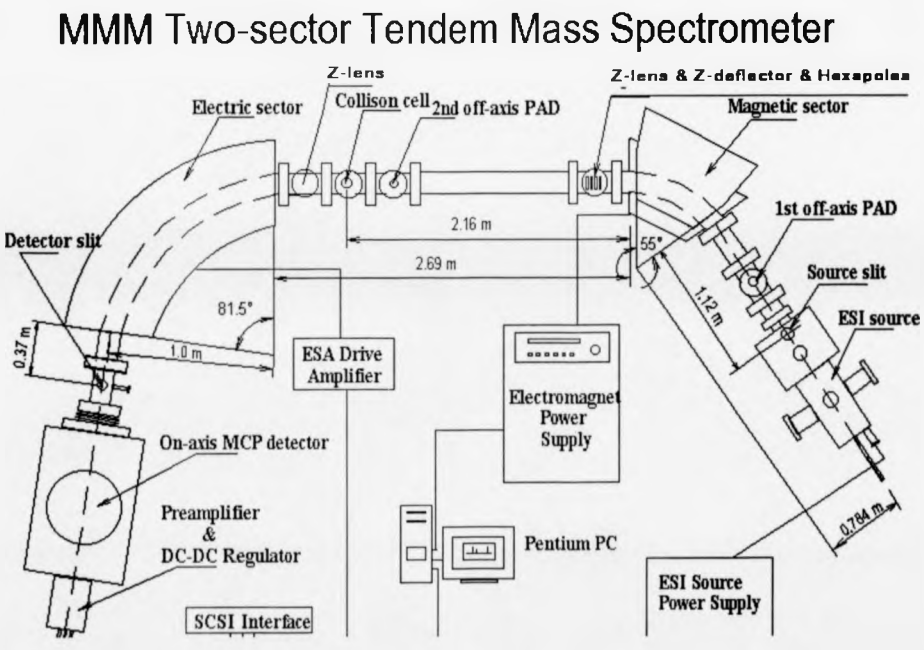

Figure 2-1

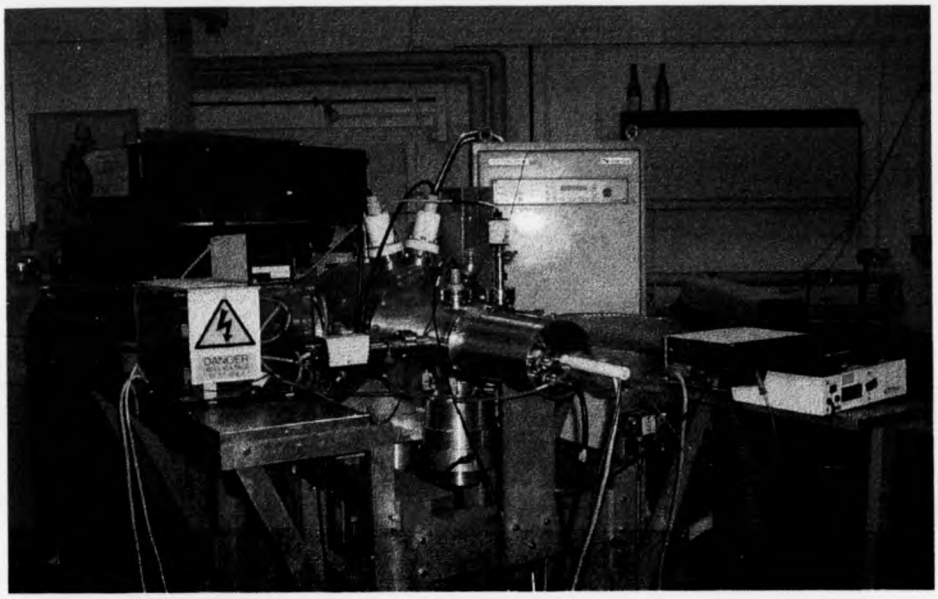
DANGER

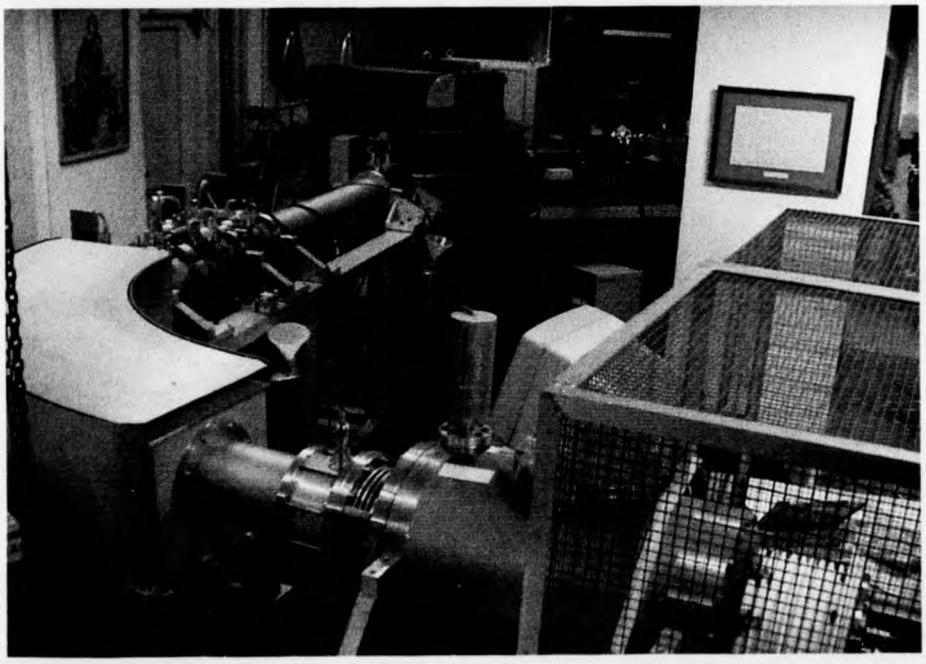

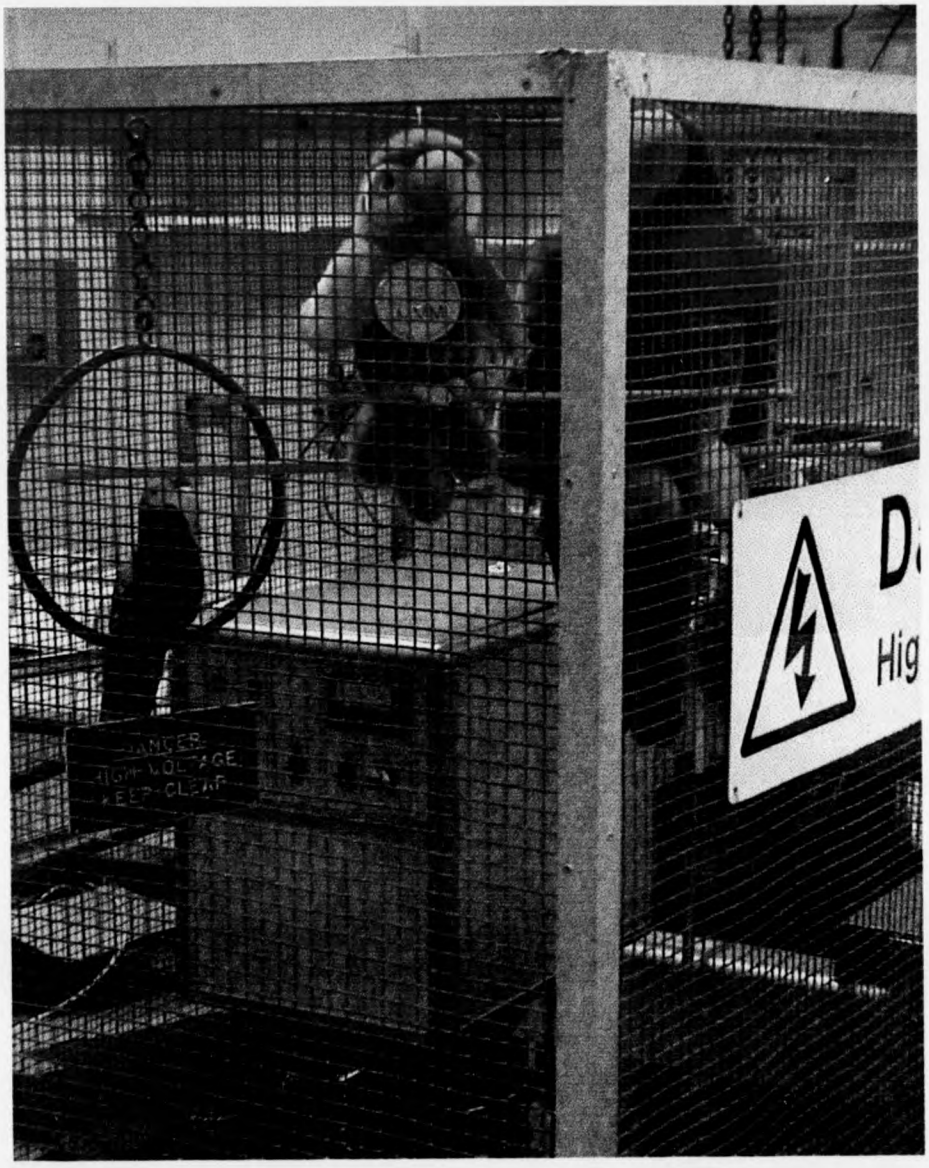

Figure 2-2 Photos of the MMM instrument

monitor their performance and the vacuum of the instrument. The ionization gauge above the detector chamber could only be used when the last detector was not in

working status. The oil diffusion pumps were backed by five rotary pumps[2-7]. There were three Edwards E2M40 rotary pumps each capable of a pumping speed of 42.5 m^3/h or 11.80 L/s (at 50 Hz, with 1×10^{-4}mbar vacuum limit)[2-7]: one for the diffusion pump under the collision cell, another one for two diffusion pumps before and after the collision cell, and the last one for two diffusion pumps under the electrostatic analyzer and the last detector. Another two small rotary pumps were backing the diffusion pumps before and after magnetic sector. The backing pressures normally in the range 3×10^{-2} ~ 7×10^{-2} mbar were monitored by the Pirani gauges[2-8] positioned near the output of the oil diffusion pumps.

There were three vacuum regions in the ESI source. The first vacuum region was pumped originally by an Edwards E2M40 rotary pump, and later by an E1M275 rotary pump with pumping speed 292 m^3/h (at 50 Hz, 4×10^{-2}mbar vacuum limit)[2-7]. The pressure in this region could not be measured for the reason of gas electric breakdown, but the pressure near the rotary pump was monitored by one detector head of the COMBIVAC IT 23 unit [LEYBOLD INFICON, Bonner Strasse 498 (Bayenthal), D-50968 Cologne]. The second vacuum region was pumped by a 360 L/s turbomolecular pump. The pressure was monitored by another detector head of the COMBIVAC IT 23 unit. The third vacuum region was pumped by the Edwards *700 L/s* oil diffusion pump which was the same as those in the main part of the instrument. The vacuum was monitored by an ionization gauge. Both turbomolecular pump and oil diffusion pump were backed up by an Edwards E2M40 rotary pump. The backing pressure was monitored by another Pirani gauge.

There was a new safety unit designed by Mr. A. W. Colburn which monitored:

1) The backing pressure readouts from all Pirani gauges (not allowed to be higher than a certain setting value — the pressure trip).
2) The heaters' electric currents values of all diffusion pumps (must be between high and low current settings — current trip). Before, in the case that one of the two heaters (especially the small central 350 W heater) of a certain diffusion pump was broken, it would be quite difficult to find the problem if the ionization gauge at that region was not working properly at the time.
3) The signals of the thermal snap switches[2-5] which were mounted on the fixing plate and which were permanently attached to the cooling coils on all diffusion pump bodies. If there was not enough cooling water, the temperature of the cooling water was too high, the backing pressure was too high or there was an excessive flow of the electric current — any of these factors could increase the body temperature of the diffusion pump above its normal operating level, in which case the heat would make the thermal snap switch operate, cutting off the current of this diffusion pump — thermal trip. The problem of this trip was its slow reaction speed.
4) There also a self-function-check performed every several seconds in the safety unit to make sure the safety unit itself was working well. If anything went wrong in the unit, it would also cut off the diffusion pumps' heating current (safety unit trip).

Any one of the tripping signals would make the safety unit operate to disconnect all diffusing pump heaters from the electrical supply instantly and leave the appropriate warning light on to indicate where the problem was.

The previous safety unit only had the thermal snap switches whose responding speeds were relatively slow. In the case of the backing vacuum being suddenly lost (all the backing rotary pumps were suddenly off but the diffusion pumps were still on), the

slow switch speed would become still slower as the cooling water system would still be working well and especially when the ambient temperature was low. This would cause serious problems to the instrument. The diffusion pump oil vapor would contaminate the whole instrument and oil remaining in the diffusion pumps could be carbonized. This happened during my study. This is the reason why the new safety unit was designed and built.

Another safety unit was the chiller control unit. The chiller circulated the cooling water for all the diffusion pumps, all the turbomolecular pumps, the magnetic coils and magnetic power supply. If the temperature of the cooling water in the chiller was too high or too low, the water level in the chiller tank was too low, or there was a flow fault, the chiller control unit would switch the chiller off and let the mains water supply do the cooling job.

There was also a safety unit for the magnetic-sector power supply and magnet coils which will be mentioned later in this chapter.

2.1.2 The electrospray ionization (ESI) source and ion optics system of the MMM instrument

The details of the ESI source and ion optics system used on the MMM instrument before and after improvements made during my study are described in Chapter 3. It should be pointed out that the source slit (α slit) was situated at the first focal point of this double-focusing instrument. The other two focal points of the MMM instrument were situated at the collision cell near the β-slit and the last detector slit (γ-slit).

2.1.3 The magnetic sector of the MMM instrument

The magnetic sector was designed and constructed to provide high mass and high resolution separations for ions according to their momenta-to-charge ratios through its large physical size and strong magnetic field. It had an angle of 55.0° with a radius of 780 mm and a pole gap of 22 mm. Its yoke was composed of 245 laminations which were electrically insulated from each other. Six coils each of 625 turns were positioned as close as possible to the pole shoes, three above and three below the gap. With a total current of 80 A through its water-cooled coils, the magnetic induction between the poles was greater than 1.5 tesla give a range to the instrument of up to m/z = 8000 for 8 kV accelerating potential.

Both the magnet and its power supply were cooled by the same water flow. The cooling water flow rate and the temperature of the power supply were monitored by a safety device in the power supply unit (System 8000 Magnetic Power Supply, DANFYSIK). It would switch off the current through the magnet when the cooling water rate was too slow or the temperature was too high. The position of the whole magnet could be finely adjusted in the perpendicular direction (y-direction) to the ion flight path (x-direction) and in the horizontal level.

A magneto resistor positioned in the pole gap monitored the field strength of the magnet and in conjunction with a sweep generator was used to control the magnetic field in either stationary or sweeping mode. The current was digitally controlled to 18 bits ($2^{18} = 2.6 \times 10^5$ total steps) providing 4 ppm setting/step resolution. To record a mass spectrum the magnetic field was swept as a function of time under the control of the operating software in the computer. To sweep from full-field to near zero required a minimum of 40s.

During the instrument tuning, electric-sector scan in collision-induced dissociation (CID) or mass-analyzed ion kinetic energy spectroscopy (MIKES) experiments, the magnetic field would be held constant and only one momentum-to-charge ratio ion would be selected to be focused into the collision cell.

The spectra of the magnetic sector scan were calibrated by a file with the mass readout value (Da) vs. the setting value of the current (mA) through the magnetic coils. Figure 2-3 shows the file presented by a Microsoft Excel picture. The function was obtained using a "least squares" method in the calculation. In the figure, it could be seen the mass readout was perfectly matched with current through the magnet coil by the function:

$$y = -8.27611E\text{-}14x3 + 7.8452E\text{-}08x2 - 6.84155E\text{-}4x + 27.92595$$

$$R2 = 0.9999 \qquad (2\text{-}1)$$

Here the y was the mass readout in Da; x was the magnet current in mA. The R^2 was the coefficient of determination comparing estimated and actual y-values and ranges in value from 0 to 1. If R^2 is 1, there is a perfect correlation in the sample - there would be no difference between the estimated y-value and the actual y-value. So in Excel or Origin, the above function could be used to calibrate the mass spectra from a magnetic scan. The calibration region in Figure 2-3 was from 19 to 3500 Da, since in ESI experiments the above region was enough. The calibration region could be extended in the same way to ~ 8500 Da.

2.1.4 The collision cell of the MMM instrument

The collision cell was situated between the sectors at their common direction-focusing point (the second focusing point of the instrument). The cell was composed of

During the instrument tuning, electric-sector scan in collision-induced dissociation (CID) or mass-analyzed ion kinetic energy spectroscopy (MIKES) experiments, the magnetic field would be held constant and only one momentum-to-charge ratio ion would be selected to be focused into the collision cell.

The spectra of the magnetic sector scan were calibrated by a file with the mass readout value (Da) vs. the setting value of the current (mA) through the magnetic coils. Figure 2-3 shows the file presented by a Microsoft Excel picture. The function was obtained using a "least squares" method in the calculation. In the figure, it could be seen the mass readout was perfectly matched with current through the magnet coil by the function:

$$y = -8.27611E\text{-}14x3 + 7.8452E\text{-}08x2 - 6.84155E\text{-}4x + 27.92595$$

$$R2 = 0.9999 \qquad (2\text{-}1)$$

Here the y was the mass readout in Da; x was the magnet current in mA. The R^2 was the coefficient of determination comparing estimated and actual y-values and ranges in value from 0 to 1. If R^2 is 1, there is a perfect correlation in the sample - there would be no difference between the estimated y-value and the actual y-value. So in Excel or Origin, the above function could be used to calibrate the mass spectra from a magnetic scan. The calibration region in Figure 2-3 was from 19 to 3500 Da, since in ESI experiments the above region was enough. The calibration region could be extended in the same way to ~ 8500 Da.

2.1.4 The collision cell of the MMM instrument

The collision cell was situated between the sectors at their common direction-focusing point (the second focusing point of the instrument). The cell was composed of

two 64-mm-i.d. stainless steel discs attached to the end of a 10-mm-long cylinder made from pactene (machinable plastic). So the cell was 10-mm-long in the direction of the travel of the ion beam (x-direction). The two stainless steel discs of the collision cell

Figure 2-3: calibration of the magnetic sector current X(mA) for the mass readout Y(Da) in the MMM instrument

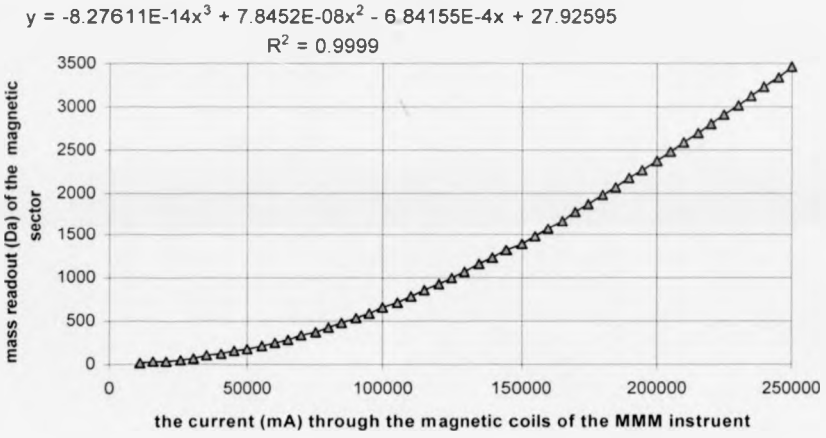

were isolated from the whole instrument, so the collision cell could be floating to the potential wanted. The dimensions of the entrance and the exit slits were 2-mm-wide (y-direction) and 10-mm-high (z-direction). The adjustable β-slit could be positioned either before or after the collision cell. In my experiments, it was kept at 1-mm (y-direction) . The collision cell and the β-slit were mounted on an aluminum support attached to the flange of the collision T-piece.

In order to restrict the collision-gas flow to the rest of the instrument, the collision cell T-piece and neighboring T-pieces were fitted with baffles at either ends containing apertures of 6-mm-thick (x-direction) and 20-mm-wide (y-direction) × 20-mm-high (z-direction).

The collision gas was introduced into the cell via a precision variable leak (Series 203, GRANVILLE-PHILLIPS CO., Boulder, Colorado, U. S. A.). The pressure in the collision was indirectly monitored by the ion gauge, which provided a measure of the pressure outside of the collision cell in the T-piece. Normally for a CID experiment, the flow of the collision gas needed was such as to depress the parent ion signal to 60% ~ 70% of its original strength[2-9].

2.1.5 The electrostatic analyzer of the MMM instrument

The electric sector was of cylindrical design and consisted of two parallel curved plates. The included angle of the electric sector was 81.510° and the radius of the central ion path was 1000.01 mm. The sector plates stood 150 mm high, with 33.51 mm gap between them and there were two Matsuda[2-10] plates at the top and bottom. Herzog[2-11] plates were positioned at the ends of the sector plates.

Two 3kV Fluke power supplies applied equal, but opposite potential to the sector plates with negative on the inner plate and positive on the outer plate for the positive ions. The potentials were applied through the electric sector drive amplifier, which was controlled by a digital-to-analogue converter (DAC) and ion counting unit. The same control software for the magnetic-sector in the computer gave an analogue voltage requirement to this unit. The unit then translated the requirement to the percentage of the sweep range that was set on the electric sector drive amplifier by hand. Finally, the electric sector drive amplifier output the required potentials to the electric sector plates.

The electric sector scan was digitally controlled to 18 bits (2^{18}) steps providing little less than 4 ppm setting/step resolution. So in order to get higher resolution spectra, it was necessary to narrow the sweep range and make the step size smaller.

As the relationship between the a fragment ion's mass and potential applied on the electric sector was linear, the calibration process was much simpler than that in the magnetic sector. Zero potential for 0 Da was used as one point and the potential of an ion and its mass (Da) was used as the second point. A line was drawn because these points. All ions' masses could be calculated from their corresponding potential readouts.

2.1.6 The detectors and the computer control system of the MMM instrument

There were two off-axis multipliers (ETP Ltd., Australia), one situated prior to the magnetic sector and other prior to the collision cell chamber. The off-axis potential used in experiments was -15 kV. The working potential for the multiplier was - 2.0 kV. The signal was measured by an electrometer (602 Solid State Electrometer, Keithley Instruments).

The final detector was an AF180H multiplier with the current gain 10^7 at -2kV working voltage(ETP Electron Multipliers, 31 Hope Street Ermington, NSW, 2115, Australia). There were two metal grids positioned after the γ slit (the collector γ slit was positioned at the last focusing point of the MMM instrument) and immediately before the last detector. The post accelerating potential applied between these two grids was - 10 or - 20 kV. These two grids made the post-accelerating field much smoother and prevented the possibility of the defocusing by the uneven electric field.

The detector could be floated up to ±30 kV or more for the post-accelerating to improve high-mass sensitivity. High-mass ions had relatively low momenta compared with small ions at the similar ion energies. This might have led to insufficient secondary electron emission when such ions bombarded upon the first dynode of the electron multiplier. Also the low-mass fragment ions formed by the CID or the MIKES processes might be discriminated against due to their correspondingly low momenta.

The ion signal counts from the electric multiplier were transferred down a fiber optic cable to a 32-bit ($2^{32} = 4.29 \times 10^9$) 400 MHz ion counting system connected to an IBM PC computer. What was obtained from the final detector was the actual numbers of ions which were detected by the last detector.

2.2 The hybrid double-focusing two-sector and time-of-flight (MAG-TOF) instrument with a MALDI source

2.2.1 The general information

Figure 2-4 shows the whole schematic layout and Figure 2-5 shows photographs of the MAG-TOF Mass Spectrometer. The whole instrument was half commercial-made and half home-made. The home designed and made MALDI ion source with its parallel TOF formed the parallel TOF stage. The MALDI ion source combined with existing the Kratos Concept H double-focusing two-sector mass spectrometer (DFMS) (Kratos Analytical, Manchester, UK) and the off-axis post accelerating detector (PAD) formed the MS1 stage. The home made ion bounch, Quadratic-field ion reflection plus the Chevron MCP detector formed the MS2 stage. The electric sector, magnetic sector and post accelerating detector were directly controlled by the Concept DFMS console. The laser, the MALDI source stepper motor, the parallel TOF, the ion buncher and the

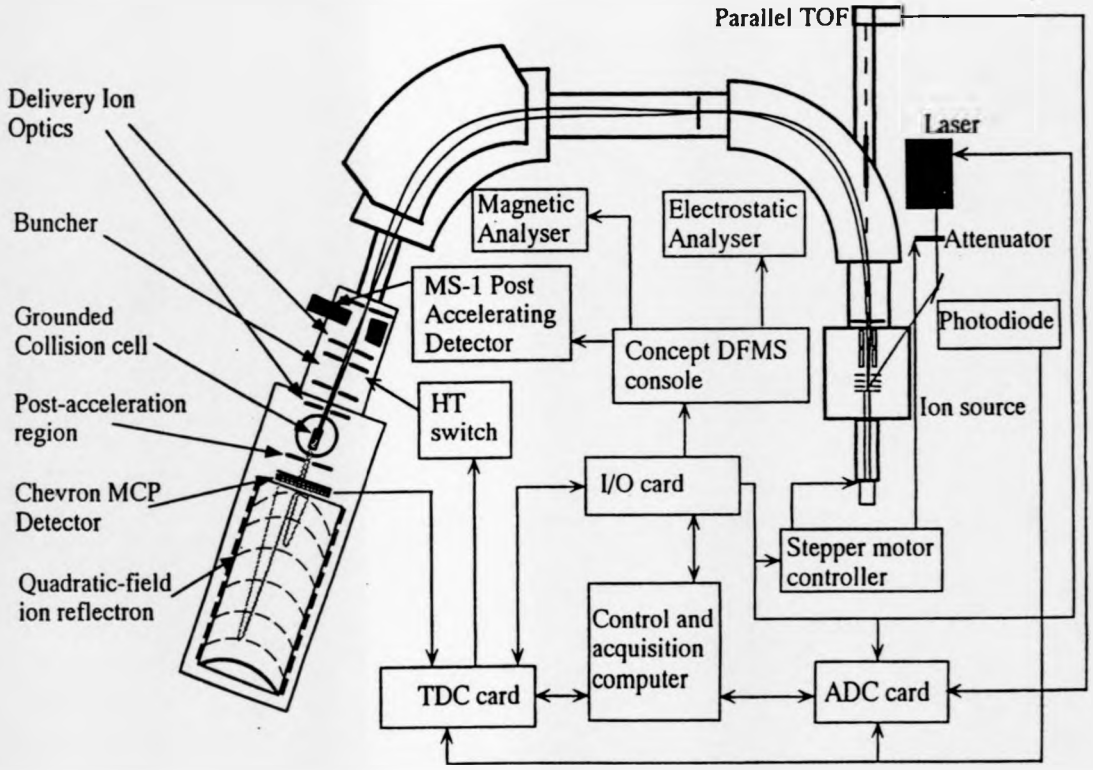

Figure 2-4 Scheme showing the layout of the magnetic-sector/time-of-flight tandem mass spectrometer (MAG-TOF). DFMS is the double-focusing mass spectrometer (referred to as MS-1); MCP is microchannel plate; HT is high tension (i.e., high electric potential).

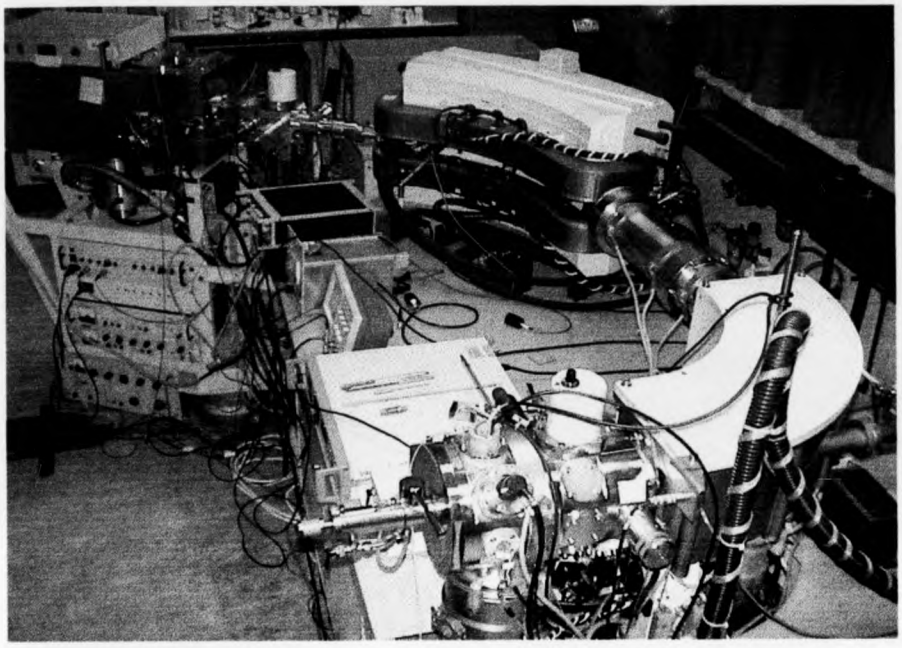

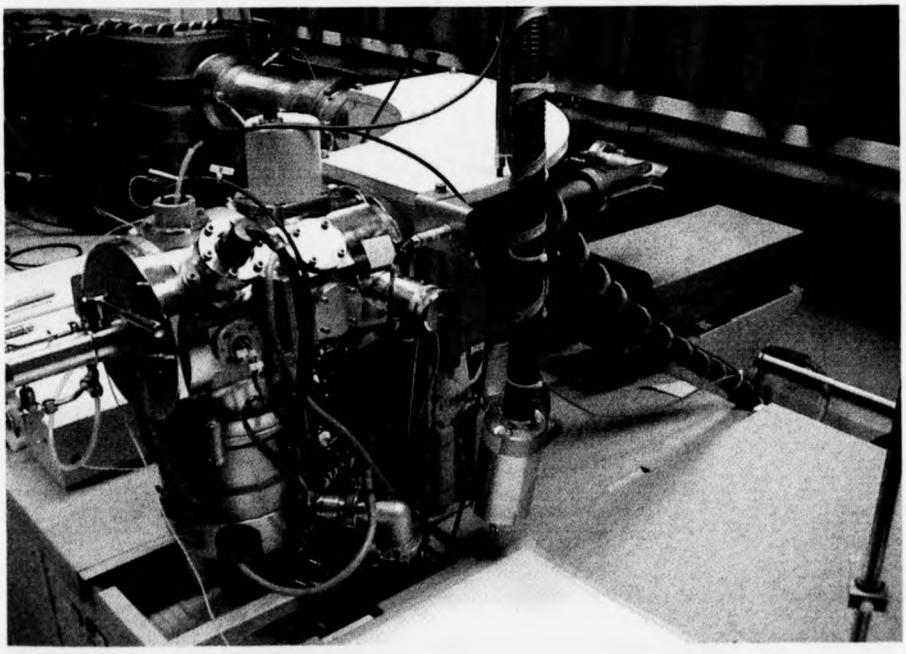

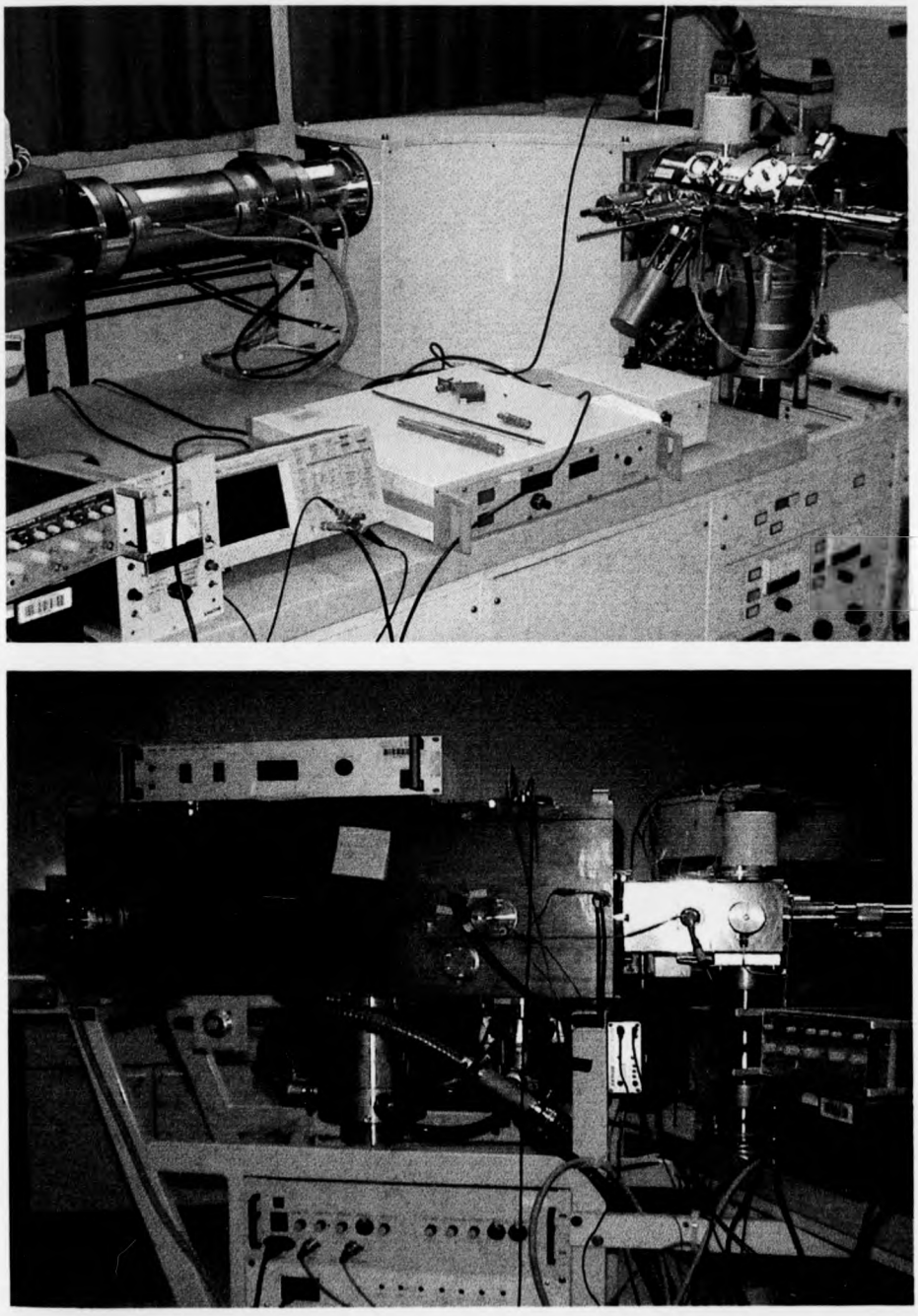

Figure 2- 5 photos of the MAG-TOF instrument

Chevron MCP detector were controlled by control and acquisition computer. The detailed designing information of the whole instrument was published in reference [2-12].

Using the TOF as the MS2 stage will largely increase the sensitivity of the tandem mass spectrometer, as all the fragments of the parent ion will be recorded without loss.

2.2.2 The MALDI source, the Parallel TOF and the TOF-1 working mode

The instrument used a nitrogen laser (Laser Science Inc., Newton USA. Model VSL337ND) as desorption and ionization laser with 337-nm wavelength, 3-ns time length of light pulse and 250-μJ maximum energy-per-pulse output power. A variable density wheel attenuator (Ealing Scientific) was used to control the final laser power reaching the sample surface.

The sample with the assisting matrix was mounted on the inner surface of the sample probe. Two stepper motors installed on the sample probe outside end allowed the computer to control the inner sample surface position in vertical (z-direction) and horizontal (y-direction) directions, in this way each laser shot would fire on new sample surface not hit before.

The accelerating electrode was held on 8 kV potential with the source slit grounded. A singly charged ion produced by the source would have 8 keV laboratory-frame translational energy after flying out of the source slit.

A hole had been drilled through the outside plate of the electric sector at the point coaxial with the optical axis of the ion source (in x-direction, ion flight direction) . There was also a hole through the vacuum chamber of the electric sector on the same

axis and a stainless steel tube had been welded at this point to form the total ion flight tube. This allowed the linear time-of-flight operation mode (TOF-1) (during this time, the electric sector was grounded). The ion signal was monitored by an ETP Pty. Ltd. electron multiplier. The resolution achieved here was relatively poor, which was directly linked with the energy spread of the ions produced by the MALDI source. This operation mode only provided a simple method for the operator to monitor the source working conditions and the results of adjustments upon ion production.

2.2.3 The electrostatic analyzer

The electric sector comprised two curved plates with a 90 degree sector angle and 381-mm mean radius. There were hexapoles after the electric sector to adjust the shape of the ion beam and to rotate the ion beam back into line with the slit system of the instrument.

The hole mentioned above on the outside plate of the electric sector was small enough to avoid the possible disturbance to the electrostatic field in the sector during the normal operation.

2.2.4 The magnetic analyzer

The magnetic field was produced by an electromagnetic with a 60 degree sector angle and 686-mm central radius. The magnet was water-cooled. Its temperature sensors monitored the temperature of the magnet coils. If the coils were overheated for some reason, for example, the cooling water supply was off., the control system would have cut off the magnet current.

The z-direction Einzel/deflector lens before the magnetic sector also adjusted the position of the beam in the vertical direction (z-direction) and let it enter the magnetic

sector in the right direction. The quadrupole current shims bonded to the pole of the magnet pole face allowed masses to be focused at the collector slit with optimum resolution over a wide mass range.

The whole magnet could be adjusted in position in the direction perpendicular to the horizontal plane of the ion flight path.

2.2.5 The MS-1 Post Accelerating Detector (PAD) and the electric-magnetic (EB) sector working mode

There was an off-axis post accelerating detector (PAD) located after the exit-slit of the magnetic sector. The electric sector and the magnetic sector could be set to pass only ions of specific m/z.. The chosen precursor could be detected by this PAD and its signal from the preamplifier was monitored by a LeCroy 7200A oscilloscope.

The electric-magnetic (EB) sector working mode provide a necessary method to tune the instrument to the optimized condition.

2.2.6 The ion buncher

The double-focusing electric-magnetic sector MS-1 reduced the spatial aberration of the ion packet, but it could not reduce the temporal aberration caused in part by the ions initial energy spread of the MALDI source. Ions with the same mass but different initial energies reached the exit-slit of the magnetic sector at different times.

The ion buncher was used here as a time-compressor to compensate the temporal aberration. It consisted of two electrodes with rectangular slits made of 1-mm thick stainless steel plates and separated by 30 mm distance. The first electrode was connected with the high-voltage push-pull switch (Behlke, Frankfurt, Germany). The

second plate was grounded. A typical potential applied on the fist electrode was 3 kV with 20 ns time duration. This allowed the containment of 8 keV ion packet with 25 eV energy spread from the MALDI source. The time of the high potential applied on the first plate was controlled by the main computer. There was a necessary delay after the computer received a zero-time signal from the photodiode placed in the path of a small reflection of the laser beam. The ion buncher, the collision cell and the post-acceleration region constituted a virtual ion source exactly in the object plane of the ion mirror. So all the ions with same mass and different energies and different angles, starting simultaneously from this virtual source (at the exit slit of the collision cell), were time-focused by the ion mirror on the detector. It should be noticed that the ions would have translational energy between 8 ~ 11 keV after they left the ion buncher.

The simple principle of the ion buncher was that before the broad ion packet fell into the buncher, both of its electrodes were grounded. So the ions flew freely with their initial temporal spread. When the ion packet fell within the ion buncher, a high voltage pulse was applied to the first electrode and the second electrode was still grounded. In this way a strong electric field was formed. Those ions which flew faster at the head of the ion packet would be much near the second electrode and would be accelerated less than those which flew slower at the end of the ion packet. The originally slow ions would be accelerated much more in the ion buncher, and they would catch up with the originally fast ions. the overall effects was that all ions reached the virtual ion source plain at the same time but with a larger energy spread.

2.2.7 The collision cell and post-acceleration region

The collision cell was situated after the ion buncher and before the ion mirror. It was designed to sustain a collision gas density of 10^{16} molecules/m^3. When the inside pressure in the collision cell was of the order of magnitude of 10^{-4} mbar, the pressure outside the collision cell in the differential pumping region would have been approximately 10^{-5} mbar. The pressure between the this pumping region and the high-vacuum region was less than 6.65×10^{-7} mbar. The collision cell was 10 mm-length in the ion-flight direction (x-direction) and slits of the collision cell were 7 mm-high (z-direction) and 1 mm-wide (y-direction). The stainless steel collision cell was mounted in the top of the differential pumping chamber. The collision gas was controlled by a Negretti leak valve and sent directly through a 2 mm internal-diameter polytrafluoroethene (PTFE) tube from the feedthrough at the bottom of the differential pumping chamber to the collision cell.

The post-acceleration region was set after the collision cell. An extraction electrode, 5 mm away from the differential chamber, was floated at -2.15 kV. It was designed with a special shape to provide a low divergence for the low m/z fragment ions.

2.2.8 The quadratic-field ion mirror, the chevron MCP detector and the TOF-2 working mode

The ion mirror was based on the following equation which describes a quadratic-field:

$$U(x,y,z) = \frac{k}{z}(x-a)^2 - \frac{k}{z}y^2 + c \qquad (2-1)$$

The coordinate system used here has x = y = z = 0 for the center of the collision cell exit slit. U(x, y, z) is electrostatic potential. a and c are constants. (x is the direction of the ion flight from the cell, z is the vertical direction and the y is the horizontal direction)

The whole quadratic-field ion mirror was made from four flat fiberglass plates (520 mm × 150 mm), initially coated with copper layer (printed circuit boards). The inner copper layer were etched to create the electrodes needed. There were 38 electrodes. The shape of electrodes on the top and bottom plates followed the quadratic equation for U (x, y). The electrodes on both side were parallel, corresponding to field-free z-direction. There were 2 mm gaps between the electrodes etched out of the copper layer with 5 μm accuracy to separate the different potential regions. The widths of the electrodes changed from 25 mm to 5 mm from the entrance to the bottom of the mirror to reduce the number of different resistors required in the resistor chain. The mirror was held together by two aluminum frame plates at each ends and three stainless steel rods. Two long screws supported the end of the mirror against the inner surface of the vacuum chamber, so it could be used to adjust the tilt angle of the mirror in the vertical direction.

The front flange was a 1 mm-thick stainless steel plate directly mounted on the aluminum frame with a 80 mm × 100 mm hole covered with high transmission Buckbee-Mears 70 mesh to allow ions to reach the detector. There were also two 60 mm-i.d. holes covered with mesh in the front flange for efficient pumping. The back flange was a stainless steel electrode of hyperbolic shape. The distance between the two flanges was 550 mm. The two 100 × 80 mm Galieo (Sturbrdge, MA, USA) microchannel plates (MCP) were mounted above the ion inlet slit and typical working potentials were 2 kV.. The pyramidal anode was located 10 mm behind the rear MCP with a potential drop of about 500 V across the gape.

The entrance of the mirror was maintained at the same potential - 2.15 kV as the extraction electrode after the collision cell. The end of the mirror was maintained at + 12 kV. Other electrodes' potential were supplied by the corresponding metal-film resistors (Welwyn, Belington, UK) of resistivities between 0.5 to 1.5 MΩ from the resistor chain which distributed the potential from a power supply (HD Technology, Manchester, UK). The two closest electrodes to the detector used outside resistors which could be adjusted during operation to achieve the best resolution.

The main computer was a Pentium 90 MHz PC with date acquisition software made by HD Technologies, Manchester , UK. The MS-1 double-focusing mass spectrometer was controlled by Mach 3 software through a Sun working station.

In the MS-2 working mode, the MS-1 stage was used to choose the parent ions with specific m/z, the ion buncher time-compressed the parent ion packet, in the collision cell the parent ions collided with the target collision gas, the ion mirror separated all fragment ions according to their mass-to-charge, and at the end the detector recorded the signals of all fragment ions and the parent ions. Resolution of 4000 was achieved in the fragment ion spectra.

2.3 The FT-ICR mass Spectrometer

2.3.1 The general information

The Bruker BioAPEX -94 e Fourier transfer ion cyclotron resonance (FTICR) mass spectrometer (Bruker Daltonics, Billerica, USA) had a passively shielded 9.4 T central-field superconducting magnet (Magnex Scientific Ltd. Abington, UK) (Figure 2-6: the photo of the FTICR instrument) with a 60 mm-i.d., 60 mm-long cylindrical INFINITY^{TM} ICR cell [2-14]. The magnet was cooled with a liquid helium core which was

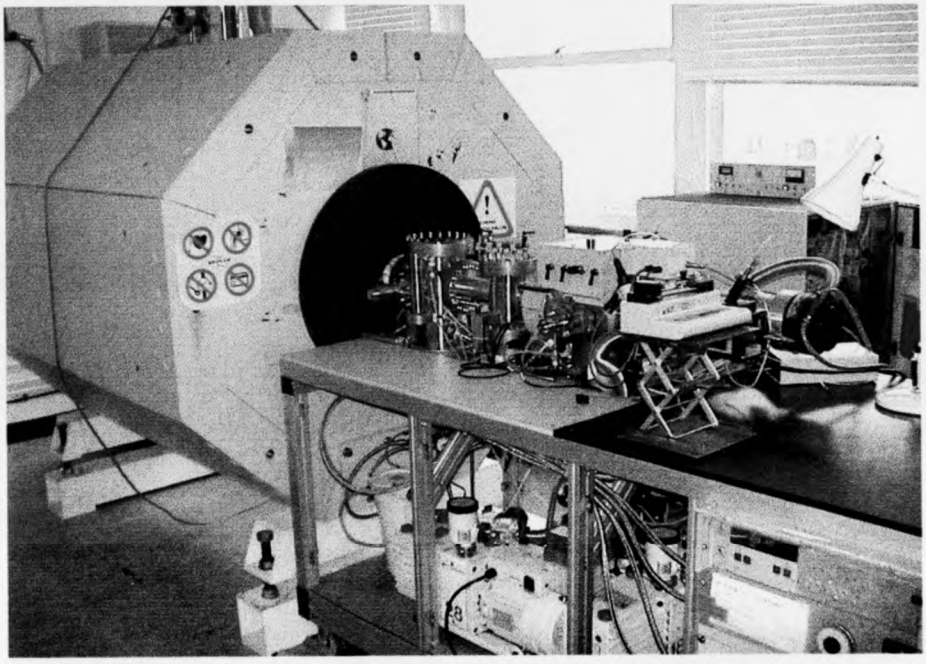

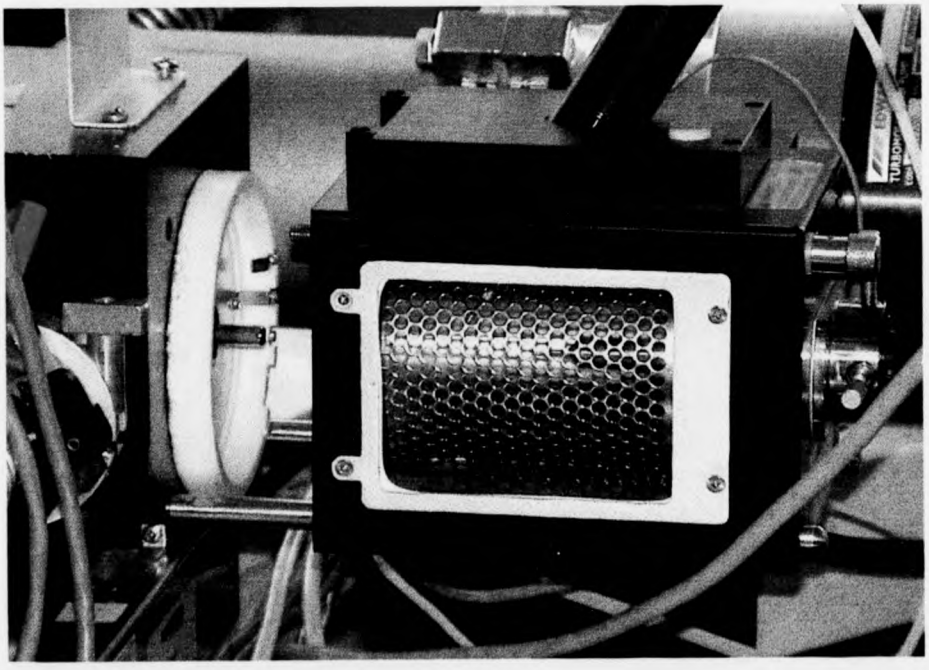

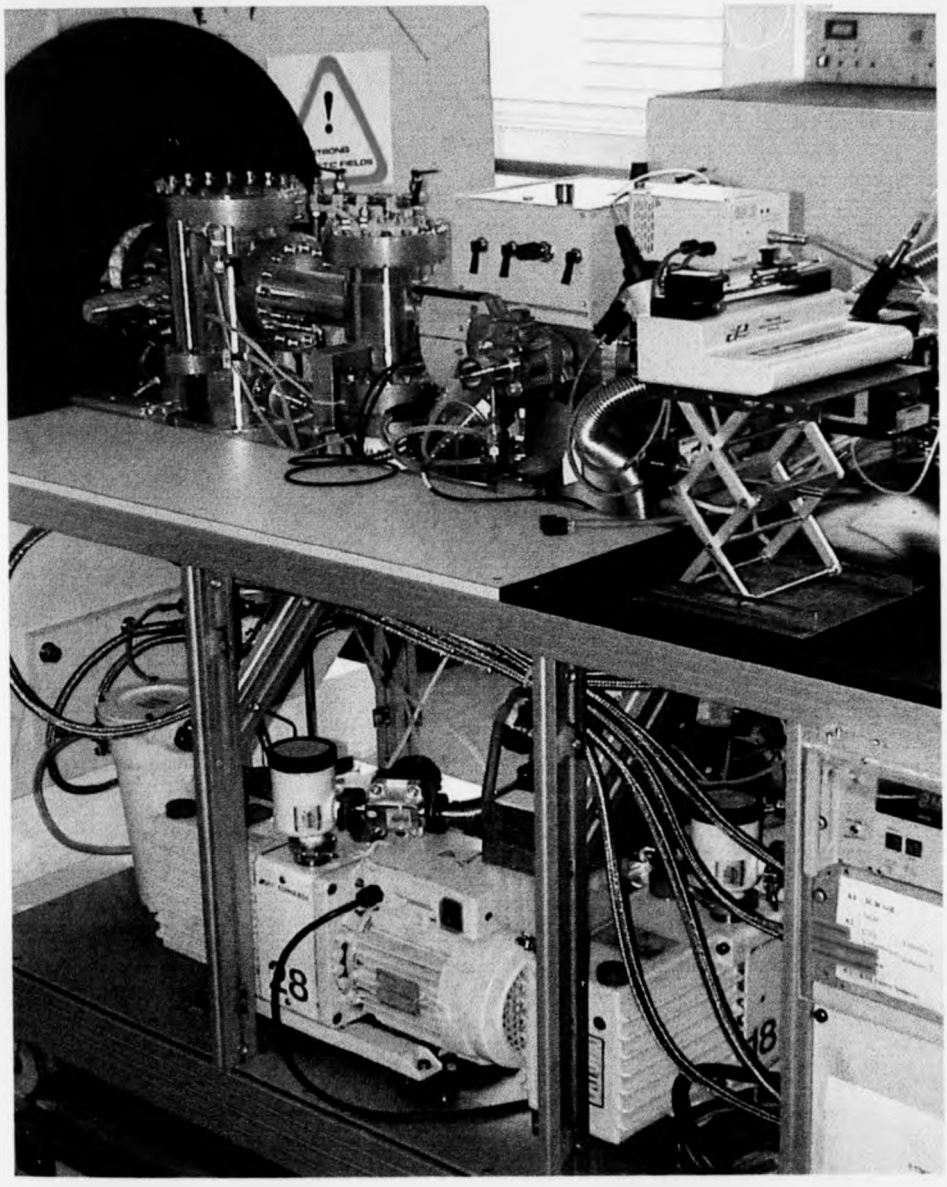

Figure 2-6: Photo of the 9.4T FT-ICR instrument

surrounded by the liquid nitrogen. It was equipped with an external electrospray ionization (ESI) source (model 103426-1, Analytica, Branford, CT, USA) which

could easily be changed to the nanospray source mode[12-15] with the components also coming from Analytica, Branford, CT, USA. The whole instrument was commercially-made.

2.3.2 The external ESI source and the source chamber of the FT-ICR mass spectrometer

The Analytica ESI source used a metal spray needle (in the normal ESI mode) or a gold-coated glass needle (in the nanospray mode) to produce the sample ions from the sample solution. The heated counter-current drying nitrogen gas was used to assist evaporation of the electrospray droplets. The glass capillary (15 cm-long, 0.5 mm-i.d) which transferred the ions from the atmosphere to the high-vacuum mass spectrometer was nickel coated at both ends. Inside the ESI source there was a skimmer immediately after the exit end of the glass capillary. The pressure between the capillary and the skimmer was 10^{-2} mbar pumped by an Edward rotary pump (28 m^3/hour). An rf-only hexapole ion guide was situated behind the skimmer. The hexapole guide was mounted on a plate which divided the ion guide chamber and subsequent source chamber. The ion guide chamber was kept at 10^{-6} mbar by an Edward turbo pump (250 L/sec.) which was backed by an Edward rotary pump (18 m^3/hour). The source chamber was kept at 10^{-7} mbar by an Edward cryopump (CS 800). Another two Edward cryopumps (CS 400 and CS 800) pumped the transfer stage and the analyzer stage of the instrument. The vacuum in the final analyzer stage was about 2×10^{-10} mbar.

The skimmer also served as one trapping electrode of the ion trap. The plate immediately after the hexapole served as another electrode of the ion trap. Ions were

accumulated in the hexapole trap for a defined time (D1), then the ions were pulsed into the FTICR cell by changing the trapping electrode voltage from the trapping value (V_{trap}) to the extract value ($V_{extract}$) for a chosen time (P2).

2.3.3 The transfer stage of the FT-ICR mass spectrometer

All the other lens and deflectors after the trapping electrode were used to optimize the ion beam transportation. There were two requirements achieved by these lenses and deflectors: one was that they applied about 2.5 kV accelerating voltage to the ions to overcome the magnetic mirror effect before being decelerated and trapped in the FTICR cell. The other was that as the ions' flight path was quite long from the trapping electrode to the FTICR cell, this path could be seen as a time-of-flight tube. It was quite important to choose the right delay before the closing voltage was applied on the electrodes. For the light ions the delay time was short and vice versa the heavier ions which needed longer delay times.

2.3.4 The analyzer stage of the FT-ICR mass spectrometer and the data system

All the experiments except the so called capillary/skimmer dissociation experiment were performed in the FTICR cell. For collision-induced dissociation (CID) and other experiments which required collision gas, two computer controlled solenoid valves (General Valves were used) were used to connect the gas cylinders to the ICR cell. The collision gas was pulsed and introduced directly into the cell via the ion optic transfer line with the pressure reached to 10^{-7} mbar in about 0.5 to 1 ms time. Then the pulse valve would be closed. Normally there would be a delay time for pumping down

the pressure before the date acquisition began. Normally during such experiments, the pressure would keep at 10^{-7} to 10^{-9} mbar.

There was one pair of curved detection plates to acquire signal and one pair of curved excitation plates to introduce the radio frequency pulses. These two pairs of plates were positioned in orthogonal directions. Two plates with annular holes were set at both ends of the cell. There was a SIDEKICK™ ion accumulation system to increase the ion trapping efficiency.

The data were acquired through a 12-bit fast 10 MHz digitizer with 1 Mb acquisition memory. Data were transferred to an Indy working station via a Ethernet connection. Another Ethernet connection linked the first working station to a second Indy working station. As the function of the first station was mainly instrument control and signal acquisition, the second one was concentrated on the date analysis and processing. All these activities were controlled using the Bruker XMASS™ software under IRIX 6.3. Data could also be transferred to a HP 8010e CD-RW to write on the CD disk for a long time storage via a PC. Other computers in the office could access the data, and analysis and processing using the same software could be carried out via internal net.

2.4 References:

[2-1] P.G. Gullis, G.M. Neumann, D.E. Rogers and P.J. Derrick

Adv. Mass Spectrom., **8,** 1729 (1980)

[2-2] *A. E. Giannakopulos, U. N. Anderson, J.R. Christie, D. J. Reynolds and P.J. Derrick,*

Eur. Mass Spectrom., **2,** 15 (1995)

[2-3] A. E. Giannakopulos, D. J. Reynolds, T-W.D. Chen, A.W. Colburn and P. J. Derrick,

Int. J. Mass Spectrom. And Ion Processes, **131,** 67 (1994)

[2-4] M. E. Belov, A. W. Colburn, and P. J. Derrick

Rev. Sci. Instrum., **69,** 1275 (1998)

[2-5] *Installation and Operation Manual*: Diffstak® Mk 2 Series Vacuum Pumping System Models 63/150, 100/300, 160/700, 250/2000 Valved and Unvalved, Edwards High Vacuum International, Manor Royal, Crawley, West Sussex, RH10 2LW, UK

[2-6] *Instruction Manual*: Ionization Gauge Heads IG5G and IG5M

Edwards High Vacuum International, Manor Royal, Crawley, West Sussex, RH10 2LW, UK

[2-7] *BOC EDWARDS VACUUM PRODUCTS 2000*

BOC Edwards Vacuum Technology and BOC Edwards 1999

Publication No C1101-98-895

[2-7] *Instruction Manual*: Rotary Vacuum Pumps E1M/E2M40, E1M/E2M80, E2M40S and E2M80S: Edwards High Vacuum International, Manor Royal,

Crawley, West Sussex, RH10 2LW, UK

[2-8] *Pirani gauges*

Edwards High Vacuum International, Manor Royal, Crawley, West Sussex, RH10 2LW, UK

[2-9] H. J. Cooper and P. J. Derrick

Mass Spectrometry in Biomolecular Science, 201-259

R. M. Caprioli, A. Malorni and G. Sindona (eds.)

Kluwer Academic Publishers. Printed in the Netherlands. (1996)

[2-10] H. Matsuda,

Int. J. Mass Spectrom. Ion Phys. **22**, 95 (1976)

[2-11] R. F. Herzog, Z. Naturforsch.

Teil A. **10**, 887 (1955)

[2-12] U. N. Andersen, A. W. Colburn, A. A. Makarov, E. N. Raptakis, D. J. Reynolds, P. J. Derrick, S. C. Davis, A. D. Hoffman, and S. Thomoson,

Rev. Sci. Instrum., **69**, 1650 (1998)

[2-13] Concept H Series Mass Spectrometers Operating Instructions, KRATOS ANALYTICAL LTD, Barton Dock Road, Urmston, Manchester, M31 2LD, England

[2-14] P. Caravatti and M. Alleman,

Org. Mass Spectrom. **26**, 514 (1991)

[2-15] M. Wilm and M. Mann,

Anal. Chem., **68**, 1 (1996)

Chapter 3: Development of the electrospray ionization source and the new ion optical system

3.1. The general situation before the development

The reason that prompted the development of a new source was the difficulty of operation, as regards to the stability over a wide range of time. The electrospray ionization (ESI) source as used previously was designed and fabricated by Belov et al.[3-1] The detail is shown in the Figure 3-1.

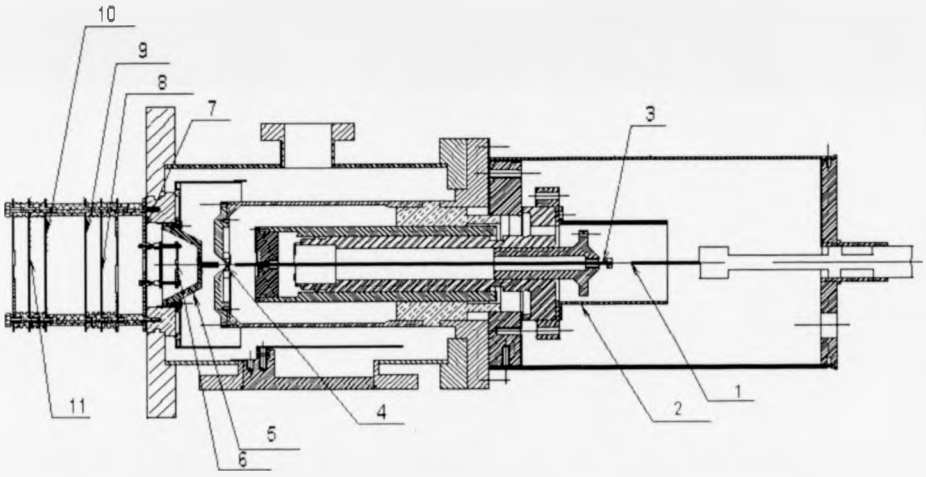

Figure 3-1: Schematic diagram of the prototype ESI source interfaced to the two-sector tandem mass spectrometer (MMM): 1, electrospray needle; 2, counter electrode; 3, heated capillary tube; 4, first skimmer; 5, second skimmer; 6, extracting electrode; 7, first differential z-steering deflector; 8, y-focus lens; 9, differential y-steering deflector; 10, second differential z-steering deflector; 11, z-focus lens.

*In above figure: The x-direction is the ion's flight direction from the ionization source to the last detector. The y-direction is the horizontal direction from left to right. The z-direction is the vertical direction from down to up. After the second skimmer in the x-direction was the

extracting electrode which had a 5(y)×15(z)-mm rectangular aperture; then the grounded plate had a 10(y)×30(z)-mm rectangular aperture; the third was the differential z-steering deflector which was formed by two half circle parts also had a 10(y)×30(z)-mm rectangular aperture in center with a 1-mm gap in y-direction between the two parts. These three plates were placed 14mm, 25mm and 35 mm away (x-direction) from the aperture of the second skimmer. The thicknesses of these three lenses were 1mm, 1mm and 2mm respectively. Other details are on the figure itself.

To develop the ESI source, there were two problems that had to be solved before it could be fitted onto the magnetic-sector mass analyzer. The first problem, which applies to every kind of mass analyzer, was how to transfer the charged droplets and ions produced by electrospray in the atmosphere region to the high-vacuum region of the mass spectrometer.

One solution would have been to let ions pass directly from the atmospheric pressure into the vacuum chamber through a single pinhole orifice (~ 125-μm-diameter)[3-2] which could have been pumped by a very efficient cryopump on the vacuum side. This would have been similar to the situation in atmosphere pressure ionization (API) [3-3] mass spectrometry. A dry nitrogen interface gas at the high-pressure side is typically introduced to help prevent unwanted clustering caused by the cooling effect of the supersonic jet from the pinhole orifice. Also an electric field is typically used to extract the ions from the gas flow.

The other solution, which is commonly encountered, would have been to use a capillary, or an orifice, with skimmers and lenses to take the ion flight path over two or three pumping stages in order to reduce the pumping load at any one stage. Ions are taken through these different vacuum stages to the mass analyzer. To help desolvation

of the droplets produced by electrospray, two methods are used. A heated countercurrent gas flowing against solvated ions facilitates desolvation[3-4]. The other is a heated capillary tube (HCT) which controls heat transfer from the capillary to the gas flow inside to help desolvation[3-5].

Using capillaries in the ESI source has been favored by designers of ESI sources, as they could choose the length of the capillary to suit the distance from the electrospray needle to the entrance point of the ion optical system. This would be especially useful in the situation in this work, because the dimensions of the new spectrometer were fixed. Not much would have to be done to the existing instrument, bar changing the capillary length to ensure that the exit of the capillary was in the correct place.

The other problem associated with the magnetic-sector mass analyzer was that it required the ions produced by the source to have accelerating potentials in the order of kilovolts. The instrument operated usually at 8kV, and the ion source had been designed accordingly.[2-1, 2-2, 2-3]. One of the dangers associated with the high voltages and low vacuum region was corona discharge or the electrical break-down, which could happen in the pressure region from a few mbar to 10^{-2} mbar[3-6]. As the ESI source was run at this high potential and the ions had to be transferred from the atmospheric pressure in the spray region to the high-vacuum region of the mass spectrometer, a number of precautions had to be taken to prevent discharges during the operation, as discussed later in this chapter.

I will discuss the developments made step-by-step following the ion pathway from the electrospray needle to the ion optics system [Figure 3-1].

3.2 The improvements at the atmosphere stage: the new needle assembly and spray stability

The spray needle assembly consisted of a micro-syringe coupled via micro-bore Peek tubing to a capillary sheathed in a hypodermic needle. The original assembly used a glass capillary which protruded about 1mm from the end of the hypodermic needle. As the spray came directly from the tip of the glass capillary, which was an insulator, charging effects could occur depending of the conductivity of the analyte solution. The effects were manifested as instability in the spray current generally producing an oscillation in the ion current from the source. To overcome this problem, the length of the glass capillary protruding out of the hypodermic needle needed to be adjusted for different sample solutions and different flow rates. As the needle assembly was fixed, there was no way to do this during operation.

Replacing the glass capillary with a stainless steel capillary (length 193-mm; outside diameter 0.007inch or 0.1778mm; inside diameter 0.001 inch or 0.0254mm) (Cooper's Needle Works LTD. 261-265, Aston Lane, Birmingham, UK) solved the charging problem at the expense of a slightly increased dead volume in the assembly. With the stainless steel capillary, it was unimportant how far the capillary protruded out of the hypodermic needle.

Chemical sharpening of the tip of the stainless steel capillary was found to be highly detrimental to spray performance, causing the analyte solution to wick back along the capillary rather than spray directly from the tip. Chemical sharpening had been used to good effect with the larger diameter capillary of the Analytica of Bradford (Bradford ,CT) ESI source on the Kratos Concept magnetic-sector mass spectrometer in operation at Warwick during 1996-1997.

The original assembly sprayed directly at the end of the heated stainless steel capillary tube (HCT) which had an outside diameter 1.6mm (1/16 inch). The performance of the spray very much depended on the alignment of the spray capillary and the HCT. Fitting a metal collar around the end of the HCT to give it an apparent diameter of 10mm was found to reduce greatly the need for precise alignment, although some form of x, y, z manipulator might still have proved useful. The underlying reason for this improvement was that by putting on a collar, the electric field between the end of the HCT and the spray capillary was changed in such a way as to make it less defocusing. The equipotential distributions calculated using the SIMION program, before and after putting a collar around the end of the HCT, are shown in the Figure 3-2 and Figure 3-3 respectively.

In a recently published paper[3-7], Schneider et al. describe how the performance of a reduced flow-rate ESI source was substantially improved by the addition of an atmospheric pressure ion lens near the tip of the tapered sprayer. The magnitude and stability of the ion signals, detected within a mass spectrometer, were significantly improved. Some ion signal intensities shown in the spectra were more than two-fold increased. In addition, the ion lens decreased the dependence of the ion signal on the spray position. These benefits, they believed, were due to an improvement in the shapes of the equipotential lines near the electrospray needle tip. The figure in their paper showed that equipotential lines at the tip of the sprayer were less defocusing as a result of adding the atmospheric pressure ion lens.

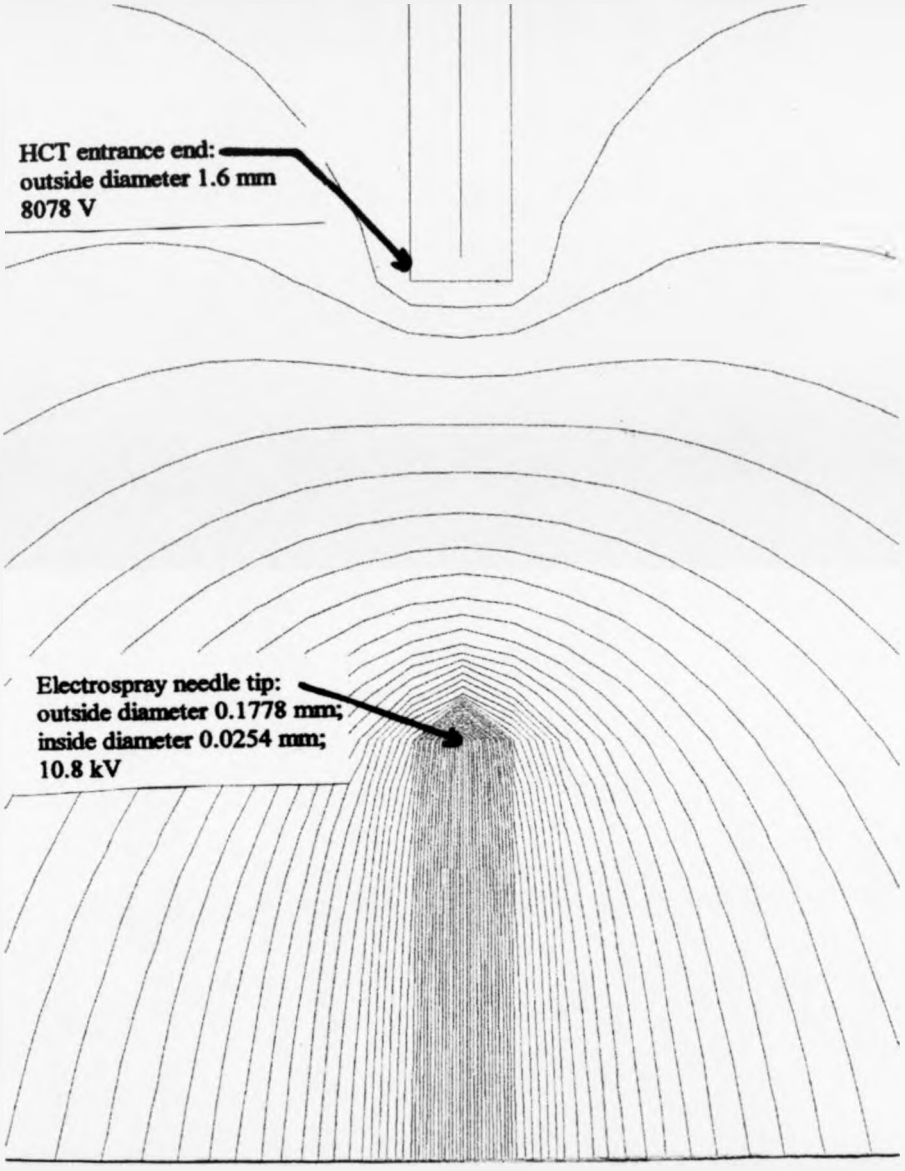

Figure 3-2 (a): The electric field near the electrospray needle assembly in the prototype design: equipotential distribution calculated using SIMION program, electrospray needle tip 10.8 kV, heated stainless steel capillary (HCT) entrance end (1.6-mm-o.d.) 8078 V, surrounding counter electrode (not been shown here) 8078 V, distance between the HCT and the ESI needle 10 mm.

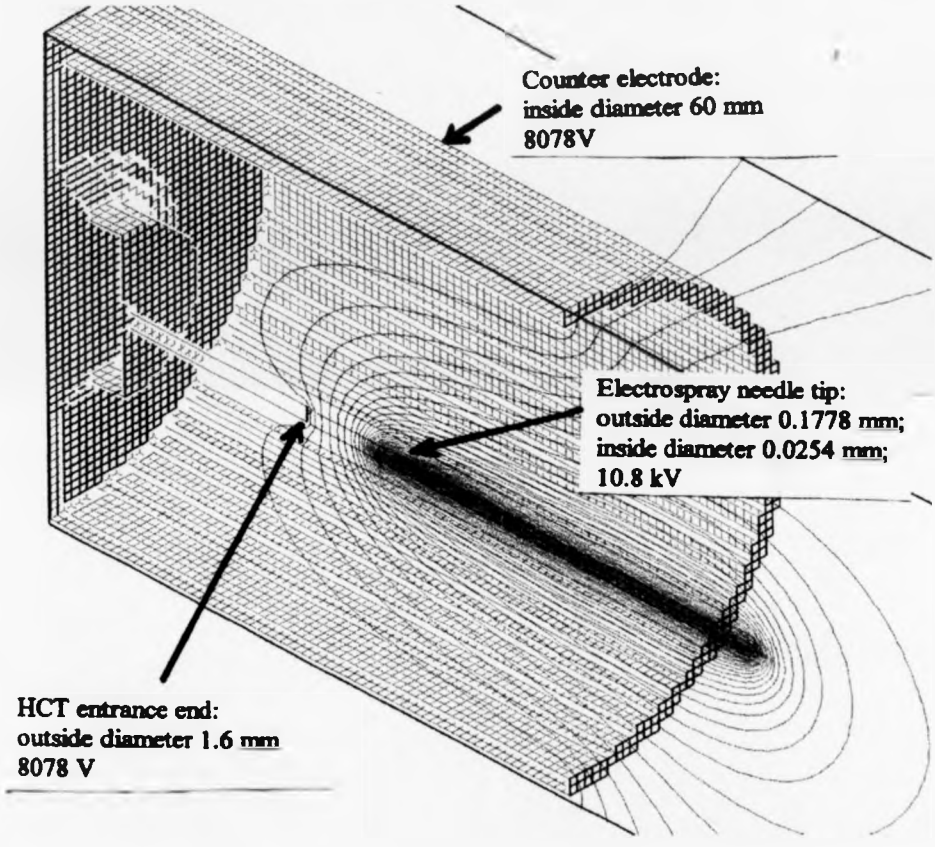

Figure 3-2 (b): The electric field near the electrospray needle assembly in the prototype design with the counter electrode shown

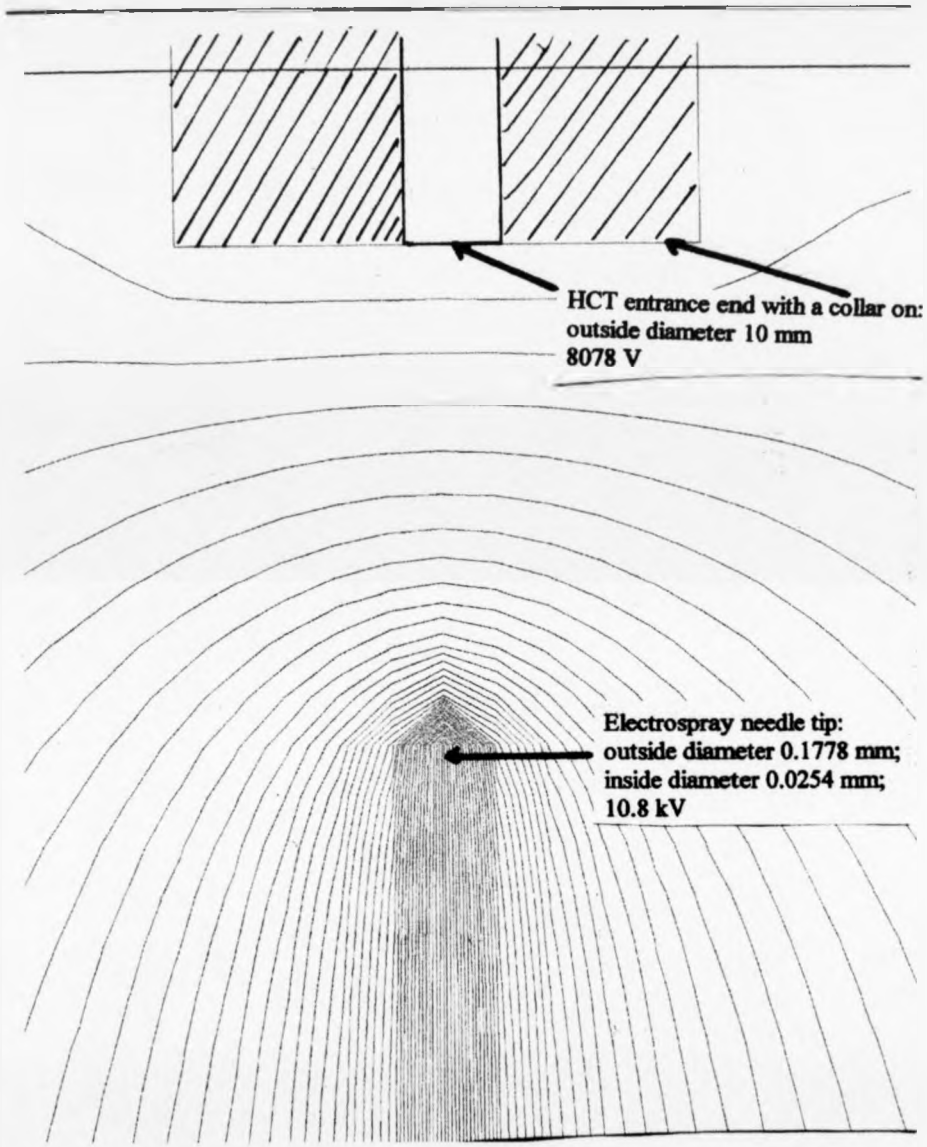

Figure 3-3 (a): The electric field near the electrospray needle assembly in the final new design: equipotential distribution calculated using SIMION program, electrospray needle tip 10.8 kV, heated stainless steel capillary (HCT) entrance end with a collar (10-mm-o.d.) 8078 V, surrounding counter electrode (not been shown here) 8078 V, distance between the HCT and ESI needle 10 mm.

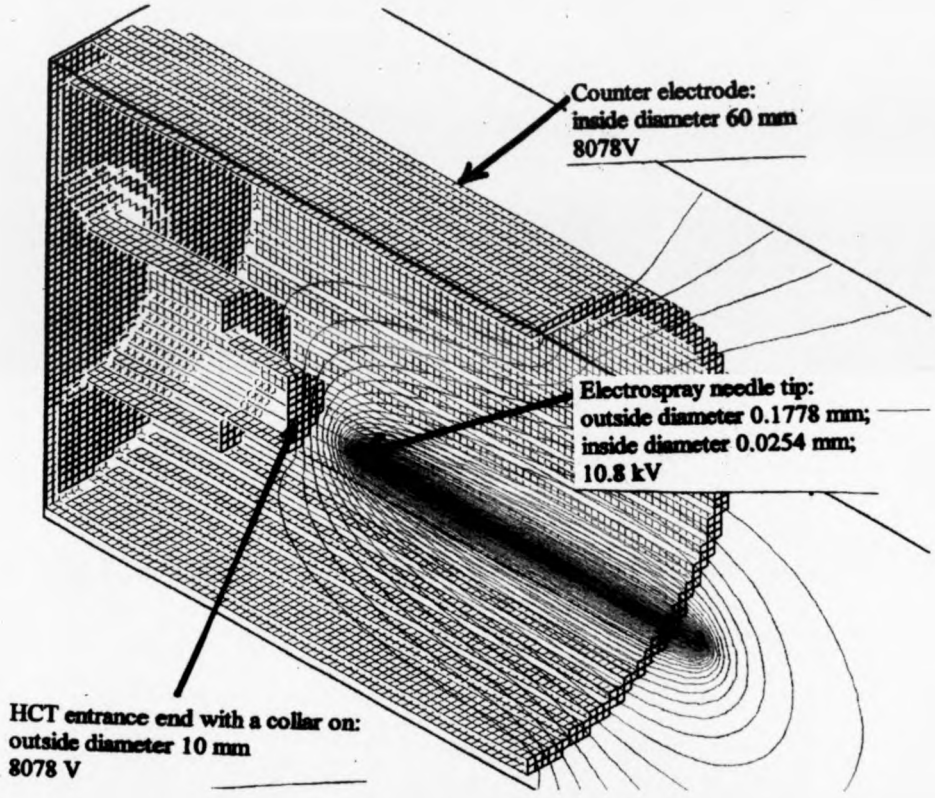

Figure 3-3 (b): the electric field near the electrospray needle assembly in the final new design with the counter electrode shown

3.3 Change of the heated stainless steel capillary (HCT): ion transmission efficiency from the atmosphere into the source

The charged droplets and ions from the spray were carried through the metal capillary tube by the viscous gas flow, and the heating of the tube promoted desolvation of the droplets. Efficient transmission through the HCT was essential to the performance of the ion source. Transmission losses were believed to be dominated by radial diffusion of the charged entities to the walls of the capillary tube. Hence the velocity of passage through the capillary and the capillary's diameter-to-length ratio largely determined the transfer efficiency.

The gas flow is known to play the most important role in this transfer process. It is well known that the viscous flow in a glass capillary as used in some ESI sources allows the ions to be transported against an electrical field. Whitehouse et al.[3-8] have reported that the ions could be "pumped" through a potential difference of more than 15kV.

In Lin and Sunner's[3-9] experiments, the capillaries were not straight, but were in the shape of a helix. Sunner's experimental results were consistent with a model in which the ion loss to the walls of the capillary was caused mainly by space-charge expansion at the entrance of the capillary, but at a later stage by radial diffusion. These loss processes could cause severe discrimination against low-mass ions. The model matched perfectly the results of corona source experiments, but did not reproduce so well the results of electrospray source experiments. The poor agreement with ESI, it was suggested, was caused by the presence about 2% of aerosol particles with radii in the 10 ~ 25-Å region. The space-charge-induced drifts towards the walls of the capillary was determined by the total space-charge. Thus the drift of small ions towards the wall

would be faster because of the presence of the heavy ions. Also the larger charged particles or other larger ions had slower diffusion rates and lower mobility, and were lost less due to the radial diffusion.

Equation (3-1) from Sunner's paper gave the limiting value for the internal diameter d (cm), of a given capillary of the length L (cm) in order to achieve efficient transmission and avoid discrimination against low-mass ions:

$$d > \left(1.315 \times 10^{-8} \times L^2\right)^{1/4} \qquad (3\text{-}1)$$

The physical constraints in the ESI source in this study required the length of the HCT to be 30.0cm. Using equation (3-1), the minimum internal capillary diameter is 0.59mm. The Belov design employed a 0.508mm (0.02inch)diameter, 30.0cm long HCT, which fell below the minimum size into the region where transmission losses become serious according to Sunner's treatment. The closest size of commercially available capillary to 0.59mm was 0.762mm (0.03inch) and this was chosen for the new design.

An experimental comparison of the transmission efficiencies for 0.508mm and 0.762mm HCT's was carried out by measuring the currents due to charged particles (which could be ions, charged droplets or ion molecule clusters) impinging on the first and the second skimmers and on an extracting plate (which was immediately behind the second skimmer in the ESI source) covered with aluminum foil under similar vacuum conditions, at the same HCT temperature and with the same spray conditions. The currents measured on the skimmers for the 0.762mm HCT were typically an order of magnitude higher than those for the 0.508mm HCT. The total throughput to the extracting plate behind the second skimmer for the 0.762mm was about four times

larger (3.8 times) than that of 0.508mm HCT. This result indicated a considerably higher transmission efficiency for the larger diameter HCT.

It must be noted here that the above experiments were conducted under conditions in which electrospray needle was at about 3kV potential. There were no potential differences between the capillary and the first skimmer; between the two skimmers or between the second skimmer and the extracting plate. These potential differences play important roles. With these potential differences applied, the improvement in the total throughput could be higher than four-fold.

With the large diameter capillary, a higher temperature of 225°C (instead of 150°C) was used in practice in order to ensure complete desolvation of the droplets, consistent with the shorter residence time in the larger HCT diameter capillary.

3.4 The improvements in the first vacuum region

3.4.1 The electrical gas-breakdown consideration :

The first vacuum region is the region called either the intermediate or the capillary/orifice - skimmer region. The vacuum in this region provides the driving force for transmission through the HCT and determines the gas load for the subsequent pumping stages. Since the source is floated at high voltage, the pressure in this region needs to be at a point where corona discharge is not a problem. The appropriate pressure can be determined from Pachen's curve for discharge in air for stainless steel [3-6]. Ideally the first region should operate on the low-pressure side, between 10^{-2} to 10^{-3} mbar, of Pachen's curve to provide minimum gas load for the subsequent stages. Equation (3-2) shows the conductance relationship for long circular cross-section pipes in the viscous flow region, (1000 to 1 mbar):

$$C = 135\frac{d^4}{L}\frac{P1+P2}{2} \qquad (3\text{-}2)$$

C is the conductance in l/s; d (cm) is the inside diameter of pipe; L (cm) is the length of the tube; P1 is the high pressure — here the atmospheric pressure (1000mbar); P2 is the lower pressure — pressure in the capillary-skimmer region (several mbar or less). As P1 was much larger than P2, the exact value of P2 could not affect the conductance results derived from the equation (3-2) in our case.

To solve the discharging problem, Ichihara et al.[3-10] insulated their oil-rotary and roots pumps from earth potential for their 5kV accelerating voltage ESI source. In this way, they lifted or floated their oil-rotary and roots pumps to high potentials. In their source, the second skimmer was on 5kV, the first skimmer and the capillary were at a slightly higher potential which could be between 0 ~ 200 V above the 5 kV. Their first vacuum region between the capillary and the first skimmer was pumped by a rotary pump. The pump sat on an acrylic resin base and was driven by an electricmotor through a V-Belt which was an insulator. The second vacuum region between the first skimmer and the second skimmer was pumped by a roots pump which was backed by another rotary pump with the same insulation measures. The roots pump was also on a acrylic resin base between itself and the rotary pump and driven by an electric-motor through a Teflon coupling. The electricmotor was mounted on the roots pump through the acrylic resin parts. So, not only their source parts but also the roots pump, the two rotary pumps and the pumping metal pipe were at high potential and became a safety hazard.

P. Dobberstein and H. Muenster[3-11] built their API/ESI source manifold entirely from plastic material to keep their source elements at ± 5kV ion accelerating potential and the vacuum pumps in the source region at ground potential. L. Jiang and M. Moini[3-

[12] used both techniques on their 5kV ion-accelerating ESI source. Except for the needle, capillary, skimmers and lens assembly, they made the source from Delrin and mounted it on a Delrin flange. At the same time, they floated the two vacuum pumps to source potential by mounting them on a piece of hardwood and isolating the pumps from the motor by using a Delrin pulley on the motor instead of the original metal pulley.

The ESI source manufactured by Analytica of Bradford (Bradford, CT), which was supplied to our laboratory for the Kratos Concept Four-sector mass spectrometer during 1996 - 1997, used a simple way to solve the problem: a glass capillary with metal coatings at the entrance and exit ends to withstand the high potential difference. In order to keep the electrospray needle at earth potential for safe operation., the entrance end of the glass capillary was at ~ -4kV, when the ESI source was running in the positive-ion mode, and the exit was at +8kV for 8kV accelerating voltage. If the ESI source was running in the negative-ion mode, the entrance potential would be at +4kV and the exit end of the glass capillary would be at -8kV. So the ions or charged droplets were carried by the viscous gas flow against a potential difference of about 12kV with the pressure gradient across the glass capillary of atmospheric down to a few mbar. Plastic pumping pipe was used to connect the source and the rotary pump. Since this pressure region is vulnerable to onset of the corona discharge, arcing could happen inside and outside of the capillary when accelerating potentials were above 6kV, causing damage to the metal-coating end and making this design impractical.

Belov et al's[13-11] design used an insulating pipe between the ESI source and the rotary pump to restrain the pressure in the capillary-skimmer region and avoid the most vulnerable vacuum region, and at the same time lengthened the gas flow or gas

discharge path. Both steps helped to suppress gas breakdown and allowed the rotary pump to be run at earth potential.

Calculating the gas conductances for both 0.508mm and 0.762mm HCT's from equation (3-2) gives 0.0150 l/s and 0.0759 l/s respectively. The gas throughput $Q = C \times (P1 - P2)$ for the HCT's are 15 mbar• l/s and 75.9 mbar• l/s respectively. Calculating the pumping speed required to maintain a safe working pressure of 5×10^{-3}mbar in the first vacuum region gives 3000 l/s and 15180 l/s respectively. Clearly these pumping speeds are physically impossible to achieve.

The gas loads involved, therefore, required operation of the first vacuum region on the high pressure side of the Pachen curve[3-6]. Considering the typical breakdown voltage curve for air between parallel metal (Fe, Zn, Al, Brass) plate electrodes, the Pachen curve (P×d) value must be larger than 150 mmHg•cm for 8 kV. P is the pressure between parallel metal plates in mmHg; d is the distance between the two plates in cm. Using the units mbar and m:

$$P \times d > 150(mmHg \bullet cm) = 2.00(mbar \bullet m) \qquad (3\text{-}3)$$

Table 3-1: The gas breakdown distances for 8 kV air between two parallel metal plate electrodes

Pressure between the parallel plate electrodes	Distance (m) between the parallel plate electrodes
0.936mbar	2.13m
1.00mbar	2.00m
3.54mbar	0.565m
6.24mbar	0.321m

For 10 kV, this breakdown voltage would be 200 (mmHg•cm) or 2.66 (mbar•m). It must be noted that in practice, the so-called electrodes are not parallel plates and the breakdown values would be higher than those shown above.

The original E2M40 rotary pump with 42.5m^3/h (at 50 Hz, 1×10^{-4}mbar vacuum limit)[3-13] was unable to achieve 1 mbar in the first vacuum region with 0.508mm HCT and only 6.24mbar with 0.762mmHCT. So the shortest distance should have been larger than 0.38m. Calculations showed that an E1M275 rotary pump with pumping speed 292m^3/h (at 50 Hz, 4×10^{-2}mbar vacuum limit)[3-13] should achieve 0.936 mbar with 0.762mm HCT. The required shortest distance should be larger than 2.13m.

In order to operate as close as possible to the discharge point, so that the pressure would be as low as possible, a long discharge path was created by using a twin pipe coaxial system.

The previous source design used a long dielectric pipe sealed on a specially designed vacuum-tight Teflon™ washer to insulate the source parts which were maintained at kilovolt potentials with respect to ground surface. The inside PVC tube was 1000-mm-long, 16-mm-inside diameter and the outside tube was grounded copper pipe. The discharge path was a little longer than 1.0 m.

The new design used a 26-mm-i.d.; 5-m-long inside PVC tube which was sealed with the vacuum-tight Teflon™ washer. The outer PVC tube was 75-mm-i.d.and 8-m-long, which connected the E1M275 rotary pump with the outside source connection. If the discharge path was from the source to rotary pump, it would be 8m long. If the discharging path was from high potential parts in the ESI source to the earth potential parts, it would be 10m long. Subsequent experiments have shown these calculation to be accurate with safe operation at 8 kV.

Calculative backwards and using the 0.503 mbar measured at the exit end of the 26-mm-i.d.-5-m-long restriction pipe, the pressure in the first vacuum-region under the working conditions should have been 3.54 mbar.

3.4.2 The supersonic jet consideration

When sample ions fly with the carrier gas out of the end of the capillary, they are in an adiabatic expansion and form a supersonic free jet. Their temperature drops quickly to ~ 30K. They keep this temperature until they reach the so-called Mach disk and the barrel shock wave, which forms around the supersonic free jet when the expanding gas molecules collide with background gas molecules or background gas penetrating into the jet. The collisions cause turbulence and increase the temperature and internal energy of the gas molecules and ions. The number densities of molecules or the pressure in the local area follow the same pattern, dropping at first then increasing sharply at the barrel shock wave and the Mach disc[3-14]. The pressure in the supersonic jet is less than the ambient pressure, following the adiabatic equation PV^{γ} = constant (for an ideal gas). The ambient pressure follows the gas equation PV = constant (for an ideal gas). The adiabatic constant or heat capacity ratio of the gas $\gamma = C_p/C_v > 1$. For a monatomic gas $\gamma = 5/3 = 1.67$, for a diatomic gas $\gamma = 7/5 = 1.4$. C_p is the constant-pressure heat capacity of the gas and the C_v is the constant-volume heat capacity.

In order to sample the jet cleanly, it was decided to insert the first skimmer within the Mach disk in the undisturbed inner regions or zone of silence. In this way, the turbulent region where the internal energy of the analyte molecules would be increased was avoided, and the pumping load on the next pump stage was reduced. The insertion of the skimmer into the Mach disc would itself be expected to cause a shock wave. But

if the external semi-apex angle of the skimmer were less than 25 degrees or the whole external angle of the skimmer were less than 50 degrees[3-15], the shock would not expected to affect the part of the jet which would be used.

The empirical relation [3 - 4] [3-16] gives the relationship between the position of the mach disk Z_{mach}, the HCT diameter d and the pressure in the first vacuum region P_1:

$$z_{mach} = \frac{2}{3} d \left(\frac{p_0}{p_1} \right)^{\frac{1}{2}} \qquad (3 - 4)$$

P_0 is the atmospheric pressure. This relation is independent of the heat capacity ratio and the adiabatic constant γ.

Calculation of the Mach disk position for the 0.762mm HCT gave a distance 8.54 mm from the capillary outlet. This was considerably greater than the distance employed in Belov's original design (4.7mm) and allowed greater flexibility in positioning of the first skimmer relative to the HCT. Gas transfer through the first skimmer is largely determined by the dynamics of the jet and the first skimmer cannot be treated as a simple orifice.

$$\lambda(mm) = \frac{6.6}{P(Pa)} = \frac{6.6}{100 \times P(mbar)} \qquad (3 - 5)$$

Equation (3-5) gives the mean free path λ in millimeter at the pressure P in pascals. (1 mbar = 100 Pa). So as the P is 3.54 mbar, the calculated λ is 0.0185 mm in the first vacuum-region.

$$K_r = \frac{\lambda}{d} \qquad (3 - 6)$$

The equation (3-6) gives the Knudsen number K_r for a skimmer whose diameter is d and mean free path is λ, both in the same units. Kr = 0.0264 for the first skimmer whose diameter d is 0.7 mm. As $K_r << 1$, an oblique shock wave on the skimmer was inevitable[3-8]. As a previous design used a 38° nose angle for the first skimmer, there would be no problem caused by this shock wave.

Both the separation distance and coaxial alignment of the HCT and the first skimmer were optimized through experiments to produce the best transmission. In the new design the final distance was 5.00mm compared with 3.8mm in Belov's source.

3.5 The improvement on the second vacuum-region (the vacuum and the electric breakdown consideration)

The second vacuum-region formed the middle stage between the rough vacuum and the high vacuum of the mass spectrometer. This middle stage was pumped by a 360 l/s turbomolecular pump which typically achieved a pressure of 5.5×10^{-4}mbar (with 0.764-mm-i.d. HCT and 26-mm-i.d., 5-m-long inside PVC tube, using an E1M275 pumping the first stage). Belov's design (with 0.508-mm-i.d. HCT; 16-mm-i.d., 1000-mm-long inside PVC tube, using an E2M40 pumping the first stage) achieved a pressure of 5.3×10^{-3}mbar in the second vacuum-region. The significantly lower pressure in this region in the new source allowed several shields previously necessary to prevent arcing to be removed, thus increasing the effective conductance from the jet region to the pump and making the pressure lower still. The stainless steel shields can be seen in the Figure 3-1, in positions around the second skimmer and above the turbomolecular pump entrance.

To prevent arcing or gas electrical breakdown in this second vacuum-region, the distance between high-potential parts and grounded parts had to be shorter than the mean free path in the region, so that there would be little chance for the ions or high-energy gas molecules to start an ionization avalanche. As with the high-vacuum side of the Pachen curve[3-6] in this region, the potential difference still had to meet the requirements of the curve.

The second skimmer in Belov's design took the form of a 1-mm-i.d. and 12-mm-long tube which acted as a conductance restriction to the final vacuum-region. Transmission of ions through the tube was likely to be relative poor, as on simple geometrical grounds losses to the walls would be large. As in the first vacuum-region, gas transfer through the second skimmer is largely determined by the dynamics of the jet and the skimmer cannot be treated as a simple orifice. It was decided to design a new skimmer for the second region to operate as a skimmer rather than as a conductance restriction. The detailed center part of the new second skimmer is shown in the Figure 3 - 4. Although the new skimmer had a calculated conductance six times that of the original , measurements showed that the gas load on the third vacuum-region had only been increased by a factor of two. The same pressure was retained in the second vacuum region.

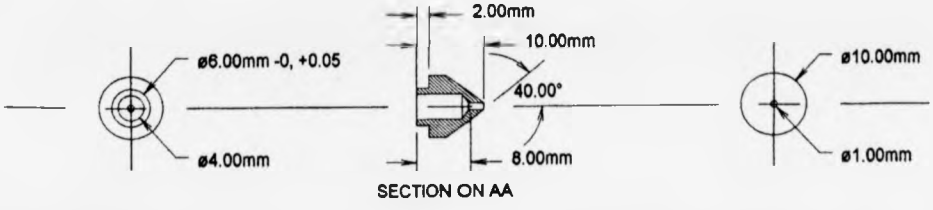

*Figure 3 - 4: The detailed center part of the new second conical skimmer with inside

diameter at the entrance as 1.00mm (maintained for 2mm length); then the diameter was enlarged to 4-mm-i.d. over a 1mm length; finally this 4-mm-i.d. was maintained for 8-mm-length.

The distance between the first skimmer and the new second skimmer was 9-mm, which was 1 mm further than previous 8mm distance. When the distance between the HCT (0.763-mm-i.d.) and the first skimmer was 5.00 mm, and the HCT temperature was 148^{0}C, the final pressure readings were as follows: the pressure near the entrance of the rotary pump was ~ 5.03×10^{-1} mbar; the pressure in second vacuum-region was ~ 1.08×10^{-3} mbar; the pressure in the third vacuum-region was ~ 9.6×10^{-6} mbar. Raising the HCT temperature to 248^{O}C, only the vacuum in the second region became better(falling to ~ 5.5×10^{-4} mbar). The vacuum in the third region might have been slightly better, but it was affected more by the time for which it was pumped after having been opened to the atmospheric pressure. The pressure near the entrance of the big E1M275 rotary pump was little affected by the HCT temperature with in the region between 98 ~ 248^{O}C. The effect of the temperature should have been strongest in the first of the three regions but the pressure in this region could not be measured directly for the reason of gas discharge.

The pressure differential across the first skimmer would have resulted in a second jet expansion. Calculation of the mean free path of the air molecules in the second vacuum-region from Equation (3-4) gave 120 mm at 5.5×10^{-4} mbar and 61 mm at 1.08×10^{-3} mbar, both of which were very much greater than the skimmer aperture (d1= 0.762 mm). Consequently the Knudsen numbers from Equation (3-5) were 157 and 80 at two pressures, both of which are much greater than 1. At high Knudsen number, no jet disturbance should have been caused by insertion of the second skimmer allowing

sampling from a free-jet region. As the background pressure was so low, the mean free path was very large relative to the jet dimensions, and the shock wave patterns and jet boundaries disappeared completely[3-12].

High transmission through the second skimmer was dependent on good coaxial alignment of the first and second skimmers. Examination of the ion burn on the second skimmer indicated that there had been some misalignment, probably due to small inaccuracies in manufacture of the source components. Measures were taken to correct this misalignment.

3.6. The third vacuum-region and the new ion optics system

The third vacuum-region of the source was pumped by a 700L/s Edward's diffusion pump.

The original design consisted of a rectangular-aperture extraction electrode and one grounded rectangular-aperture lens, followed by a series of y and z steering/focus lenses [Figure 3 - 1]. There were other z steering/focus lenses and y steering/focus lenses situated before the source slit of the mass spectrometer. Taken as a whole these lenses proved to be a poor match to the mass spectrometer, requiring extensive additional lenses in the second field-free region which can be seen in Figure3 - 5. The mechanical stability was also poor.

A new lens-assembly based on the concept shown previously to be successful (in the mass spectrometry group in Warwick University) was designed using SIMION 6 for trajectory simulations. This new design employed small apertures for tight beam control. The design consisted of a strong extraction field, followed by a circular focus lens and then a slotted lens for y-direction beam shaping/focusing [Figure3 - 6]. Beam

deflection was handled by existing y and z lenses. The whole of this new ion optics system in the ESI source can be seen in [Figure 3 - 7].

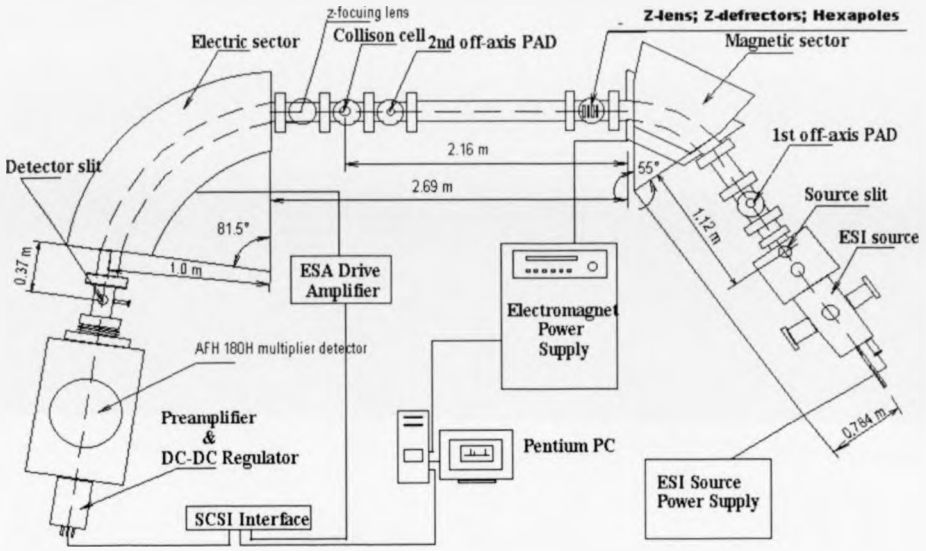

[Figure 3-5] Schematic diagram of the two-sector tandem mass spectrometer with part of the old ion optical system.

*[Figure 3 - 6] and [Figure 3 - 7]: The details of a new lens design from two different perspectives. There was a circular extracting lens with 4-mm-i.d.aperture, three circular focusing lenses with the same size apertures, and then three slotted lenses with 4 mm (z) ×14 mm (y) -rectangular apertures. The last grounded lens had eight 16-mm-i.d. holes to improve the pumping speed in the proximity of the second skimmer. The potentials applied were the second skimmer V_{second}, the extracting lens $V_{extracting}$, the circular focusing lens $V_{focusing}$, the first grounded slotted y-shaping lens, the slotted y-shaping/focusing lens $V_{focusing-2}$ and finally the second grounded slotted y-shaping lens

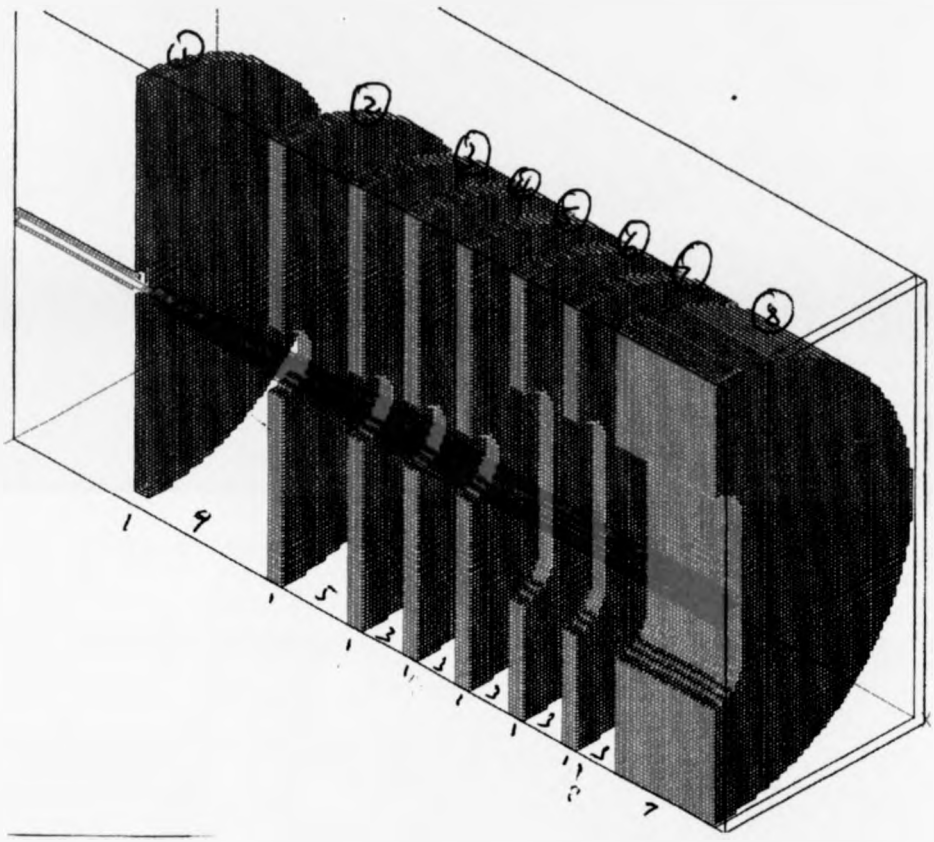

1) second skimmer: with gas flow restricting tube, 8100 V, 1-mm-i.d.-aperture)

2) extracting lens: 3600 V, 4 mm-i.d. aperture

3) first focusing electrode: 0 V, grounded, 4 mm-i.d. aperture

4) second focusing lens, 5100 V, 4 mm-i.d. aperture

5) third focusing lens: 0V, 4 mm-i.d. aperture

6) first y shaping/focusing lens, 0 V, with slotted 4 mm (z) ×14 mm (y) -rectangular apertures

7) second y shaping/focusing lens, 1600 V, with slotted 4 mm (z) ×14 mm (y) -rectangular apertures

8) third y shaping/focusing lens, or holding plate, 0 V, with slotted 4 mm (z) ×14 mm (y) -rectangular apertures and 8 16-mm-i.d. pumping holes.

Figure 3-6-a: The vertical (y-x) section of the new lens design. The number under each lens is its lens thickness (in mm)and the number between lenses is the distance between the two adjacent lenses (in mm)

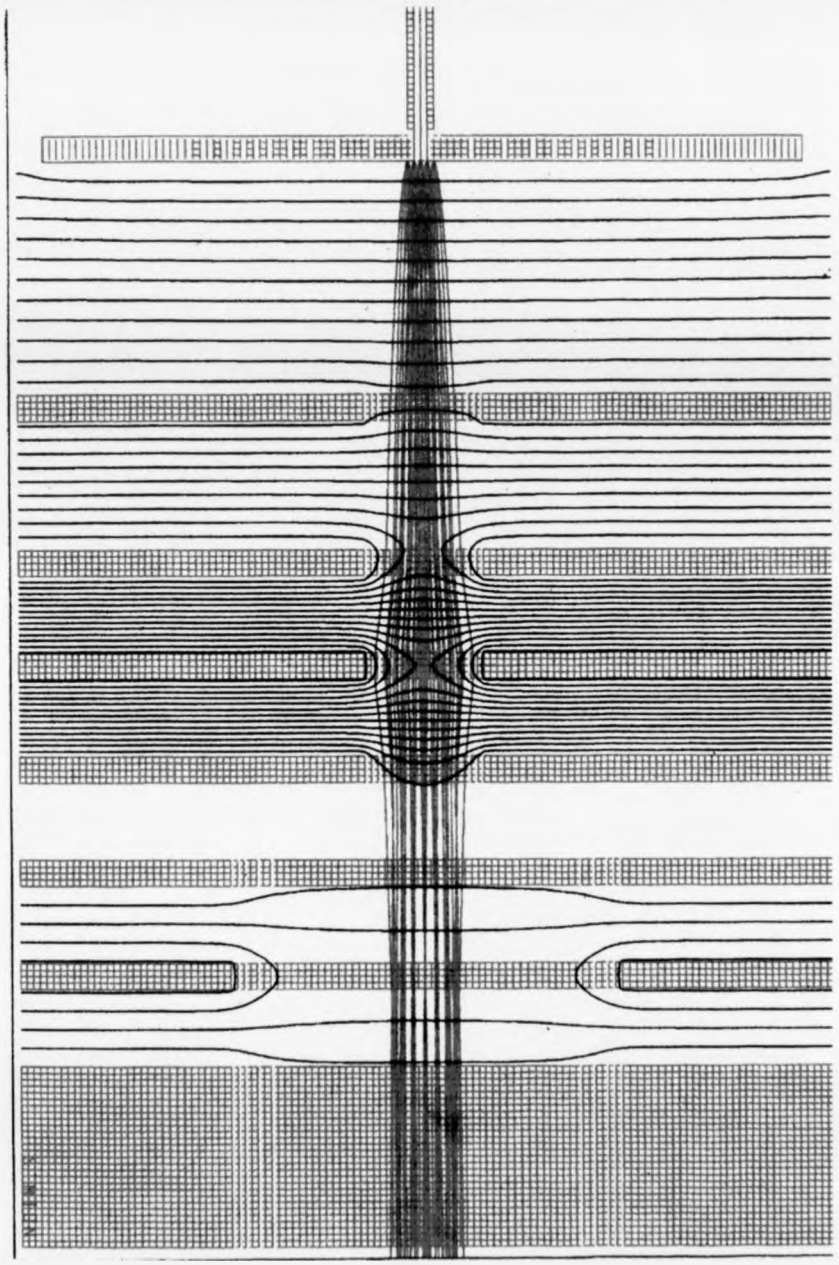

Figure 3-6-b: the x-y section of the new lens design with ion beam and equipotential line shown

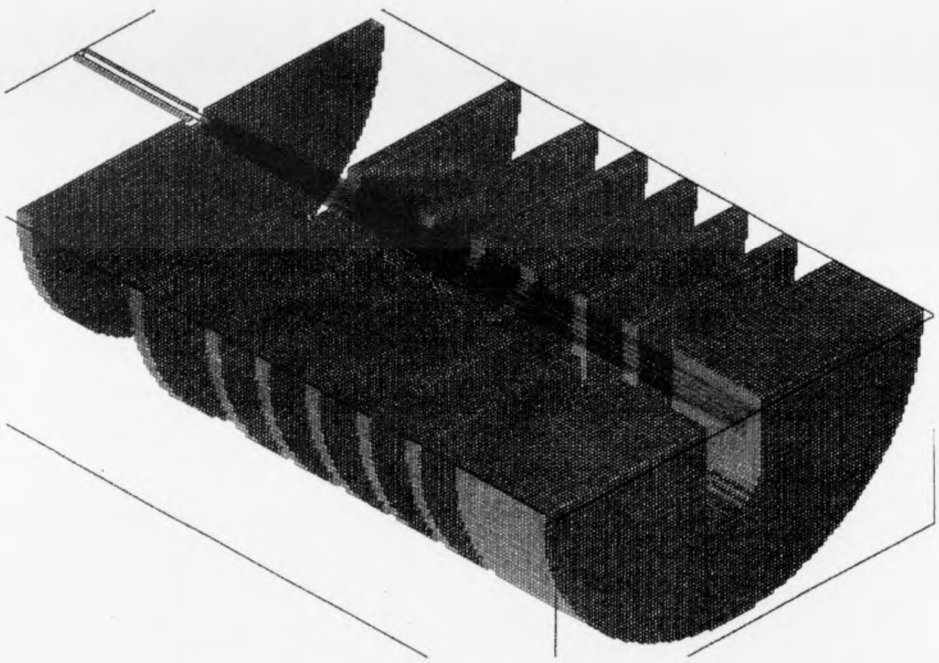

Figure 3-6-c: the z-x section of the new lens design with ion beam shown. Same condition as in [Figure 3-6-a].

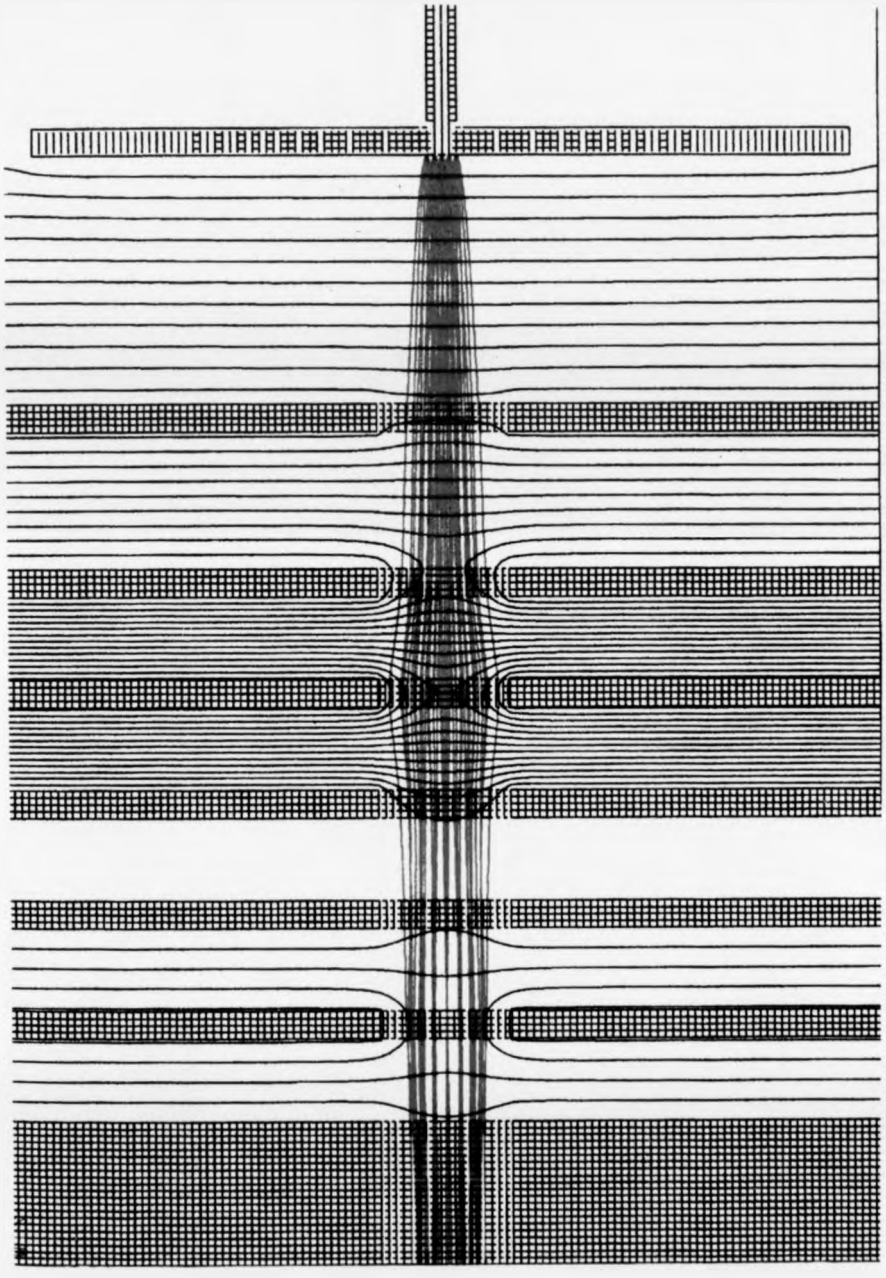

Figure 3-6-d: the x-z or horizontal section of the new lens design with equipotential lines and ion beam shown. Conditions are the same as in [Figure 3-6-a]

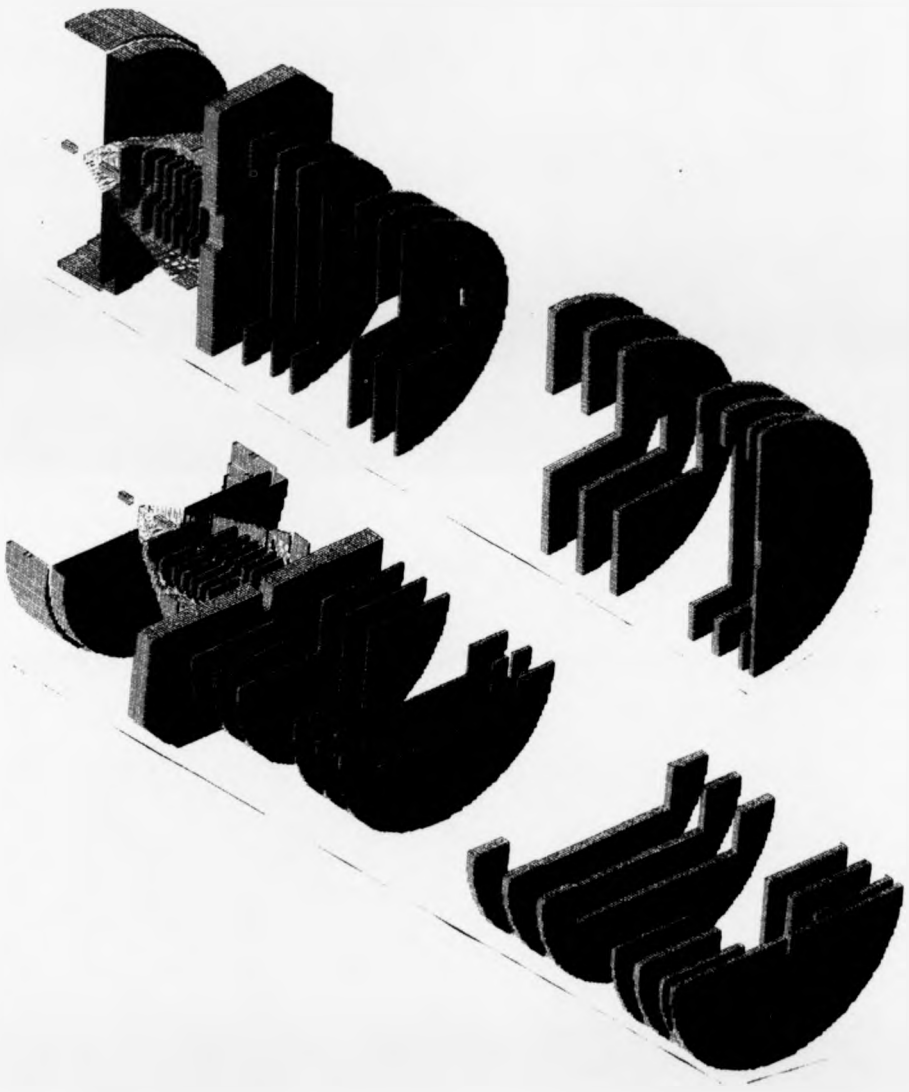

Figure 3-7 Cross section view showing (starting from the left): the second skimmer; the newly designed lenses and the Y1, Z1, Z2 and Y2 - deflector/focus lenses and source slit

Experimental testing of this new design showed the transmission to be extremely low. The "burn" marks on the second and third lenses were much larger than they should have been if the electric field had controlled the ions flight-path fully. Gas dynamics still played some role here and the pressure was still relatively high, and the sharp drop in field might have caused the test results. The distance over which the potential fell from V_{second} to earth potential was 15 mm in the new design, compared to 24 mm in Belov's design. Removing the three grounded lenses, the new design became as shown in [Figure 3 - 8] and this design plus the ion optical system in the source shown in [Figure 3 - 9]. Now the distance over which V_{second} fell to earth potential was 35 mm, longer than that in Belov's source. The focusing lenses had become the counter electrodes. This reduction in the extracting field improved the transmission considerably, however it was still poor compared to that of the Belov design.

Changing the inside diameters (all lenses used circular apertures with 4, 5, 6, 5, 4, 3 mm respectively from the extracting electrode to the thick grounded lens) of the lenses in the new design [Figure3 - 10] did not lead to the predictions of the SIMION 6 calculation being reproduced experimentally. It was thought that a combination of two factors could be responsibility: lack of knowledge of the initial conditions of the ion beam and localized high pressure in the second skimmer-region.

An immersion field lens suggested by Prof. Mark G. Dowsett, in (Figure3 - 11) was predicted by SIMION 6 calculations to be a perfect choice if only ion optical effects were important. Since experiments indicated that a strong field near the second skimmer was detrimental to transmission and gas dynamics may play an important role in this near second skimmer region, this ion immersion lens would not be a good choice.

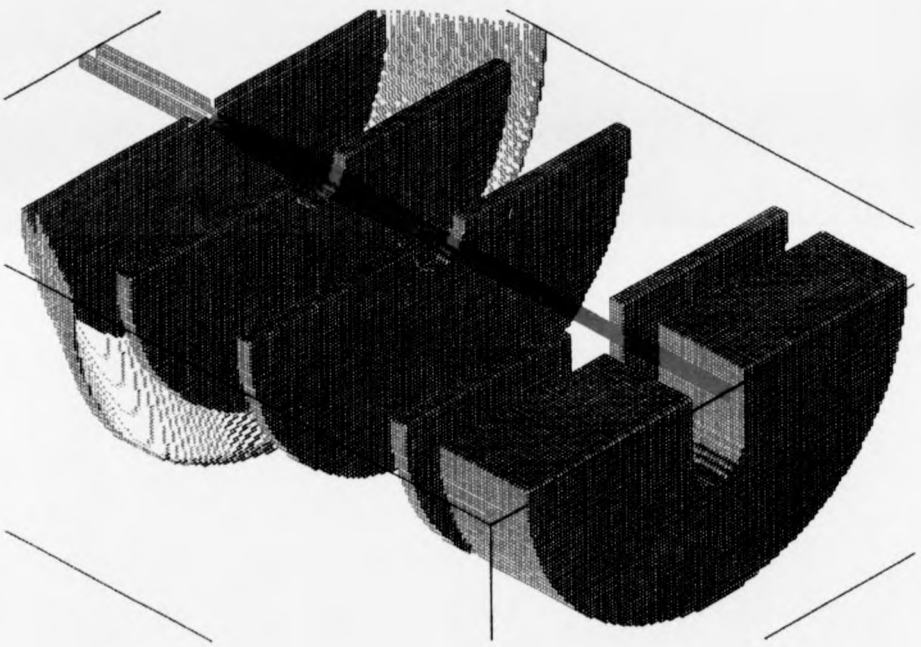

Figure 3-8: The changes from the [Figure 3-6] design (three grounded lenses removed). The second skimmer was in 8 kV and the thick lens in the graph was grounded.

Figure 3-9-a shows the Fig 3-8 design with Y1, Z1, Z2, Y2 deflecting and focusing lenses and source slit

Figure 3-9-b shows the Fig 3-8 design with all Y1, Z1,Y2, Z2, Y3 deflecting and focusing lenses and source slit

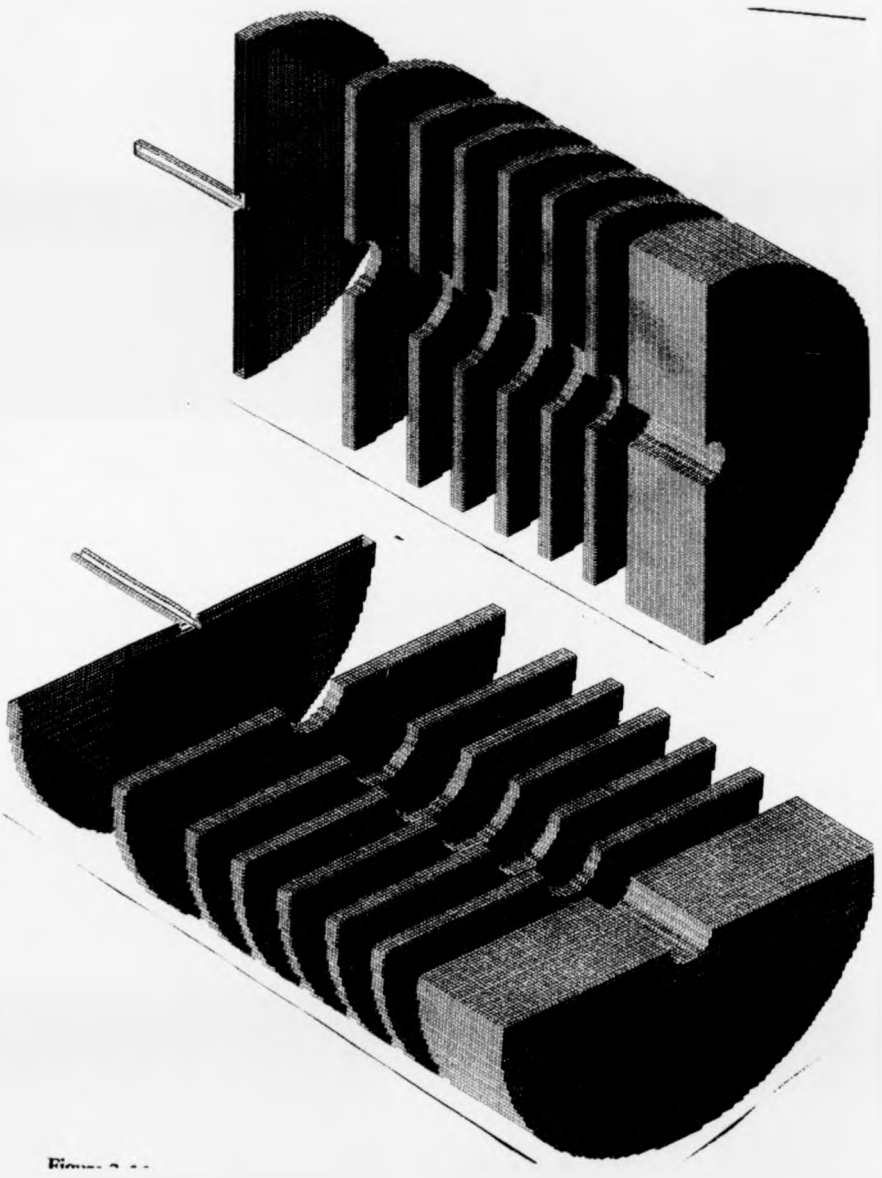

Figure 3-10 changing the diameters of the lenses in Figure 3-6

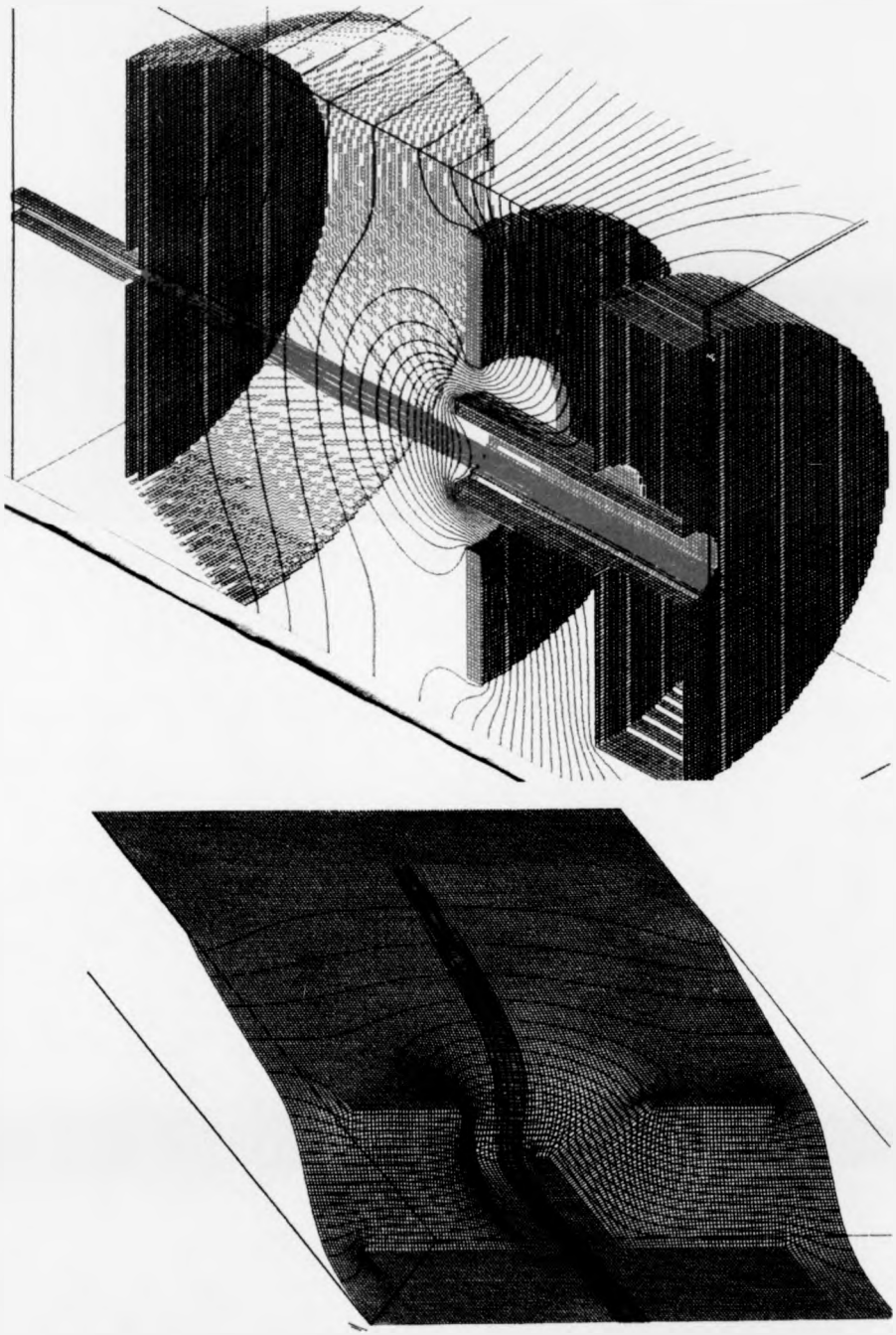

Figure 3-11-a: ion funnel field lens

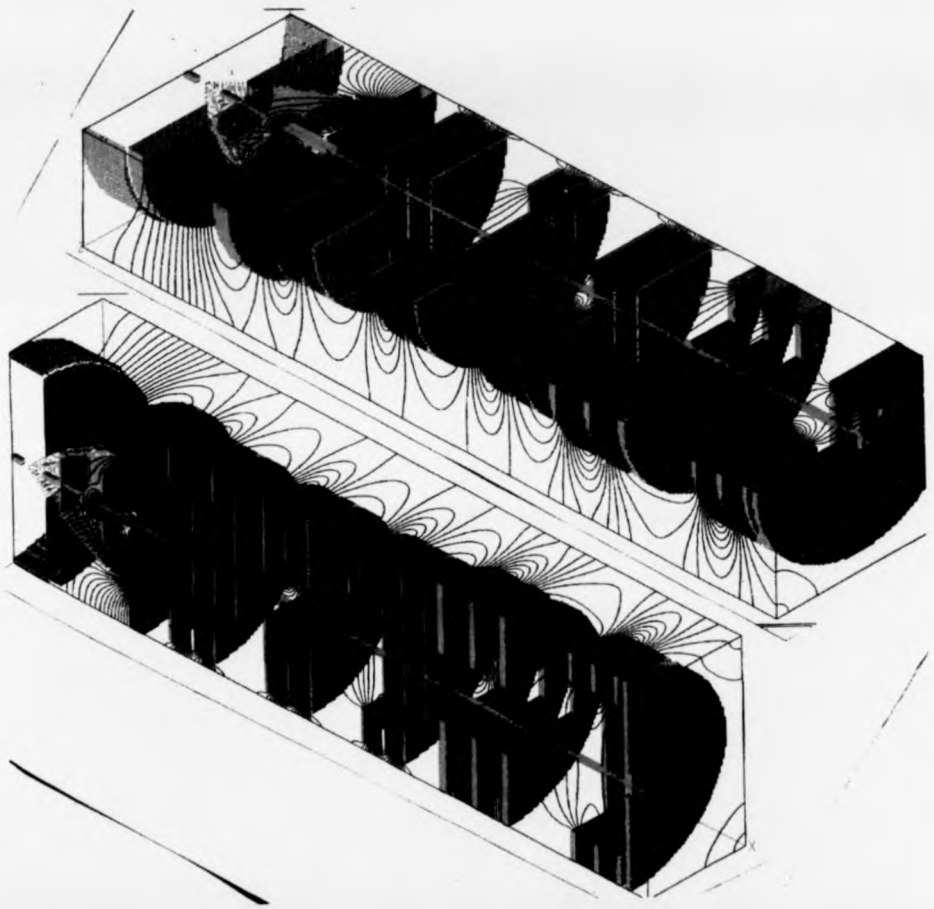

Figure 3-11-b: ion funnel field lens with whole sets of lens before the source slit

A new lens was conceived which would allow the jet from the second skimmer to expand into a low-field region for some distance before any focusing was applied. The solution took the form of a large aperture cylindrical electrode (14-mm-i.d. 25-mm-long) placed in the middle position between the second skimmer and the ground lens with the same 14-mm-i.d. size aperture plus eight-16-mm-I.D. holes to provide effective pumping of the region. Figure 3 - 12 shows the center parts of the system.

SIMION 6 studies showed that in order to reduce the strong field in the second skimmer aperture region, the length of the cylindrical lens on the counter electrode side had to be shortened in the final design: the distance between the second skimmer and the tube lens was 5 mm, the tube lens was 15 mm long and the distance between the tube lens and the grounded electrode was 16 mm [Figure 3 -13]. If the second skimmer was at 8100 V, the tube lens would be at 7000 V, and the final field strength would be 180 V/mm in the second skimmer region and 437.5 V/mm in the counter electrode region.

It should be noted that the grounded electrode in Figure 3 - 13 was tightly fixed on the PEEK base so no gas could enter from the outside of the lens. The large aperture tube lens allowed faster gas pumping than before. Compared with Belov's design [Figure3 - 1], the first differential z-steering deflector with a 10×30 mm slit in which rectangular aperture and a 1 mm gap in the middle of the two parts was in the position of the grounded lens in the new design, the improvement in pumping with the new design would be considerable. The large cylindrical extracting lens, aperture and eight 16 mm-i.d. pumping holes made the local pressure in the near second skimmer aperture region much lower than in Belov's design. The final consideration was that the low

electrical field in the second skimmer region resulted in fewer collision. Focusing was applied only after the ions had reached a lower pressure region.

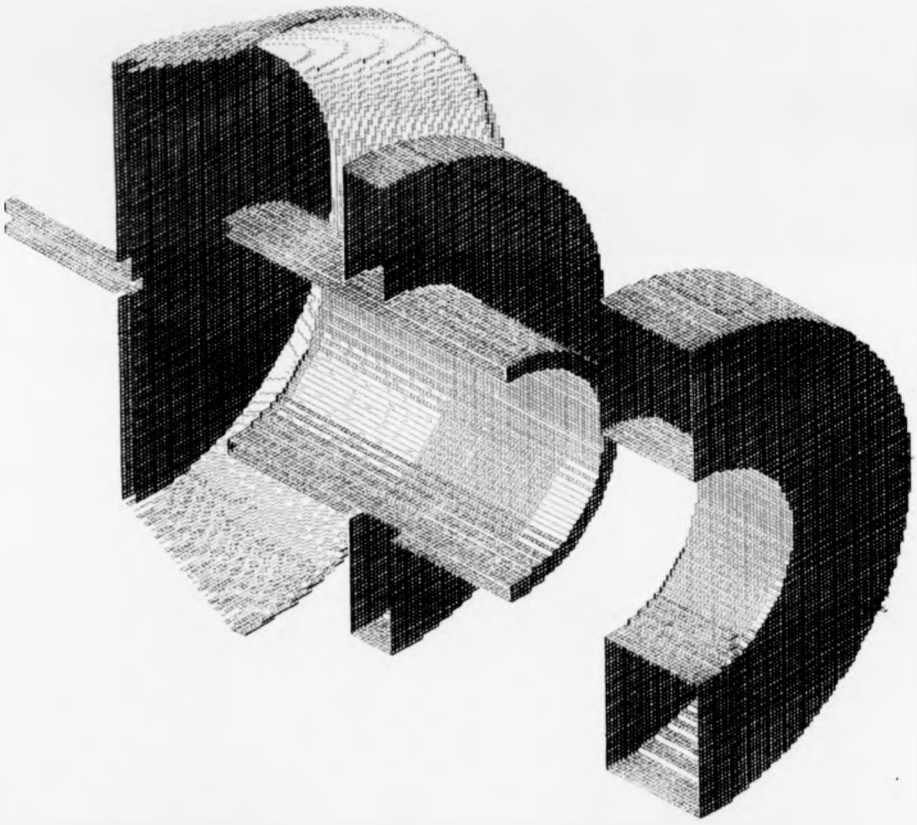

Figure 3 -12: 25-mm-long cylindrical electrode with 14-mm-i.d. aperture placed in the middle position between the second skimmer and the ground lens with the same 14-mm-i.d. size aperture.

The optimum position according to the SIMION 6 results was that when the cylinder was 7 mm long and placed just in the middle between the second skimmer and the ground plate. Since the distance between the second skimmer and the ground plate was 35 mm, the distance between the second skimmer and cylinder electrode and distance between the cylinder electrode and the ground plate were both 9 mm [Figure 3 - 12]. The second skimmer was at 8100 V, the cylindrical lens would be at 6500 V with field strengths 114.3 V/mm and 462 V/mm at each end. This result has not been explored in the experiments, as the above conditions were net tested. Since the gas dynamics played a major role here, the cylindrical electrode near (the distance was 5 mm in final design, not 9 mm as predicted above) the aperture of the second skimmer might have helped the ions in the gas flow pass through this relative high-pressure region and enter the low-pressure region where focusing occurred.

Additional y and z Einzel lenses (deflecting/focusing) were used to shape and steer the ion beam into the mass spectrometer entrance slit [Figure 3 - 14]. It should be noticed that in Belov's design in Figure 3 - 1 the y-focusing lens, the first differential y-steering deflector, the second differential z-steering deflector and the z-focusing lens were mounted consecutively. Any change of the potential of a certain lens would not only affect the field produced by itself but also affect the field produced by the neighboring lenses. All of the four lenses had to be tuned if the potential of any one lens was changed. This made tuning very complicated. The other z and y lenses which were positioned after the above lenses suffered the same problem, as the focusing lens and deflector lens were situated next to each other.

In the new ion optics [Figure 3 - 14], the central plates of the y and z Einzel lenses played the dual role of focusing and steering (differential deflection). The

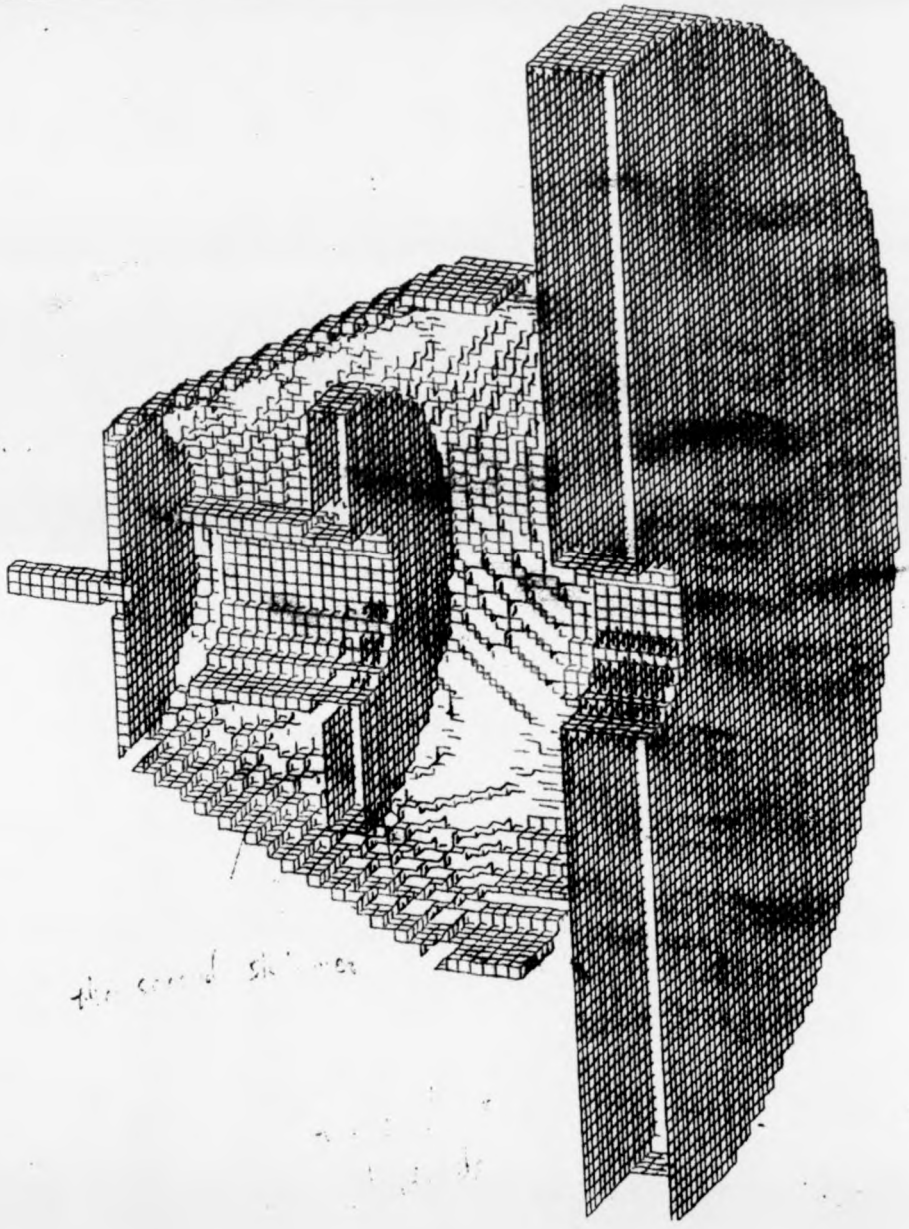

Figure 3-13 Final design of new tube lens after the second skimmer (the eight pumping hole s on the large grounded lens are not shown in the graph)

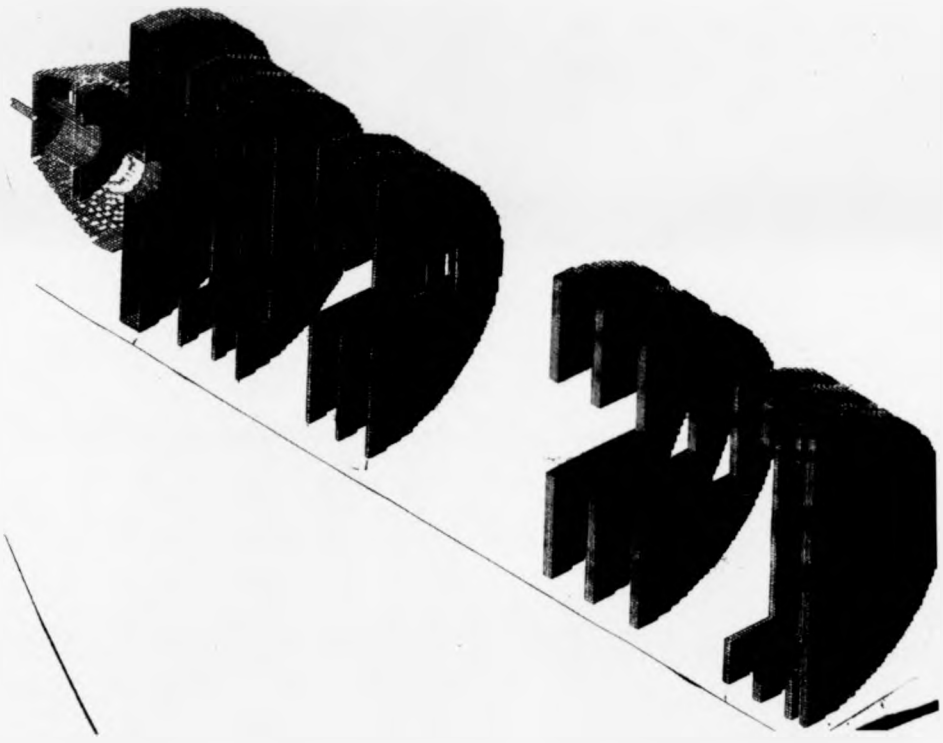

Figure 3-14 Final design of the tube lens with Y1, Z1, Z2, Y2 deflecting/focusing lenses and source slit

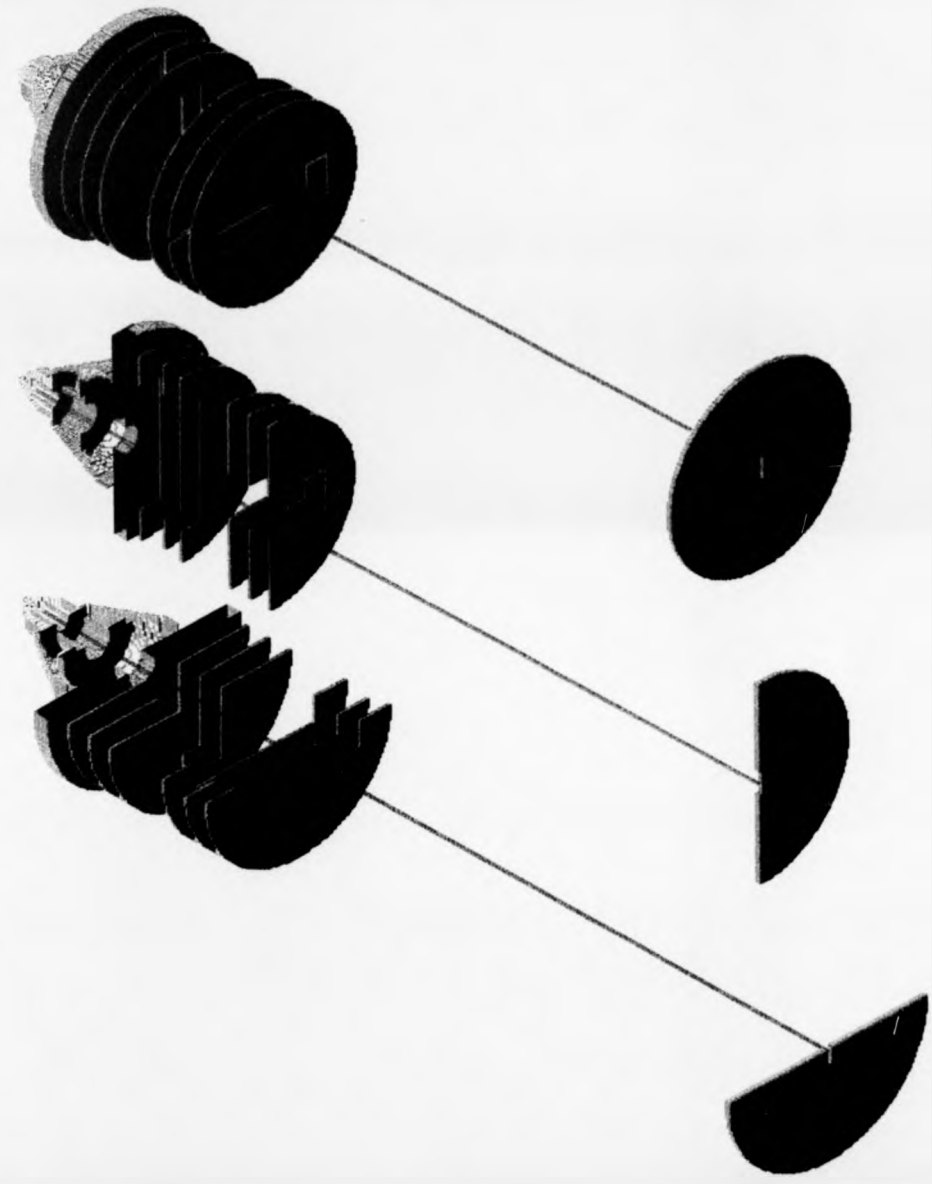

Figure 3-15: the final arrangements: the second skimmer, tube lens, grounded lens Y1, Z1 deflecting/focusing lenses are shown, the additional Z2 deflecting/focusing lenses and grounded metal mesh are not shown.

price paid for this was that the differential deflecting power supply's output potential had to be floated with the focusing potential.. There were two grounded electrodes between the extracting lens and the y deflecting/focusing lens, and two grounded electrodes between the y deflecting/focusing lens and z deflecting/focusing lens. A change in any one lens only affected the field produced within itself.

The performance of the cylindrical design was much better than that of the previous design. There was no need for lensing in the second field-free region. The larger sizes of z2 and y2 Einzel lenses (deflecting/focusing) positioned before the source slit were shown to be of no help in the new design [Figure 3 - 14]. In the final arrangement [Figure 3-15], therefore, smaller z2 Einzel lenses (deflecting/focusing) (same size as z1 and y1) was put immediately after the z1 Einzel lenses (deflecting/focusing). A grounded metal mesh cylinder enclosed the ion flight-path from the last grounded lens of z2 to the source slit, preventing interference from the unwanted fields produced by the lenses power supply lines.

Figure 3 - 16 shows the transfer ion optics in Belov's design. Figure 3 - 17 shows the transfer ion optics in the final new design. It found that the beam shape was much better and the emittance angle was much smaller in both the z and y directions in the new design.

3.7. The overall improvement and conclusion

The result was that for the same sample under the same conditions, the final signal intensity at the mass spectrometer detector would be more than 10 times better than that with the previous design. At the same time, the operation became much easier and signal became more stable.

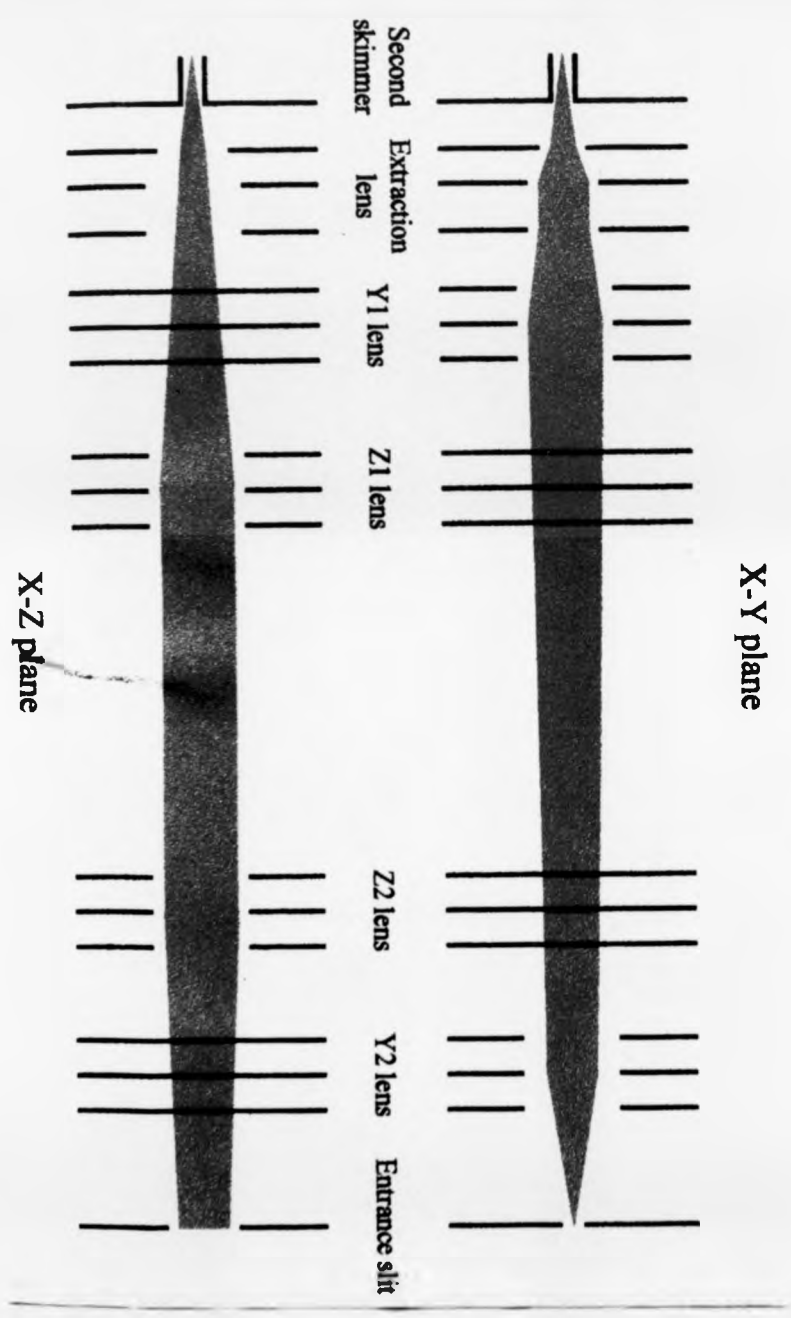

Figure 3 - 16 the transfer ion optics in the prototype design.

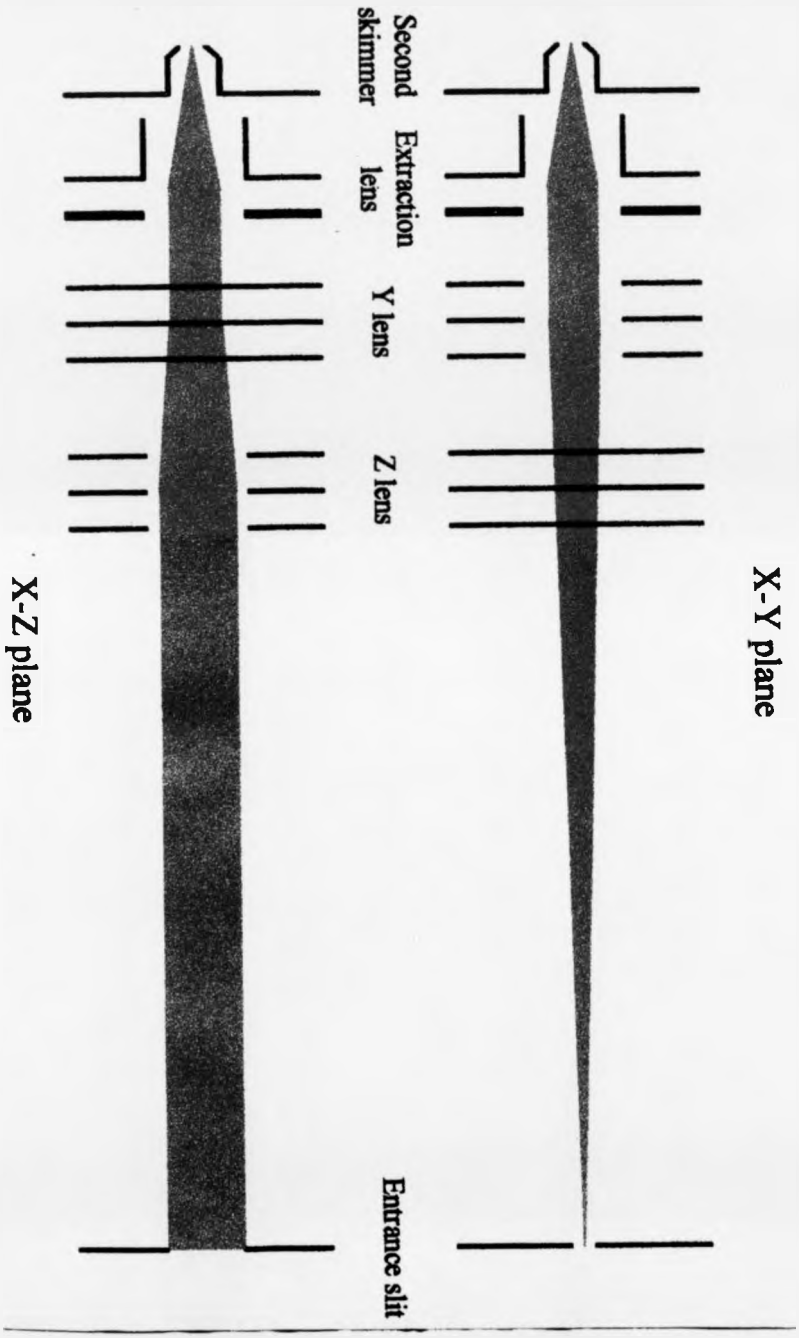

Figure 3 - 17 the transfer ion optics in the final new design

3.8 Reference:

[3-1] M. E. Belov, A. W. Colburn, and P. J. Derrick

Rev. Sci. Instrum., **69**, NUMBER 2, 1275 (1998)

[3-2] B. A. Thomson

J. Am. Soc. Mass. Spectrom., **8**, 1053 (1997)

[3-3] N. M. Reid,.; J. A. Buckly. J. B. French, C. C. Poon,

Advanced Mass Spectrometry, **8b**, 1843 (1997)

[3-4] J. B. Fenn, M. Mann, C. K. Meng, S. F. Wong, and C. M. Whitehouse

Mass Spectrom. Rev., **9**, 37 (1990)

[3-5] S. K. Chowdhury, V. Katta, and B. T. Chait,

Rapid Commun. Mass Spectrom., **4**, 81 (1990).

[3-6] "Electrical Breakdown of Gases"

J. M. Meek and J. D. Craggs.

Oxford, Clarendon Press, 1953

[3-7] B. B. Schneider, D. J. Douglas and D. D. Y. Chen

Rapid Communi. Mass Spectro., **15**, 2168 (2001)

[3-8] C. M. Whitehouse, R. N. Dreyer, M. Yamashita, J. B. Fenn,

Anal. Chem., **57**, 675, (1985)

[3-9] B. Lin and J. Sunner

J. Am. Soci. Mass Spectrom., **5**, 873, (1994)

[3-10] T. ICHIHARA, I. KATAKUSE, H. ITO, T. SAKURAI, T. MATSUO,

and R. ARAKAWA

Mass Analysis (Japanese), **40**, N0. 5, 277, (October 1992)

[3-11] P. Dobberstein, and H. Muenster

Journal of Chromatography A, **712**, 3, (1995)

[3-12] L. Jiang and M. Moini

J. Am. Soci. Mass Spectrom., **6**, 1256, (1995)

[3-13] BOC EDWARDS VACUUM PRODUCTS 200

BOC Edwards Vacuum Technology and BOC Edwards 1999

Publication No C1101-98-895

[3-14] D. J. Creasey, D. E. Heard, M. J. Pilling, B. J. Whitaker, M. Berzins, R. Fairlie

Applied Physics B Lasers and Optics, **65**, 375, (1997)

[3-15] *U. Bossel*, **ENTROPIE, 42**, 12, (1971)

[3-16] John B. Fenn

International J. Mass Spectrom. **200**, 459, (2000)

Chapter 4: High-energy collision-induced dissociation (CID) of multiply charged peptides and proteins produced by electrospray ionization (ESI)

4.1 Introduction and background

Electrospray ionization (ESI) mass spectrometry has been used extensively to study the structures of large biological molecules[4-1 to 4-7]. Multiply charged ions have been found to be more susceptible to collision-induced dissociation (CID) than their singly charged counterparts at the same collision energy[4-8, 4-9], presumably due to the higher collision cross-sections and increased electrostatic forces. In principle, the characteristic generation of multiply charged species makes ESI attractive for sequence analysis of peptides and proteins by tandem mass spectrometry.

There are two methods to approach the CID of electrosprayed ions. The first is nozzle/skimmer dissociation, in which the precursor ions fragment in the source by collisions with air and solvent molecules in the atmospheric pressure /vacuum interface at elevated nozzle/skimmer potentials. The interpretation of the fragment ion spectra can be difficult, because of the uncertainty surrounding charge states and because all ions in the region are fragmented. The second method is that in which the multiply charged precursor ions are selected by a mass spectrometer and fragmented in a collision cell after interaction with a collision gas. The fragment ions are analyzed by a second mass spectrometer.

Experiments [4-10, 4-11] have shown that in low-energy collisions large peptides give limited fragmentation and the fragmentation strongly depends on precursor ion's

structure. This is usually due to too little internal energy being deposited into the precursor ion on collision[4-12].

The efficiency of fragmentation of peptides is generally increased by raising the kinetic energy of the peptide ion[4-13]. Relatively high-energy collisional activation of multiply charged peptides has given the sequence of melittin (2846.6 Da)[4-14], human pancreatic peptide (4181.7 Da)[4-15] and human Tyr−corticotropin releasing factor (4920.7 Da)[4-15]. The laboratory-frame kinetic energies in these experiments were restricted to the range equivalent to an acceleration potential of ≤ 10 kV.

The problem in interpretation of high-energy CID spectra measured using the MMM instrument is translational energy loss. Translational energy loss has been found to increase with increasing precursor-ion mass, and has values of about tens of eV[4-12] for ions of around m/z 1000. Apart from mass−calibration considerations, translational energy losses are very important in the study of the collision dynamics as translational energy loss is related to the internal energy uptake. The generation of high numbers of structurally diagnostic fragment ions from larger peptides and proteins implies appropriate internal energy uptakes.

The original plan in this doctoral project was to perform mass-analyzed ion kinetic energy spectroscopy (MIKES) using the MMM instrument and to explore CID of proteins under different ion charge states and different source acceleration potentials. As discussed in Chapter 1, the maximum energy available to an ion in collision with a target gas molecule (collision gas) is limited by their relative velocity and cannot exceed the center-of-mass collision energy E_{cm}. When the laboratory-frame translational energy of the target gas is assumed to be zero, E_{cm} is given by:

$$E_{cm} = \frac{m_g}{m_i + m_g} E_i \qquad (4-1)$$

Here m_g is the mass of the target gas (collision gas), m_i is the mass of the ion, E_i is the laboratory-frame energy of the ion ($E_i = z \times V_{acceleration}$). From the above equation, it can be seen that the center-of-mass collision energy E_{cm} would drop when the mass of the incident ion (m_i) increased. In order to study the CID of protein ions, it was considered necessary to achieve high values of E_{cm}. There are three ways to increase E_{cm}: increase the mass m_g of the collision gas, use higher charge states of the ion (increasing z) or increase the source acceleration potential ($V_{acceleration}$). The last of these represented the basis of the original study. As the ESI source could run up to 11 kV acceleration potential in the MMM instrument, and given the multiple charging feature of the ESI source, the laboratory-frame energy of an incident ion could be very high. Considering, for example, a 9 + charged ion, E_i would be 72 keV under 8 kV source acceleration potential. To the best of my knowledge, only Sørense et al.[4-16] using their home-made ESI source plus a 50 kV acceleration tube, could produce ions with higher accelerating voltage than on the MMM. Sørense et al. used their instrument to probe the shapes and cross-sections of gas-phase biomolecular ions. ESI sources on commercially available sector mass spectrometers operate at accelerating voltages of 4 kV or less. The expectation was that at high collision energies protein ions would undergo extensive fragmentation and that methods for direct sequencing of proteins by tandem mass spectrometry could be developed. These expectations were based on the earlier work using the MMM of Sheil[4-17] on singly charged peptides formed by field desorption and of Belov[4-18] on multiply charged peptides and proteins formed by ESI.

4.2 Attempts to Reproduce Earlier Spectra from the MMM[4-18]

Earlier spectra of a number of large peptides and small proteins measured on the MMM[4-18] appeared to show extensive fragmentation which could be interpreted to give the amino acid sequences. Kosevich[4-19] had examined the fragmentation patterns in close detail, and had spotted what appeared to be deviations in peak positions from those expected. The widths of the peaks were also interesting, because they were narrower than expected. The first step in my doctoral project was to reproduce these spectra, in order that the findings could be published. The intention was to characterize the dependence of CID of these proteins upon various experimental parameters. The spectra shown in [Figure 4-1] were measured[4-18] on the MMM. They had been stored in Microsoft Excel form. There had always been some questions about the spectra concerning the resolution of the fragments peaks. There was no record of the full-height of the parent peak and the resolution of the parent peak was therefore not actually known. From the Excel data of the spectra in [Figure 4-1], it was clear that the two experiments had been combined to give whole electric-sector voltage region spectra: one was a scan from the lowest voltage to the left side of the parent peak, and the other a scan from the right side of the parent peak to the highest voltage. Tentative assignments had been made for peaks interpreted as being due to fragment ions from quintuply charged ubiquitin. Experiments to reproduce the spectra ([Figure 4-1] described as "treated") were performed for an extensive period of time. Initial attempts were unsuccessful, for the reason it was believed that the ubiquitin precursor was insufficiently intense. On experimenting with different ESI-source conditions and on gaining greater experience in operating the MMM,

Figure 4-1 Treated Ar CID of 8+ ubiquitin ion

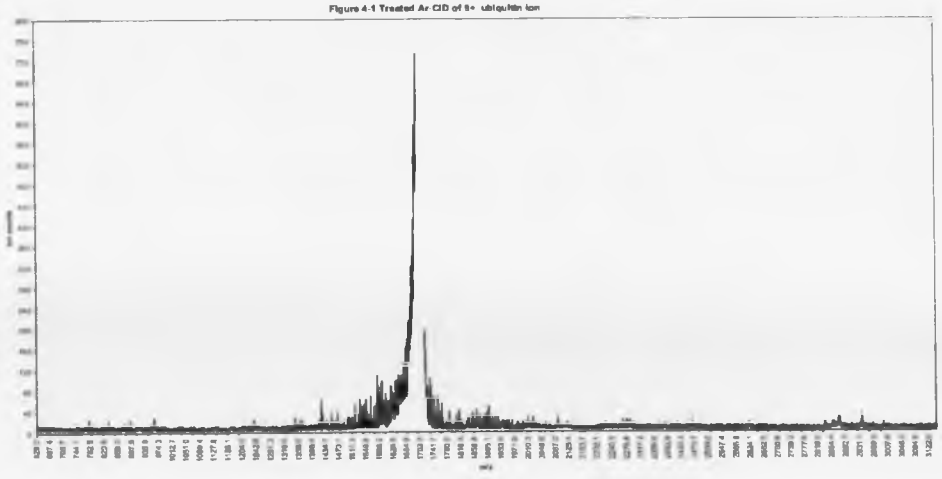

Figure 4-1 -a: enlarged treated spectrum of Figure 4-1 with peak assignments (mass region: 1800 to 2000 m/z)

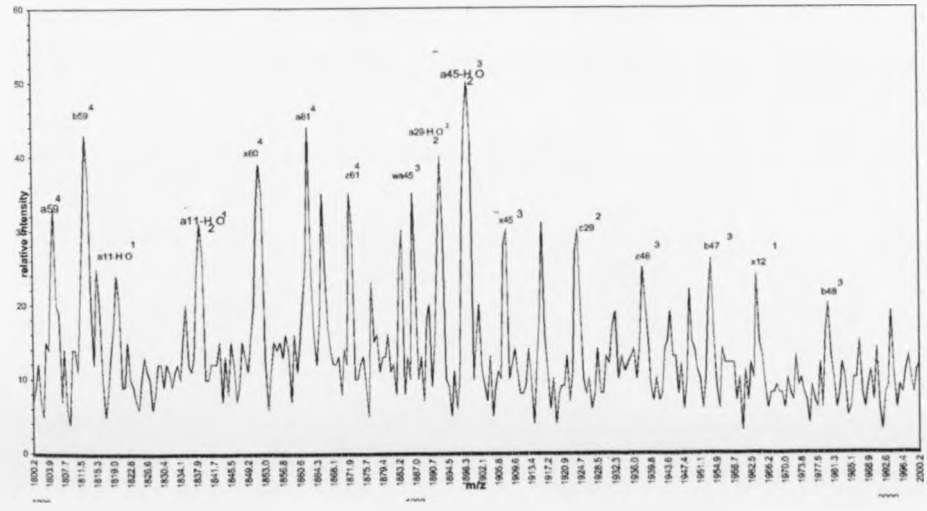

Figure 4-1 Treated Ubiquitin Ar-CID of 5+ ion (mass region 1500 to 1600) with data point shown in red triangle

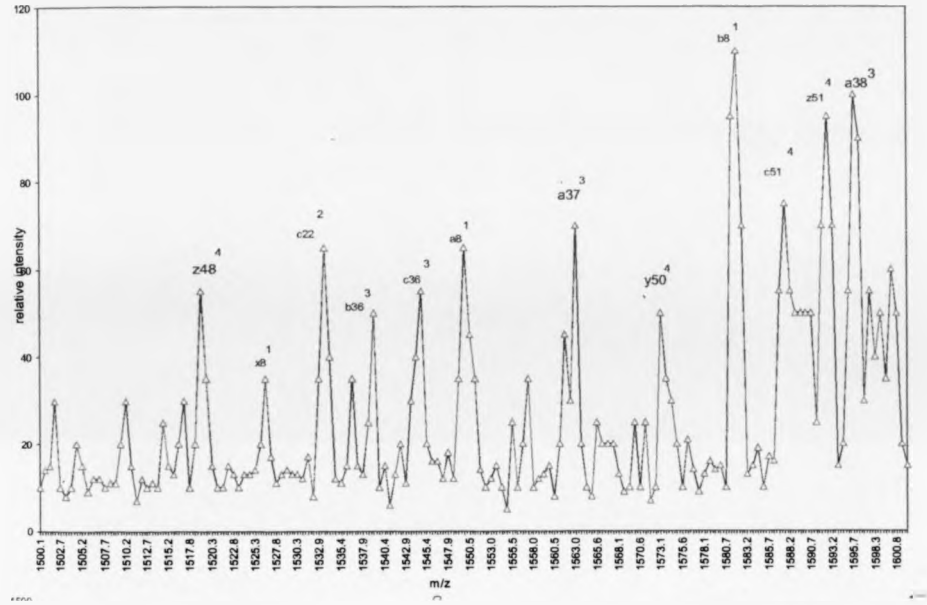

*[Figure 4-1] CID of quintuply protonated bovine ubiquitin (8564.8 Da) at a laboratory-frame collision energy of 40 keV with argon as a collision gas. The complete mass range, over which signal was observed (m/z 600-3500) and enlargements of two selected regions are presented (The last one of [Figure 4-1] and [Figure 4-1- B] show with data points marked). [Figure 4-1-B] is discussed in the text and shown at the end of text discussion.

it was possible to match and indeed surpass the intensities achieved by in the earlier work for the ubiquitin precursor and other samples. At comparable precursor intensities to those recorded in the earlier experiments[4-18], fragment peaks could still not be observed for ubiquitin despite performing extensive and varied series of experiments with different conditions. The tentative conclusion drawn at this stage was that the source conditions in the earlier work ([Figure 4-1]) might have been such as to induce high internal energies for the protein ions, so that they were pre-disposed to dissociate

upon collision. Attention therefore turned to lines of enquiry designed to throw light on the question of how ubiquitin could be induced to fragment. These were:

(a) theoretical analysis and development of the ESI source so as to permit control of the internal energy and raise the transmission through the source. This line of work was to develop into the major concern of my doctoral studies.

(b) Experiments with ubiquitin using ESI and FT-ICR to explore how fragmentation might depend on source conditions.

Experiments were also carried out with peptides using MALDI and a sector/TOF instrument (MAG-TOF) to confirm that high energy CID was indeed typically distinct and different from low-energy methods and to remove any possible doubts about sample authenticity or sample handling (the CID spectra of the peptides had been measured before on the MAG-TOF).

The modest performance of the prototype ESI source at the time the initial experiments in my studies were carried out led to the development of the ESI source and of the new ion optical system described in Chapter 3 of this thesis. These successful developments of the instrument greatly increased the numbers of ions reaching the detector, plus operation and performance were made more stable and reproducible. Following these developments, there was, therefore, the opportunity to try again the original experiments. [Figure 4-2-a (3 ~ 5)], [Figure 4-2-b (3 ~ 5)] and [Figure 4-3-b, c (5 ~6)], show comparisons of parent ion and fragment ion peaks of substance P and bradykinin (with the acquisition data points). From these spectra acquired from the developed ESI source (substance P sample, [Figure 4-2-a, 4-2-b]) and the near-prototype source (bradykinin sample, [Figure 4-3- a, 4-3-b an 4-3-c], using the small

i.d. HCT and small i.d. restrain pumping pipe, so the vacuum in HCT-skimmer region was nearly the same as prototype ESI source with the first skimmer out of the Mach disk), it is clear that the fragment ion peaks were much wider than the parent peaks, or, to say it another way, the resolutions of the fragment ion peaks were lower than those of the parent ion peaks. This conclusion matched well with the basic knowledge of MIKES experiments (which has been discussed in Chapter 1 of this thesis). Using the same experimental conditions as in the earlier work for ubiquitin in either 5+ charge state (as in [Figure 4-1]) or 9+ charge state, it was still not possible to acquire the fragment peaks with the same signal/noise level as in the treated spectra. Comparing small regions of the spectra, it was found that the resolutions of the noise "peaks" in my experiments [Figure 4-4] and the resolutions of fragments peaks in [Figure 4-1] were very nearly equal for the 5+ charged ubiquitin ion. If the peaks in [Figure 4-1] were considered to be noise, the question is why the intensities were so much higher than normal noise levels.

Though intensive energy and time had been spent, the treated spectra ([Figure 4-1]) had still not been reproduced. The tests performed including using larger widths of all three slits (from $\alpha = \beta = \gamma = 1.0$ mm to 2.0 mm) to obtain higher ion intensities, and even changing back to the old small-size HCT, old first vacuum-stage pumping system and the restricting stainless shields between two skimmers (see Chapter 3 of this thesis) to obtain a higher pressure in the capillary-skimmer region (the pressure was nearly the same in the HCT-skimmer region as in the prototype ESI source used in the earlier work).

Facing this deadlock, attention was drawn again to the ESI source. One thing which had been discovered during the ESI source improvement was that the dual inner pumping tube between the ESI source and the rotary pump for the first vacuum stage in the prototype ESI source had not always been a 16-mm-i.d., 1000-mm-long PVC tube as mentioned in reference 3-14[4-20], but rather had at one stage been a 10-mm-i.d. 1500-mm-long PVC tube. If this latter tube had been in place when the earlier results ([Figure 4-1]) were acquired, the first skimmer would have been out of the Mach disc. The pressure in the first vacuum region (capillary-skimmer region) would have been 8.00 Torr (not 3.85 Torr[4-20]), and the Mach disc would have been 3.27 mm away from the end of the HCT. As the second skimmer was 3.7 mm away from the HCT in the prototype ESI source, the first skimmer would have been out of the Mach disc. In the new ESI source, the first skimmer was inserted through the Mach disc to sample the undisturbed analyte ions. The internal energies of the ions produced in the new ESI source could have been much lower than those from the prototype ESI source, as in the former case they did not have the chance to collide with background gas in the Mach disc and in the volume after the Mach disc before they were sampled by the first skimmer. It is possible that the carrier gas temperature of ions in the new source was only several tens K, compared to 423 K (150°C) in the prototype ESI source[4-20]. In the so-called zone of silence, which is the free expansion volume of the free jet, the temperatures of the gas molecules, ions or other particles would have dropped very quickly following the adiabatic expansion, then increased sharply when they reached the Mach disc or the surrounding shock waves to rise to the ambient temperature of the ESI source[4-21, 4-22]. It was not sure absolutely clear which diameter and length PVC tube

was used in the ESI source when the spectrum in [Figure 4-1] was acquired, but the above considerations started the study described in Chapter 5 of this thesis.

Only very recently, it was found by carefully checking the detailed values of data in the Excel files left, that peaks in the spectra in [Figure 4-1] were the result of scaling. Considering the raw data points, some of these had been treated with the result that they appeared much higher in intensity. The actual Ar-CID spectrum of 5^+ charge ubiquitin acquired is shown in [Figure 4-1-B]. My conclusion is that the peaks in [Figure 4-1] were probably spurious.

Figure 4-1-B: untreated Ar-CID of 5+ charged ubiquitin Ion

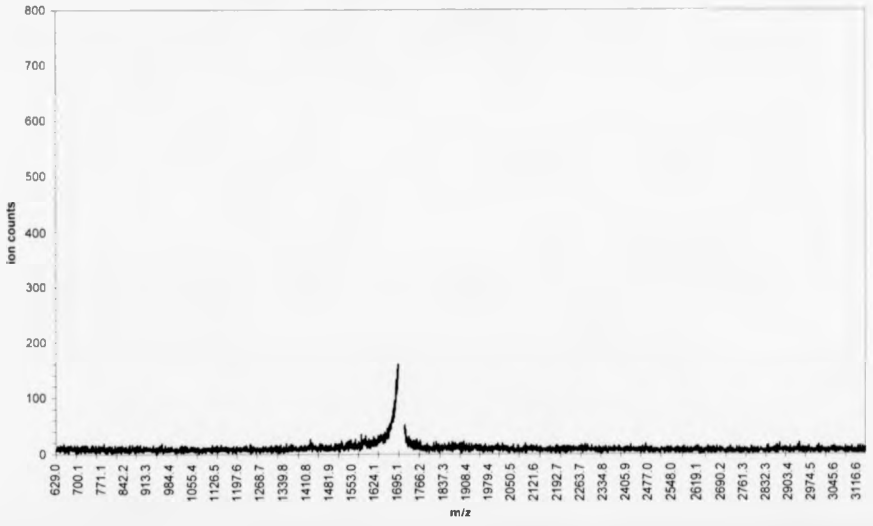

Figure 4-1-B: untreated Ar-CID of 5+ charged ubiquitin ion

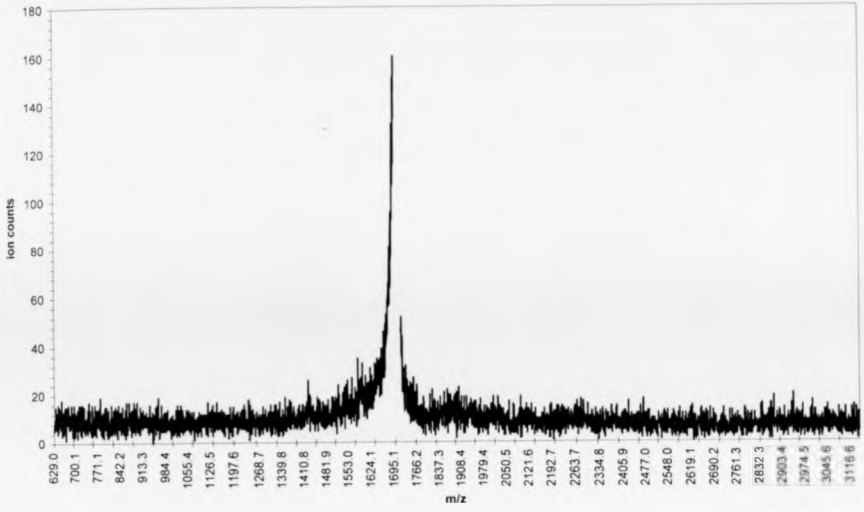

Figure 4-1-B: enlarged untreated spectrum (mass region:1800 to 2000 m/z)

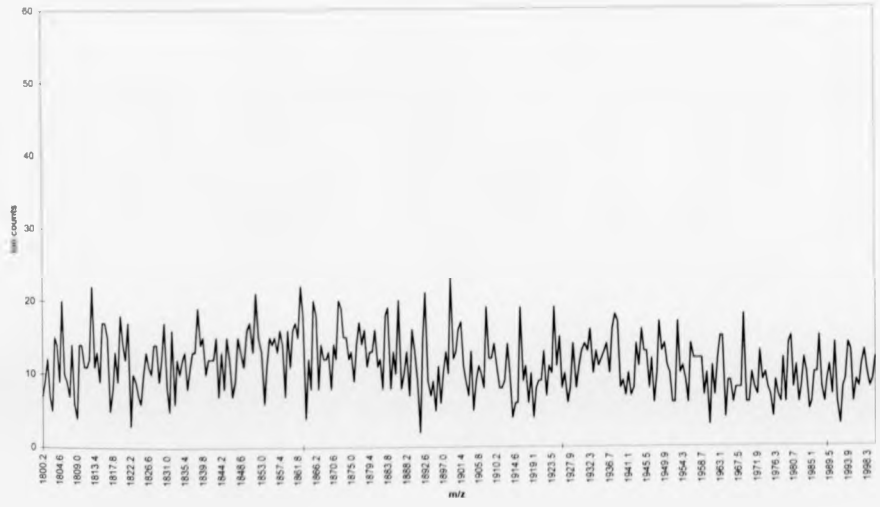

Figure 4-1-B: enlarged spectrum of untreated Ar-CID of 5+ charged ubiquitin ion (mass region: 1500 to 1600 m/z) with data point shown in red triangl

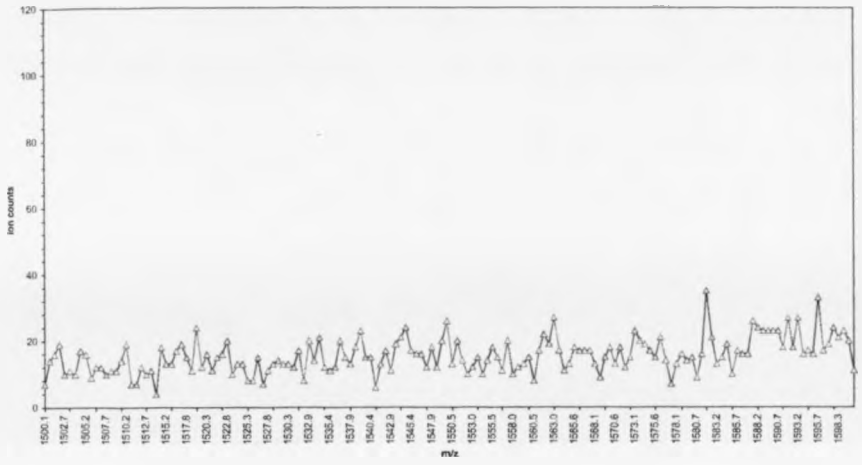

4.3 Experimental results and discussion of substance P, bradykinin and ubiquitin on the MMM instrument

Both substance P and bradykinin were purchased from the SIGMA Chemical Company (St.Louis, Mo) and were used without further purification. Both were made up to 5×10^{-5} M in water: acetonitrile: acetic acid = 49 : 49 : 2 (in volume). The ubiquitin was also purchased from the SIGMA Chemical Company (St.Louis, Mo) and were used without further purification. It was 1.25×10^{-5} M in the same solvent solution.

The experiments were performed using in new ESI source. Sample solution in the 500 μL syringe was passed through the PEEK pipe and the stainless steel spray needle at a flow rate of 2 μL/min by a Harvard Apparatus (South Natick, Ma, USA) syringe pump and sprayed under the electric field before the entrance of the HCT. The charged droplets were desolvated under the heat of the HCT, the voltage

between the HCT and skimmer and the vacuum. Ions formed in the ESI source were focused to pass through the source slit with a suitable beam-diverge angle and shape by the ion optical system. The magnetic-sector was used to choose the parent ions which then collided with the collision gas in the collision cell. The parent ion intensity was depressed to ~ 60 % of its original value. Scanning the electric-sector, the fragments ions from CID would be collected by the instrument's detector. For the metastable fragmentation experiments, the parent ions were again chosen by the magnetic-sector. Without collision gas, scanning the electric-sector would collect fragments from metastable ions formed by dissociation of the parent ions in flight between the two sectors (second field-free region of the MMM instrument).

[Figure 4-2-a, b] give the spectra of He-CID and metastable fragmentation of singly and doubly charged substance P ions acquired with the developed ESI source. [Figure 4-3-a, b, c] give the spectra of He (helium)-CID, Ar (argon)- CID and Kr (krypton) - CID of singly and doubly charged bradykinin acquired under near-prototype ESI source conditions. As the total number of data points was larger than 4000, the Excel software used could only show parts of the spectra in [Figure 4-2-a, b (1) and 4-3- b, c (1)] missing the higher mass part. [Figure 4-4] gives He-CID of the 5^+ charged ubiquitin results acquired before the ESI source developments were made .

4.3.1 He-CID and metastable dissociation of singly charged substance P:

Experimental conditions for [Figure 4-2-a (1)] were: E-sector scan from 20 V (98.9 m/z) to 274.0 V (1355.4 m/z, using 272.5 V for parent ion of singly charged substance P, at 1348 m/z) with step size 0.1 V and step duration time 200 ms (the step

duration time was double that in [Figure 4-2-b]). The scan condition can be shown as simply as (20 V, 274 V, 0.1 V, 200 ms). The ESI source (developed) conditions were: first skimmer 8080 V; second skimmer 8050 V; voltage between HCT and the first skimmer $V_{HCT\text{-}S}$ = 100 V; distance between HCT and the first skimmer $d_{HCT\text{-}S}$ = 5.0 mm; HCT temperature 225^{O}C; sample solution flow rate 2 μL/min. slits $\alpha = \beta = \gamma$ =1.0 mm.

In [Figure 4-2-a (3)], the resolution of the parent ion peak is 1348 (at half height) for the metastable and 1225 for the He-CID experiment. Comparing [Figure 4-2-a (3)] with [Figure 4-2-a (4) and (5)], the parent ion peaks have higher resolutions than the fragment peaks. The resolutions of metastable fragment peaks are higher than those of the CID fragment peaks.

Figure 4-2-a (1) (full intensity scale): He-CID (black line) and metastable dissociation (pink line) spectra of singly charged substance P ion. The He-CID baseline has been raised by 20 counts for easy distinction between two spectra.

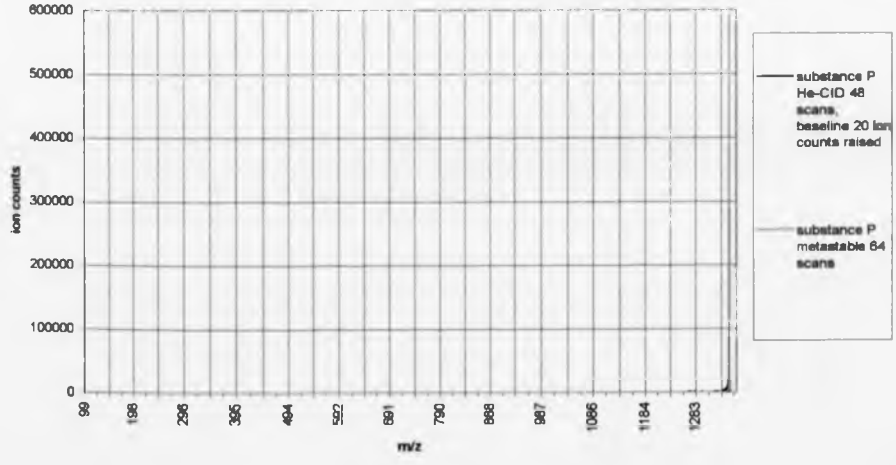

Figure 4-2-a (2) (enlarged intensity scale) He-CID (black line) and metastable dissociation (pink line) spectra of singly charged substance P ion. The He-CID baseline has been raised by 20 counts for easy distinction between two spectra.

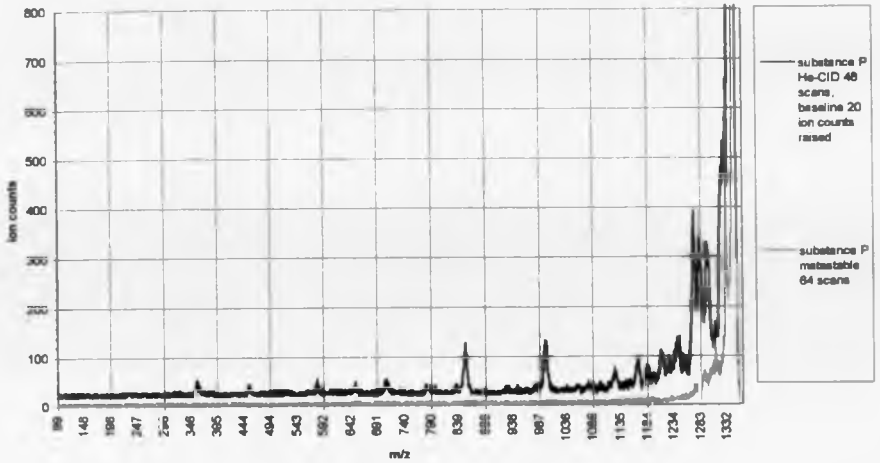

Figure 4-2-a (3): enlargement of Figure 4-2-a (1) : parent ion peak of He-CID (black line, data points marked) and metastable dissociation (pink line, data points marked)

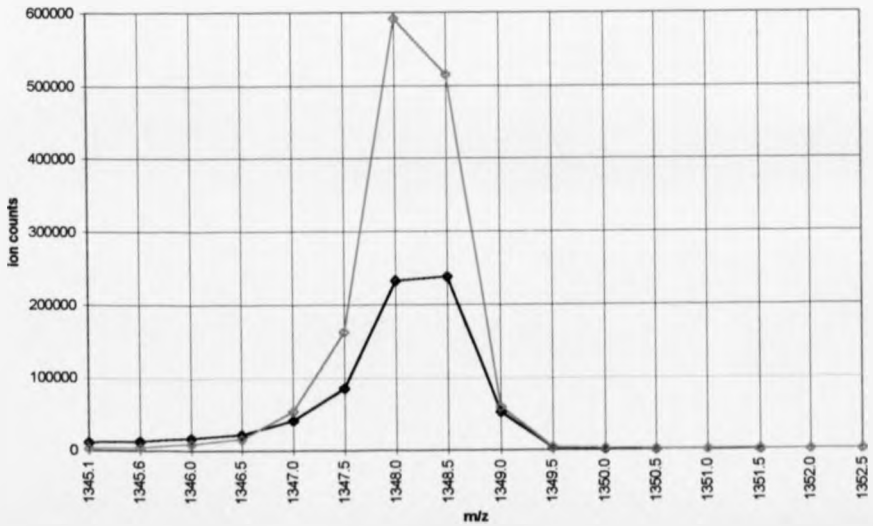

Figure 4-2-a (4): enlargement of Figure 4-2-a (1) He-CID (black line, data points marked) and metastable dissociation (pink line, data points marked)

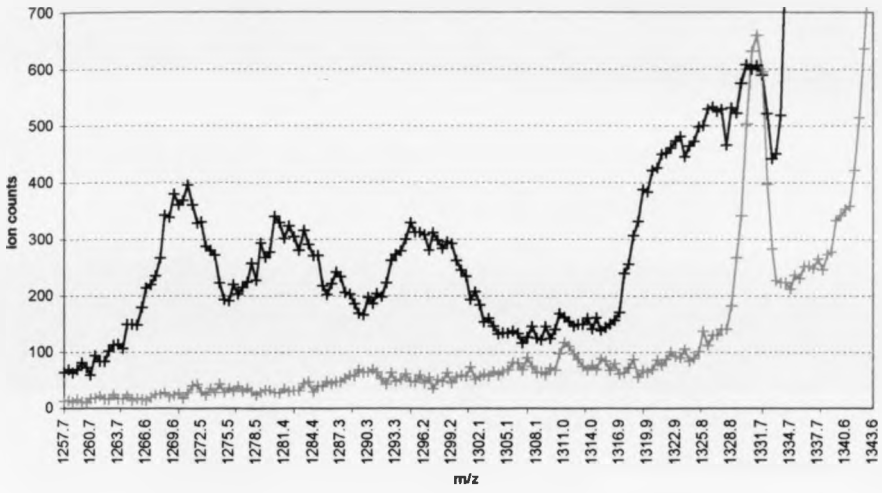

Figure 4-2-a (5): enlargement of Figure 4-2-a (1) He-CID (black line, data points marked) and metastable dissociation (pink line, data points marked)

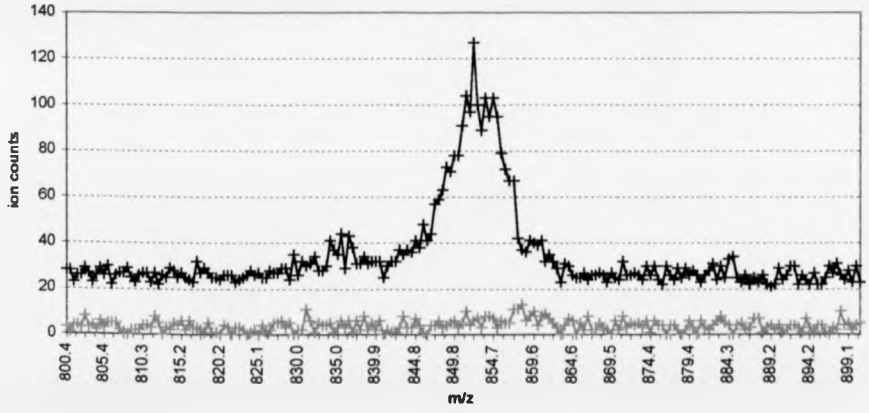

4.3.2 He-CID and metastable dissociation of doubly charged substance P

Experimental conditions for [Figure 4-2-b (1)]: E-sector scan from 20 V (49.5 m/z) to 274.0 V (678.7 m/z, using 272.5 V for the parent ion of the doubly charged substance P, at 675 m/z) with step size 0.1 V and step duration time 100 ms. The ESI source conditions were the same as in [Figure 4-2-a]. In [Figure 4-2-b (2)] E-sector scan conditions were as follows: scan from 274.0 V (678.7 m/z) to 540.0 V (1337.6 m/z) (all the other conditions were the same as for [Figure 4-2-a (1)]).

[Figure 4-2-b (1), (2), (3), (4) and (5)] give the spectra of the He-CID and metastable dissociation processes of the doubly charged substance P ion. It was found that even the narrowest fragment peaks from the metastable dissociation processes in [Figure 4-2-b (4) and (5)] were wider than the parent ion peak in [Figure 4-2-b (3)]. Also from [Figure 4-2-b (4) and (5)], the effects of the translational energy loss during the CID process (or the so-called Derrick shift) could be seen with the fragment ion peaks shifted in the low-energy direction in CID spectra. Comparing [Figure 4-2-b (1) and (2)], the resolutions of the fragment peaks were higher in (1) than in (2) though their other acquisition conditions were exactly the same except the scan regions. The same phenomena (fragment ion peaks on the low energy side have higher resolutions than that of those on the high energy side of the parent peak in the CID spectra of the MIKES experiments) could also be seen in the bradykinin spectra in [Figure 4-3-b an c]. The reason behind this phenomenon is the higher translation energy of the singly charged ions in (2), leading to higher energy dispersion and causing the widening of the peaks. With the metastable dissociation process there was no

translational energy loss caused by collision, so the peak positions were not moved and the peak resolutions were higher than those of same ions' peaks in the CID spectra.

Comparing the He-CID and metastable dissociation spectra of singly charged and doubly charged substance P in [Figure 4-2-a and b], it was found that the doubly charged ion gave more fragments in the CID process.

Figure 4-2-b (1): He-CID and metastable dissociation of doubly charged substance P ion (E-sector scan mass region 49.5 ~ 678.7 m/z).The He-CID baseline has been raised by 20 counts for easy distinction between the two spectra

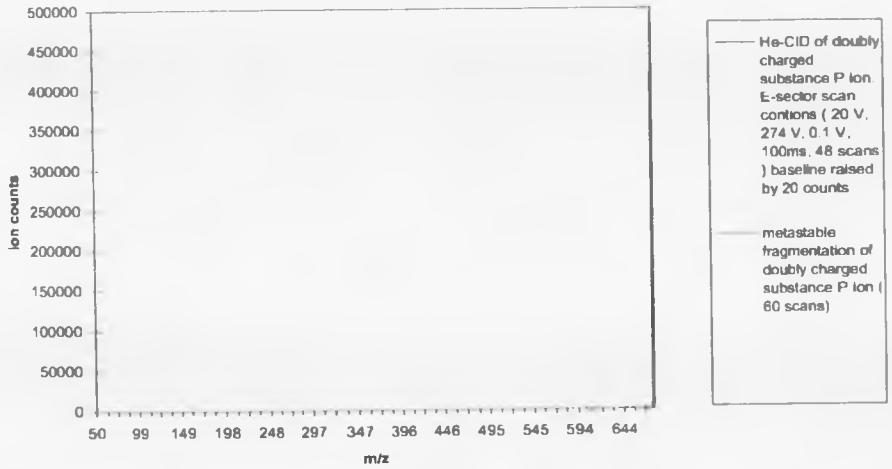

Figure 4-2-b (1) (enlarged intensity scale): He-CID and metastable dissociation fragment peak of doubly charged sustance P ion. (E-sector scan mass region 49.5 ~ 678.7 m/z)

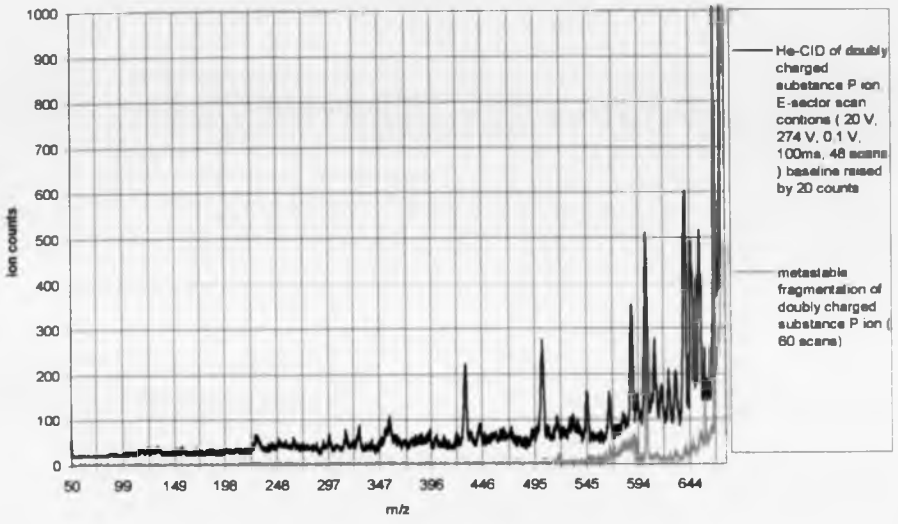

Figure 4-2-b (2) (enlarged intensity scale): He-CID and metastable dissociation of doubly charged substance P ion. E-sector mass scan region 678.7~1337.6 m/z. The He-CID baseline has been raised by 20 counts for easy distinction between the two spectra.

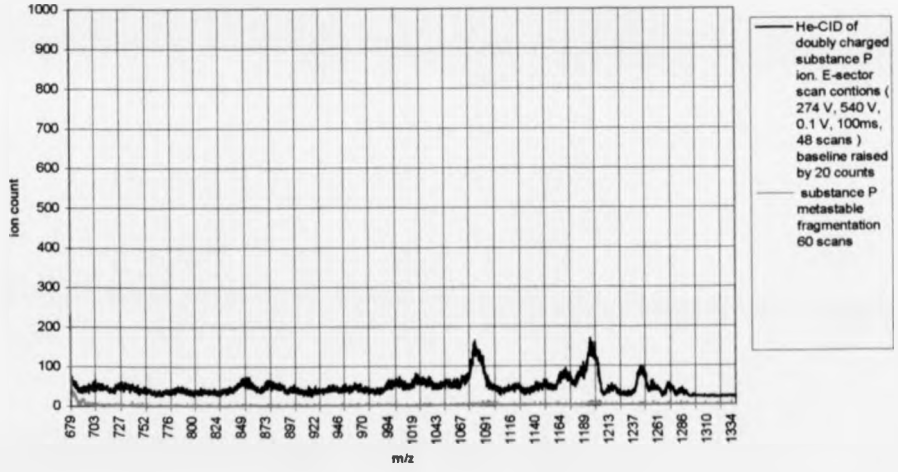

Figure 4-2-b (3): Enlargement of Figure 4-2-b (1) : parent ion peak of He-CID (black line, data points marked) and metastable dissociation (pink line, data points marked).

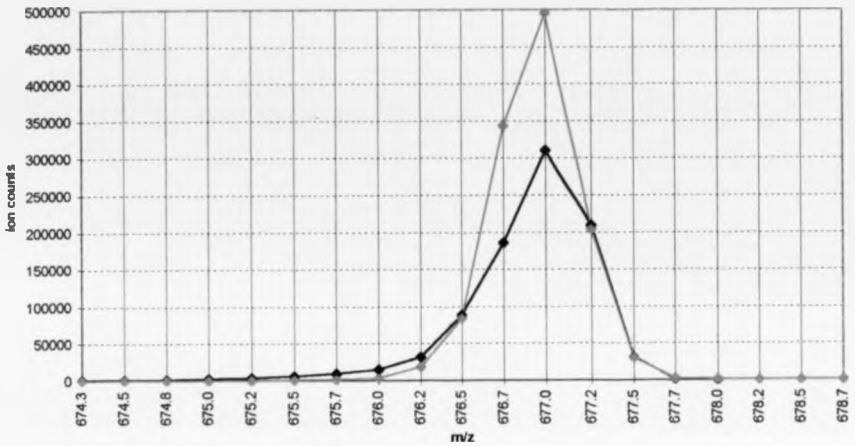

Figure 4-2-b (4): Enlargement of Figure 4-2-b (1) fragment peaks of He-CID (black line, data points marked) and metastable dissociation (pink line, data points marked)

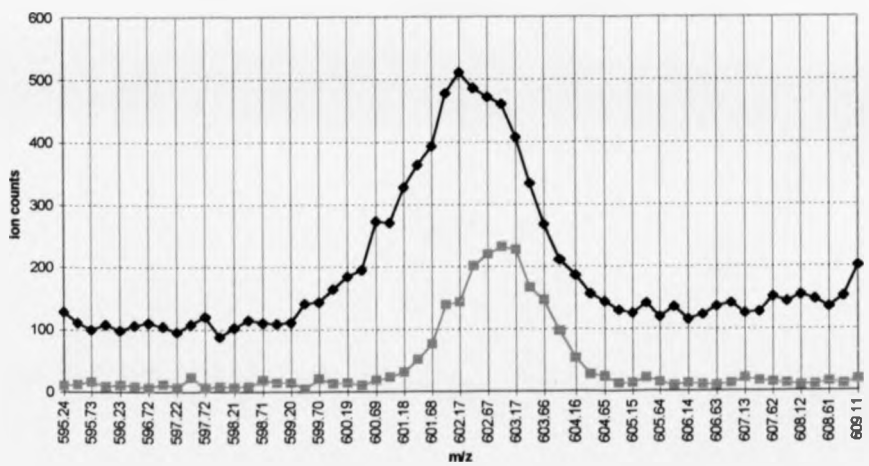

Figure 4-2-b (5): Enlargement of Figure 4-2-b (1) fragment peaks of He-CID (black line, data points marked) and metastable dissociation (pink line, data points marked)

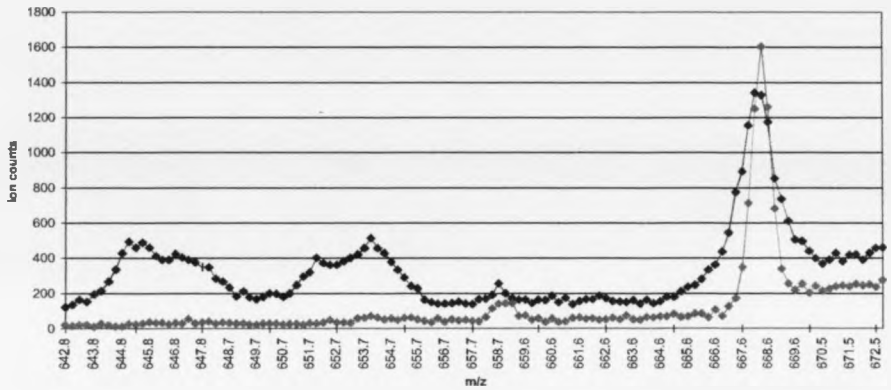

4.3.3 He-CID and Ar-CID of singly charged bradykinin

Experimental conditions are shown on the spectra.

Figure 4-3-a (1)He and Ar-CID of singly charged bradykinin, first skimmer 8082 V, second skimmer 8050 V, V_{HCT-S}=196V, 250^{O}C, 271.53 V for parent ion on E-sector, 0.5-mm-i.d HCT

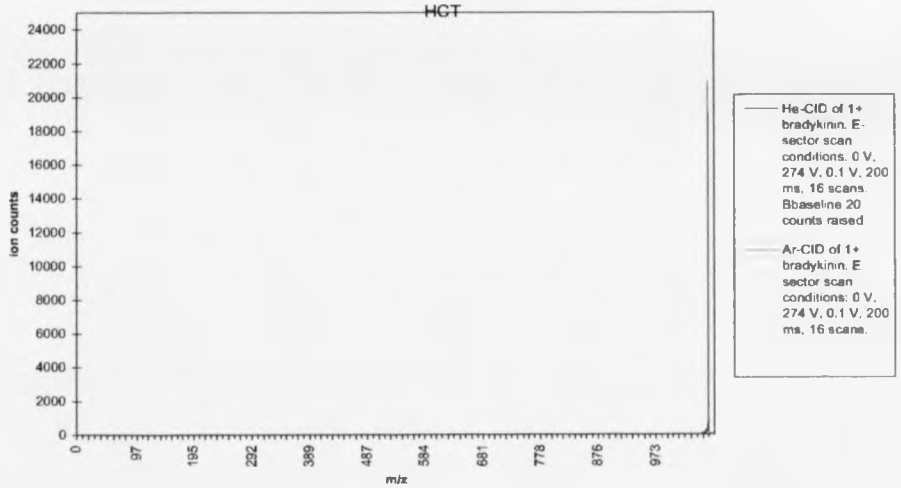

Figure 4-3-a (2)He and Ar-CID of singly charged bradykinin, first skimmer 8082 V, second skimmer 8050 V, V_{HCT-S}=196V, 250°C, 271 53 V for parent ion on E-sector, 0.5-mm-i.d.

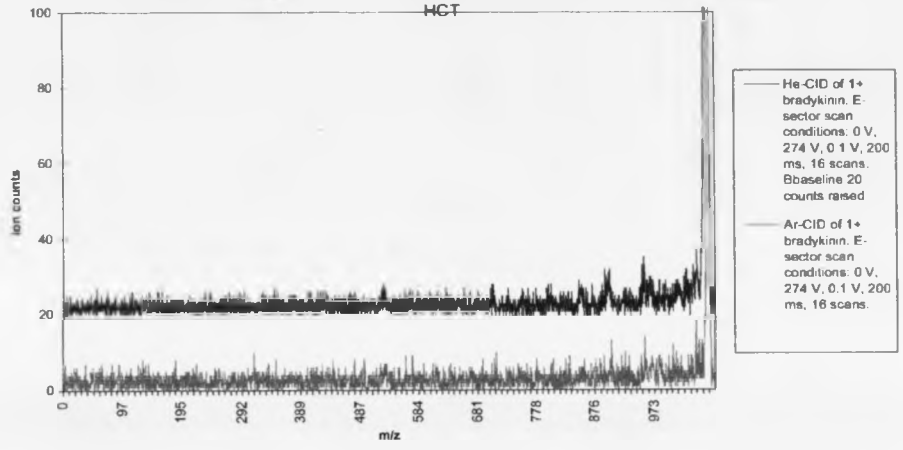

4.3.4 He-CID and Ar-CID of doubly charged bradykinin:

The experimental conditions for [Figure 4-3-b (1)] were: { 0 V (0 m/z), 550.0 V (1075.9 m/z), 0.1 V, 200 ms, 32 scans for He-CID and 16 scans for Ar-CID} (271.45 V on E-sector for the parent ion of doubly charged bradykinin, 531 m/z). The ESI source conditions were: first skimmer 8082 V; second skimmer 8050 V; voltage between HCT and the first skimmer V_{HCT-S} = 0.4 V; 0.5-mm-i.d.-30-cm-long HCT; 12-mm-i.d.-3-m-long restricting pumping pipe; HCT, distance between HCT and the first skimmer d_{HCT-S} = 5.5 mm; HCT temperature 250°C; sample solution flow rate 2 μL/min.

Figure 4-3-b (1) He-CID and Ar-CID of 2+ bradykinin, first skimmer 8082 V, second skimmer 8050 V,V_{HCT-S}= 0.4 V, 250°C,d_{HCT-S}=5 5 mm, 0.5mm-i.d. HCT

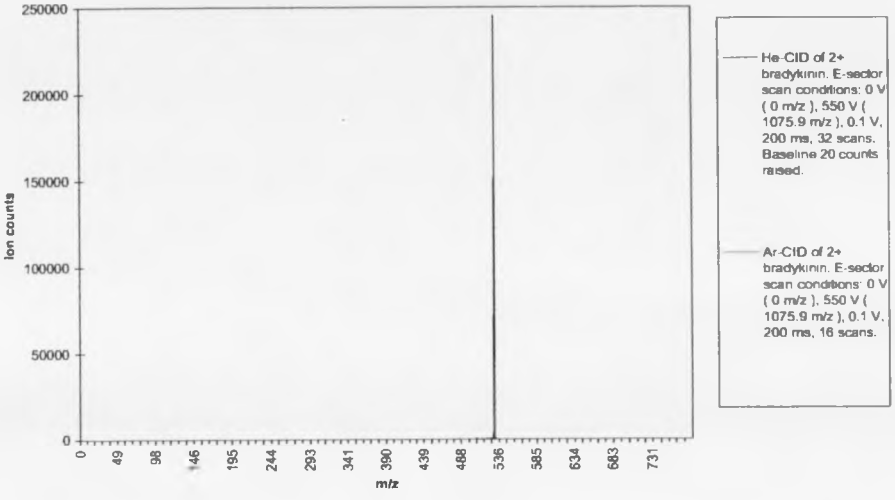

Figure 4-3-b (2)Enlargement of Figure 4-3-b (1) He-CID and Ar-CID of 2+ bradykinin, first skimmer 8082 V, second skimmer 8050 V,V_{HCT-S}= 0.4 V, 250°C,d_{HCT-S}=5.5 mm, 0.5mm-i.d. HCT

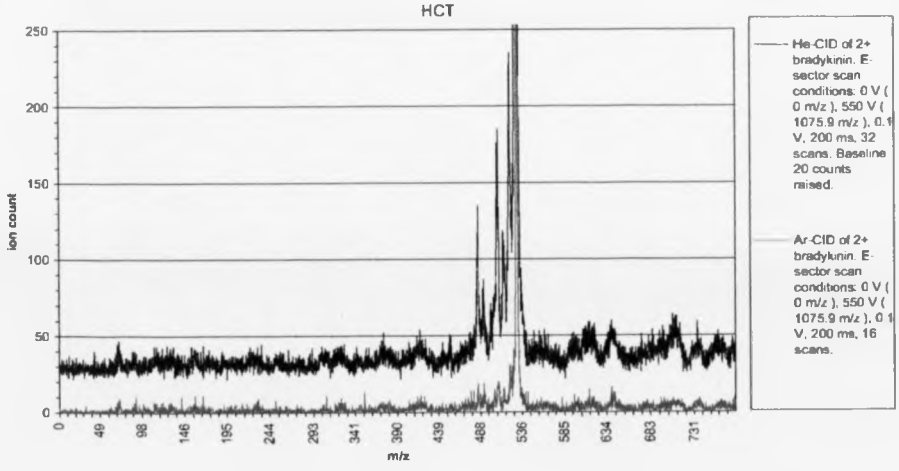

Figure 4-3-b (3) Enlargement of Figure 4-3-b (1) (black, He-CID, 32 scans with baseline 20 counts raised; pink, Ar-CID, 16 scans)

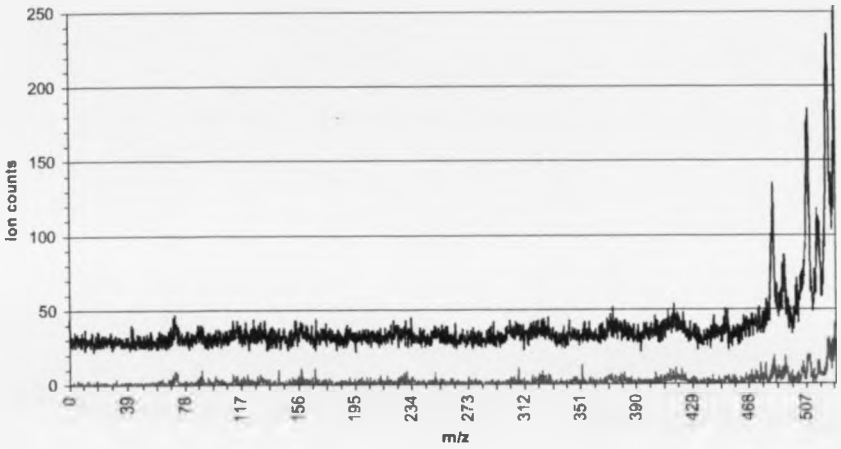

Figure 4-3-b (4): Enlargement of Figure 4-3-b (1) (black, He-CID, 32 scans with baseline 20 counts raised; pink, Ar-CID, 16 scans)

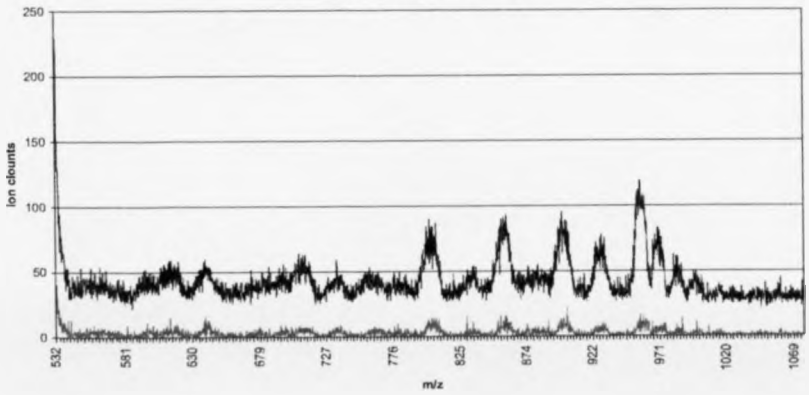

Figure 4-3-b (5) Enlargement of Figure 4-3-b (1) with data points shown (black, He-CID, 32 scans with baseline 20 counts raised; pink, Ar-CID, 16 scans)

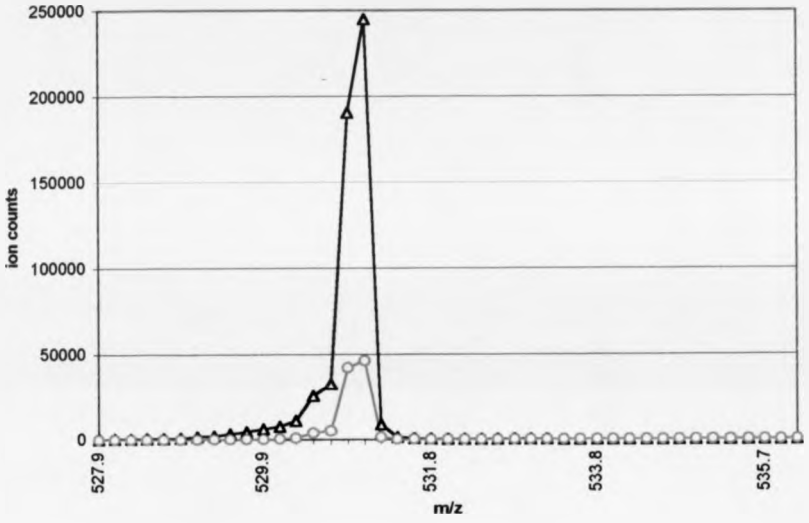

Figure 4-3-b (6) Enlargement of Figure 4-3-b (1) with data points marked (black, He-CID, 32 scans with baseline 20 counts raised; pink, Ar-CID, 16 scans)

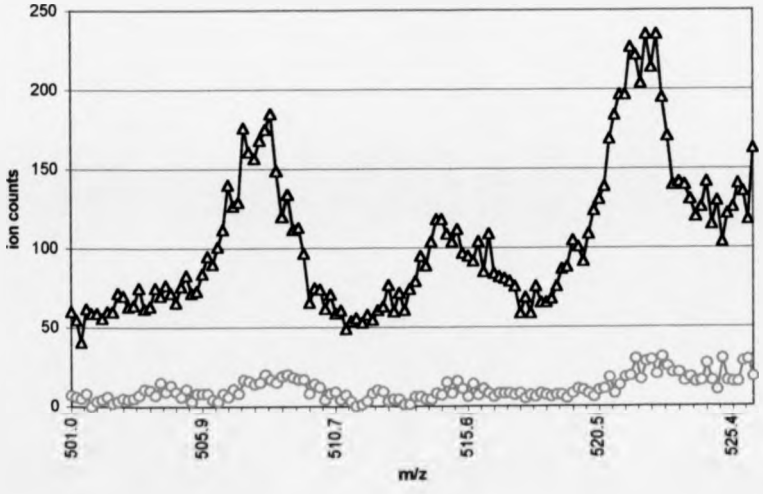

4.3.5 Ar-CID and Kr-CID of doubly charged bradykinin ion (source conditions changed)

The experimental conditions in [Figure 4-3-c] were: first skimmer 8078V, second skimmer 8050 V, V_{HCT-S} = 100 V, 246^{O}C, 271.25V for parent ion on the E-sector, 52 scans for Ar-CID spectrum and 16 scans for Kr-CID spectrum. Other conditions were the same as in [Figure 4-3-b].

Comparing the spectra in [Figure 4-3-b (2)] and [Figure 4-3-c (2)], it was found that, among collision gases used for doubly charged bradykinin, helium was better than argon and argon was better than krypton. According to formula 4-1, the center-of-mass collision energies E_{CM} for doubly charged bradykinin ion with He, Ar and Kr were 60 eV, 582.0 eV and 1172.6 eV respectively.

Figure 4-3-c (1) Ar-CID and Kr CID of 2 + bradykinin

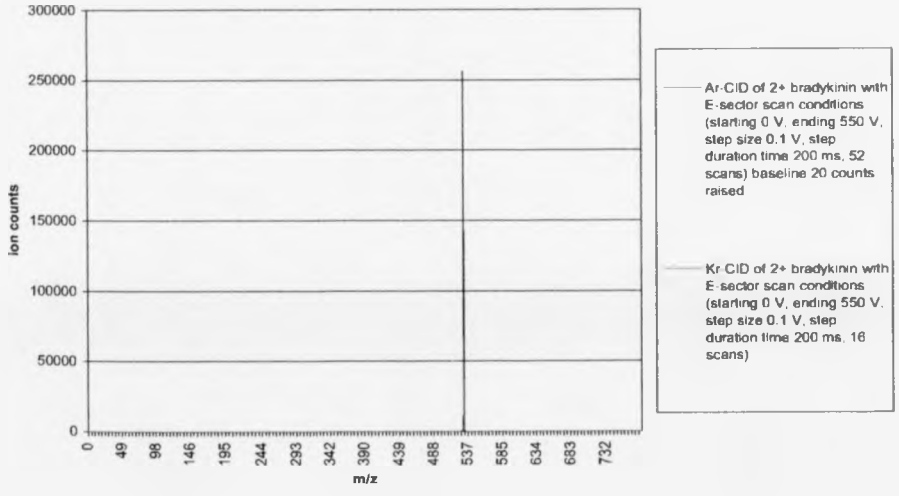

Figure 4-3-c (2) Enlargement of [Figure 4-3-c (1): Ar-CID and Kr-CID of 2 + bradykinin

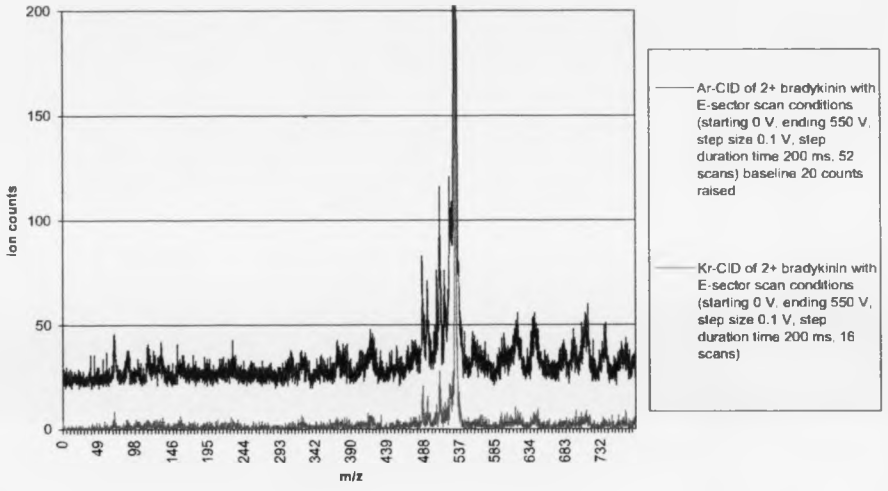

Figure 4-3-c (3) Enlargement of [Figure 4-3-c (1)]: black, Ar-CID of 2+ bradykinin, 52 scans, base line 20 counts raised; pink, Kr-CID of 2 + bradykinin, 16 scans

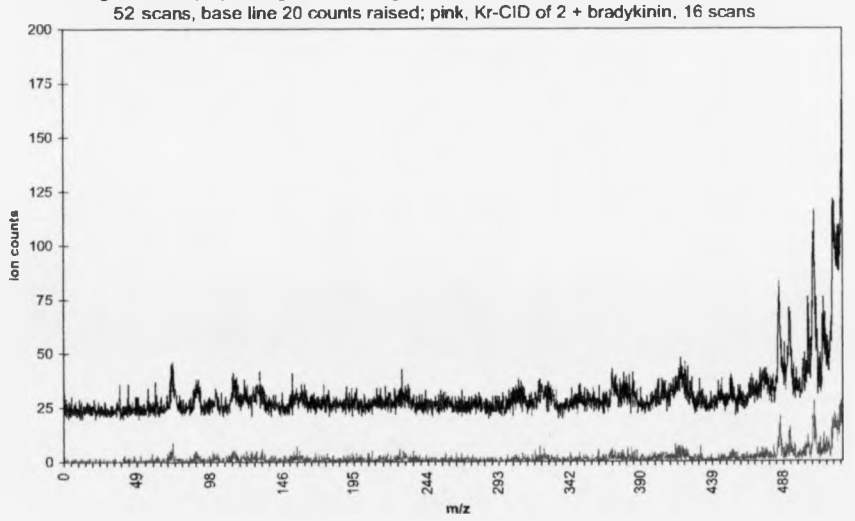

Figure 4-3-c (4) Enlargement of [Figure 4-3-c (1)]: black, Ar-CID of 2+ bradykinin, 52 scans, base line 20 counts raised; pink, Kr-CID of 2 + bradykinin, 16 scans

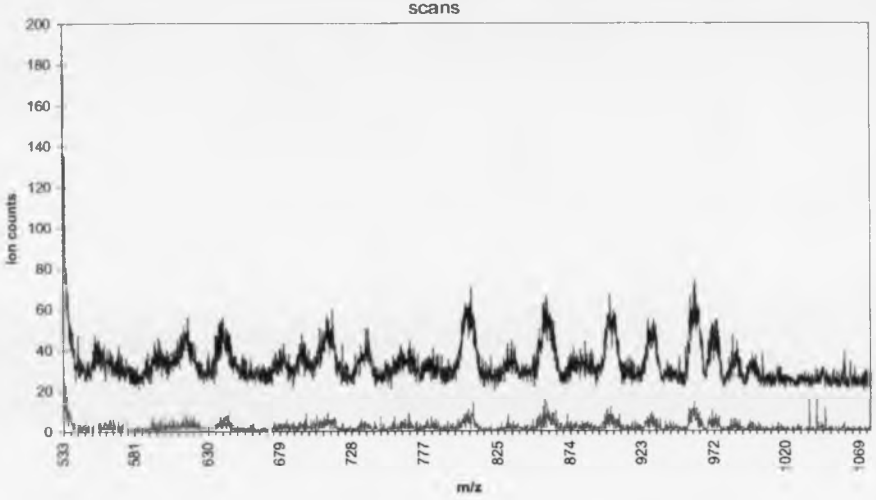

Figure 4-3-c (5) Enlarged mass region of Figure 4-3- b (1): parent ion peaks with data points marked (black line: Ar-CID, 52 scans, base line 20 counts raised; pink line, Kr-CID, 16 scans)

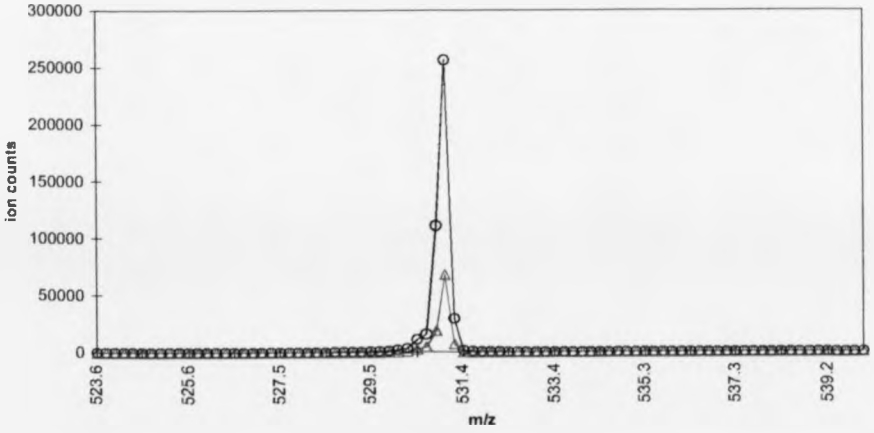

Comparing [Figure 4-3-b (2, 3 and 4)] with [Figure 4-3-c (2, 3 and 4)], from the Ar-CID spectra, it could be seen that recording more experimental scans would

make the spectra more clear about the fragment peaks. The same conclusion could be applied to the singly charged bradykinin He and Ar-CID spectra of [Figure 4-3-a (2)]

4.3.6 Ar-CID spectra of multiply charged ubiquitin

Figure 4-4 gives the Ar-CID of 5+ ubiquitin acquired on the prototype ESI source. The E-sector conditions were: starting from 150 V (955.3 m/z), ending at 300V (1910.4m/z), step size 0.05V, step duration time 200ms, total 115 scans. 269.2V on E-sector for 5+ ubiquitin parent ion, first skimmer 8040V, second skimmer 8000V, optimized $V_{HCT\text{-}S}$. There were no clear fragment peaks in [Figure 4-4].

Figure 4-4(1) Ar-CID of 5+ ubiquitin ion, prototype ESI source, starting 150 V(955.3 m/z), ending 300V(1910.4m/z), step size 0.05V, duration time 200ms,total 115 scans 269.2V for parent ion, first skimmer 8040V, second skimmer 8000V, optimized $V_{HCT\text{-}S}$

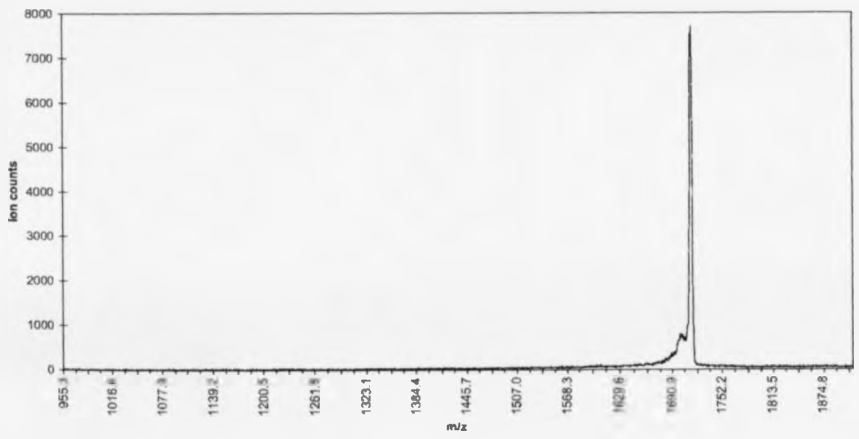

Figure 4-4(2) Enlargement of Figure4-4 (1)

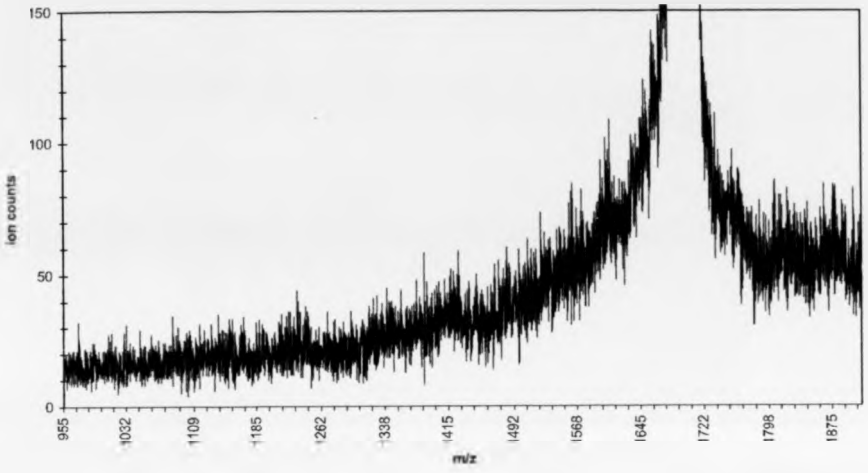

Figure 4-4 (3) Enlargement of Figure 4-4 (1) with data points marked

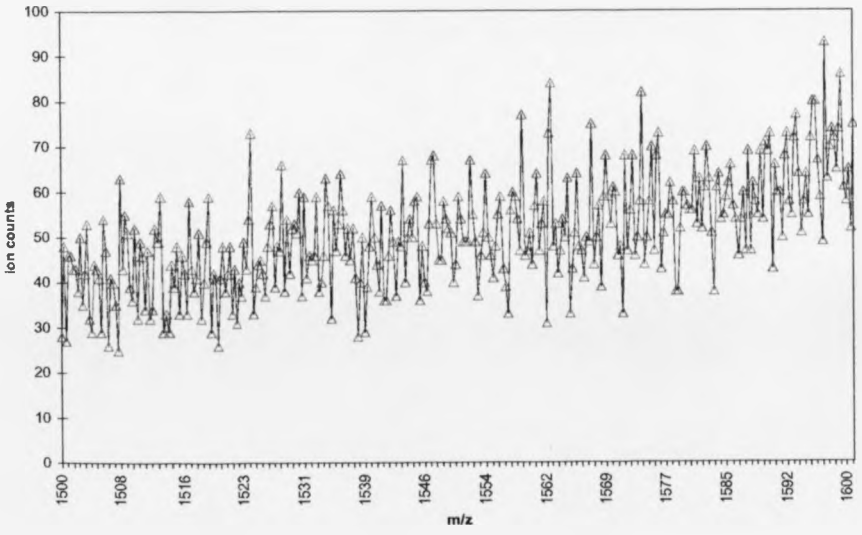

Figure 4-4 (4) Enlargement of Figure 4-4 (1): parent ion peak with data points marked

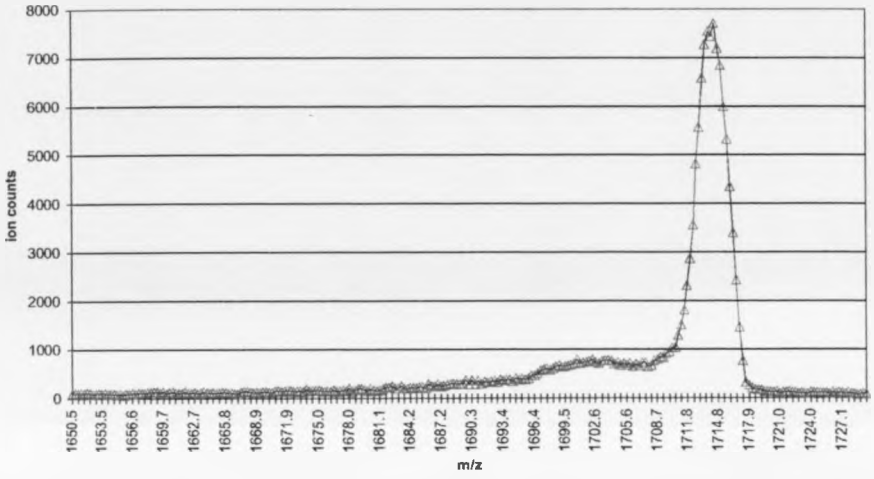

The reasons why in MIKES experiments on the MMM instrument the results for substance P and bradykinin were different from those for ubiquitin could be as follows.

1) One main reason was that the parent ion intensity was still too low for ubiquitin, and its fragment ion peaks would have been much lower. In the substance P and bradykinin experiments, the parent ions' intensities were about 50,000 ~ 135,000 ion counts per second before the collision gas was introduced into the collision cell. For ubiquitin experiments, the parent ion intensity was only about 2,200 ~ 6,000 ion counts per second under the same conditions. From [Figure 4-2-a], it can be seen that the intensity of the substance P parent ion peak was about 240,000 counts and the intensities of the fragment ion peaks were about 600 counts (intensity of parent ion : intensity of the fragment = 240,000 : 600 = 400 : 1) when their positions were near the parent peak, about 40 counts (the ratio becomes to 6000 :1) when they were positioned in other places (for He-CID spectra). In [Figure 4 - 4 (4)], 115 scans only gave about 7,700

counts for the 5+ charged ubiquitin ion by the prototype ESI source. So if using the ratio of parent ion intensity : fragment ion intensity = 400 : 1, the fragment ion peaks would be about 20 counts high which was the same value as noise intensities changing region in [Figure 4-4 (3)].

2) Ubiquitin was much larger (in mass) than substance P and bradykinin and the charged states used (5+, 9+ and 13+) in the experiments were also higher than those of substance P (2+ and 1+) and bradykinin (2+ and 1+). There was the possibility with ubiquitin to give off more fragments ions with resulting reductions in intensity of each individual ion.

3) The detector noise test only gave the random noise signal which was usually one or two ion counts per second. (During the test, the isolation valve between the ESI source and the main part of the MMM instrument was closed and the detector's post-accelerating potential and multiply working potential were the same as in normal experiments.) It was suggested that the background noise truly came from ubiquitin. The background noise level was high near the parent peak and was low at lower or higher voltage regions of the spectrum. This noise or peak broadening came from (or could be seen as) the unfocused parent ion and fragment ions signals, which might have lost some translation energy during the CID processes.

Different fragments would have had different energy losses, since they would have been formed in different ways from the parent ion. Floating the collision cell electrically has been recommended for the purpose of distinguishing metastable peaks from CID peaks[4-23] .

4.4 Experimental results and discussion of ubiquitin on the Fourier transform ion cyclotron resonance (FT-ICR) instrument

Ubiquitin was used in the same solution as in the above experiment on the MMM. The sample was electrosprayed on the Fourier transform ion cyclotron resonance (FT-ICR) instrument. The experimental conditions for the sustained off-resonance irradiation-collision-induced dissociation (SORI-CID) of 8^+ charged ubiquitin ion was: 50 scans, data set size 512 k, excitation range 490.517-2000.000 m/z, the detection range 490.517 - 2000.000 m/z, hexapole accumulation time (D1) 3 second, hexapole offset potential -0.2 V, skimmer potential 1.68 V, extracting potential 0.36 V, trap potential 10.00 V, excitation time (P3) 100 μs, excitation attenuation (PL3) 4 dB. The drying gas was CO_2. N_2 as the collision gas was pulsed into the cell to a pressure of 1×10^{-6} mbar. Following ion activation, a four-second reaction delay was employed to allow fragmentation of the activated ions and the cell pressure to return to near-background level ($\sim 8\times10^{-10}$ mbar).

[Figure 4-5] gives the parent peak of the 8^+ charged ubiquitin. [Figure 4-6] gives the SORI-CID spectrum of the 8^+ charged ubiquitin. [Table 4-1] gives the assignments of the fragments peaks.

From Table 4-1, it can be seen that the SORI-CID experiment only gave part of the sequence information, but there was clear and definite fragmentation.

SORI-CID is a low-energy, multiply-collision process. Using other differently charged ubiquitin ions might give other sequence information. This was seen in charge-state-dependent fragmentation of protonated ubiquitin reported by Reid et al[4-24]. They studied the $[M+12H]^{12+}$ to $[M +H]^+$ charged ubiquitin ions with gas-phase ion/ion

reactions by quadrupole ion trap mass spectrometry and with low-energy CID. They achieved 50% sequence coverage from +8 charged ion along.

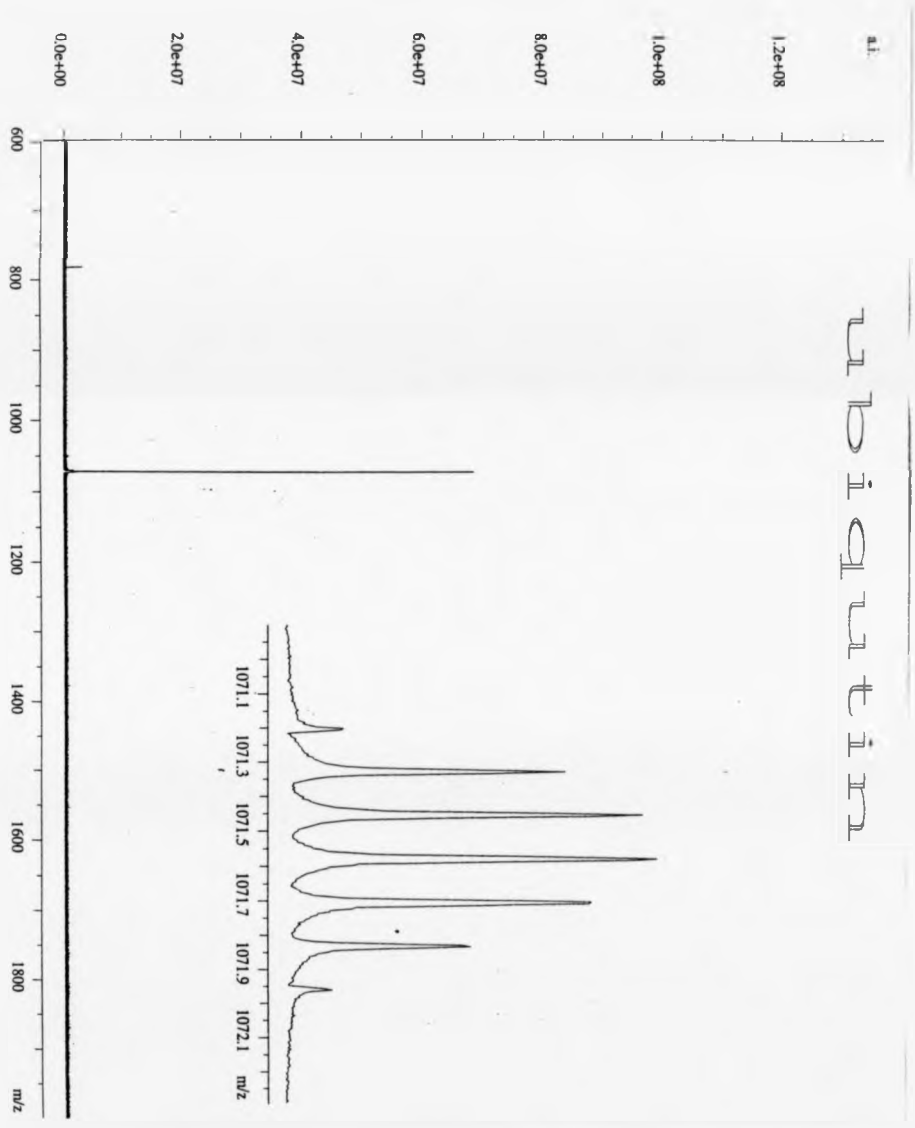

Figure 4-5 : ESI spectrum of ubiquitin, conditions optimized for the 8+ charge ion

Figure 4-6 FT-ICR spectrum of SORI-CID of 8+ ubiquitin ion

Table 4-1 Fragments ion's assignment for SORI-CID of 8^+ charge ubiquitin

central peak of the peak group (m/z read from the spectra)	charge state	experimental and theoretical (asterisked) fragment masses (neutral mass in Da)	assignments
699.9038	3+	2096.6876 / *2096.440	$[y_{18}]^{3+}$
909.84	3+	2726.4962 / *2726.111	$[y_{24}]^{3+}$
999.2455	5+	4991.1878 / *4990.677	$[y_{44}]^{5+}$
1049.5997	2+	2097.1835 / *2096.440	$[y_{18}]^{2+}$
1071.4585	8+	8563.6045 / *8564.851[Av.]	8 + ubiquitin (parent ion)
1078.7443	5+	5388.6818	?
1086.4192	6+	6512.4676 / *6513.352	$[z_{58}]^{6+}$
1089.3366	6+	6529.9720 / *6530.383	$[y_{58}]^{6+}$
1108.0104	6+	6642.0148 /*6642.468	$[z_{59}]^{6+}$
1127.5217	6+	6759.0826 /*6758.631	$[y_{60}]^{6+}$
1146.0276	6+	6870.1180 /*6870.716	$[z_{61}]^{6+}$
1184.8857	6+	7102.8486 /*7102.011	$[y_{63}]^{6+}$
1187.4345	7+	8304.9852 /*8304.514	$[y_{74}]^{7+}$
1191.9770	3+	3572.9072 /*3574.174	$[b_{32}]^{3+}$?
1212.4032	4+	4845.5810 /*4845.473	$[z_{43}]^{4+}$
1220.5733	6+	7317.3922 /*7317.2869	$[y_{65}']^{6+}$
1294.3902	5+	6466.9113 /*6468.411	$[b_{58}]^{5+}$?

The calibration file for the above spectra relied on 4 points in the region from 157 m/z to 904 m/z. For the parent ion mass of the 8+ charged ubiquitin, the experimental mass was 8563.6045 Da, compared to the calculated average mass 8564.851 Da. Probably the difference arose from the choice of peak experimentally.

4.5 Experiments with matrix-assisted laser desorption/ionization (MALDI) on the tandem double-focusing magnetic-sector time-of-flight (MAG-TOF) instrument

The CID and the metastable spectra of several peptides were acquired on the MALDI-MAG-TOF instrument. The experimental conditions and process were as follows.

The matrix used in the experiment was α-cyano-4-hydroxycinnamic acid dissolved in water : methanol = 30: 70 (in volume). The samples were $1 \sim 3 \times 10^{-3}$M in the same solvent. In doing the experiment, 0.5 μL matrix solution was put on the probe tip and dried under gas flow by a small electric fan. Then 0.5 μL of the sample solution was put above the dry layer of the matrix and dried in the same way. The probe was inserted into the MALDI source. The experiments began with tests in the linear TOF-1 working-mode for the purpose of tuning. The electric-magnetic (EB) sector working-mode was used to get the MS1 spectrum. Having chosen the precursor ion with MS1 and introduced the collisional gas into the collision cell, the CID spectrum was acquired in the TOF-2 working-mode. Further tuning might have been performed to get the best spectra. The metastable spectra were acquired in the same way only without introdusing the collision gas. The metastable spectra recorded the fragments from CID of the

precursor ions flying between the exit of the magnetic sector and the entrance of the quadratic-field reflectron.

[Figure 4-7] gives the He-CID spectrum of a peptide with 4 amino acids: Gly-Gly-Tyr-Arg (GGYR) (451.483 Da-average mass). [Figure 4-8] gives an Ar-CID spectrum of a peptide with 6 amino acids: Lys-Arg-Gln-His-Pro-Gly (average mass 720.84 Da). [Figure 4-9] gives the Ar-CID spectrum of angiotensin II (8 amino acids: Asp-Arg-Val-Tyr-Ile-His-Pro-Phe and average mass 1045.21 Da). Angiotensin II spectrum was assigned with the help from (now) Dr. A. R. Bottrill. [Figure 4-10] gives the metastable and Ar-CID and He-CID spectra of buccalin $[M+Na]^+$. Buccalin has 11 amino acids: Gly-Met-Asp-Ser-Leu-Ala-Phe-Ser-Gly-Gly-Leu with average mass 1054.19 Da. [Figure 4-11] gives the metastable and Ar-CID spectra of alytesin $[M+Na]^+$. Alytesin has 14 amino acids: pGlu-Gly-Arg-Leu-Gly-Thr-Gln-Trp-Ala-Val-Gly-His-Leu-Met and average mass 1536.80 Da. It was found that there were more fragments ion in CID-spectra than in metastable decay spectra. With buccalin, Ar-CID gave stronger fragment peaks than He-CID.

Though mass calibration was a problem causing delay in assignment of most of the spectra, it still could be seen that the excitation from MALDI combined with the 8 kV accelerating potential was effective and imparted to the precursor ion sufficient energy to undergo both CID and metastable processes. The acquisition times used for the MAG-TOF spectra were much shorter than for those spectra acquired with the MMM spectrometer which reflects the high signal collecting efficiency of the TOF instrument compared with the sector instrument. Because of the MALDI source, the MAG-TOF instrument was restricted to singly charged ions and the accessible mass

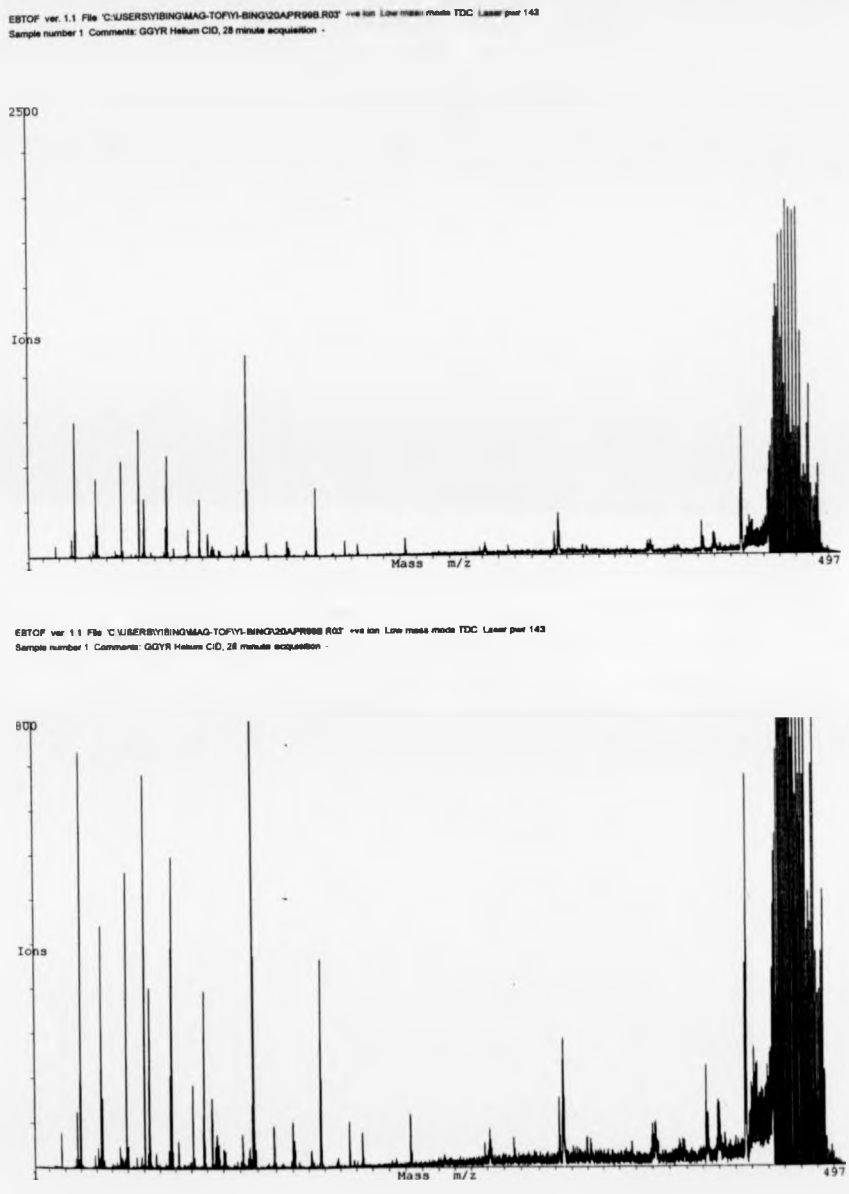

[Figure 4-7] MAG-TOF: He-CID spectrum of Gly-Gly-Tyr-Arg (GGYR)

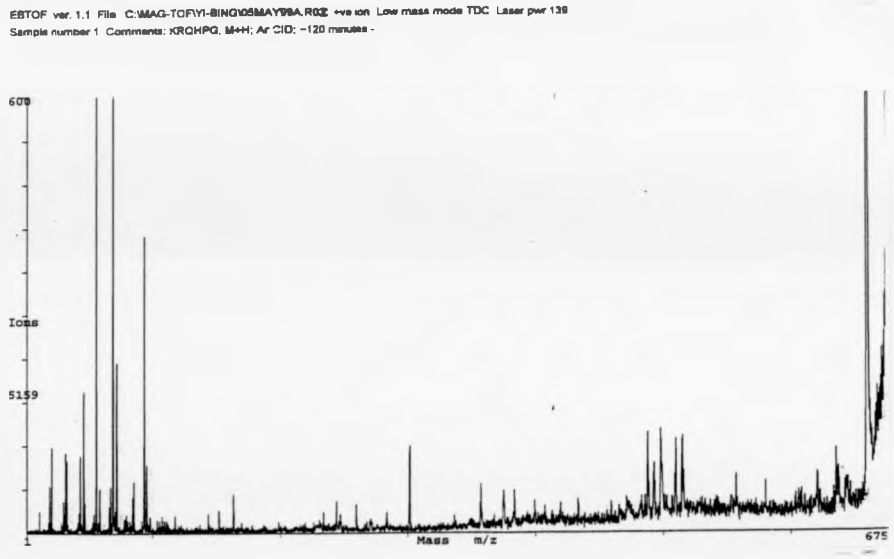

[Figure 4-8] MAG-TOF Ar-CID spectrum of Lys-Arg-Gln-His-Pro-Gly (KRHPG).

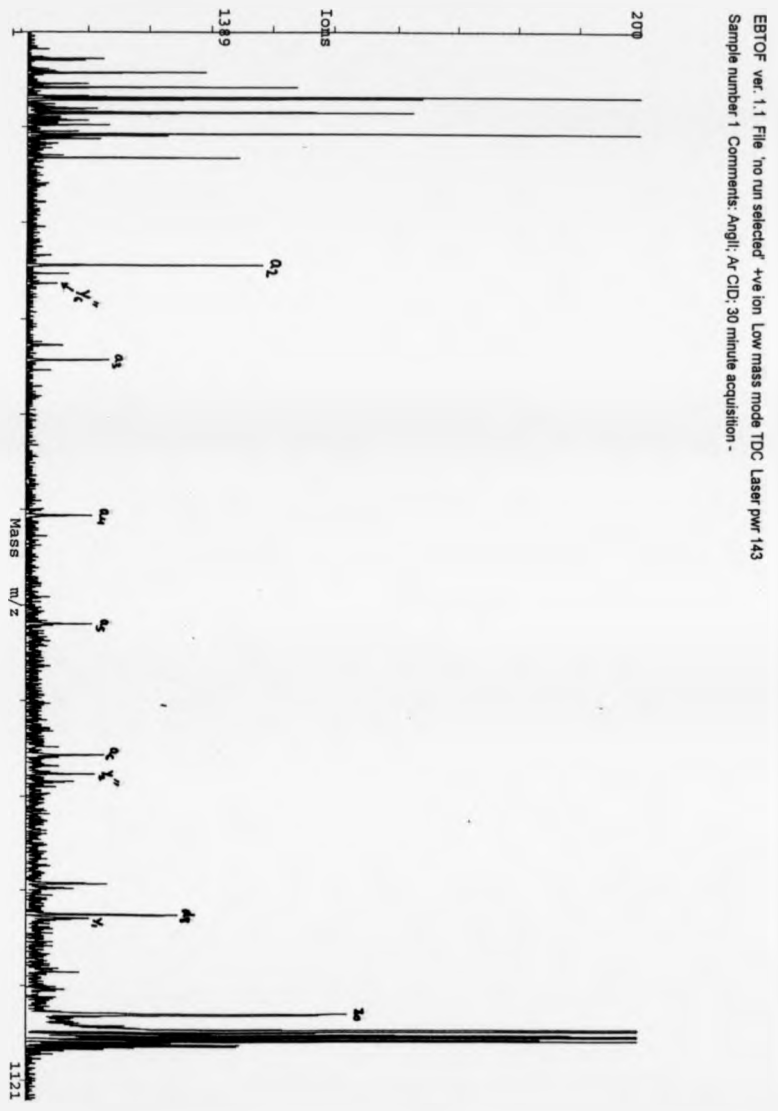

[Figure 4-9] MAG-TOF: Ar-CID spectrum of angiotensin II (: Asp-Arg-Val-Tyr-Ile-His-Pro-Phe)

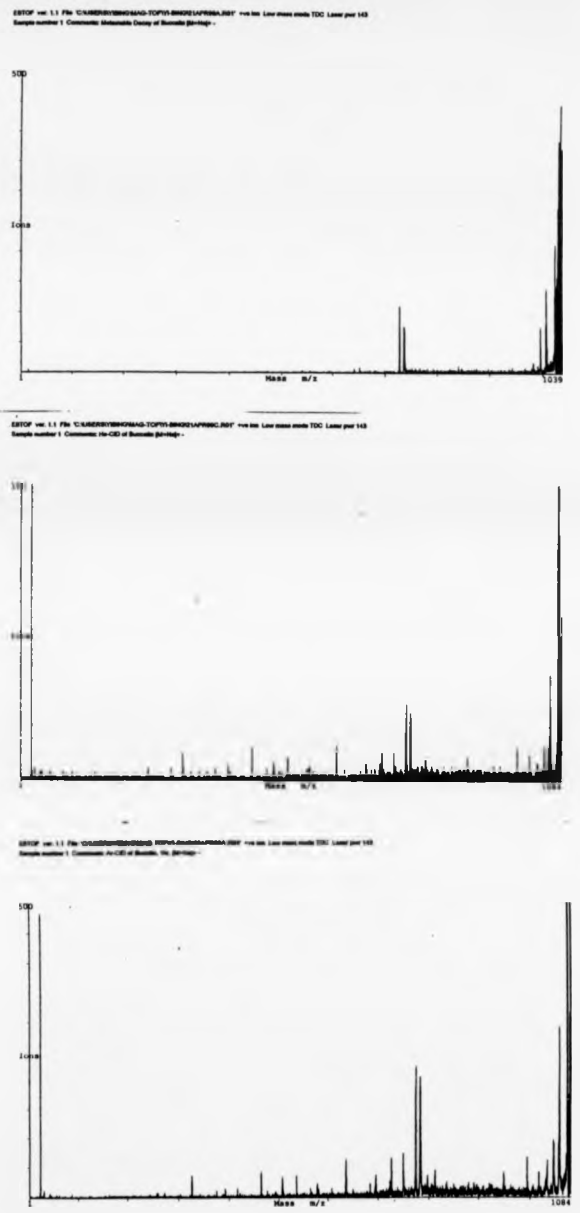

[Figure 4-10] MAG-TOF: metastable, He-CID and Ar-CID spectra (from the top to bottom) of buccalin $[M+Na]^+$.(Gly-Met-Asp-Ser-Leu-Ala-Phe-Ser-Gly-Gly-Leu)

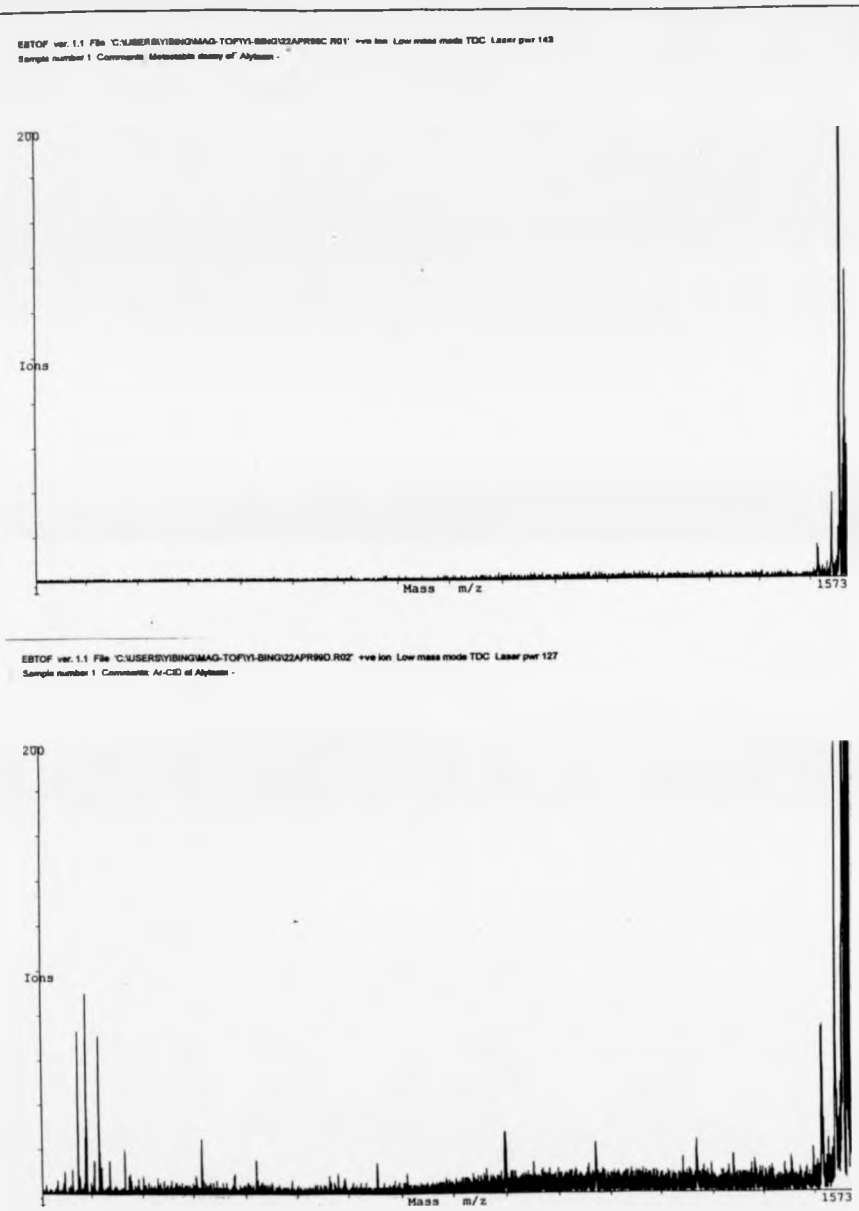

[Figure 4-11] MAG-TOF: metastable and Ar-CID spectra of alytesin $[M+Na]^+$.

(pGlu-Gly-Arg-Leu-Gly-Thr-Gln-Trp-Ala-Val-Gly-His-Leu-Met)

MAG-TOF instrument was restricted to singly charged ions and the accessible mass region was limited to about 3000 Da above which the signal intensities dropped very quickly. This was the reason that ubiquitin could not be studied with the MAG-TOF instrument.

The mass calibration of the spectra was truly difficult and time consuming. The control software allowed the input of up to eight calculated peak m/z's that could be compared against the observed peak positions. A first-order polynomial (linear) fit was used to correct the mass spectrum. But due to the instrument design, incorporating a quadratic-field TOF, a first-order polynomial function was not suitable for creating a calibration file that could be applied to different CID spectra. Internal calibration was nearly impossible when doing CID and the metastable fragmentation experiments. As the energy conditions would have changed easily with different experiments, external calibration was also difficult. The only way was to create an external calibration file and at the same time use the best knowledge to guess the masses of several peaks like the parent ion peak and sodium ion peak, etc. These were used and to perform a calibration. This was followed by checking the data, making the best guess again in the newly calibrated spectra and repeating the process until satisfied. It was necessary to create a calibration file for each parent ion selected for the CID process, which meant that in each spectrum a number of peaks had to be known or at least assumed[4-25]

4.6 Reference:

[4-1] R. D. Smith, J. A. Loo, R. R. Orgozalek Loo, M. Busman and H. R Udseth, *Mass Spectrom. Rev.*, **10**, 359 (1991)

[4-2] A. L. Burlingame, R. K. Boyd and S. J. Gaskell,

Anal. Chem., , **66,** R634. (1994)

[4-3] R. D. Smith, J. A. Loo, C. J. Barinaga, C. G. Edmonds and H.R. Udseth,

J. Amer. Soc. Mass Spectrom, **1,** 53 (1990)

[4-4] O. A. Mirgorodskaya, A. A. Shevchenko, I. V. Chernushevich, A. F. Dodonov and A. I. Miroshnikov,

Anal. Chem., , **66,** 99 (1994)

[4-5] K.D. Henry, E. R. Williams, B.H. Wang, F.W. McLafferty, J. Shabanowitz and D. F. Hunt,

Proc. Natl. Acad. Sci. USA, **1989**, *86*, 9075.

[4-6] M. G. Qiang and D. M. Lubman, *Anal. Chem.*, , **67,** 234A. (1995)

[4-7] R.B. Cody, J. Tamura and B. Musselman, *Anal. Chem.*, , **64**. 1561. (1992)

[4-8] R. D. Smith, J. A. Loo, C. G. Edmonds, C. J. Barinaga and H.R. Udseth,

Anal. Chem., **62**, 882. (1990)

[4-9] S.A. McLuckey, G.J.V. Berkel and G. L. Glish,

J. Amer. Soc. Mass Spectrom. **3,** 60, (1992)

[4-10] R. D. Smith, J. A. Loo and C. G. Edmonds,

Anal. Chem., **63,** 2488. (1991)

[4-11] T. D. Wood, L. H. Chen, C. B. White, P.C. Babbitt, G. L. Kenyon, and F.W Mclafferty,

Proc. Natl. Acad. Sci. USA, **92,** 11451. (1995)

[4-12] H. J. Cooper and P. J. Derrick,

Mass Spectrometry in Biomolecular Science, 201-259, (1996)

Kluwer Academic Publishers

[4- 13] M. M. Sheil and P. J. Derrick, *Org. Mass Spectrom.* **23**, 429 (1988)

[4-14] D Fabris, M. Kelly, C. Murphy, Z. Wu, and C. Fenselau

J. Am. Soc. Mass Spectrom. **4**, 652 (1993)

[4-15] V. S. K. Kolli and R. Orlando, *J. Am. Soc. Mass Spectrom.*, **6**, 234 (1995)

[4-16] T. J. D. Jϕgensen, J. U. Andersen, P. Hvelplund and M. Sϕrense

Int. J. Mass Spectrom., **207**, 31 (2001)

[4-17] M. M. Sheil, Ph.D. Thesis University of New South Wales, Australia (1987)

[4-18] M. E. Belov, personal communication, University of Warwick (1998)

[4-19] M. Kosevich, personal communication, University of Warwick (1997)

[4-20]/ [3-1] M. E. Belov, A. W. Colburn and P. J. Derrick

Rev. Sci. Instrum., **69**, Number 2, 1275 (1998)

[4-21]/ [3-13] J.B. Fenn *Inter. J. Mass Spectrom.* **200**, 459 (2000)

[4-22] / [3-14] D. J. Creasey, D. E. Heard, M. J. Pilling, B. J. Whitaker, M. Berzins and R. Fairly

Applied Physics B Lasers and Optics. **65**, 375, (1997)

[4-23] Busch K. L., Glish G. L. and McLuckey S. A.,

Mass Spectrometry / Mass Spectrometry:

Techniques and Applications of Tandem Mass Spectrometry,

VCH, New York, 1988, p.50.

[4-24] G. E. Reid, J. Wu, P. A. Chrisman, J. M. Wells and S. A. Mcluckey

Anal. Chem. **73**, 3274 (2001)

[4-25] A. R. Bottrill, Ph.D. thesis, University of Warwick, UK, (2000)

Chapter 5 Electrospray ionization: effects of source conditions on the charge state distribution of mass spectra

5.1 Introduction: background and aim

Since the invention of the electrospray ionisation (ESI) method by Fenn et al.[5-1, 5-2], following the early work by Dole et al.[5-3, 5-4], quite a lot of effort has been spent in investigating the unique phenomenon of extensive multiple charging of ions. The purpose of these efforts was to link the shapes, intensities and the placements of the final distributions of ion charge-states in ESI mass spectra with different properties of the initial sample (sample solution conditions, droplets, ionic and other gas-phase conditions, instrumental and operating conditions) and ultimately to understand the ESI process in terms of a mechanism. It was found that nearly all of these experimental factors could play their roles in influencing the final charge-state distributions. Wang et al.[5-5] have written a very good review chapter in the book "*Electrospray Ionization Mass Spectrometry*" in which all these factors, especially the solution and the gas-phase factors, are considered. Some of the above factors will be described simply in the beginning part of this chapter, and the main part of the chapter will concentrate on my experimental results concerning one of the principal ESI-source conditions, namely the potential difference between the capillary and skimmer (or the orifice and skimmer) in the so-called intermediate-pressure region.

It should be pointed out that the electrospray ionization (ESI) process is not a straightforward ionization method, in contrast to other methods used for various different mass spectrometers. For example, in the electron ionization (EI) source, the neutral molecules are converted into the ions in the gaseous state by bombardment with

a high-energy electron beam produced by a high-temperature filament. The ESI process is actually a transfer of analyte species, from the solution where they are generally interacting with many other molecules into the gas phase where they are isolated entities. During this process, the analyte species acquire extra charge through attachment of, for example, H^+, Na^+, K^+ or NH_4^+ in the positive mode or loss of ions in the negative mode. Some gas-phase ion-molecule reactions may occur in the ESI source, but this is not the main process. In general, the ESI process is not an energetic process, indeed, the inherent desolvation process effectively cools the ions. In the appropriate conditions, such as in the ESI source used in this study, where the first skimmer was inserted into the "zone of silence" of the supersonic jet of the capillary (see Chapter 4), ions of low internal energy are introduced into the mass spectrometer. Wysocki et al.[5-6] have shown that ions from the ESI process are considerably 'cooler' than the same ions from the fast atom bombardment (FAB) process, through consideration of the fragmentation and collision energy in surface-induced decomposition experiments. This is why the charge-states of the gas-phase ions in the ESI mass spectrometry may "remember" or reflect the conditions in the solution, or so-called condensed phase. That the ESI process is a transfer is the fundamental reason why so many things can affect the final charge-state distributions of the ions in the mass spectra and the reason why ESI can be used to study non-covalent interactions.

As mentioned in Chapter 1, the first mechanism of ESI was suggested by Dole et al.[5-3]. Their proposal was that during the ESI process very small droplets which only contained one macromolecule with multiple charges could be formed. After the solvent molecules evaporated from this droplet, the free multiply charged gas-phase sample ion

was formed. This mechanism was referred to as the charged-residue model (CRM). The

second mechanism of ESI was proposed by Thomson and Iribarne[5-7, 5-8], and was referred to as the ion-evaporation model (IEM). Their model suggested that the emission of the ions occurred from small, highly charged droplets. The droplets did not undergo fission into offspring droplets, but emitted gas-phase ions following an appropriate degree of the evaporation of the solvent molecules. The driving force was the repulsion between the charged ions and other charges of the droplet. The IEM did not initially address multiple charging. To solve this deficiency, Fenn et al[5-9] gave the third mechanism suggesting that the charge distribution of the samples reflected the ion desorption rate which depended on the droplet charge density. As the droplet charge density increased following the solvent evaporation, the low-charge ions began to desorb. The high-charge ions would desorb later, but at a faster rate following further solvent evaporation giving higher signal intensities. Fenn[5-10] refined this mechanism, linking ion desorption with the surface charge density of the droplet. The ions' charge states were determined by the droplet surface charge density and the size and configuration of the sample molecule, or the number of charges that the droplet surface could accommodate, rather than by the number of charges the sample molecule could carry. So any effects which increased the solvent evaporation speed of the droplets would lead to fewer low-charge ions and would shift the charge-state distribution to higher charge states (low m/z values). Fenn reported experiments in which increasing the flow rate of the heated bath gas in an ESI source shifted the charge-distribution of ESI spectra to the higher charge states. Raising the temperature of the heated bath shifted the charge-state distribution towards higher values (lower m/z values) for the

same reason. Increasing the flow rate of the concurrent gas (or so-called shield gas) shifted the distribution to lower charge states (higher m/z values) as this lowered the evaporation speed of droplets.

It has been found that for positive ions, the upper limit of charge number for peptides and proteins appears to have been determined by the number of basic residues they carried[5-11, 5-12, 5-13].

Tightly folded native conformations of protein molecules offer less access and the extended denatured conformations offer more access to the ionization sites. Therefore, anything helping the denaturing process of a protein might be expected to shift the charge state distribution of the spectra in the higher charge direction (lower m/z value). Such factors could be the pH changing[5-14], organic solvent introduced[5-15,5-16], heating[5-16, 5-17, 5-18] or denaturing reagents[5-19]. As an example, Clemmer and co-workers[5-16] claimed that there were three conformations of ubiquitin ions in the gas-phase: compact forms or highly folded conformers (favored for low charge states +6 and +7), partially folded conformers (favored for +8 and +9 charge states) and unfolded conformers (favored for +10 to +13 charge states). The proportions of conformers were very sensitive to the solvent composition and capillary temperature used in the ESI source of the high-resolution ion mobility apparatus. They found that gas-phase ions formed from a "pseudonative" solution (one containing more than 90% water) were more likely to be compact forms than ions from "denatured" solution (one containing more non-aqueous solvent). Their explanation was that increased coulombic repulsion among charges forced high-charge states to adopt more open conformations and that this effect would be pronounced in the gas-phase where the dielectric constant was lower (1 compared to 80 for water). The experiments were interpreted as showing

that there were multiple conformations present and conformers interconverted as they travelled through the drift tube. They found that when the capillary temperature was increased, partially folded and unfolded conformers were formed as evidenced by changes in cross-section distributions. The temperature required for the change of conformation was higher in the "pseudonative" solution. Clemmer and co-workers suggested that the thermal denaturing of the protein could occur in the solution before the ESI droplets had shrunk and formed the gas-phase ions in corresponding conformations. In these experiments, the temperature of capillary was in the region from 25^0C to 132°C. It should pointed out that their experiments were performed at high pressures (150 to 200 Torr), and the ions were formed and probed at high pressures without exposure to energetic collisions that could occur in the interfacial regions of most mass spectrometers. There would not be collision-induced dissociation, declustering or focusing factors in the ion mobility studies.

As the ESI process is a low-energy process, the initial solvent conditions might be important through determining the starting conditions of the sample molecules. It might be supposed that anything that could aid the formation of the sample ions in solution might finally help the formation of the gaseous ions. Low pH value would favour a protonation of the sample molecules, which could help detection of the sample in the positive mode. Increasing the higher dielectric constant solvent in the solution would tend to stabilise multiply charged species in solution, and might favour the formation of gas-phase ions of higher charge states.

At higher dielectric constant solvent could help the "electrophoretic" process associated with the charged-droplet formation at the ESI-needle exit. In this process, the negative ions migrate toward the positively charged ESI-needle metal surface (positive

ion mode) where they can undergo oxidation under the high electric voltage. In this way, the negative counterions are removed from the solution and the formation of the droplets with excess positive charge occurred. In the negative ion mode, the positive ions would migrate to the negatively charged ESI-needle metal surface, be reduced there and help to form the droplets with excess negative charge. Aronson et al. [15-20] have claimed that a redox reaction, taking place in the metal capillary of an ESI source to maintain the charge balance, can alter the composition of the initial solution entering the capillary. Under certain ESI conditions, such as a non-buffered solution near neutral pH, using metal spray capillaries or metal contacts to the solution made of difficult to oxidize material (e.g. platinum or gold), the solution pH may be decreased significantly (4 pH units) as a result of the electrolytic oxidation of water in the positive ion mode. Any pH change would increase in magnitude as the flow rate decreased and/or the electrospray current increased.

Smith et al[15-21] have reported that a higher level of protonation was observed with cytochrome c when using nitrogen as a countercurrent drying gas, compared to a heated-capillary ESI source with no drying gas. They thought that more proton abstraction was possible in the heated capillary as in the absence of drying gas a higher level of solvent species enter the ESI source. The conclusion to be drawn would be that a source geometry allowing less solvent species to enter the mass spectrometer would produce more highly charged ions, all other things being equal. Smith et al also found that an increased distance between the capillary and the skimmer caused discrimination against higher charged states.

Clarifying the role of the potential difference between the capillary and skimmer (or orifice and skimmer) in the so-called intermediate-pressure region is central to

understanding the ESI process. It has been found that the change of the capillary or skimmer potential in an ESI source does affect the charge-state distribution. This potential difference plays two effects:

(i) one is a focusing effect to guide the ion beam through the skimmer orifice into the next part of the mass spectrometer.

(ii) the second is to accelerate ions through this intermediate pressure or free-jet region. In doing so, the ions acquire additional energy, which could help the desolvation of attached solvent molecules from the sample ions, declustering of the sample ion clusters or even cause collision-induced dissociation.

The question is which is the main effect and under what conditions? The aim of many of experiments in this study was to answer this question and therefore to understand more about the mechanism of the ESI process particularly in this region.

Thomson [5-22] has claimed that charge loss or gain through collisional detachment of a proton or electron does not occur in this intermediate-pressure region when the potential difference is increased. He proposed that the higher collision energy results in better declustering of lower charge-state ions (higher m/z) and fragmentation of higher charge-state ions (lower m/z). The net result is an apparent shift toward lower charge-state (higher m/z) as the collision energy in this free-jet region is increased. He has claimed that a mixture of heavily clustered monomers and possibly dimers and multimers is typically present in the free-jet expansion, and it is this mixture which is acted on by declustering fields to produce the observed mass spectrum. To support his views, he conducted experiments with a triple quadrupole mass spectrometer (PE SCIEX API III +) with an ion-spray source. The instrument used a nitrogen counter-current drying gas. With apo-myoglobin sample, collision-activated dissociation (CAD

) was performed in the middle quadruple (collision cell). A whole mass spectrum with charge states from 8+ to 15+ was observed, compared with a spectrum of only poorly resolved peaks at high m/z in the absence of CAD.

Sheil et al[5-23] have concluded that the only important effect of capillary/skimmer (cone/skimmer) potential is the focusing effect which is dependent upon the mass-to-charge ratios of the ions. Results were obtained with a triple quadrupole (VG Quattro mass spectrometer with a hexapole collision cell (VG Biotech, now Micromass , Alrincham, UK)) and a VG Autospec magnetic-sector mass spectrometer (VG Analytical, now Micromass, Wythenshawe, UK). The ESI source used a nebuliser gas (nitrogen), a chicane counter-electrode, nitrogen-drying curtain gas, a sampling cone (rather than a capillary) and a skimmer. They measured the ion currents of the different charge states with different skimmer potentials with peptides and polymers. They proposed a mathematical model to analyse their results from varying the cone (orifice)/skimmer potential (0 - 200 V). The experimental results matched well with the mathematical predictions. For the same mass but different charge state (same sample), the optimum cone potential varied as approximately m/z (linear dependence), but as approximately $(m/z)^{1/2}$ for the same charge and different mass. They claimed that in this intermediate-pressure region CAD, charge (proton or electron) transfer and declustering processes under the experimental conditions could be considered to be unimportant.

Schneider and Chen[5-24] have provided a semi-quantitative model to predict the value of the orifice/skimmer voltage needed to start fragmentation of the ion in the intermediate-pressure region. They have asserted that this model can be used to predict the types of solvent adducts likely to be observed for analytes at various orifice/skimmer

voltages. In their model, after the sample ion flies into "zone of silence" of the supersonic free-jet expansion in the orifice/skimmer region, it will collide with a curtain gas molecule and each collision is treated as the inelastic collision between a moving ion and a stationary target gas molecule. All of the center-of-mass energy is assumed to be converted into the internal energy of the analyte ion. The internal energy of the ion builds up with each collision until it reaches the skimmer inserted into the supersonic jet. According to their model, the amount of energy converted into internal energy depends in a linear fashion upon the orifice/skimmer potential.

The factors at play in an ESI source have been discussed at some length, in order to emphasise both the complexity and the conflicting theories existing in the literature. The experiments which follow were designed to probe focusing effects in the intermediate-pressure region and the effects of collisions upon internal energy of analyte ions.

5.2 Experiments:

5.2.1 Instrument:

The instrument used was the large-scale reverse-geometry two-sector mass spectrometer described in Chapter 2, equipped with the electrospray ionisation (ESI) source incorporating the improvements discussed in Chapter 3.

The situation as regards power supplies for the ESI source components was as follows: the ESI spray needle, the first skimmer, the second skimmer, the extracting electrode, y-focusing/deflecting lens and z-focusing/deflecting lens all had their own high-voltage power supply. There was an isolation transformer isolating the main power supply, within which a variable transformer supplied the electric current to the heating

wire coiled around the heated capillary tube (HCT). A DIGTRON thermal meter (ZENITH ELECTRIC, Waltham Cross, Herts, England) was used to monitor the temperature of the HCT via a thermocouple put near to the outside surface of the HCT heating copper block. The isolation transformer could withstand a potential difference of more than 20 kV. The isolation transformer, the variable transformer and thermal meter were all put in a plastic box for reason of safety. A floating power supply with two frequency-amplitude converters supplied the potential difference between the HCT and first skimmer [Figure 5 -1: Photo of the HCT power supply unit]. As the outputs of the converters were linked in series, the total output could be changed between 1.4 V and 400.0 V. In order to reduce the chance of a gas breakdown caused by applying too large a potential difference between the HCT and skimmer, the power supply output for the first skimmer was connected with the floating reference point of the isolation transformer. The two converters were optically controlled by a low-voltage transceiver through two fibre optic cables. The isolation transformer and the two frequency-amplitude converters were put in another plastic box for the same reason of safety. Directly linking the counter electrode and HCT ensured that they were at the same potential. Their potential would be that of the first skimmer plus the difference introduced by the two converters.

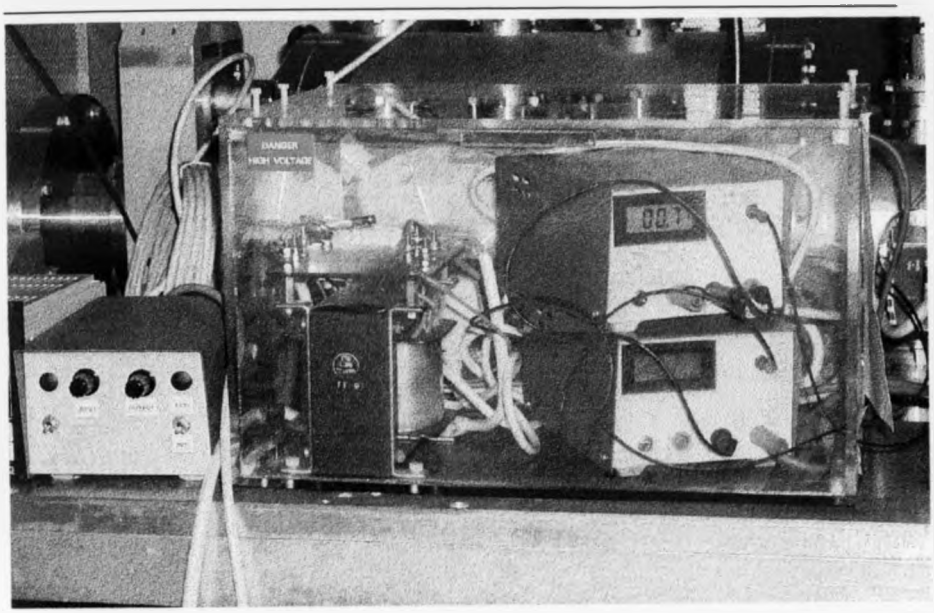

Figure 5 -1: Photo of the HCT power supply unit

5.2.2 Typical sample solution conditions:

(1) Substance P 5×10^{-5}M in $CH_3CN:H_2O:CH_3COOH$= 49:49:2 (by volume respectively);

(2) Insulin 5×10^{-5}M in $CH_3CN:H_2O:CH_3COOH$= 49:49:2 (by volume);

(3) Ubiquitin 2×10^{-5}M in $CH_3CN:H_2O:CH_3COOH$= 49:49:2 (by volume);

(4) Vancomycin 5×10^{-5}M & KAA (N-acetyl-lysine-D-alanine-D-alanine) 10×10^{-5}M in $CH_3CN:H_2O:CH_3COOH$= 49:49:2 (in volume);

(5) Polyethylene glycol (PEG) 800: 1×10^{-4}M in $(CH_3)_2CO:H_2O$=90:10 (by volume);with 1.2mM CH_3COONa in the solution;

(6) (a)PEG 1500: 1×10^{-4}M in $(CH_3)_2CO:H_2O$=90:10 (by volume) with 1.2 mM CH_3COONa in the solution or (b) in 5×10^{-5}M in 5 mM CH_3COONH_4 /H_2O: CH_3OH: CH_3COOH = 49.5 : 49.5 :1 (by volume).

Substance P was bought as the acetate salt. Its molecular mass for the free peptide was 1347.6 Da. The insulin molecular mass was 5733.5 Da from bovine pancreas. The ubiquitin molecular mass was 8564.8 Da from bovine red blood cell. They were all bought from SIGMA® CHEMICAL CO. St. Louis, MO, USA. The PEG 800 sample was obtained from Imperial Chemical Industries plc (ICI). Sample reference number was SUEF2218. The water was distilled. Acetonitrile and methanol were standard HPLC solvents. The acetone and acetic acid were the standard for general laboratory use. These were all bought from Fisher Scientific UK Limited, Bishop Meadow Road, Loughborough, Leics, UK.

5.2.3 Experimental procedures:

The sample solution was placed in a 500μl syringe (HAMITON CO. RENO, NEVADA GASTIGHT®) which was driven by a Harvard Apparatus (South Natick, USA) syringe pump at a flow rate 1 ~ 2 μl/min. The solution was driven first through the PEEK pipe (0.25 mm-i.d.), and then through the stainless steel spray needle. Finally the sample solution was sprayed out before the entrance end of the HCT in the electric field of the ESI needle.

Changing the potential on the HCT (which was at the same potential as the counter electrode because they were directly linked with each other), the signal intensity (ions per second) at the final detector with both magnetic and electric sectors' settings fixed (which meant that only the specific ion with the chosen m/z could pass through

the instrument) was monitored. During the experiments, the potentials on the electrospray needle and on the first and the second skimmers were all fixed. The potentials on the ion optical system after the second skimmer sometimes needed tuning slightly to achieve better focusing during the experiments. The slits of the source (α-slit), the collision cell (β-slit)and final detector (γ-slit) were set at widths of 0.5-mm, 1-mm, 1-mm-wide respectively. The HCT was 0.762-mm-i.d. and 30-cm-long. The distance between the end of the HCT and the first skimmer was 5.00-mm. The electrospray solution flow rate was 2μL/min. The temperature of the HCT was fixed during an experiment.

The accessible range of potential difference $V_{HCT\text{-}S}$ between the HCT and the first skimmer was from 1.4 V to 400.0 V. Voltage of $V_{HCT\text{-}S}$ higher than 400.0 V would have been above the maximum output of the series-linked two converters power supply and also near the gas breakdown voltage of the intermediate-pressure region. Using the same Paschen curve[3-5] (Chapter 3) for the potential difference 400 V and 5 mm distance between the HCT and the first skimmer, the electric breakdown value was 1.2 mmHg•cm (= P× d). As the pressure here was 3.54 mbar, the experimental figure was: P×d = 3.54 mbar × 5 mm = (3.54 / 1.33) ×(5/10) mmHg•cm = 1.33 mmHg•cm. This value was just a little above 1.2 mmHg•cm.

It should be pointed out that when doing the experiments the instrument conditions were fine-tuned to maximise the ion signal at the final detector. For different ions of the same sample, the instrument conditions would tend to be slightly different from each other. For the magnet scan spectra, the instrument conditions were exactly the same for all ions as only the magnetic field was scanned.

5.3 Results and the discussions

5.3.1 Substance P

Substance P is a peptide with 11 amino acid residues, Arg-Pro-Lys-Pro-Gln-Gln-Phe-Phe-Gly-Len-Met-NH_2. With N terminus H and C terminus OH, its monoisotopic molecular mass is 1347.71 Da, nominal molecular mass is 1347.00 Da, average molecular mass is 1348.64 Da. Using the monoisotopic figure, [M+H]+ would be 1348.72 Da ≈ 1349 Da. [M+2H]2+ should be 675 Da and [M+3H]3+ should be 450 Da.

[Figure 5-2] gives results for the substance P solution (average of 3 experiments). In this figure, the y-axis is the absolute final signal intensities in ion counts per second and the x-axis is V_{HCT-S} (the voltage difference V_{HCT-S} between the HCT and the first skimmer) in the source. The HCT temperature was at 248°C. [Figure 5-3] gives the same experimental results, but the y-axis shows the normalised intensities. [Figure 5-4], [Figure 5-5] and [Figure 5-6] show the results of the three different measurements from which the averages were obtained.

The detailed instrument conditions except those shown on the Figures themselves were as follows: the solution flow rate was 2 μL/min, the electrospray needle voltage was 10.3 kV, the HCT and counter electrode voltages equalled the first skimmer voltage 8078V + V_{HCT-S}, the extracting voltage was 6.7 kV, the y-focusing voltage was 8.0 kV, the y-deflecting setting was 5.25, the z-focusing was 6.0 kV, the z-deflecting setting was 4.26. During the experiments the setting of the extraction voltage and the y- and z- focusing/deflecting lenses might have been adjusted slightly.

[Figure 5-7] and [Figure 5-8] give the substance P results (average of 4 experiments) under the same conditions as before, except that the temperature of HCT

had been lowered by 50°C to 198°C. [Figure 5-9] gives the substance P experimental results at 148°C.

Figure 5-2: Substance P. $[M+H]^+$, $[M+2H]^{2+}$ and $[M+3H]^{3+}$ ions intensities vs the V_{HCT-S} voltage between the HCT and the first skimmer at 248°C ; 5-mm HCT-skimmer distance; first skimmer 8078V; second skimmer 8050 V

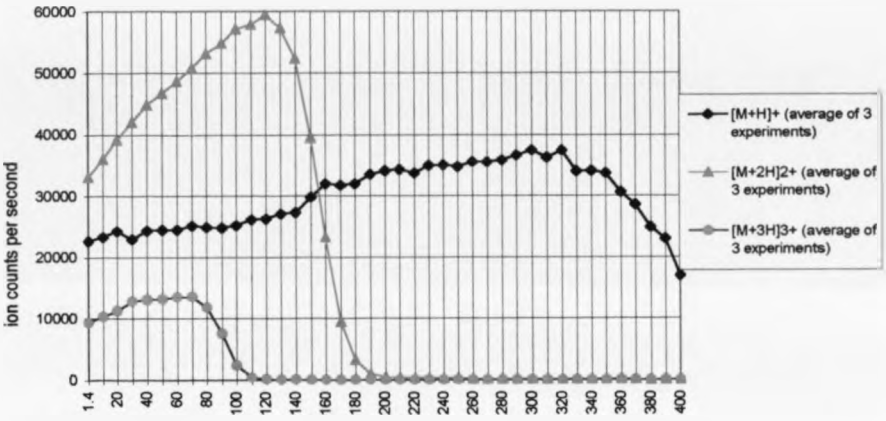

voltage between the heated stainless steel capillary (HCT)(0.762-mm-i.d. 30-cm-long) and the first skimmer in the ESI source of the MMM instrument

Figure 5-3: Substance P. $[M+H]^+$, $[M+2H]^{2+}$ and $[M+3H]^{3+}$ ions normalised intensities vs the voltage V_{HCT-S} between the HCT and the first skimmer at 248°C; 5-mm HCT-skimmer distance; first skimmer 8078V; second skimmer 8050 V

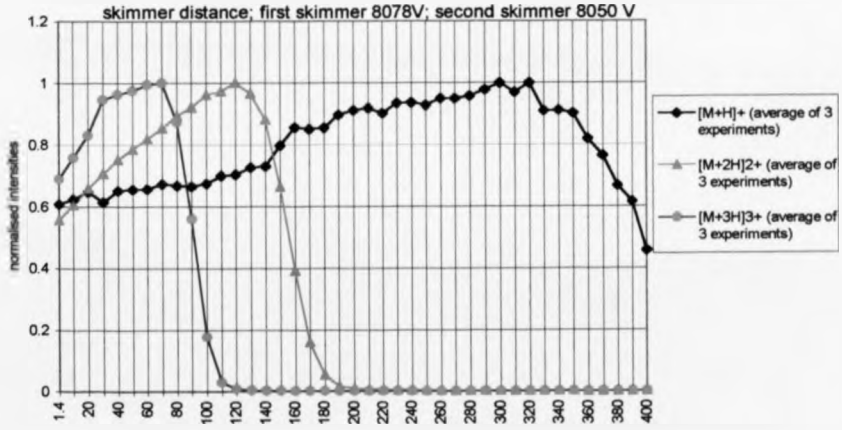

voltage between the heated stainless steel capillary (HCT)(0.762-mm-i.d. 30-cm-long) and the first skimmer in the ESI source of the MMM instrument

Figure 5-4 : Subtance P. $[M+3H]^{3+}$ (450 m/z) ion intensities vs the voltage V_{HCT-S} between the HCT (0.762-mm-I.d.-30-cm-long)and the first skimmer at 248°C ; 5mm capillary-skimmer distance; first skimmer 8078V; second skimmer 8050 V

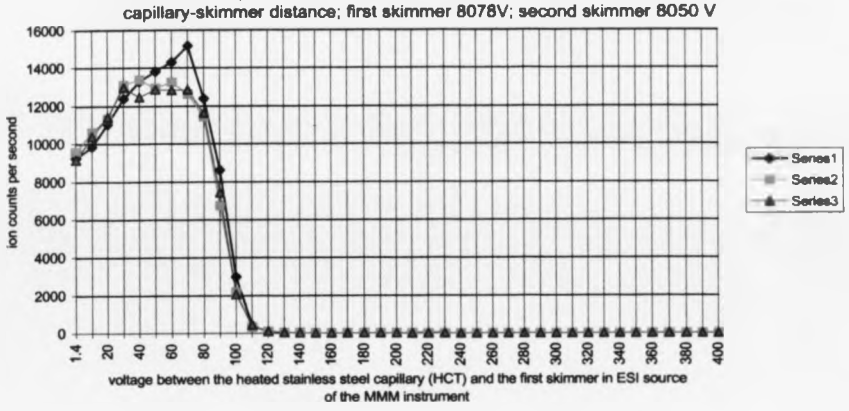

Figure 5-5: Substance P. $[M+2H]2+$ (675m/z) ion intensity vs the voltage V_{HCT-S} between the HCT (0.762-mm-I.d.-30-cm-long) and the first skimmer at 248°C ; 5mm capillary-skimmer distance; first skimmer 8078V; second skimmer 8050 V

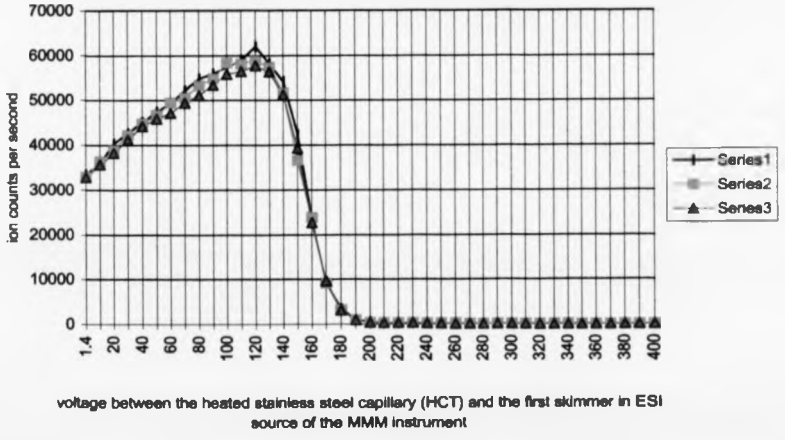

Figure 5-6 : Substance P. [M+H]+ (1348 m/z) ion intensity vs the voltage V_{HCT-S} between the HCT and the first skimmer at 248°C ; 5mm capillary-skimmer distance; first skimmer 8078V; second skimmer 8050 V

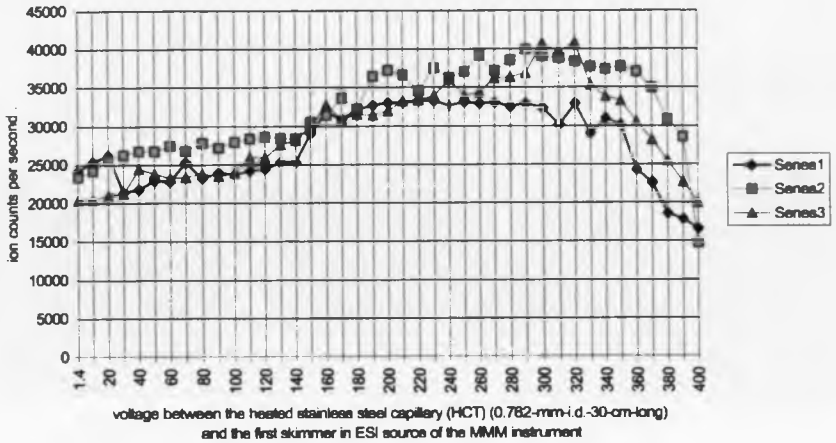

Figure 5-7: Substance P $[M+H]^+$ and $[M+2H]^{2+}$ ions signal intensities vs the voltage V_{HCT-S} between the HCT and the first skimmer at 198°C, 5.00-mm HCT-skimmer distance, first skimmer 8078 V, second skimmer 8050V

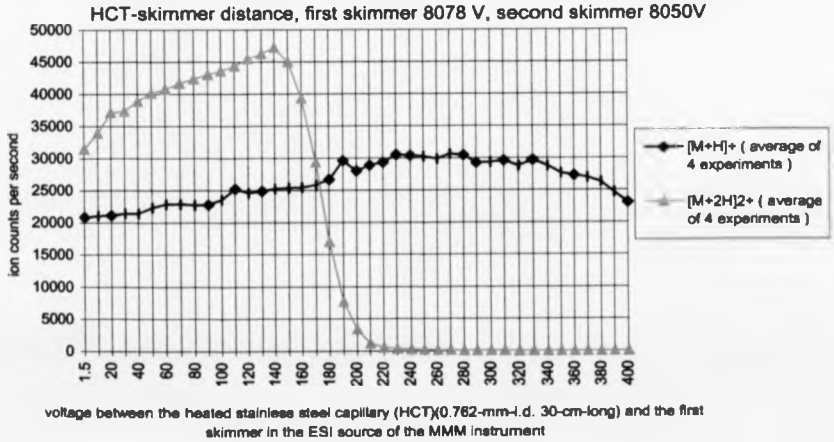

Figure 5-8 Substance P. $[M+H]^+$, $[M+2H]^{2+}$ ions normalised intensities vs the voltage V_{HCT-S} between the HCT and the first skimmer at 198°C, 5.00-mm HCT-skimmer distance, first skimmer 8078 V, second skimmer 8050V

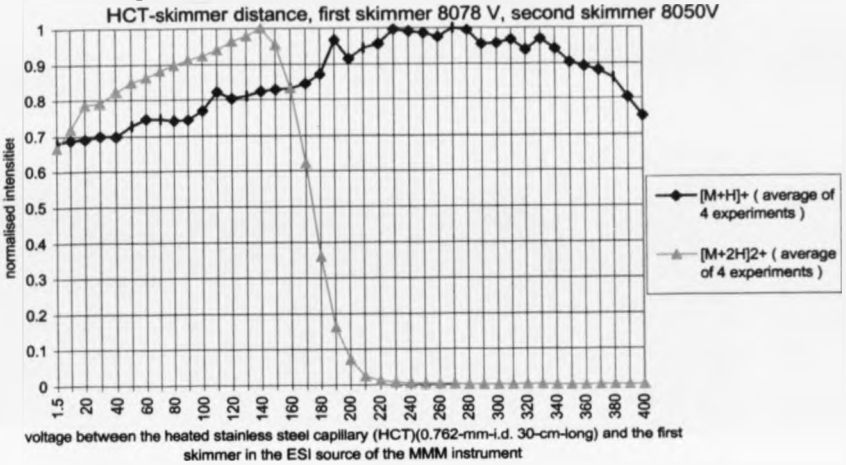

*Because of pressure of time, the doubly charged substance P ion had not been measured in above 198°C experiment.

Figure 5-9: Substance P. $[M+H]^+$, $[M+2H]2+$ and $[M+3H]3+$ ions intensity vs the voltage V_{HCT-S} between the HCT and the first skimmer at 148°C, 5.00-mm HCT-skimmer distance, first skimmer 8078 V, second skimmer 8050V

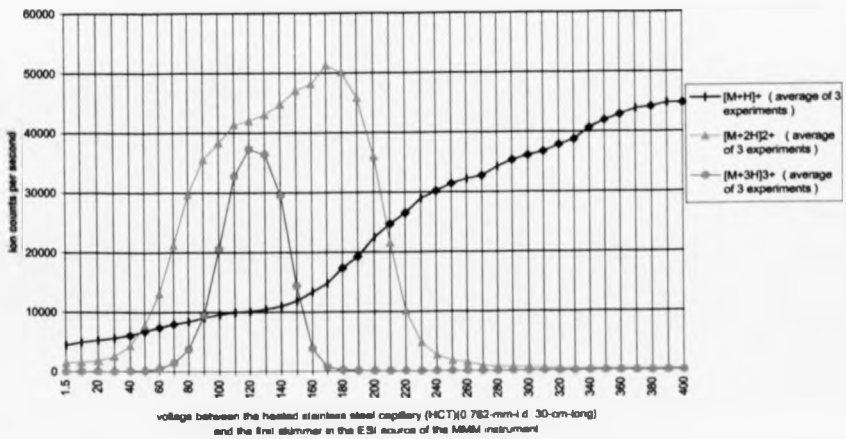

It should be pointed out that in [Figure 5-2] or any one of the graphs of signal intensities vs. V_{HCT-S} , the graphs show only the intensities of ions interest. Each voltage point corresponds to a mass spectrum obtained by a normal magnetic-sector scan (B-sector scan). For example, [Figure 5-10] shows three B-sector scan spectra with V_{HCT-S} = 1.4 V, 100.0 V and 200.0 V. Other ESI source operating conditions were nearly the same as those of [Figure 5-2]. There was 8079 V (not 8078 V) on the first skimmer and 270.95 V setting on the electrostatic sector (E-sector). The B-sector scan conditions were: start current (passing through the magnetic coil)180,000 mA (1967 m/z), end current 10,000 mA (19 m/z), step size 50 mA, the scan time 1,700 seconds and scanned once. These conditions are shown simply on the spectra as (180000, 10000, 50, 1700, 1 scan respectively).

[Figure 5-11] shows four B-sector scan spectra at 204°C with V_{HCT-S} of 50.0 V, 100.0 V, 150.0 V and 200.0 V. [Figure 5-12] shows five B-sector scan spectra at 198°C with V_{HCT-S} of 200.0 V, 250.0 V, 300.0 V, 350.0 V and 400.0 V. [Figure 5-13] shows six B-sector scan spectra at 148°C with V_{HCT-S} of 1.4 V, 50.0 V, 100.0 V, 150.0 V, 300.0 V and 4 00.0 V. All these B-sector scan spectra were measured under the same scan conditions.

From [Figure 5-2], the V_{HCT-S} voltage region of $[M+3H]^{3+}$ ion was the lowest of the three charge states of substance P. Its optimum V_{HCT-S} was about 70 V and its signal intensity was the lowest compared with its doubly and singly charged counterparts under the same V_{HCT-S} conditions. For the $[M+2H]^{2+}$ ion, its voltage region was in the middle. The three charge states of substance P did not exactly obey the conclusion drawn by Sheil et al[5-23]. that the optimum potential varied as m/z (i.e.

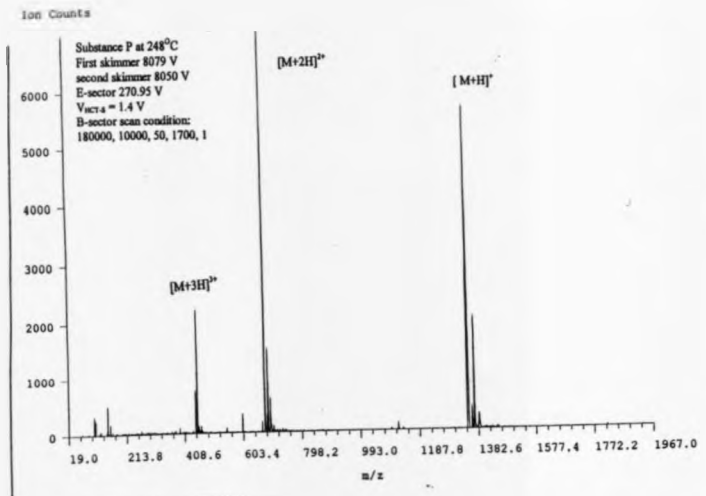

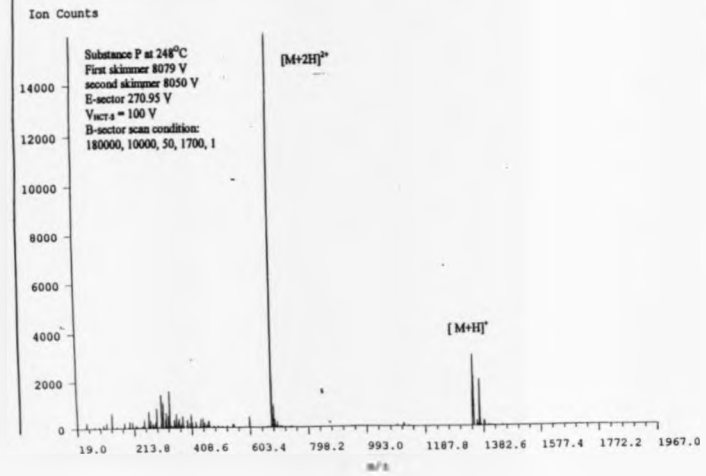

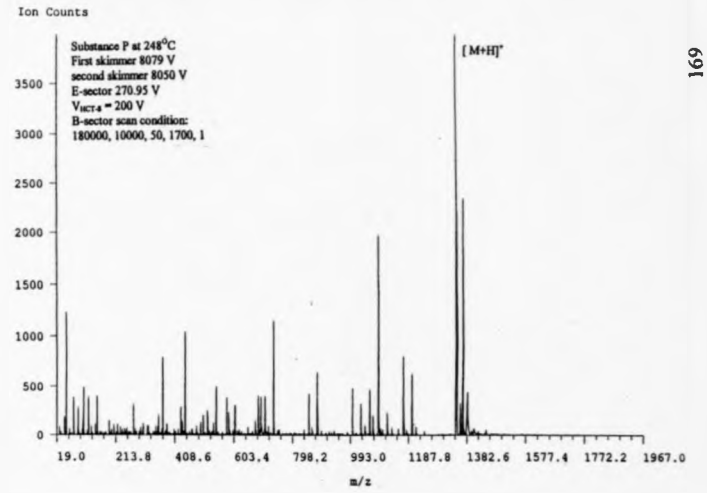

Figure 5 - 10: Substance P B-sector scan spectra under V_{HCT-4} = 1.4 V; 100 V and 200 V. (magnetic sector: start current 180,000 mA (1967 m/z), end current 10,000 mA (19 m/z), step size 50 mA, the scan time 1,700 seconds and scanned once. These conditions are shown simply on other spectra as (180000, 10000, 50, 1700, 1 scan respectively).

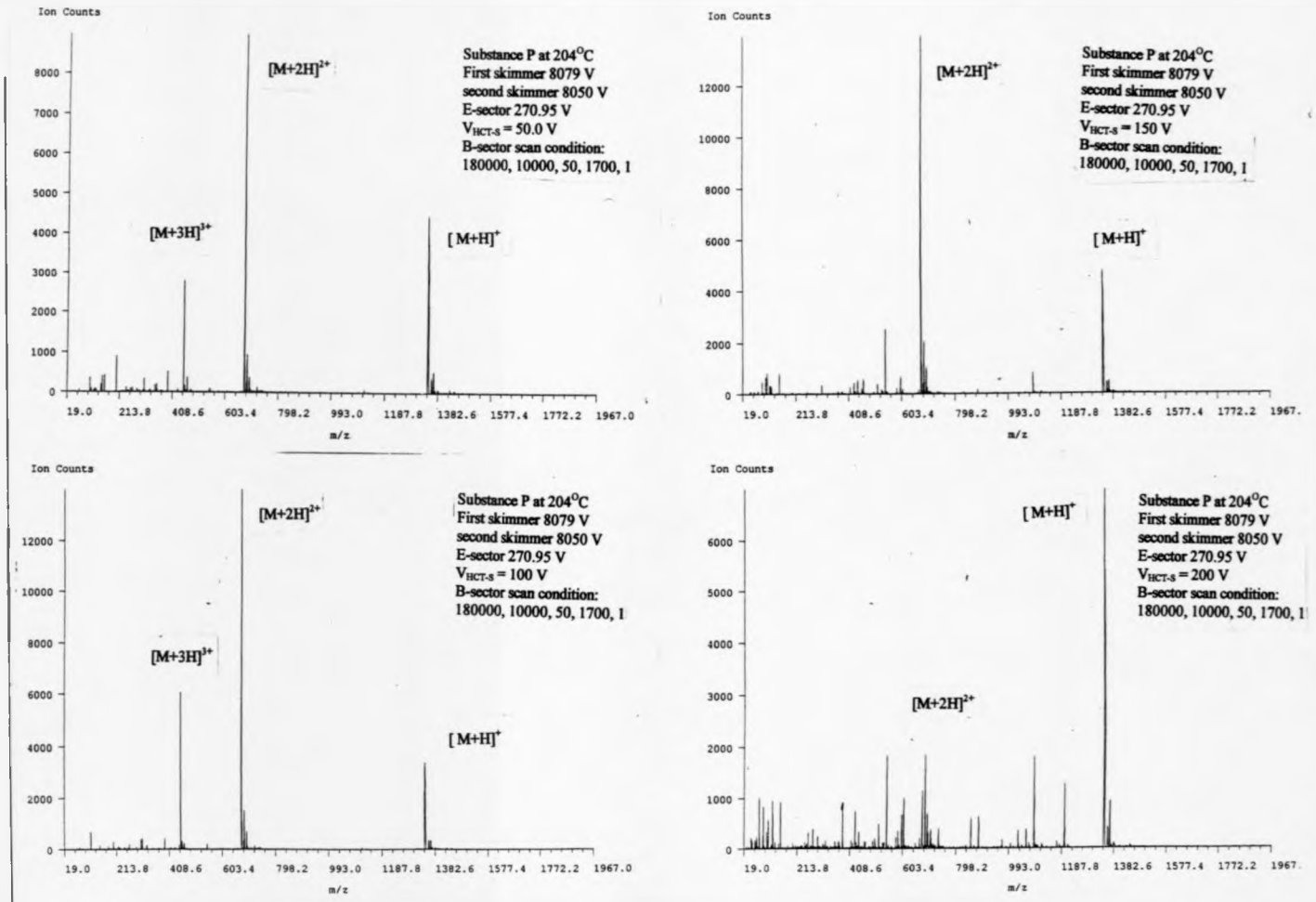

[Figure 5-11] Substance P B-sector scan spectra at 204°C with $V_{HCT\text{-}S}$ of 50.0 V, 100.0 V, 150.0 V and 200.0 V.

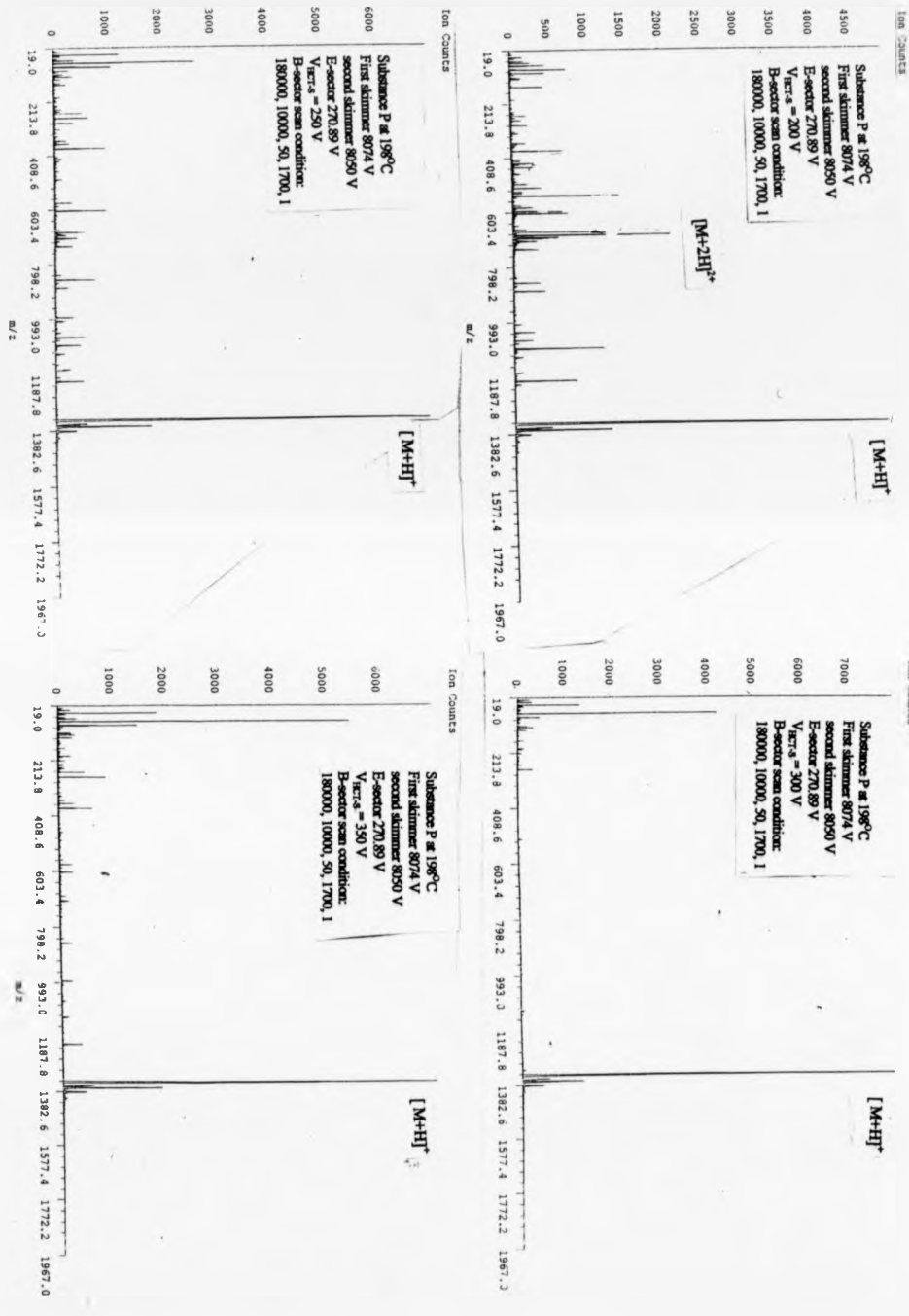
Ion Counts
Substance P at 198°C
First skimmer 8074 V
second skimmer 8050 V
E-sector 270.89 V
V_ACC+4 = 200 V
B-sector scan condition:
180000, 10000, 50, 1700, 1
[M+2H]2+
[M+H]+
m/z
Substance P at 198°C
First skimmer 8074 V
second skimmer 8050 V
E-sector 270.89 V
V_ACC+4 = 250 V
B-sector scan condition:
180000, 10000, 50, 1700, 1
Substance P at 198°C
First skimmer 8074 V
second skimmer 8050 V
E-sector 270.89 V
V_ACC+4 = 300 V
B-sector scan condition:
180000, 10000, 50, 1700, 1
Substance P at 198°C
First skimmer 8074 V
second skimmer 8050 V
E-sector 270.89 V
V_ACC+4 = 350 V
B-sector scan condition:
180000, 10000, 50, 1700, 1

[Figure 5-12] Substance P B-sector scan spectra at 198°C with $V_{HCT\text{-}S}$ = 200.0 V, 250.0 V, 300.0 V, 350.0 V and 400.0 V.

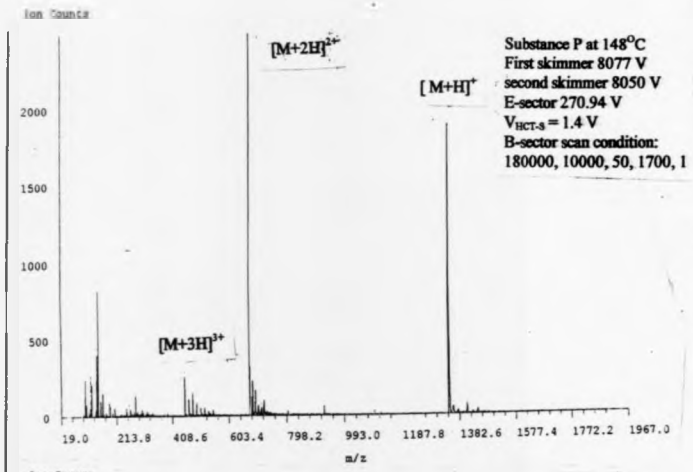
Ion Counts
[M+2H]2+
[M+H]+
[M+3H]3+
Substance P at 148°C
First skimmer 8077 V
second skimmer 8050 V
E-sector 270.94 V
VHCT-S = 1.4 V
B-sector scan condition:
180000, 10000, 50, 1700, 1
m/z

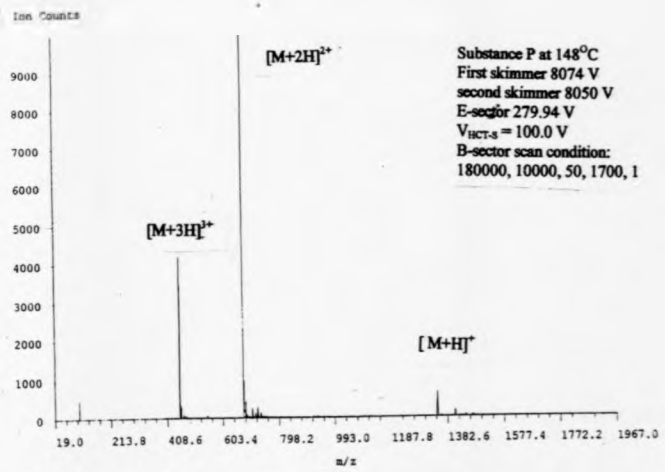
Ion Counts
[M+2H]2+
[M+3H]3+
[M+H]+
Substance P at 148°C
First skimmer 8074 V
second skimmer 8050 V
E-sector 279.94 V
VHCT-S = 100.0 V
B-sector scan condition:
180000, 10000, 50, 1700, 1
m/z

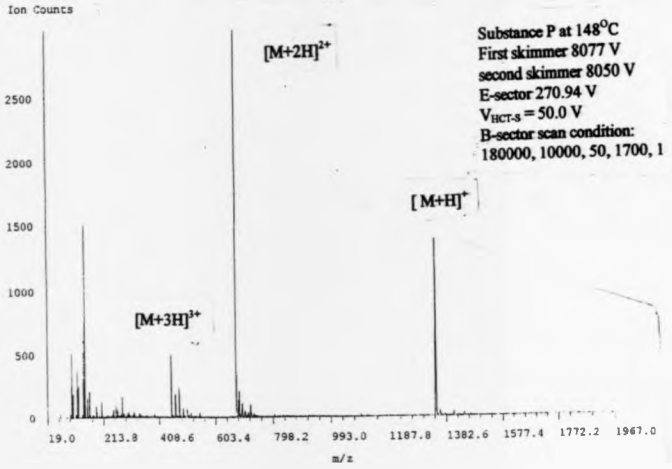
Ion Counts
[M+2H]2+
[M+H]+
[M+3H]3+
Substance P at 148°C
First skimmer 8077 V
second skimmer 8050 V
E-sector 270.94 V
VHCT-S = 50.0 V
B-sector scan condition:
180000, 10000, 50, 1700, 1
m/z

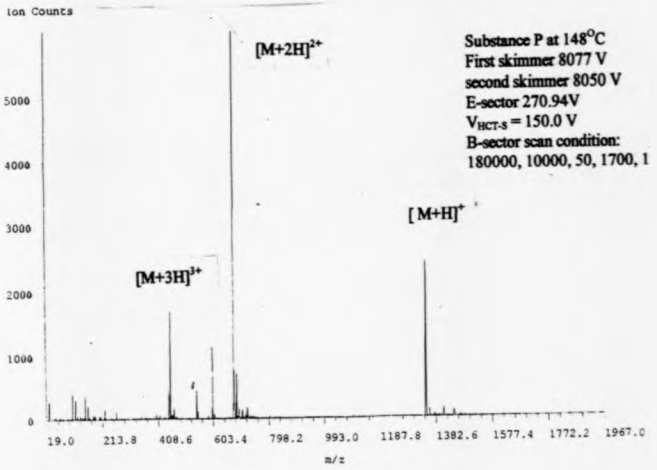
Ion Counts
[M+2H]2+
[M+H]+
[M+3H]3+
Substance P at 148°C
First skimmer 8077 V
second skimmer 8050 V
E-sector 270.94V
VHCT-S = 150.0 V
B-sector scan condition:
180000, 10000, 50, 1700, 1
m/z

linear dependence) for multiply charged ions of the same mass. From [Figure 5-4], [Figure 5-5] and [Figure 5-6], it can be seen that the optimum values of $V_{HCT\text{-}S}$ might slightly shift from one series to another. The optimum $V_{HCT\text{-}S}$ voltage was 120 V for the doubly charged ion and its signal intensity from 1.4 V to 155 V was the highest of the three. The singly charged ion was present in the whole experimental voltage region, the optimum voltage was around 320 V and its signal intensity did not change much as $V_{HCT\text{-}S}$ increased. The voltage regions over which the ions were observed were quite reproducible.

Comparing [Figure 5-2] with [Figure 5-7] and [Figure 5-9], the condition which had been changed was the temperature of the HCT (248°C, 198°C and 148°C). It was found that the ions' optimum voltages ($V_{HCT\text{-}S}$) and the voltage regions over which the ions were observed shifted to high $V_{HCT\text{-}S}$ as the HCT temperature decreased. The $V_{HCT\text{-}S}$ voltage regions of doubly and triply charged ions were narrowed following the decrease of the HCT temperature.

For substance P at fixed HCT temperature:

1) optimum $V_{HCT\text{-}S}$ voltages were in the order $[M+3H]^{3+} < [M+2H]^{2+} < [M+H]^{+}$

2) the $V_{HCT\text{-}S}$ voltage regions over which the ions were observed were $[M+3H]^{3+}$ (narrower than) $< [M+2H]^{2+} < [M+H]^{+}$.

For substance P when the HCT temperature was decreased:

1) both the optimum $V_{HCT\text{-}S}$ voltages and the $V_{HCT\text{-}S}$ voltage regions over which the ions were observed shifted to higher voltages and both kept the relative positions of the differently charged ions;

2) the $V_{HCT\text{-}S}$ voltage regions over which the ions were observed were narrowed for the doubly and triply charged ions.

The question is why the signal intensities of differently charged ions of the same molecule changed when V_{HCT-S} was changed in the experiments? Why did the HCT temperature being lowered cause optimum V_{HCT-S} and the whole V_{HCT-S} voltage regions over which the ions were observed to shift in the higher voltage direction, and at the same time narrow the optimum voltage region? What factors were behind these phenomena? As mentioned in the introduction part of this chapter, the V_{HCT-S} effects could be: (a) the focusing effect to guide the ion beam through the skimmer orifice into the next part of the mass spectrometer or (b) the accelerating energy effect to accelerate ions through this intermediate-pressure or free-jet region causing the ions to acquire additional energy by collision with surrounding air molecules. The HCT temperature effects could be the desolvation of the charged ESI droplets, thermal induced dissociation (TID)[5-25] or pressure/ gas density effects.

Checking the B-sector scan spectra from [[Figure 5-10] to [Figure 5-13], the intensities of substance P ions matched well with the signal intensities vs. V_{HCT-S} graphs from [figure 5-2] to [Figure 5-9]. Only one point should be noticed which is that when V_{HCT-S} was around 200 V, there were relatively more peaks in the spectra than in those measured at lower or higher V_{HCT-S}. Since in the sample solution there was only one analyte, some of these peaks must have been fragments from capillary-skimmer collision-induced dissociation (capillary-skimmer CID) or thermal induced dissociation (TID)[5-25] of sample ions. Even so, this observation showed that the ion optical effect of V_{HCT-S} played a larger role than CID. If CID were the main effect, then when V_{HCT-S} was increased higher than 200 V, the B-sector scan spectra should have given more fragments and stronger fragment signal as the parent ions should have acquired more internal energy[5-24]. One possible explanation is that fragments were formed but lost on

the way to the detector as they were over-focused, not fitting the requirements of the ion optical system at the new $V_{HCT\text{-}S}$. values. Another possible explanation is that most of any small charged fragments or cations had a large angular divergence[5-26], and were not focused by the ion optical system.

Considering the HCT temperature effect, the ESI source relied on the heat of the heated capillary to carry out the task of desolvation. Lowering the HCT temperature would have lowered the desolvation rate, so that eventually the number of ions produced would have been so low that no signal would be detected by the mass spectrometer. When the temperature of the HCT sat at 98°C, the signal intensity of the doubly charged substance P ion from the same solution used above at the optimum $V_{HCT\text{-}S}$ was more than two orders of magnitude lower than that at 248°C. With the ubiquitin sample, only a very weak signal could be obtained at 98°C. This was the reason why extensive experiments were not carried out at 98°C. The upper temperature of the HCT was limited by the maximum tolerance temperature of the PEEK and "O" ring material in the ESI source. Lowering the HCT temperature through reducing the desolvation rate of the charged droplets would have moved the positions of ion formation further into the ESI source. As desolvation and re-solvation are two-way processes, they would have occurred continuously as a consequence of the heat and the high level of solvent molecules in the HCT, as the sample droplets or ions passed through the HCT.

Another possible picture is presented by a consideration of the condensation effect of the free jet expansion, which has already been discussed in chapter 3 and chapter 4 of this thesis. After the carrier gas molecules passed the exit end of the capillary, they would have experienced an adiabatic free expansion and would have formed a supersonic free jet bounded by the shock wave and Mach disk. In the so-called

zone of silence, which is the free expansion volume of the free jet, the temperatures of the gas molecules, ions or other particles would have dropped very quickly followed the adiabatic expansion. Under the instrument conditions used in this study, according to Fenn's[5-27] paper and treating the air as a diatomic gas ($\gamma = C_P/ C_V = 7/5$), the temperature of ions at the orifice of the first skimmer could have dropped to 41 K for 248 °C HCT and 34 K for 148 °C HCT. As pointed out by Fenn re-solvation and clustering could occur during the free jet expansion. To overpower these effects, one approach uses heated bath gas to blow away solvent molecules before the ions enter the source, so the ions will be devoid of the solvent molecules in the free expansion jet and resolvation can not occur. A second approach is to heat the bath gas (or carrier gas) so that its temperature remains above the saturation value during free jet expansion. The equivalent in an ESI source with a HCT is to keep the temperature of the HCT at a high level, so that the temperature of the carrier gas remains above the saturation value during free jet expansion. The last approach is to apply an axial potential gradient in the free jet expansion to induce suprathermal desolvating collisions between ions and ambient neutral gas molecules. It is pointed out that if the first skimmer is inserted through the Mach disk and into the zone of the silence, the gas molecules and the ions will not have the chance to collide with the background gas and to heat up[5-28], hence the consequences of re-solvation are not combatted.

The overall picture in the experiments reported here could have been as follows. At the higher HCT temperatures of 248°C and 198°C, most of the ions were formed in the HCT capillary and carried out from the exit end of the HCT by the gas flow. During free jet expansion, the re-solvation process of condensation happened. With the HCT at 248°C, the re-solvation level would have been lower than at 198°C HCT. At the lowest

V_{HCT-S} (V_{HCT-S}=1.4 V), where there was nearly no field to cause suprathermal desolvating collisions, the ions' intensities marginally higher at 248°C in [Figure 5-2] than those at 198°C in [Figure 5-7]. As both ion signal intensities were quite high at V_{HCT-S} = 1.4 V, it is concluded that most of the ions were formed in the HCT and the re-solvation level in the free jet expansion was low. At the lowest HCT temperature of 148°C in [Figure 5-9], either the desolvation speed was so low or the re-solvation speed was so high that only a small proportion of the ions either were formed or remained in existence before being sampled by the first skimmer. Comparing the signal intensities at V_{HCT-S} = 1.4 V at the three temperatures ([Figure 5-2], [Figure 5-7] and [Figure 5-9]), it could be said the re-solvation effect of the free jet expansion was quite low in the temperature region 248°C to 198°C but reached a very serious level when the HCT temperature was lowered to 148°C. Increasing V_{HCT-S} at 148°C would have helped suprathermal desolvation and ions finally would have been formed further into the capillary-skimmer region where they would have experienced acceleration through a smaller potential difference, compared to ions formed at the capillary exit using higher HCT temperatures. In order to experience acceleration through the appropriate potential drop and match the requirements of the ion optical system, the whole V_{HCT-S} region over which the ions were observed and the ions' optimum V_{HCT-S} values have been would shifted in the higher voltage direction. This would be the reason that from V_{HCT-S} = 1.5 to 50 V in [Figure 5-9], the intensities of all three differently charged ions were quite low compared with the intensities at these voltages region at higher HCT temperatures [Figure 5-2] and [Figure 5-7]. In order to be detected in these experiments, the ions produced by the ESI source had to have had the correct translational energy to pass through the magnetic and electric sectors.

Another effect of the HCT temperature could be on the pressure in the ESI source. Decreasing HCT temperature would have increased the gas throughput of the heated capillary and raised the pressure in the source. Because of possible gas electric breakdown, the pressure in the capillary-skimmer region (first vacuum stage) was not measured [see chapter 3]. In the skimmer-skimmer region (second vacuum stage), the pressure readouts were around $8.7\times10^{-4} \sim 1.15\times10^{-3}$ mbar at 148°C compared to $5.5 \times10^{-4} \sim 8.44 \times10^{-4}$ mbar at 248°C. Though the pressure increasing in the capillary-skimmer region might not have been experienced directly by the ions as they were in the zone of silence until sampled by the first skimmer, the number density of neutral carrier gas molecules in the free expansion jet would have been higher. The ions would have needed higher $V_{HCT\text{-}S}$ to overcome the resistance caused by the increased ambient gas density in the capillary-skimmer region and the pressure increasing in the skimmer-skimmer region in order to reach the same final velocity before entering the orifice of the second skimmer.

As described by Sheil et al.[5-23], when the skimmer is inserted through the Mach disk and samples from the zone of silence, the ion mobility does increase on increasing the potential difference across the capillary-skimmer region. The ion mobility μ is directly proportion to the charge q on the ion from Einstein's relationship: $\mu = \frac{qD}{kT}$. Here, D is the diffusion coefficient and k is Boltzmann's constant. The absolute temperature T was the same for all ions at the same HCT temperature. According to Sheil et al.[5-23], ions of higher charge state spend less time in collisions with background molecules and are more tightly focused at the skimmer. Ions of higher charge states at a given mass are focused at lower potential $V_{HCT\text{-}S}$ under the same HCT temperature. Also

higher charge states acquire more energy given the same potential drop, hence voltage range of $V_{HCT\text{-}S}$ over which ions are observed is smaller than in the case of lower charge counterparts, according to Hunt et al.[5-23]. These theoretical predictions would explained in broad terms the experiments regarding difference among charge states (Figure 5-2, Figure 5-7 and Figure 5-9).

At lower HCT temperatures, it is suggested that higher $V_{HCT\text{-}S}$ values were needed to help the desolvation. The ions finally formed would have been in a stronger electric field and would have started at a shorter distance from the first skimmer orifice to experience the same potential drop. Thus the $V_{HCT\text{-}S}$ voltage range over which the ions were observed would have been narrower, compared to higher HCT temperatures.

Also from [Figure 5-2] (248°C) and [Figure 5-9] (148°C) again, as the HCT temperature dropped from 248°C to 148°C, the triply charged ion's absolute and normalised intensities increased and became more sensitive to $V_{HCT\text{-}S}$, compared to the doubly and singly charge ions. This could have been because the triply charged ion was more stable when solvated than when unsolvated and had less chance to undergo thermal dissociation at the lower temperature.

Was there any other evidence to support the above picture? What would have been happened if the potential difference between two skimmers had been changed ? At first, it was not supposed that changing the potential of the first skimmer and keeping that of the second skimmer constant would call for any change to the settings of the electric and magnetic sectors. Under this later-obvious misapprehension, the experiments were carried out and the results of these are shown in [Figure 5-14]. During these experiments, the E-sector was set at 270.68 V (not at 270.98±0.03 V as in [Figure 5-2], [Figure 5-7] and [Figure 5- 9] for which the first skimmer voltage was

8078 V and the second skimmer was 8050 V), but the B-sector setting was still set as earlier experiments. The lower potential on the first skimmer (8068 V) would have lowered the translational energy of the ions produced by the ESI source, shifting the optimum

Figure 5-14 Substance P ions intensity vs the V_{HCT-S} between the HCT and the first skimmer at 148°C , 5.00-mm HCT-skimmer distance, first skimmer 8068V, second skimmer 8050V. Magnetic sector setting unchanged compared with 8078 and 8050 V on the skimmers

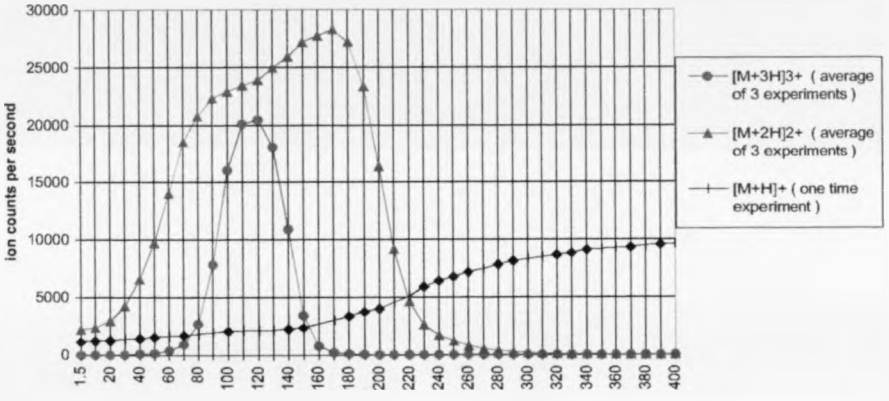

setting of the E-sector to lower voltage (lower energy). The momentum of the ions would also have been shifted to lower value. Using the same current setting on the B-sector would have allowed the ions on the highside (higher m/z direction) of peaks to pass through the B-sector and would have cut out the peak maxima. Comparing [Figure 5-14] with [Figure5-9], the only differences were the potential on the first skimmer and the E-sector setting. The shapes of the graphs for all three ions were the same. The relative intensities for triply and doubly charge ions were the same, but the singly charge ion intensity was much lower at the lower skimmer potential. The explanation could be that the ions monitored using the lower skimmer potential [Figure 5-14] were isotope

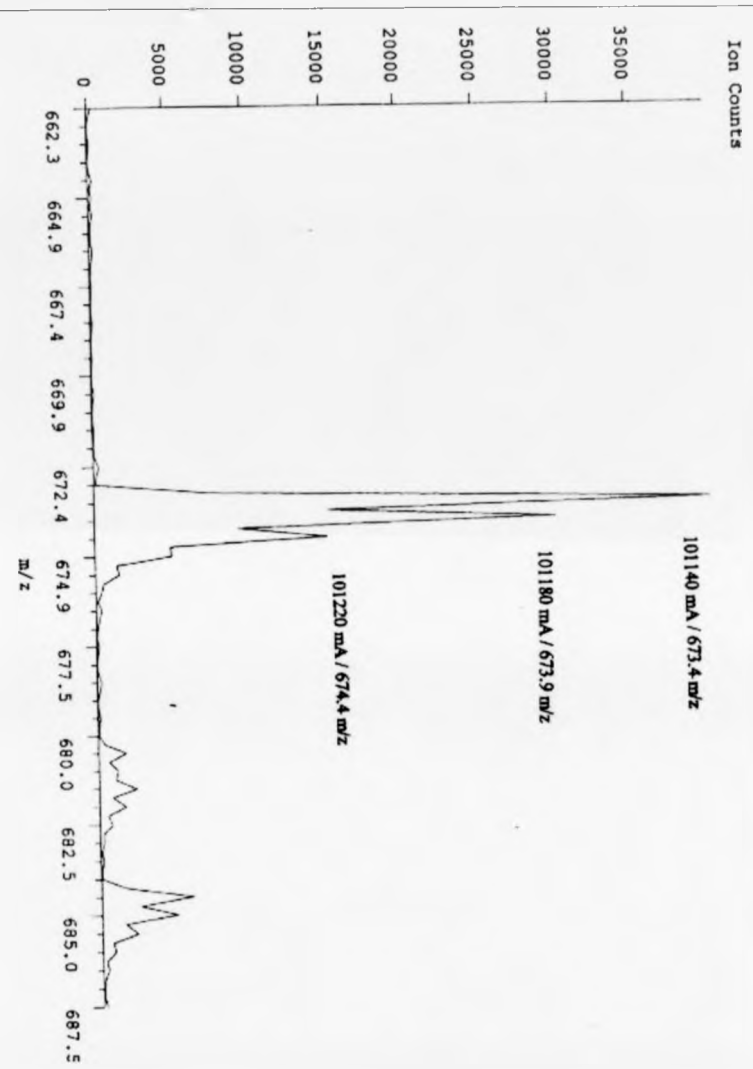

[Figure 5-15] narrow-region B-sector scan spectrum of the doubly charged substance P ion with magnetic coil current value (mA) / mass (m/z) read out marked on main peaks. working conditions: HCT temperature 148^{0}C, parent ions' setting on the E-sector 270.68 V; first skimmer 8068 V, second skimmer 8050 V, single scan starting from 102265 mA, ending at 100265 mA, step size 20 mA and total scan time 400 s.

peaks. For triply charged ion, the first isotope peak was 1/3 m/z unit away, for doubly charged ion was ½ unit away and for singly charged ion was 1 mass unit away. This would also explain why the absolute ion intensities dropped. [Figure 5-15] shows a narrow-region B-sector scan spectrum of the doubly charged substance P ion under conditions of 270.68 V on the E-sector, 8068 V on the first skimmer, 8050 V on the second skimmer, single scan starting from 102265 mA, ending at 100265 mA, step size 20 mA and total scan time 400 ms. The setting used in [Figure 5-14] for the doubly charged ion would fall on the third peak in [Figure 5-15].

[Figure 5-16] gives experimental results of substance P at 148°C with 8118 V on the first skimmer and 8050 V on second the skimmer. 272.20V was the setting of the E-sector and optimised settings were used for each charge state on the B-sector.

Figure 5-16 Substance P ions signal intensities vs voltage V_{HCT-S} between the HCT and the first skimmer at 148°C, 5.00-mm HCT-skimmer distance, first skimmer 8118 V, second skimmer 8050V, settings optimised on both electric and magnetic sectors

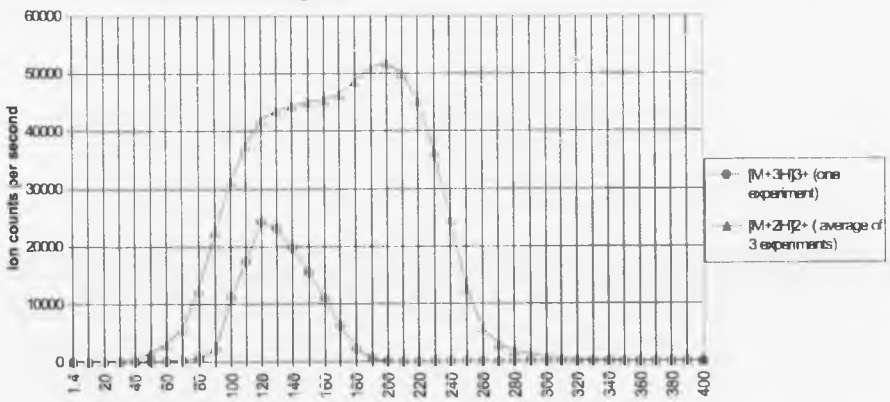

Because of pressure of time, the singly charged substance P ion was not measured and triply charged ion was measured only once. But their signal intensities could still be read off from the B-sector scan spectra [Figure 5-19] at V_{HCT-S} values of 1.4 V, 100.0 V,

200.0 V, 300.0 V, 350.0 V and 400.0 V. These matched the results in [Figure 5-16] and showed the same relative intensity relationships with each other as in [figure 5-2], [Figure 5-7] and [Figure 5-9]. The only obvious difference between [Figure 5-16] and [Figure 5-9] is that when the potential on the first skimmer was increased from 8078 V to 8118 V, the optimum V_{HCT-S} and the V_{HCT-S} voltage range of the doubly charged ion were shifted to higher voltages. The triply charged ion distribution [Figure 5-16] became skewed to higher voltage. Since the potential on the HCT was applied relative to the first skimmer potential as the reference point, changing the potential on the first skimmer did not affect the electric field between the capillary and skimmer, and the ions experienced exactly the same conditions at the same V_{HCT-S} voltage until they reached the orifice of the first skimmer. It could be said that the lower V_{HCT-S} signal for each charged ion in [Figure 5-9] was lost due to an over-focusing effect under the conditions of [Figure 5-16], and at the same time the higher V_{HCT-S} signal for each charged ion in [Figure 5-9] was picked back up as the ion optical conditions were changed in [Figure 5-16].

[Figure 5-17], [Figure 5-18] and [Figure 5-19] show the results of B-sector scans at 148°C with 8088 V, 8098 V and 8118 V respectively on the first skimmer and 8050 V on the second skimmer. In order to obtain the highest signal, the E-sector settings were changed from 270.68 V for 8068 V on the first skimmer to 272.20 V for 8118 V on the first skimmer, with a constant setting 8050 V on the second skimmer. It can still be seen that more small peaks showed up when V_{HCT-S} was around 200 V at 8088 V [Figure 5-17] and 8098 V [Figure 5-18], but a little higher V_{HCT-S} was needed at 8118 V [Figure 5-19].

With the fixed 8050 V potential on the second skimmer, changing from 8068 V to 8118 V on the first skimmer (the change percentage is (8118 - 8068) / 8068 = 0.006197 = 0.6197 %) required the E-sector setting to be changed by a smaller proportion from 270.68 V to 272.20 V ((272.20 - 270.68) / 270.68 = 0.005615 = 0.5615 %) to allow the same ion beam to pass through. This means that the virtual ion source for the mass spectrometer or the ions' virtual formation point in the ESI source was a certain distance in front of the second skimmer.

$$\frac{0.5615\%}{0.6197\%} \times 9.00(mm) = 8.16(mm)$$

Here 9.00 mm was the distance between second skimmer and first skimmer. The potential at this point determined the accelerating potential of the ions. So when increasing the potential on the first skimmer while keeping the potential on the second skimmer constant, the potential on the above point increased and the ions' accelerating potential increased too. To match this increase, the settings on both sectors had to be increased to allow the ion beam to pass through.

Finally, examining the figures 5-2, 5-7, 5-9 and 5-16, was there evidence of charge stripping? The triply charged ion was the highest charged ion which could not be formed from the other ions by charge stripping. The doubly charged could be formed from the triply charged by stripping one $[11]^+$ ion, and the graphs gave a shoulder at the $V_{HCT\text{-}S}$ corresponding to the intensity drop of the triply charged. A shoulder was also seen for the singly charged ion but was at much less obvious level. The rises in intensity were however, not sufficiently great to account for the whole of the falls in intensities of the higher charged ions.

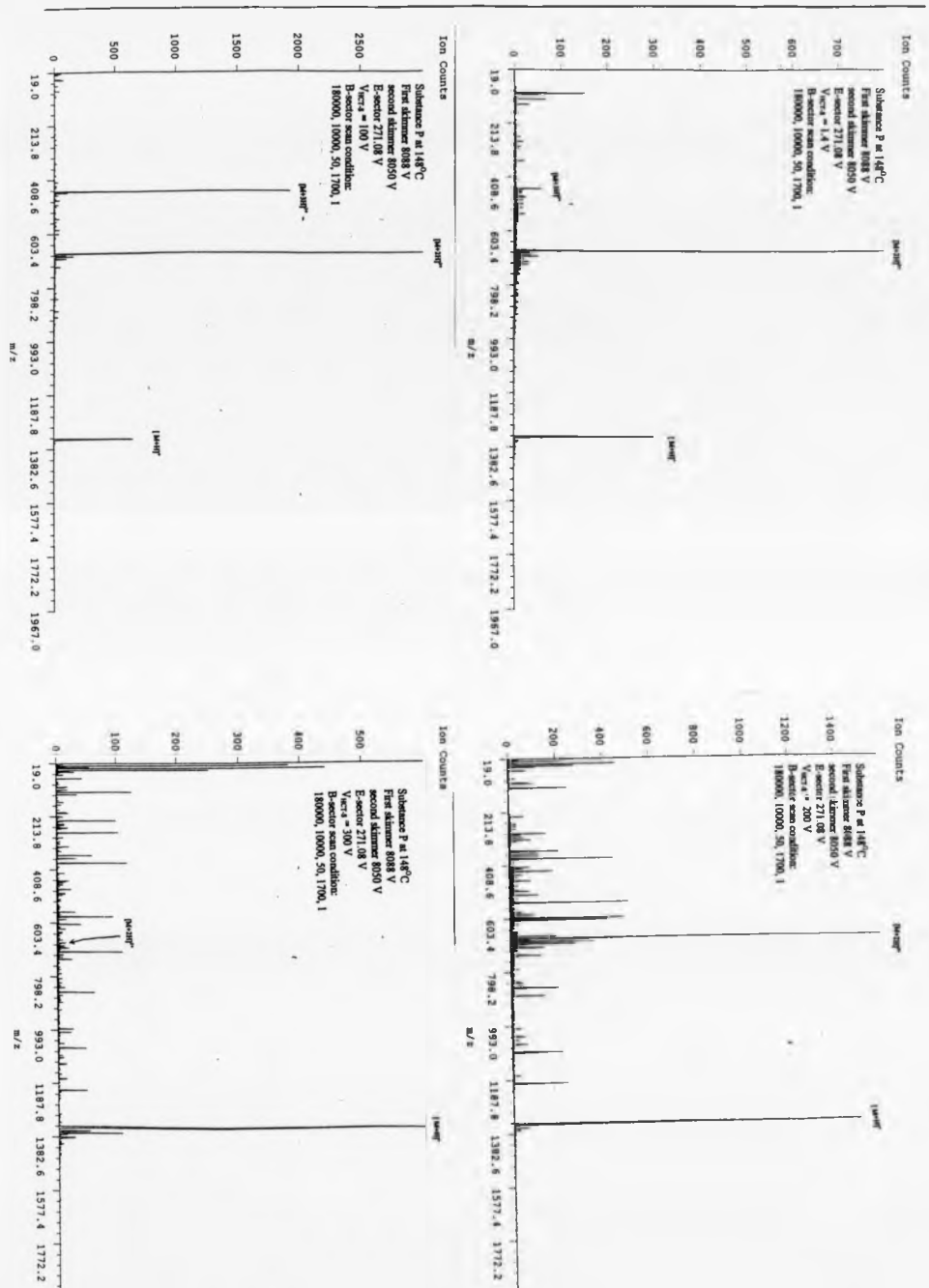
Ion Counts
Substance P at 140°C
First skimmer 8088 V
second skimmer 8050 V
E-sector 271.08 V
Vacc.= 1.4 V
B-sector scan condition:
180000, 10000, 50, 1700, 1
[M+H]+
[M+2H]2+
m/z
Ion Counts
Substance P at 140°C
First skimmer 8088 V
second skimmer 8050 V
E-sector 271.08 V
Vacc.= 100 V
B-sector scan condition:
180000, 10000, 50, 1700, 1
[M+H]+
[M+2H]2+
m/z
Ion Counts
Substance P at 140°C
First skimmer 8088 V
second skimmer 8050 V
E-sector 271.08 V
Vacc.= 200 V
B-sector scan condition:
180000, 10000, 50, 1700, 1
[M+H]+
m/z
Ion Counts
Substance P at 140°C
First skimmer 8088 V
second skimmer 8050 V
E-sector 271.08 V
Vacc.= 300 V
B-sector scan condition:
180000, 10000, 50, 1700, 1
[M+H]+
m/z

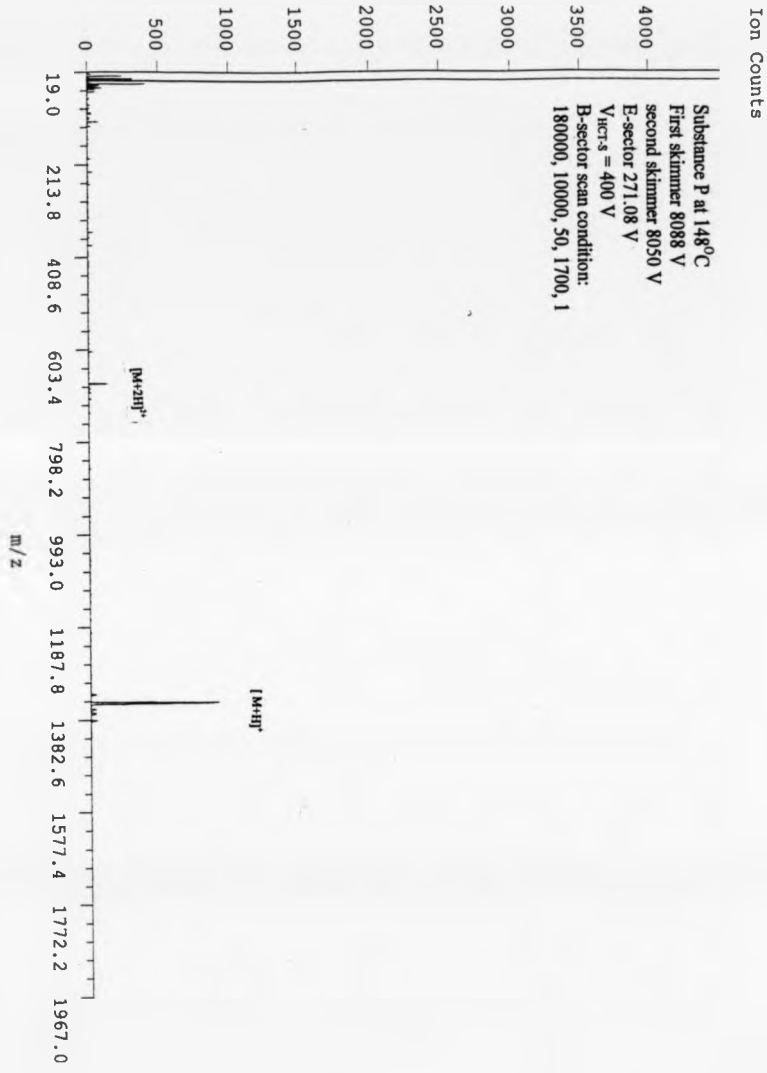

Figure 5-17: Substance P B-sector scan spectra with V_{HCT-S} = 1.4 V; 100 V; 200 V; 300 V and 400 V at 148^{O}C, under experiment condition as First skimmer 8088V, second skimmer 8050 V, 271.08 V for E-sector setting.

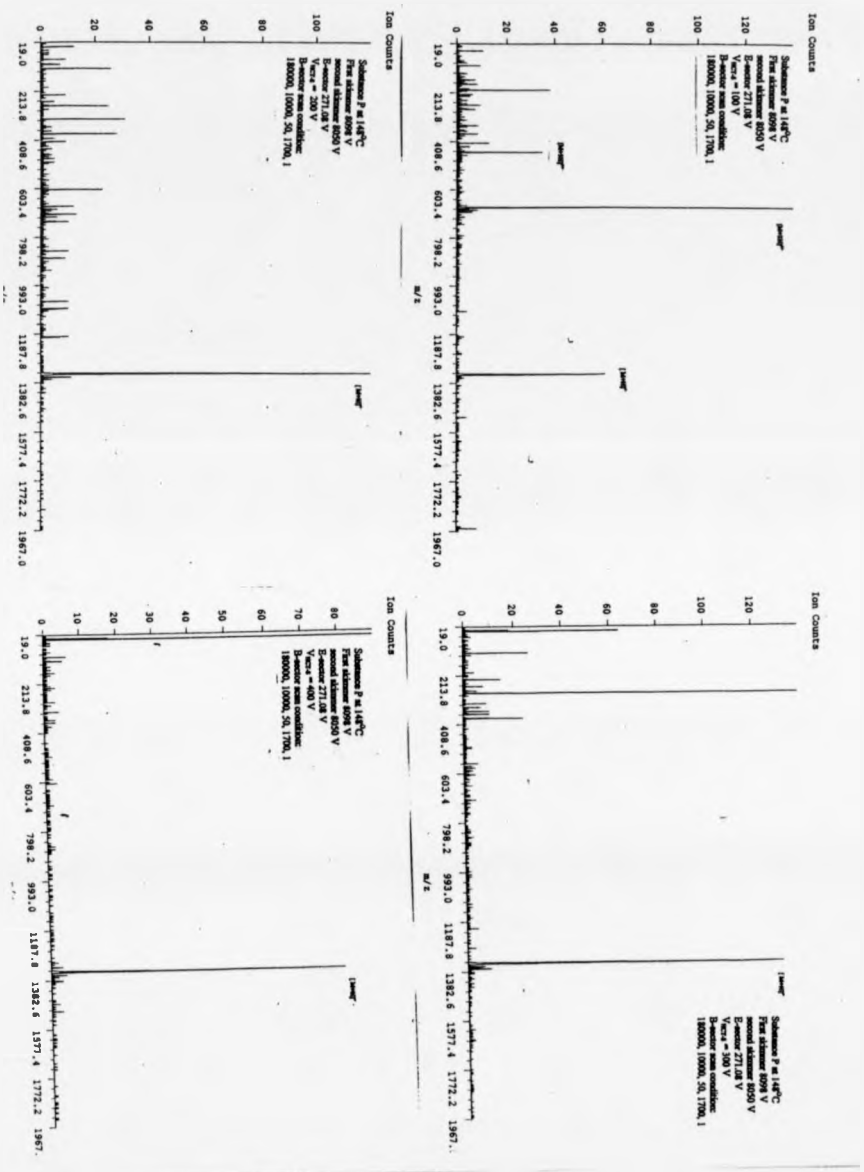

Figure 5-18: Substance P B-sector scan spectra with V_{HCT-S} = 100 V; 200 V; 300 V and 400 V at 148°C, under experiment condition as First skimmer 8098V, second skimmer 8050 V, 271.08 V for E-sector setting.

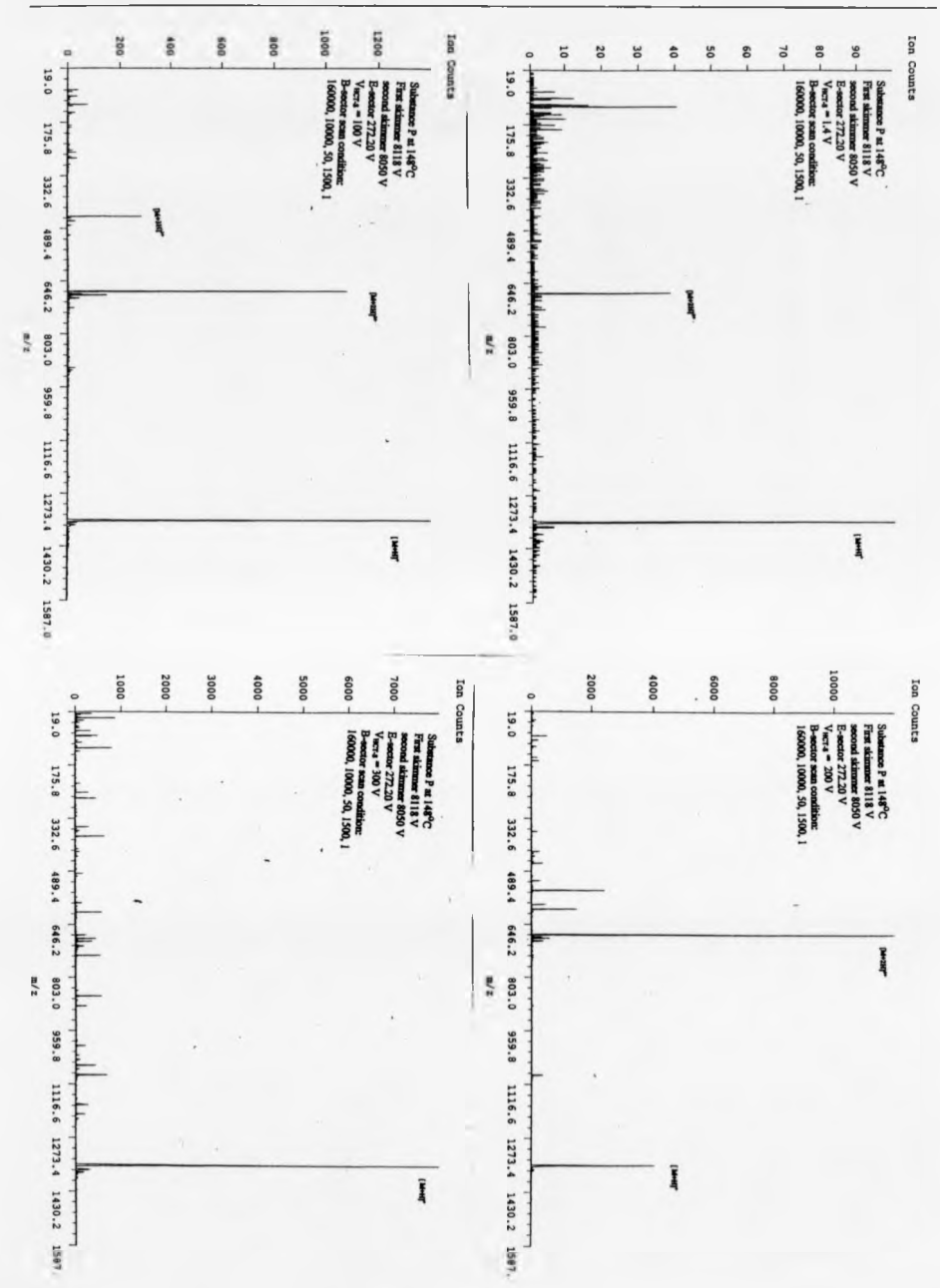
Ion Counts
Substance P at 140°C
First skimmer 8118 V
second skimmer 8050 V
E-sector 272.20 V
V_acc.s = 1.4 V
B-sector scan condition:
160000, 10000, 50, 1500, 1
[M+H]+
m/z
Ion Counts
Substance P at 140°C
First skimmer 8118 V
second skimmer 8050 V
E-sector 272.20 V
V_acc.s = 100 V
B-sector scan condition:
160000, 10000, 50, 1500, 1
[M+H]+
m/z
Ion Counts
Substance P at 140°C
First skimmer 8118 V
second skimmer 8050 V
E-sector 272.20 V
V_acc.s = 200 V
B-sector scan condition:
160000, 10000, 50, 1500, 1
[M+H]+
m/z
Ion Counts
Substance P at 140°C
First skimmer 8118 V
second skimmer 8050 V
E-sector 272.20 V
V_acc.s = 300 V
B-sector scan condition:
160000, 10000, 50, 1500, 1
[M+H]+
m/z

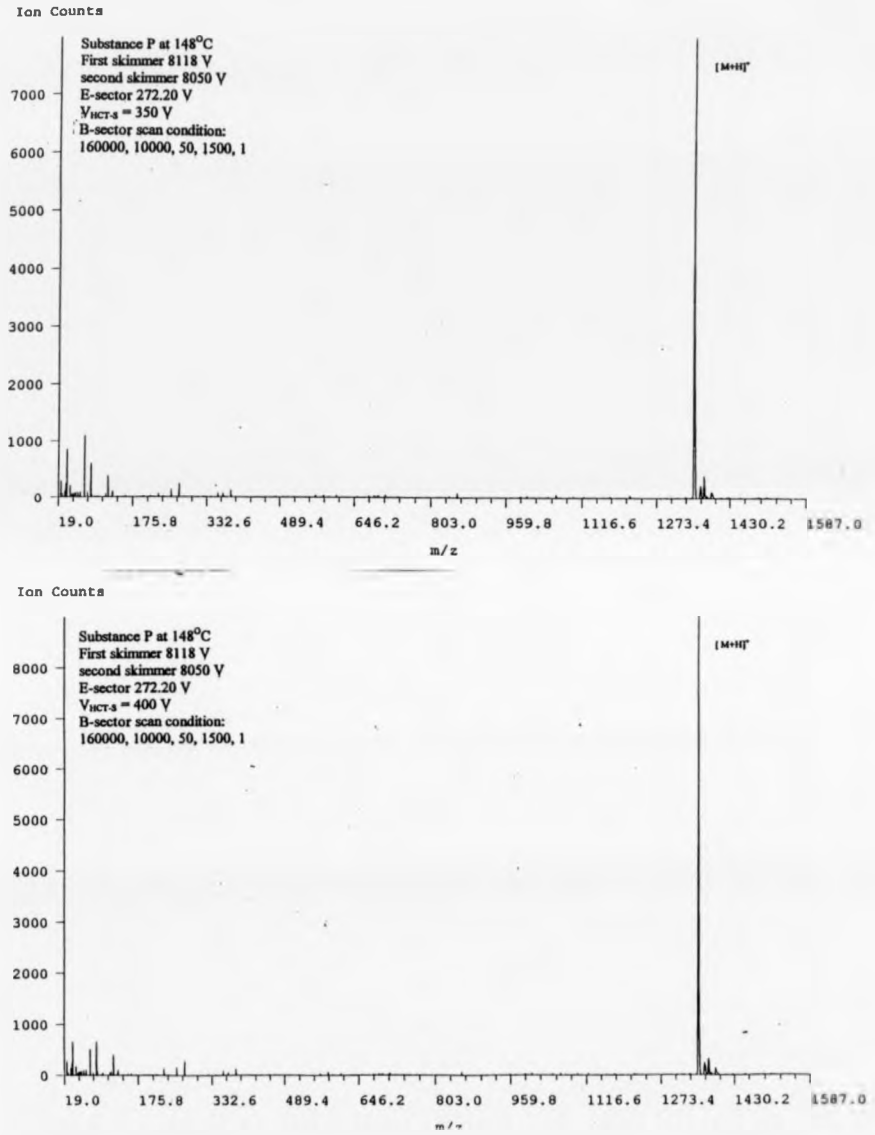

Figure 5-19: Substance P B-sector scan spectra with V_{HCT-S} = 1.4 V; 100 V; 200 V; 300 V; 350 V and 400 V at 148°C, under experiment condition as First skimmer 8118V, second skimmer 8050 V, 272.20 V for E-sector setting.

5.3.2 Insulin

The insulin used here came from bovine pancreas. Its molecular mass was 5733.5 Da. Insulin contains two chains (one contains 21 amino acids, the other contains 30 amino acids). There are 3 S-S cross-linkages.

[Figure 5-20], [Figure 5-21], [Figure 5-22] and [Figure 5-23] give the results on the insulin sample at 248°C and 148°C, and show how the absolute and normalised intensities of the differently charged ions changed with the voltage V_{HCT-S} between the HCT and the first skimmer. Results are summarised in [Table 5-1]. [Figure 5-24] and [Figure 5-25] give the B-sector scan spectra at 248°C and 148°C.

Inspecting the insulin graphs, the same pattern of changes is evident as in the substance P results when the HCT temperature was dropped from 248°C to 148°C. The more highly charged ions had lower V_{HCT-S} values at any one HCT temperature. There were no clear shoulders on the graphs to support the possibility of charge stripping processes. B-sector scan spectra in [Figure 5-24] and [Figure 5-25] matched well with the relative graphs in [Figure 5-20] and [Figure 5-22]. The one thing which should be pointed out is the signal due to contamination from PEG 800 in the 600 ~ 1400 m/z region (mainly the single charged ions). PEG results will be discussed later in 5.3.5 part this chapter. [Figure 5-24] and [Figure 5-25] show the same phenomenon remarked on earlier that when V_{HCT-S} reached 200 V, there were more fragments.

Table 5-1 Insulin ions' optimum V_{HCT-S} values under different HCT temperature

Insulin	248°C		148°C	
Charge states	optimum $V_{HCT-S\,(V)}$	full width at half height / V	optimum $V_{HCT-S\,(V)}$	full width at half height / V
$[M+2H]^{2+}$	330	>180	370	>115
$[M+3H]^{3+}$	220	267	270	170
$[M+4H]^{4+}$	130	>230	250	225
$[M+5H]^{5+}$	110	>170	210	157
$[M+6H]^{6+}$	80	112	190	75

Figure 5-20 Insulin 6+, 5+, 4+, 3+, 2+ ions signal intensities vs. the voltage V_{HCT-S} between the HCT and the first skimmer at 248°C, 5.00-mm HCT-skimmer distance, first skimmer 8078 V, second skimmer 8050V

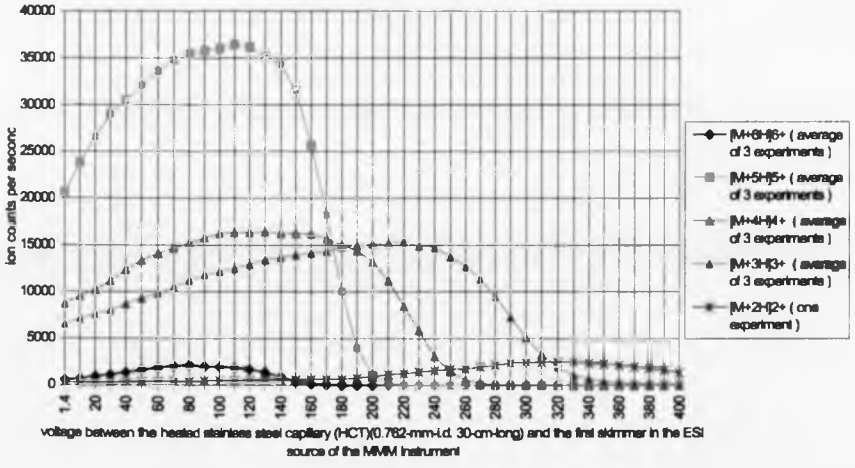

Figure 5-21 Insulin 6+, 5+, 4+, 3+, 2+ ions normalised intensities vs. the voltage V_{HCT-S} between the HCT and the first skimmer at 248°C, 5.00-mm HCT-skimmer distance, first skimmer 8078 V, second skimmer 8050V

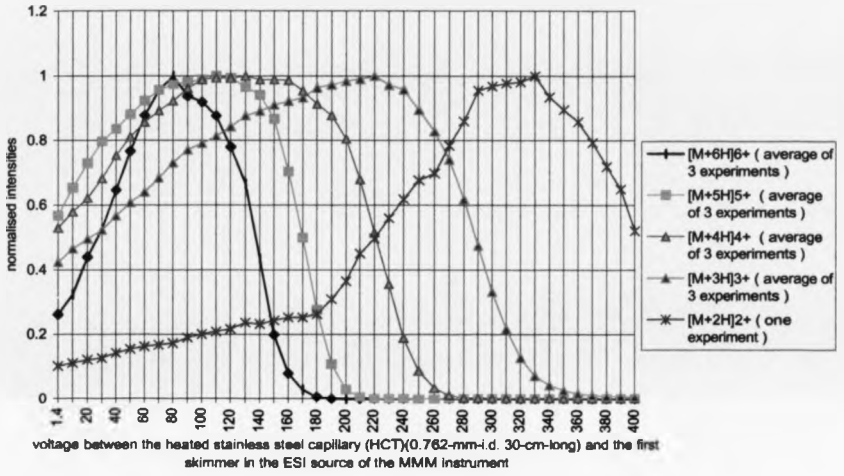

Figure 5-22 Insulin 6+, 5+, 4+, 3+, 2+ ions signal intensities vs. the voltage V_{HCT-S} between the HCT and the first skimmer at 148°C, 5.00-mm HCT-skimmer distance, first skimmer 8078 V, second skimmer 8050V

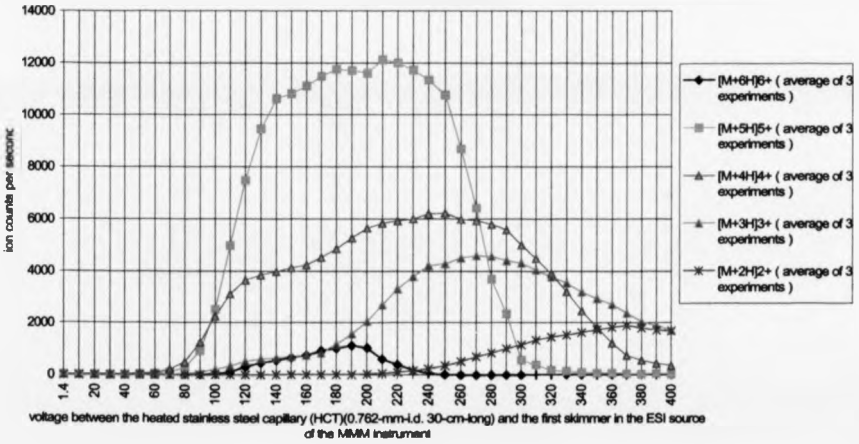

Figure 5-23 Insulin 6+, 5+, 4+, 3+, 2+ Ions normalised intensities vs. the voltage V_{HCT-S} between the HCT and the first skimmer at 148°C, 5.00-mm HCT-skimmer distance, first skimmer 8078 V, second skimmer 8050V

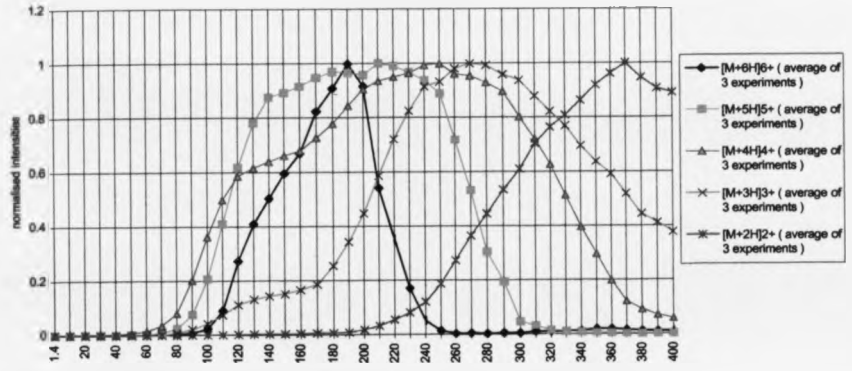

voltage between the heated stainless steel capillary (HCT)(0.762-mm-i.d. 30-cm-long) and the first skimmer in the ESI source of the MMM instrument

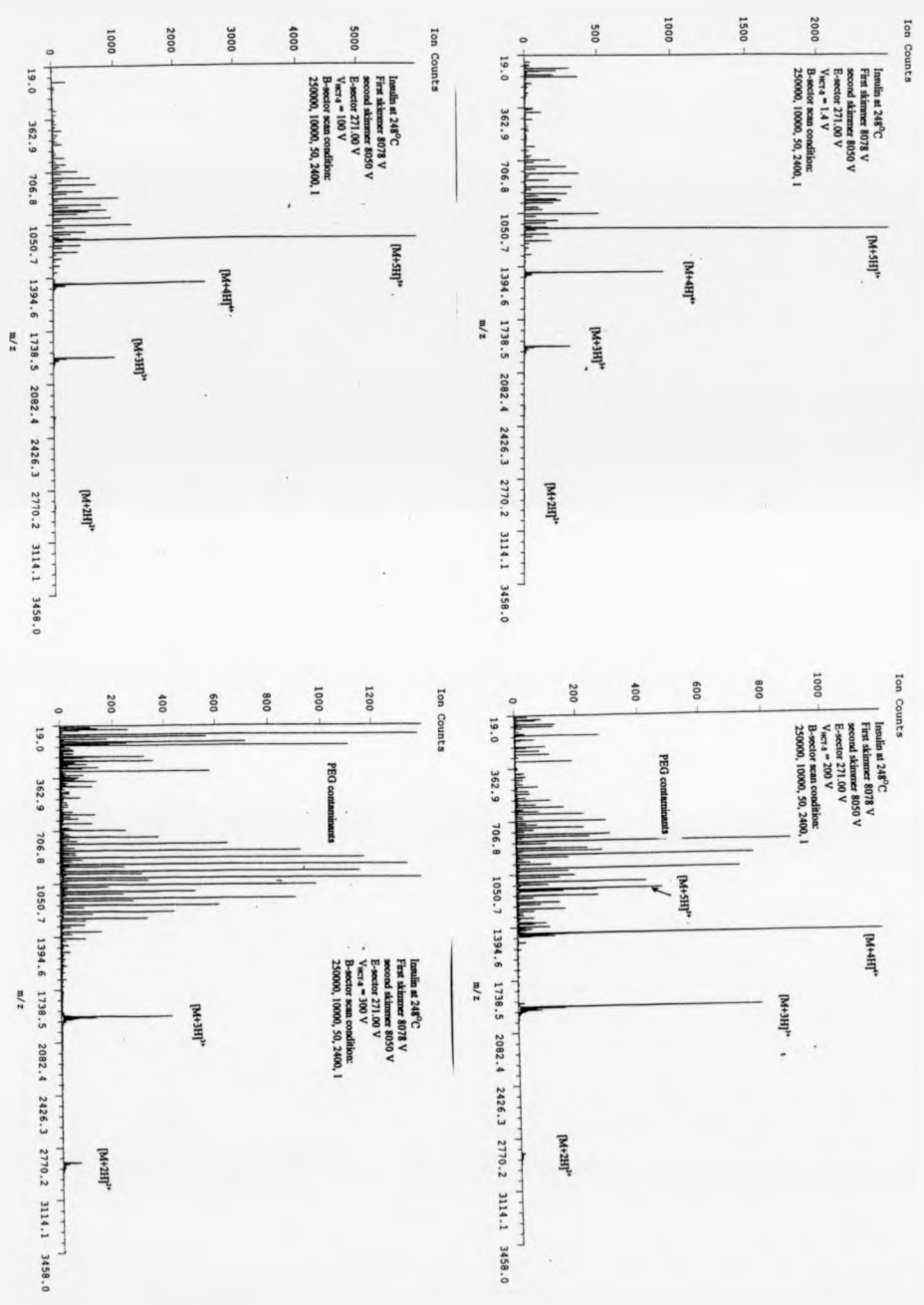
Ion Counts
Insulin at 248°C
First skimmer 8078 V
second skimmer 8050 V
E-sector 271.00 V
Vacc.s = 1.4 V
B-sector scan condition:
250000, 10000, 50, 2400, 1
[M+5H]+
[M+4H]+
[M+3H]+
[M+2H]+
m/z
19.0 362.9 706.8 1050.7 1394.6 1738.5 2082.4 2426.3 2770.2 3114.1 3458.0
Insulin at 248°C
First skimmer 8078 V
second skimmer 8050 V
E-sector 271.00 V
Vacc.s = 100 V
B-sector scan condition:
250000, 10000, 50, 2400, 1
Insulin at 248°C
First skimmer 8078 V
second skimmer 8050 V
E-sector 271.00 V
Vacc.s = 200 V
B-sector scan condition:
250000, 10000, 50, 2400, 1
PEG contaminants
Insulin at 248°C
First skimmer 8078 V
second skimmer 8050 V
E-sector 271.00 V
Vacc.s = 300 V
B-sector scan condition:
250000, 10000, 50, 2400, 1

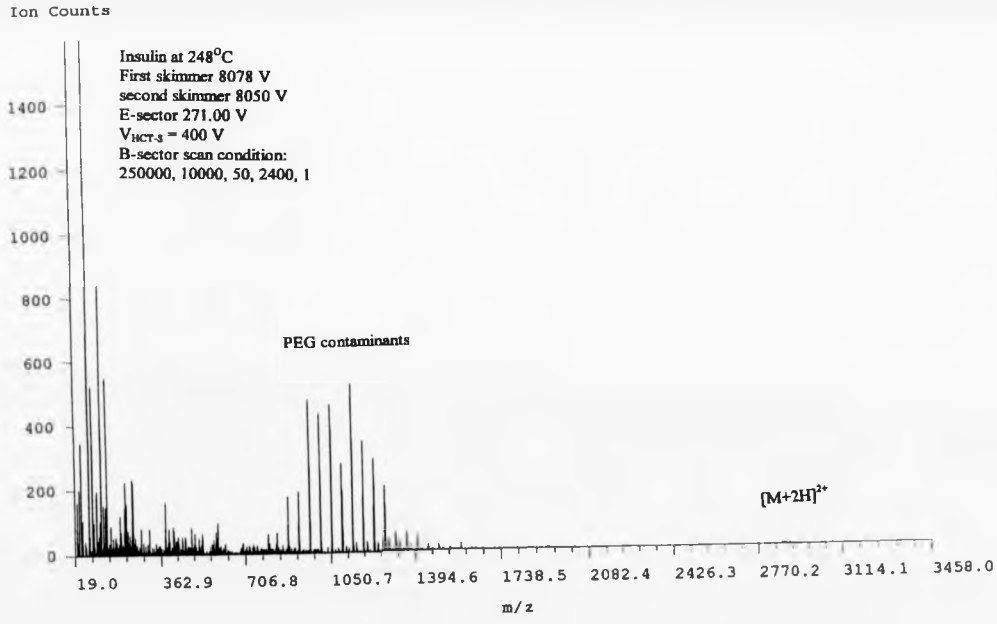

Figure 5-24: Insulin B-sector scan spectra with V_{HCT-S} = 1.4 V; 100 V; 200 V; 300 V and 400 V at 248°C, under experiment condition as First skimmer 8078V, second skimmer 8050 V, 271.00 V for E-sector setting

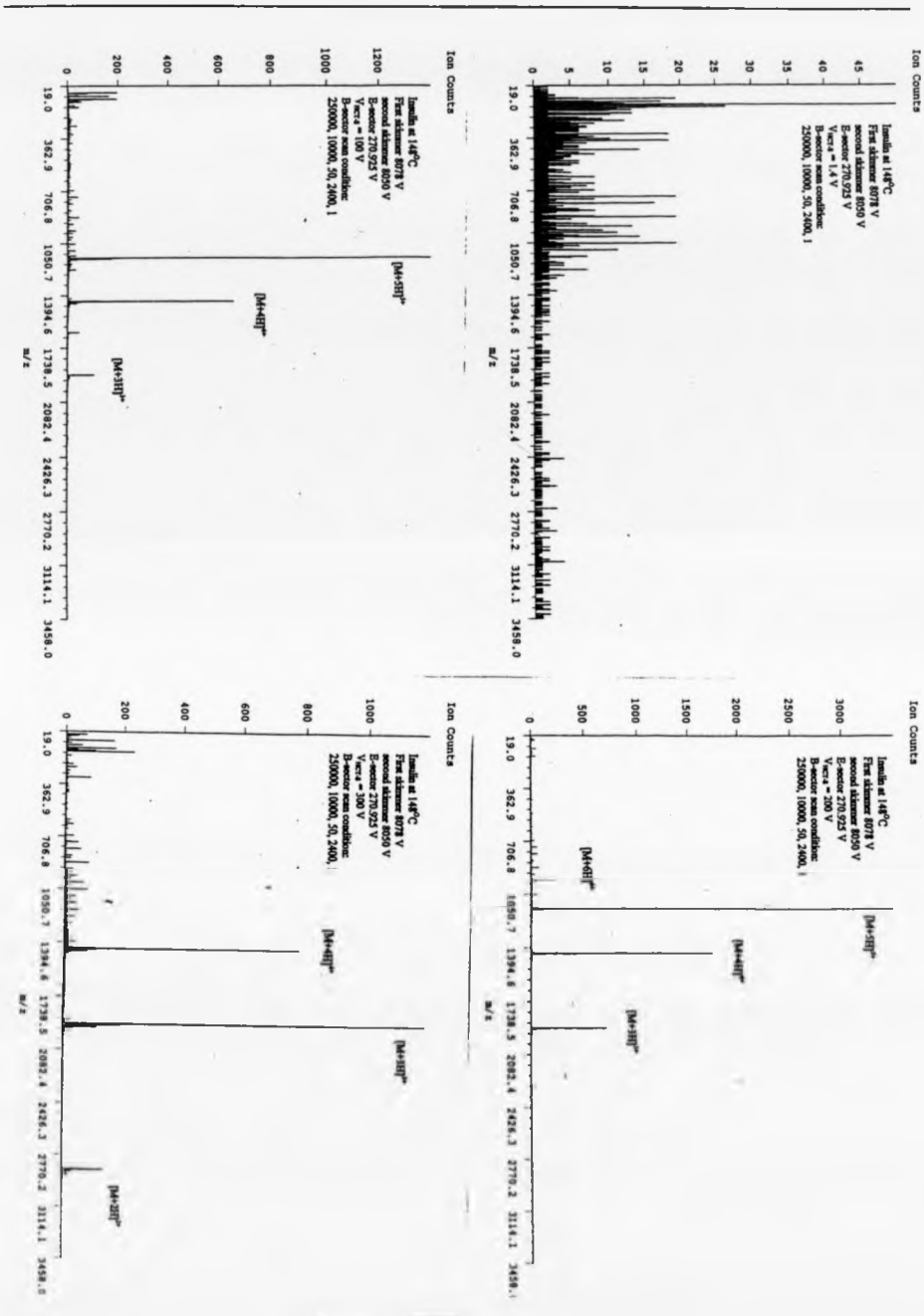
Ion Counts
Insulin at 14°C
First skimmer 8078 V
second skimmer 8050 V
E-sector 270.525 V
Vacc.s = 1.4 V
B-sector scan conditions:
250000, 10000, 50, 2400, 1
[M+5H]5+
[M+4H]4+
[M+3H]3+
m/z
Insulin at 14°C
First skimmer 8078 V
second skimmer 8050 V
E-sector 270.525 V
Vacc.s = 100 V
B-sector scan conditions:
250000, 10000, 50, 2400, 1
Insulin at 14°C
First skimmer 8078 V
second skimmer 8050 V
E-sector 270.525 V
Vacc.s = -200 V
B-sector scan conditions:
250000, 10000, 50, 2400, 1
Insulin at 14°C
First skimmer 8078 V
second skimmer 8059 V
E-sector 270.525 V
Vacc.s = 300 V
B-sector scan conditions:
250000, 10000, 50, 2400,

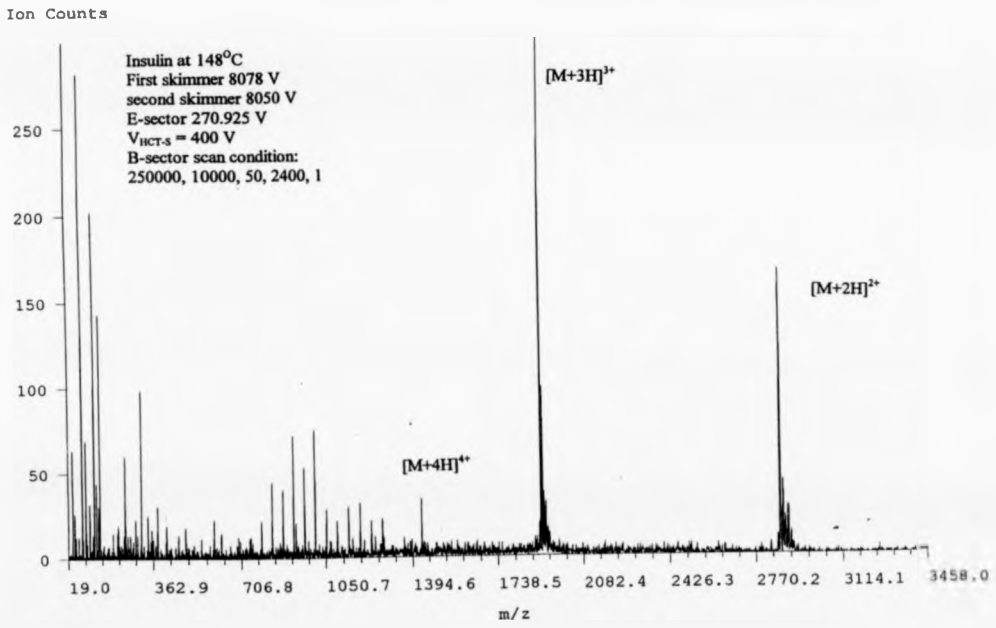

Figure 5-25: Insulin B-sector scan spectra with V_{HCT-S} = 1.4 V; 100 V; 200 V; 300 V and 400 V at 148°C, under experiment condition as First skimmer 8078V, second skimmer 8050 V, 270.925 V for E-sector setting

5.3.3 Ubiquitin

Ubiquitin is a small protein containing 67 amino acids. Its molecular mass was 8564.8 Da.

[Figure 5-26], [Figure 5-27] and [Figure 5-28] give results of experiments with ubiquitin. Dependencies of absolute and normalised ion signal intensities upon $V_{HCT\text{-}S}$ at 248°C and at 148°C were determined. Because of pressure of time, the ubiquitin $[M+10H]^{10+}$ ion at 248°C and most of the ubiquitin ions at 148°C were not measured in these experiments, but the information still could be read off from the B-sector scan spectra at 248°C and 148°C ([Figure 5-29] and [Figure 5-31] respectively). For each of these figures, the spectra were acquired continuously. Of the spectra, the first spectrum in [Figure 5-29] was acquired using the scan condition: start current 190000 mA (2165 m/z), end current 4000 mA (126 m/z), step size 50 mA, scan time

Figure 5-26 Ubiquitin: [M+13H]13+ ~ [M+3H]3+ ions signal intensities vs. the voltage $V_{HCT\text{-}S}$ between the HCT (0.762-mm-i.d. 30-cm-long) and the first skimmer at 248°C, 5.00-mm HCT-skimmer distance, first skimmer 8078 V, second skimmer 8050V

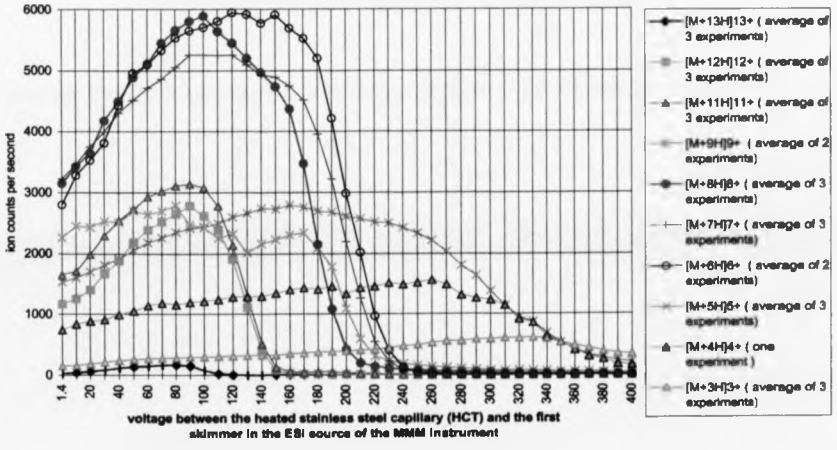

Figure 5-27 Ubiquitin [M+13H]13+ ~ [M+3H]3+ ions normalised intensities vs. the voltage V_{HCT-S} between the HCT (0.762-mm-i.d. 30-cm-long) and the first skimmer at 248°C, 5.00-mm HCT-skimmer distance, first skimmer 8078 V, second skimmer 8050V

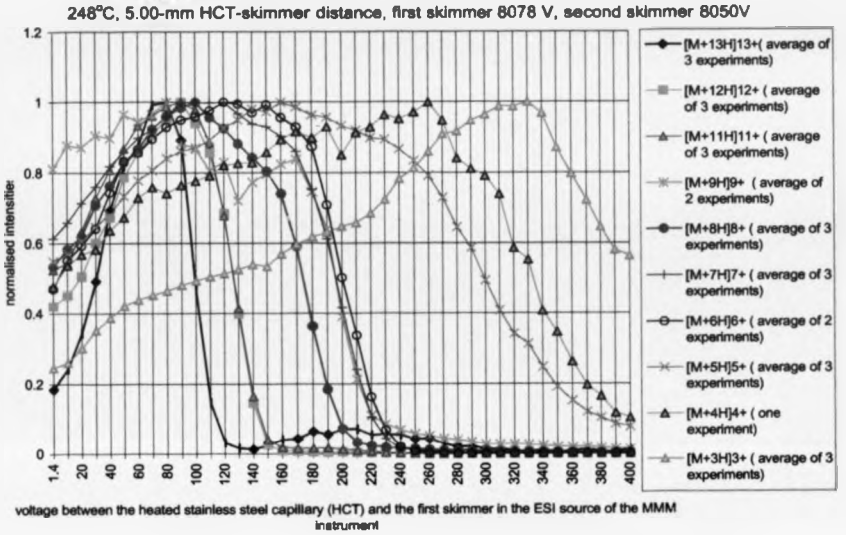

Figure 5-28 Ubiquitin [M+9H]9+ & [M+4H]4+ ions signal intensities vs. the voltage V_{HCT-S} between the HCT and the first skimmer at 148°C, 5.00-mm HCT-skimmer distance, first skimmer 8078 V, second skimmer 8050V

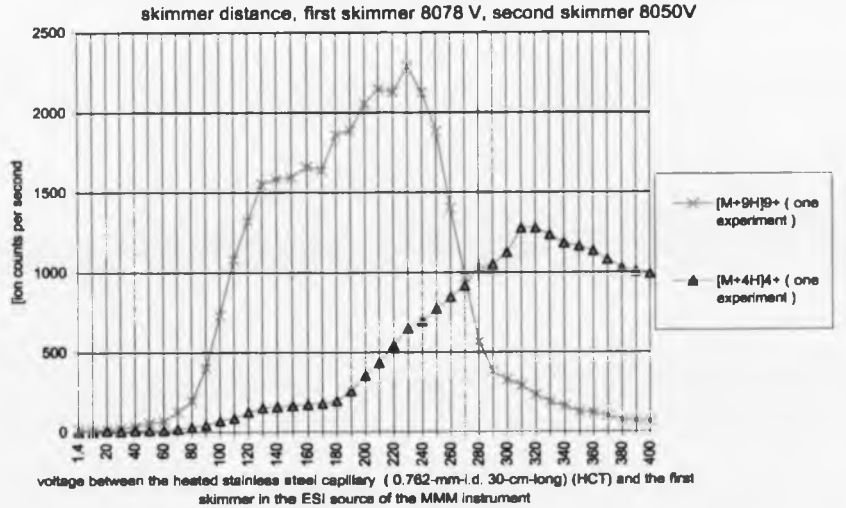

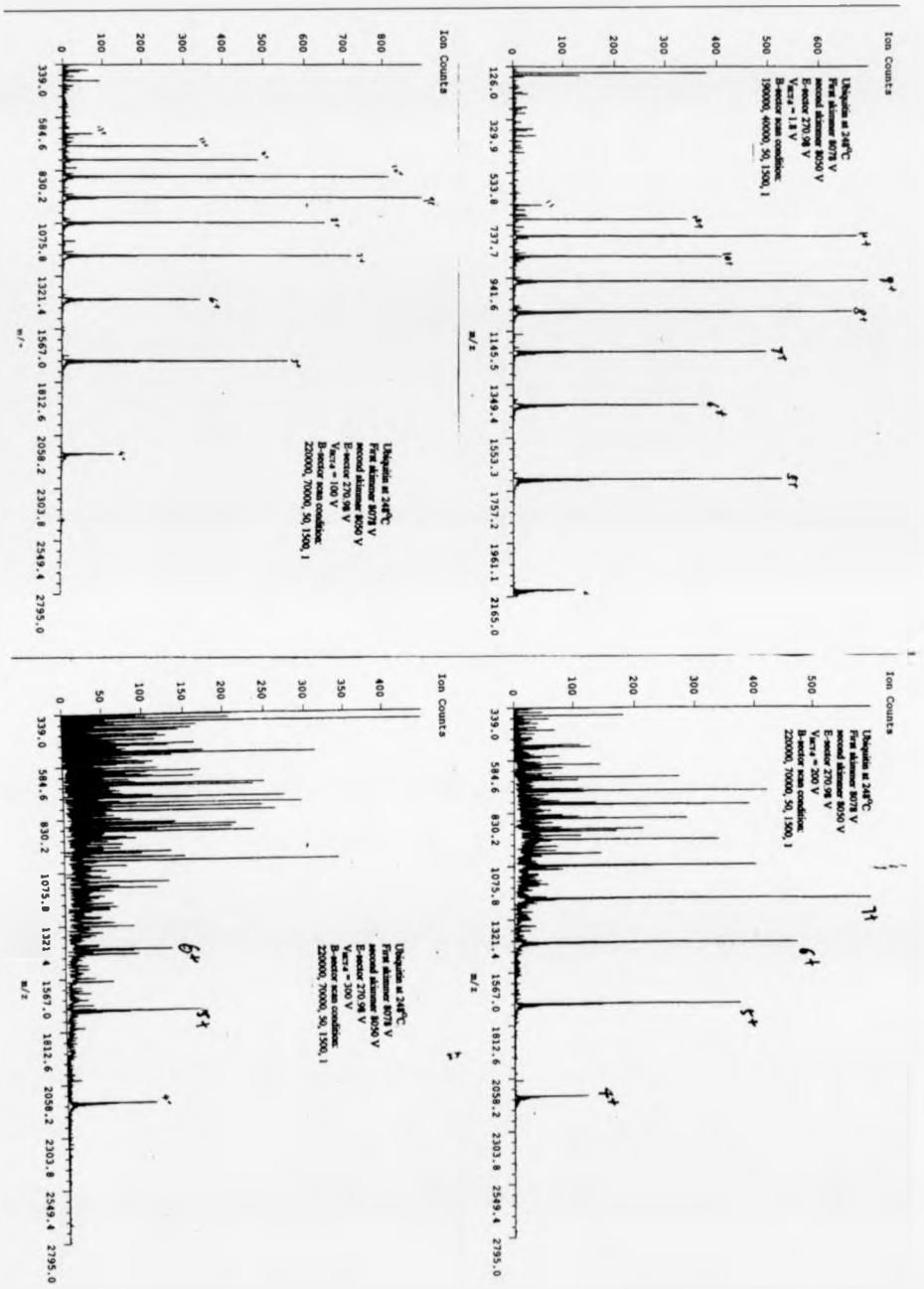
Ion Counts
m/z
Ubiquitin at 24°C
First skimmer 8078 V
second skimmer 8050 V
E-sector 270.98 V
Vacc.e = 100 V
B-sector scan condition:
220000, 70000, 50, 1500, 1
Ubiquitin at 24°C
First skimmer 8078 V
second skimmer 8050 V
E-sector 270.98 V
Vacc.e = 200 V
B-sector scan condition:
220000, 70000, 50, 1500, 1
Ubiquitin at 24°C
First skimmer 8078 V
second skimmer 8050 V
E-sector 270.98 V
Vacc.e = 300 V
B-sector scan condition:
220000, 70000, 50, 1500, 1
Ubiquitin at 24°C
First skimmer 8078 V
second skimmer 8050 V
E-sector 270.98 V
Vacc.e = -1.8 V
B-sector scan condition:
190000, 40000, 50, 1500, 1

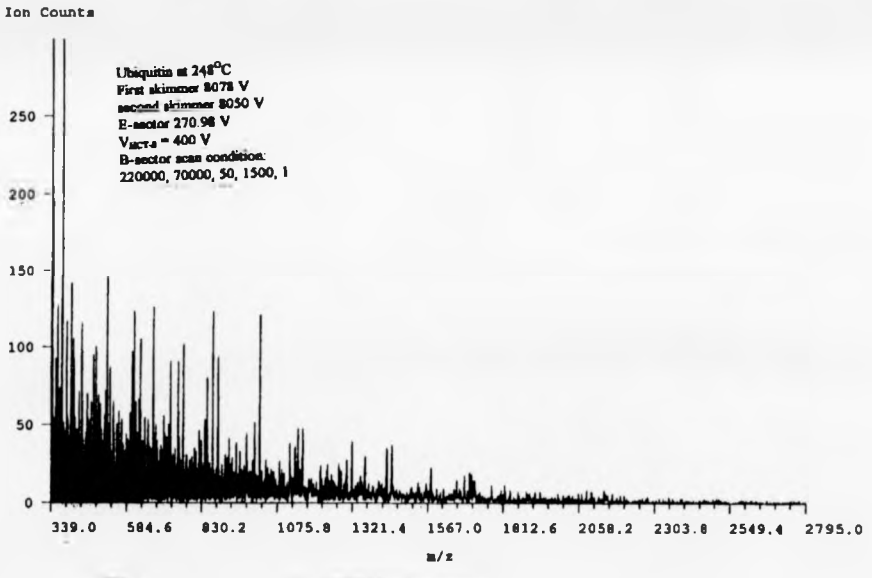

Figure 5-29: Ubiquitin B-sector scan spectra with $V_{HCT\text{-}S}$ = 1.8 V; 100 V; 200 V; 300 V and 400 V at 248^{O}C, under experiment condition as First skimmer 8078V, second skimmer 8050 V, 270.98 V for E-sector setting

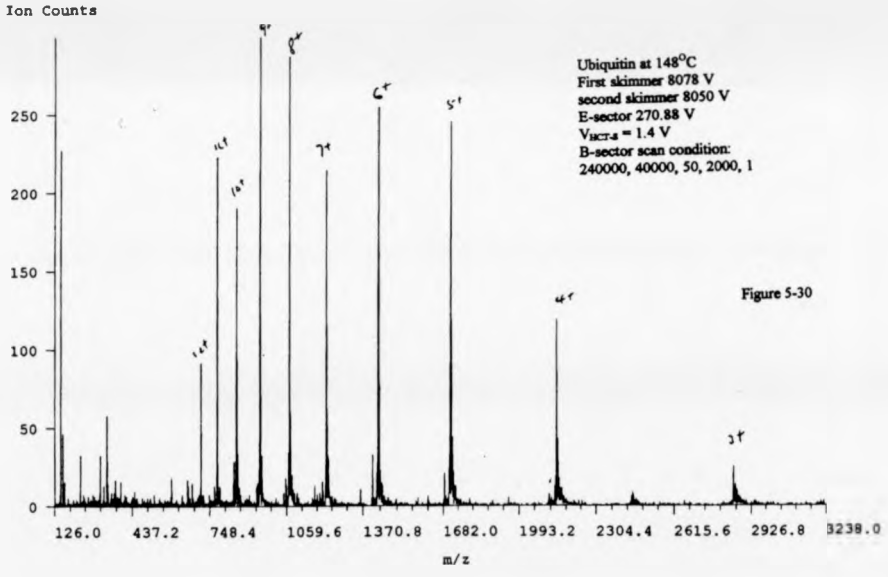

Figure 5-30 the B-sector scan spectrum of ubiquitin: scan conditions: (240000 mA (3238 m/z), 40000 mA (126 m/z), 50 mA steps, 2000 s per scan, 1 scan) at 148°C when $V_{HCT\text{-}S}$ = 1.4 V

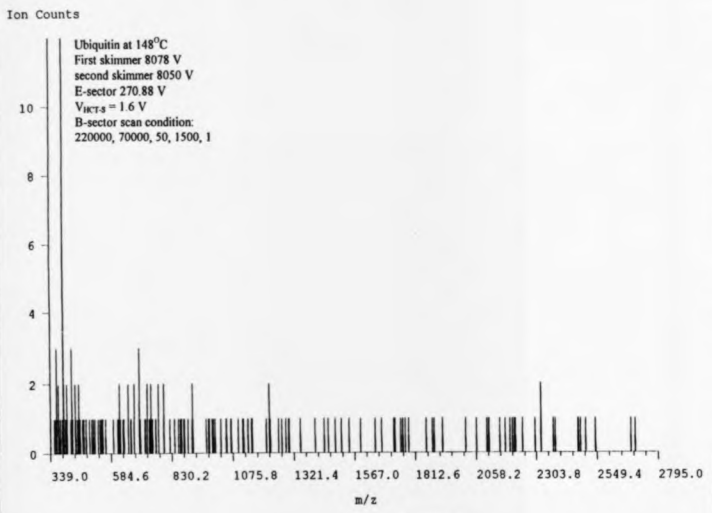
Ion Counts
Ubiquitin at 148°C
First skimmer 8078 V
second skimmer 8050 V
E-sector 270.88 V
V_IKCT-S = 1.6 V
B-sector scan condition:
220000, 70000, 50, 1500, 1
0
2
4
6
8
10
339.0 584.6 830.2 1075.8 1321.4 1567.0 1812.6 2058.2 2303.8 2549.4 2795.0
m/z

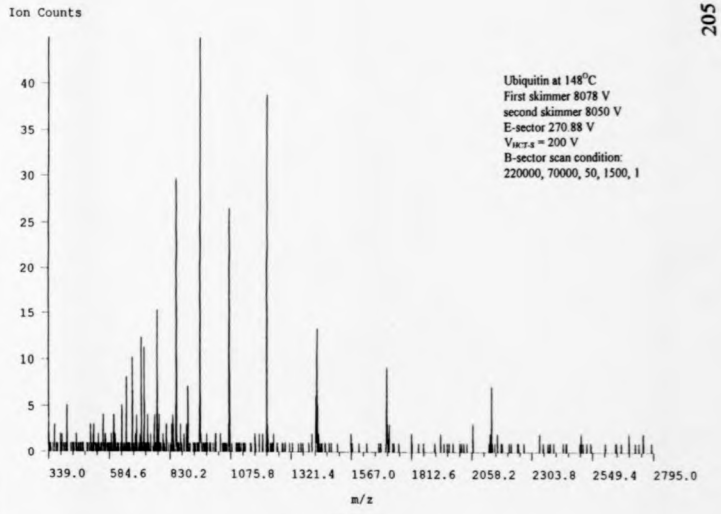
Ion Counts
Ubiquitin at 148°C
First skimmer 8078 V
second skimmer 8050 V
E-sector 270.88 V
V_IKCT-S = 200 V
B-sector scan condition:
220000, 70000, 50, 1500, 1
0
5
10
15
20
25
30
35
40
339.0 584.6 830.2 1075.8 1321.4 1567.0 1812.6 2058.2 2303.8 2549.4 2795.0
m/z

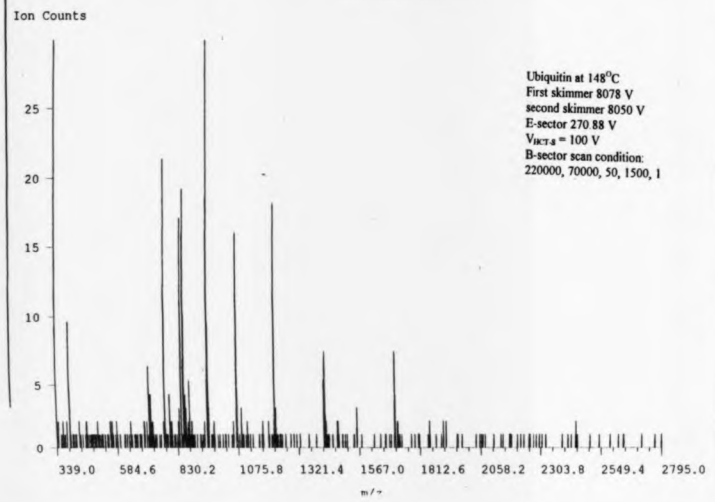
Ion Counts
Ubiquitin at 148°C
First skimmer 8078 V
second skimmer 8050 V
E-sector 270.88 V
V_IKCT-S = 100 V
B-sector scan condition:
220000, 70000, 50, 1500, 1
0
5
10
15
20
25
339.0 584.6 830.2 1075.8 1321.4 1567.0 1812.6 2058.2 2303.8 2549.4 2795.0

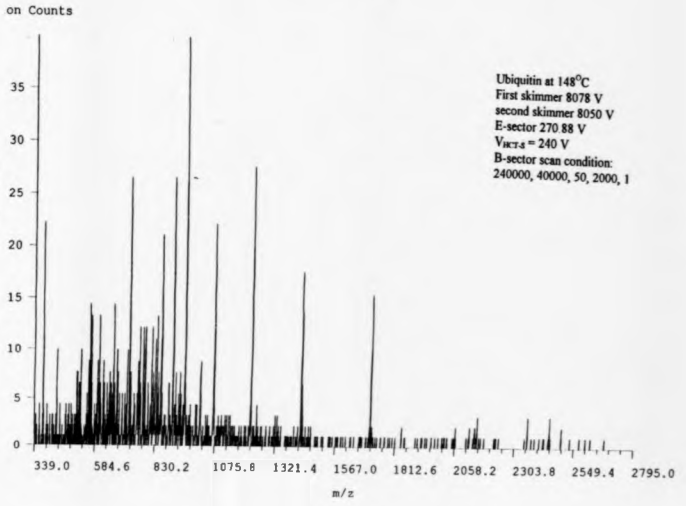
on Counts
Ubiquitin at 148°C
First skimmer 8078 V
second skimmer 8050 V
E-sector 270.88 V
V_IKCT-S = 240 V
B-sector scan condition:
240000, 40000, 50, 2000, 1
0
5
10
15
20
25
30
35
339.0 584.6 830.2 1075.8 1321.4 1567.0 1812.6 2058.2 2303.8 2549.4 2795.0
m/z

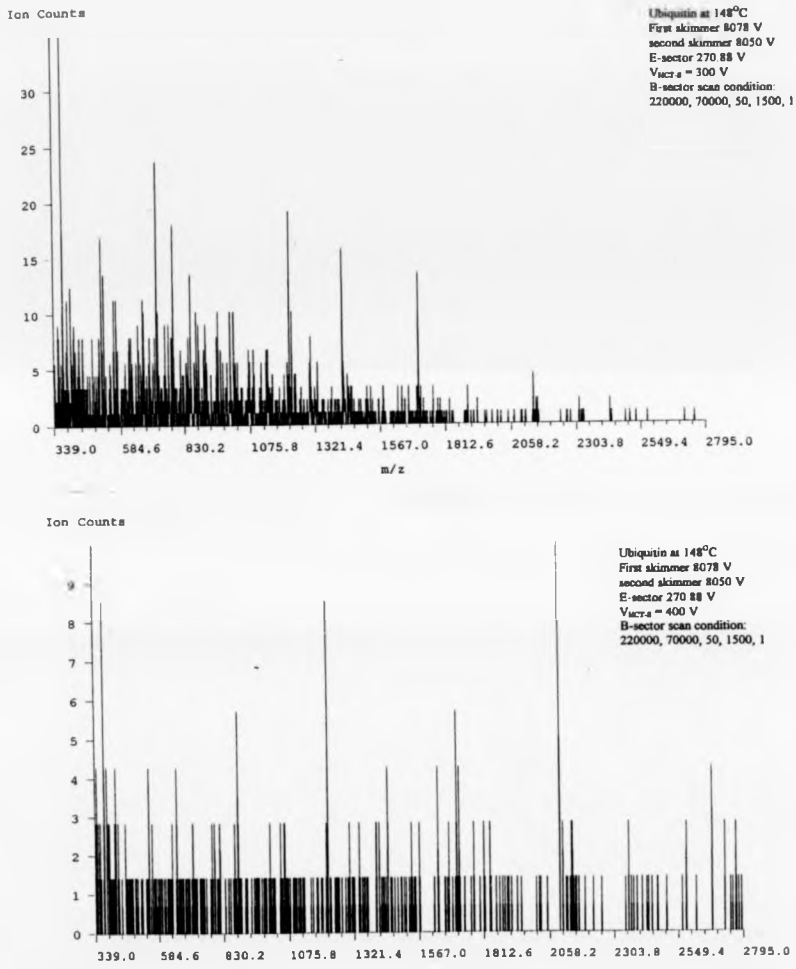

Figure 5-31 Ubiquitin B-sector scan spectra: at 148°C with V_{HCT-S} = 1.6 V, 100V, 200V, 240V, 300 V and 400 V

1500 ms and single scan. All other spectra were under the following conditions: 220000 mA (2795 m/z) start current, 70000 mA (339 m/z) end current, 50 mA step size, 1500 ms scan time and single scan. It should be pointed out that nearly all the B-sector scan spectra reported in this thesis were single scans. They were not average spectra. [Figure 5-30] shows the B-sector scan spectrum of ubiquitin over a little larger mass (m/z) scan range [scan conditions: (240000 mA (3238 m/z), 40000 mA (126 m/z), 50 mA steps, 2000 ms scan time, 1 scan) at 248°C when $V_{HCT\text{-}S}$ = 1.4 V.] which shows the triply charged ubiquitin ion.

With the spectra in [Figure 5-29], $V_{HCT\text{-}S}$ was set at 1.8 V, 100.0 V, 200.0 V, 300.0 V and 400.0 V. Fragmentation peaks were observed and were most intense when $V_{HCT\text{-}S}$ =200.0 V and the base line began to rise around 850 m/z. These peaks became more and more relatively intense on increasing of $V_{HCT\text{-}S}$, but the absolute intensities did not rise. The greater fragmentation was attributed to the higher laboratory-frame energies acquired by the higher charged ions in the capillary-skimmer region at the same $V_{HCT\text{-}S}$ values employed for substance P and insulin.

Among ions of the same charge but different masses, heavier m/z ions need higher $V_{HCT\text{-}S}$ to achieve focusing[5-24]. Comparing the results with substance P, insulin and ubiquitin (or see the experiment results of the PEG 800 and PEG 1500 in 5.3.5 of this chapter) led to the same conclusion.. For example, at 248°C, the triply charged ions: 1) substance P $[M+3H]^{3+}$ 450 m/z, optimum $V_{HCT\text{-}S}$ voltage 90V, range 1.4 V ~ 110 V; 2) insulin $[M+3H]^{3+}$ 1912 m/z, optimum $V_{HCT\text{-}S}$ voltage 220 V, region 1.4 V ~ 340 V; 3) ubiquitin $[M+3H]^{3+}$ 2855 m/z, optimum $V_{HCT\text{-}S}$ voltage 330 V, region 1.4 V ~ 400 V (full experimental $V_{HCT\text{-}S}$ range). This is another reason why in B-sector scan spectra of

ubiquitin at V_{HCT-S} higher than 200 V, there were more fragment peaks than there were in spectra of insulin and substance P at the same V_{HCT-S}.

The signal intensities of ions in [Figure 5- 29] relative to each other might not have exactly matched with the graphs in [Figure 5-26], as the former were the single B-sector scan spectra and the latter represented summed results from the measurements on separately optimized ions. Other results were well matched.

At the lower HCT temperature 148°C, there were no ubiquitin signals in the first spectrum in [Figure 5-31] at the lowest V_{HCT-S} (V_{HCT-S} =1.6 V). Ubiquitin ions appeared when V_{HCT-S} = 100 V. Fragments appeared when V_{HCT-S} =200.0 V, but the highest intensities were at V_{HCT-S} = 240.0 V. This supports the idea that at low HCT temperature, it is necessary to increase the V_{HCT-S} voltage to help the desolvation process and ions need higher V_{HCT-S} voltage to experience the same V_{HCT-S} voltage drop.

Checking [Figure 5-26] and [Figure 5-28], it is found that the pattern of change was the same as with substance P and insulin when the HCT temperature was lowered. The effects of charge stripping processes cannot be seen in the graphs. If there were such processes occurring, they might have been too complicated to be evident from the graphs.

5.3.4 Non-covalent complex — Vancomycin and N-acetyl-lysine-D-alanine-D-alanine (KAA)

Vancomycin is a naturally occurring glycopeptide antibiotic which is active against Gram-positive bacteria[5-29]. Both it and related β-lactam antibiotics have been studied for their resistance to the infections. Its structure is shown in [Figure 5-32] and contains a heptapeptide chain of which both the amino and carboxy termini are free.

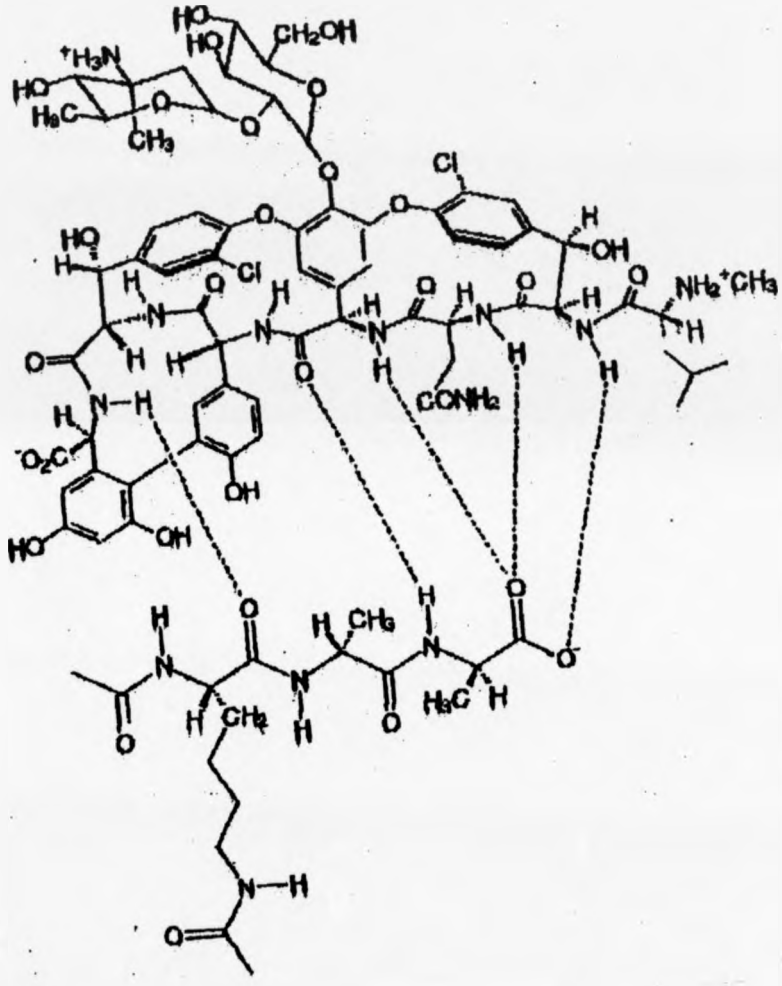

Figure 5-32 Vanconmycin with Ac_2 L - Lys D-Ala D-Ala

There are also three weakly acidic aryl hydroxy groups and a basic vancosamine. Vancomycin can form a non-covalent complex with KAA (N-acetyl-lysine-D-alanine-D- alanine)[5-30, 5-31], in which the non-covalent bond is quite weak and easily

dissociated by heat (heat induced dissociation HID). Heck and co-workers[5-32] claimed that the solution binding constants of vancomycin with bacterial cell wall peptides decreased with increasing tube lens voltages (which controlled the V_{HCT-S}) in ESI source and deduced that this decrease was due to collision-induced dissociation of the complex ions in the tube lens region (capillary-skimmer region). Lebrilla and co-workers[5-25]. used an FT-ICR mass spectrometer equipped with a differentially heated capillary ESI source to study the thermal dissociation of non-covalently bound complexes produced by the electrospray ionization. As the temperature of the first part was fixed and the temperature of the second part could be changed, the complexes were first desolvated and then dissociated by the heating. They used the experiments to monitor the dissociation temperature, above which the complex would not be observed. They found that the dissociation of the complexes happened in the gas-phase and not in solution-phase of an intact droplet in the ESI process.

[Figure 5-33], [Figure 5-34] [Figure 5-35], [Figure 5-36] [Figure 5-37], and [Figure 5-38] give the experimental results of vancomycin and KAA at 248°C, 198°C and 148°C respectively. Signal intensities of [Vancomycin + KAA + H]$^+$ ion were very weak with highest value only 112 counts per second compared to 13,000 counts per second for [Vancomycin + H]$^+$ ion in [Figure 5-33]. Table 5-2 gives the summed optimum V_{HCT-S} values of four relevant ions under different HCT temperatures. [Figure 5-39] and[Figure 5-40] give the B-sector scan spectra of vancomycin + KAA solution at 198°C and 148°C. [Figure 5 - 41] gives the vancomycin (no KAA) results at 198°C.

Comparing [Figure 5-33], [Figure 5-35] and [Figure 5-37], it can be seen that from 248°C to 198°C the optimum V_{HCT-S} values of the four ions were not changed and

Table 5-2 Vancomycin + KAA. Optimum V_{HCT-S} for various ions at different HCT temperatures

name of ion	248°C	198°C	148°C
[Vancomycin + KAA + 2H]$^{2+}$	100V	100V	190V
[Vancomycin + KAA + H]$^{+}$	~ 170 V	170 V	—
[Vancomycin + 2H]$^{2+}$	100 V	100 V	170 V
[Vancomycin + H]$^{+}$	210 V	220 V	260 V

Figure 5-33 Vancomycin + KAA. Ion intensities vs. the voltage V_{HCT-S} between the HCT and the first skimmer at 248°C, 5.00-mm HCT-skimmer distance, first skimmer 8077 V, second skimmer 8050V

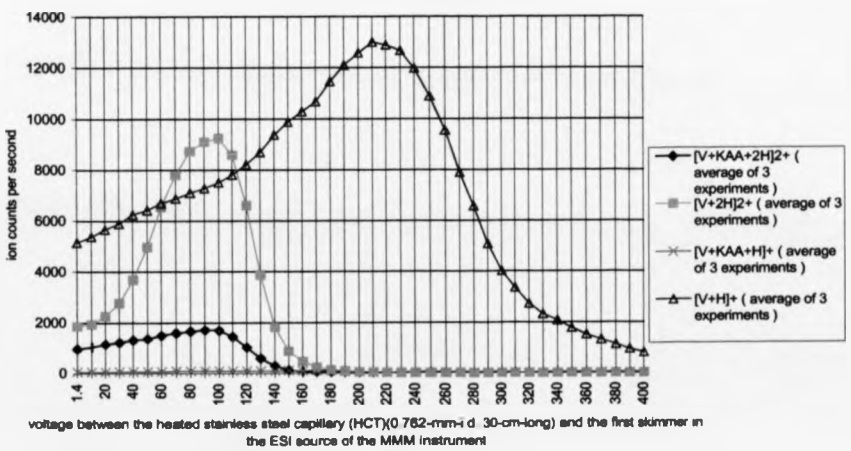

Figure 5-34 Vancomycin + KAA: Normalised intensities vs. the voltage V_{HCT-S} between the HCT and the first skimmer at 248°C, 5.00-mm HCT-skimmer distance, first skimmer 8077 V, second skimmer 8050V

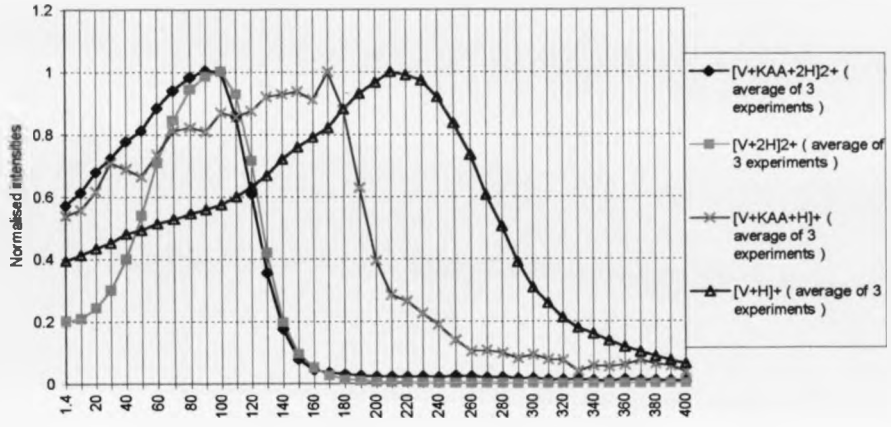

voltage between the heated stainless steel capillary (HCT)(0.762-mm-i.d. 30-cm-long) and the first skimmer in the ESI source of the MMM instrument

Figure 5-35 Vancomycin + KAA. Ion signal intensities vs. the voltage V_{HCT-S} between the HCT and the first skimmer at 198C, 5.00-mm HCT-skimmer distance, first skimmer 8077 V, second skimmer 8050V

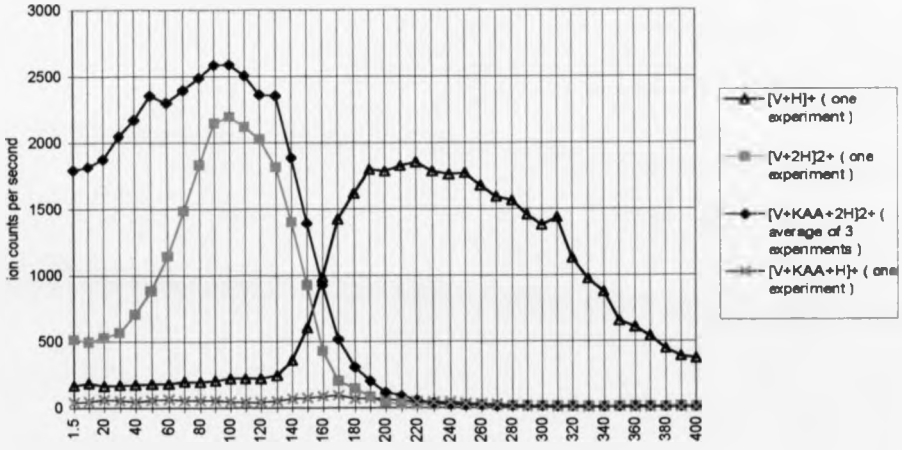

voltage between the heated stainless steel capillary (HCT) (0.762-mm-i.d. 30-cm-long)and the first skimmer in the ESI source of the MMM instrument

Figure 5-36 Vancomycin + KAA: Normalised intensities vs. the voltage V_{HCT-S} between the HCT and the first skimmer at 198C, 5.00-mm HCT-skimmer distance, first skimmer 8077 V, second skimmer 8050V

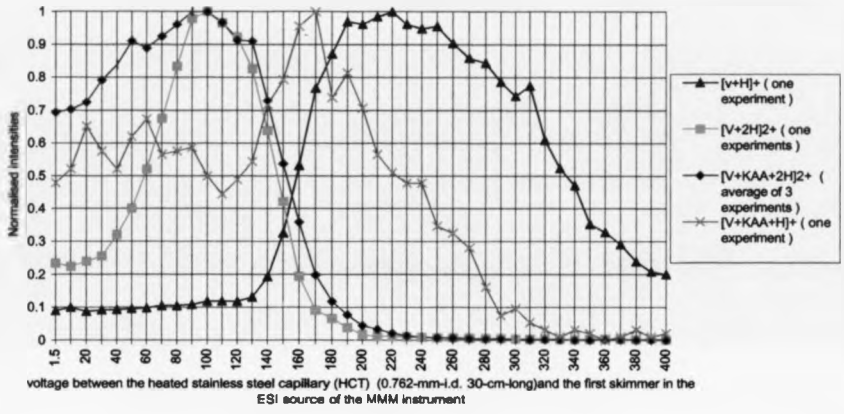

Figure 5-37 Vancomycin + KAA. Ion signal intensities vs. the voltage V_{HCT-S} between the HCT (0.762-mm-i.d. 30-cm-long) and the first skimmer at 148°C, 5.00-mm HCT-skimmer distance, first skimmer 8077 V, second skimmer 8050 V

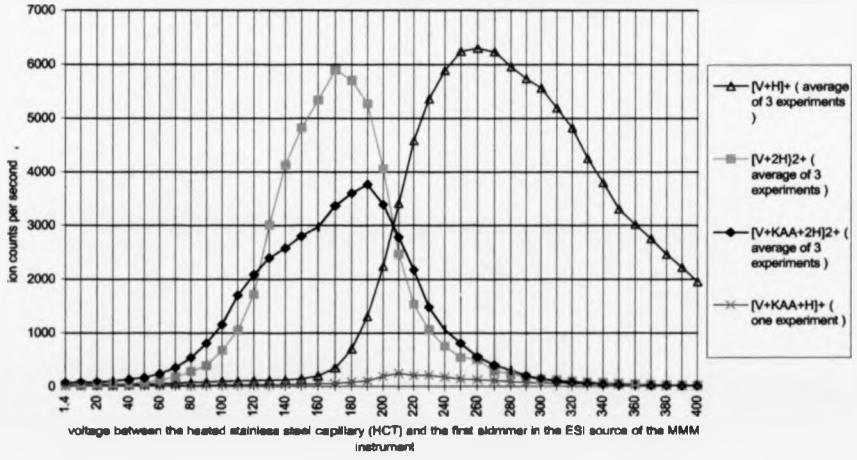

Figure 5-38 Vancomycin + KAA. Normalised intensities vs. the voltage V_{HCT-S} between the HCT (0.762-mm-i.d. 30-cm-long) and the first skimmer at 148°C, 5.00-mm HCT-skimmer distance, first skimmer 8077 V, second skimmer 8050 V

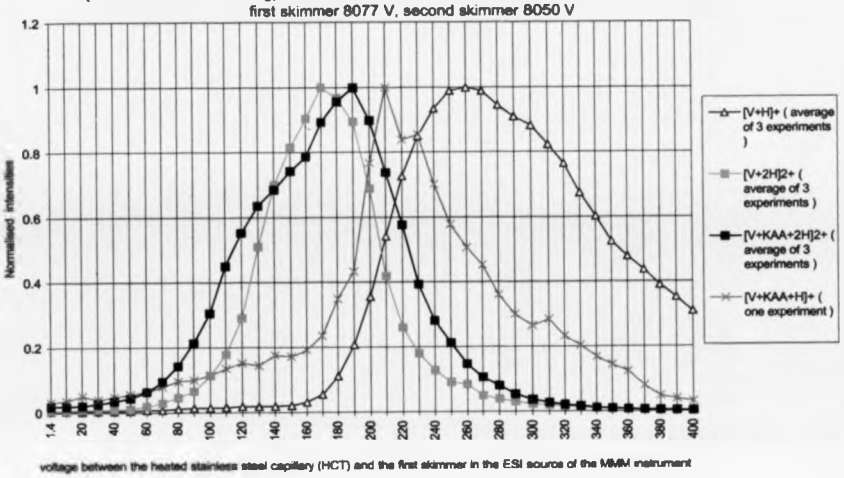

Figure -41 Vancomycin [V+2H]2+ and [V+H]+ ions signal intensities vs. the voltage V_{HCT-S} between the HCT and the first skimmer at 198°C, 5.00-mm HCT-skimmer distance, first skimmer 8077 V, second skimmer 8050V

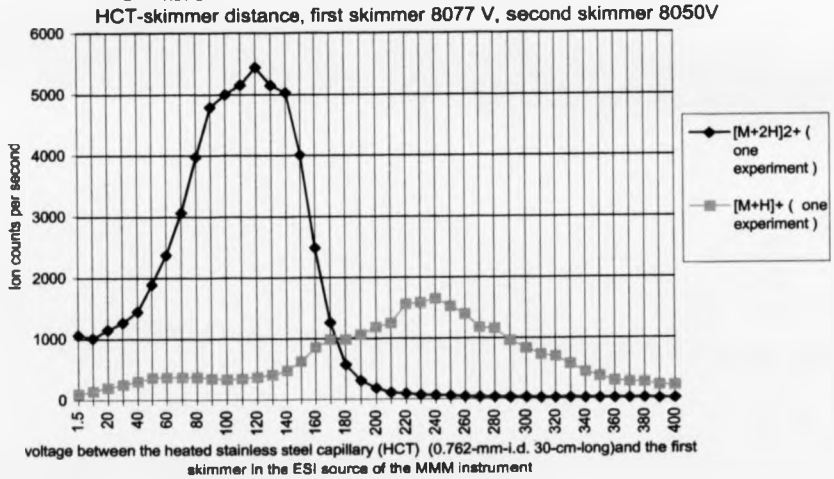

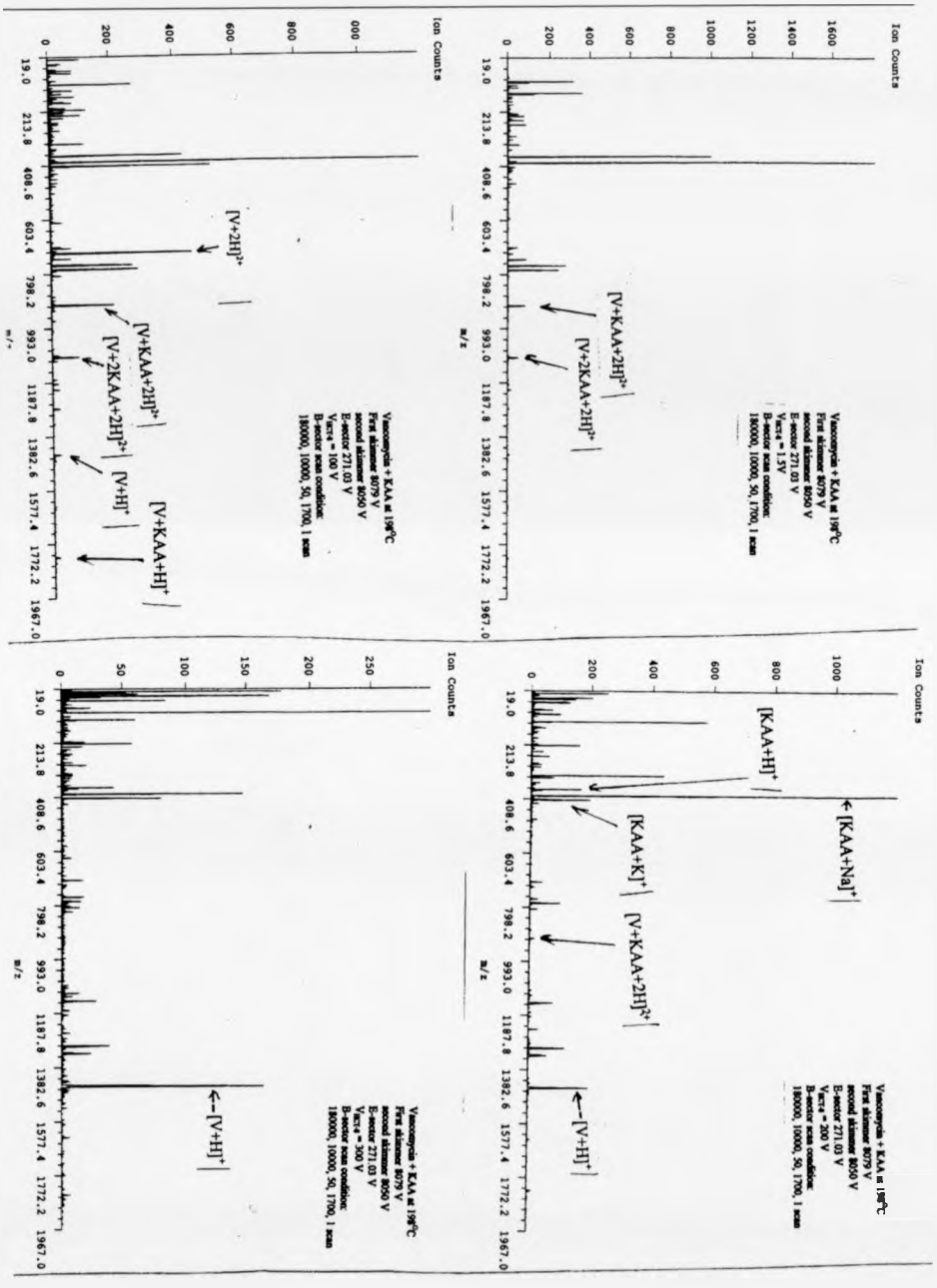
Ion Counts
m/z
[V+KAA+2H]2+
[V+2KAA+2H]2+
[V+2H]2+
[V+KAA+2H]2+
[V+2KAA+2H]2+
[V+H]+
[V+KAA+H]+
[KAA+Na]+
[KAA+H]+
[KAA+K]+
[V+KAA+2H]2+
[V+H]+

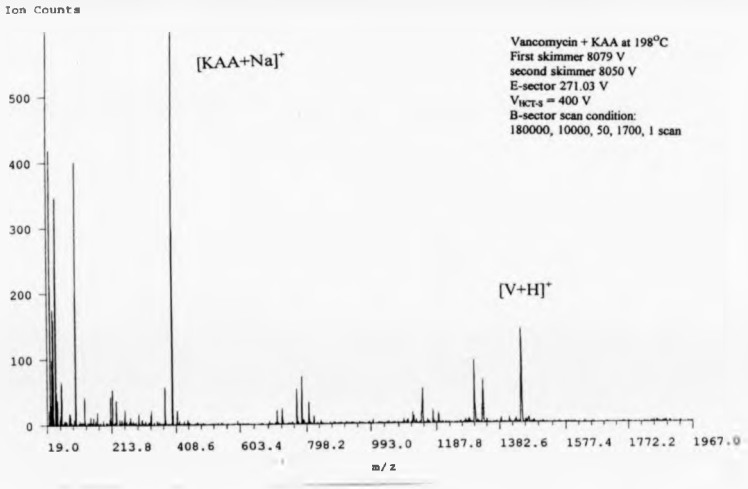

[Figure 5-39] B-sector scan spectra of vancomycin + KAA at 198°C with V_{HCT-S} =1.5 V, 100 V, 200 V, 300 V and 400 V

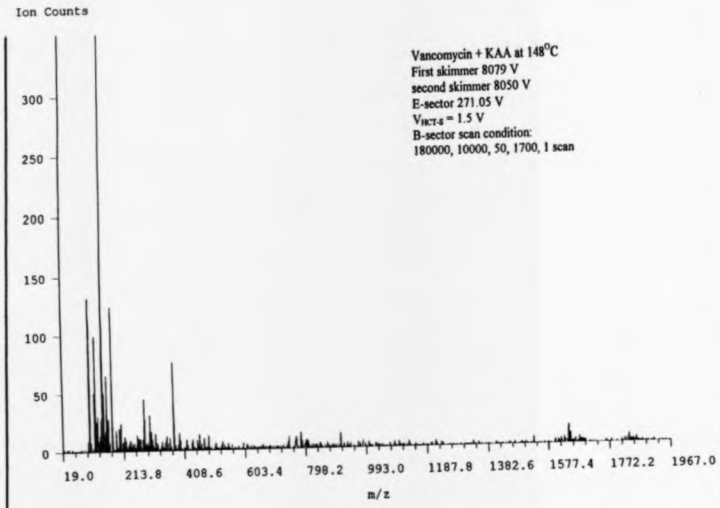
Ion Counts
Vancomycin + KAA at 148°C
First skimmer 8079 V
second skimmer 8050 V
E-sector 271.05 V
V_HCT-8 = 1.5 V
B-sector scan condition:
180000, 10000, 50, 1700, 1 scan
m/z

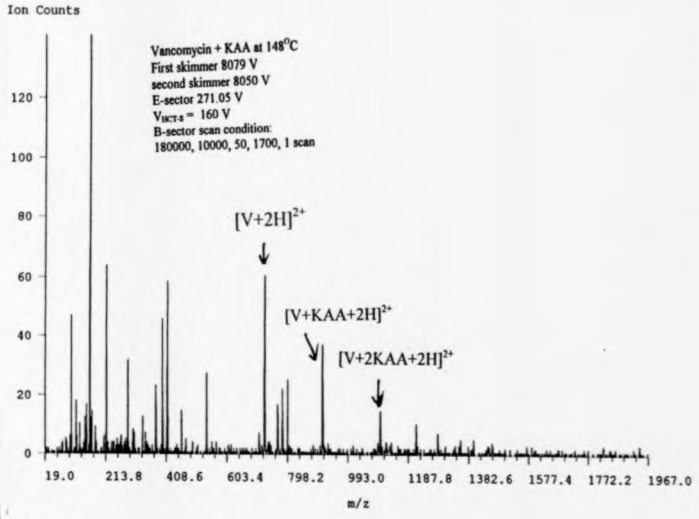
Ion Counts
Vancomycin + KAA at 148°C
First skimmer 8079 V
second skimmer 8050 V
E-sector 271.05 V
V_HCT-8 = 160 V
B-sector scan condition:
180000, 10000, 50, 1700, 1 scan
[V+2H]2+
[V+KAA+2H]2+
[V+2KAA+2H]2+
m/z

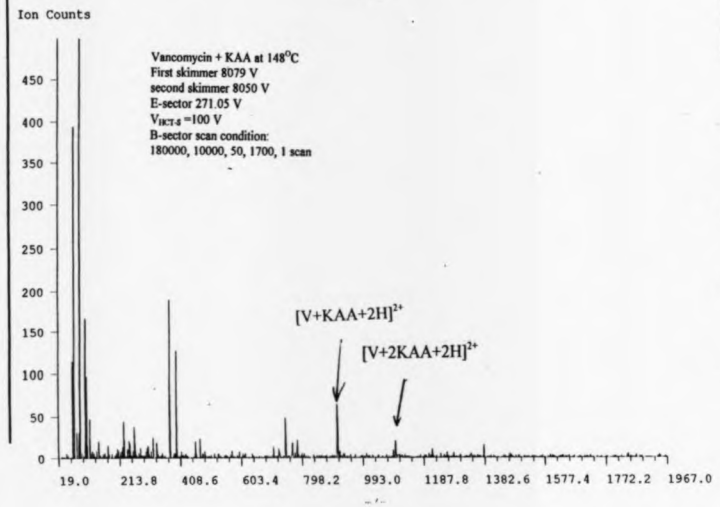
Ion Counts
Vancomycin + KAA at 148°C
First skimmer 8079 V
second skimmer 8050 V
E-sector 271.05 V
V_HCT-8 =100 V
B-sector scan condition:
180000, 10000, 50, 1700, 1 scan
[V+KAA+2H]2+
[V+2KAA+2H]2+

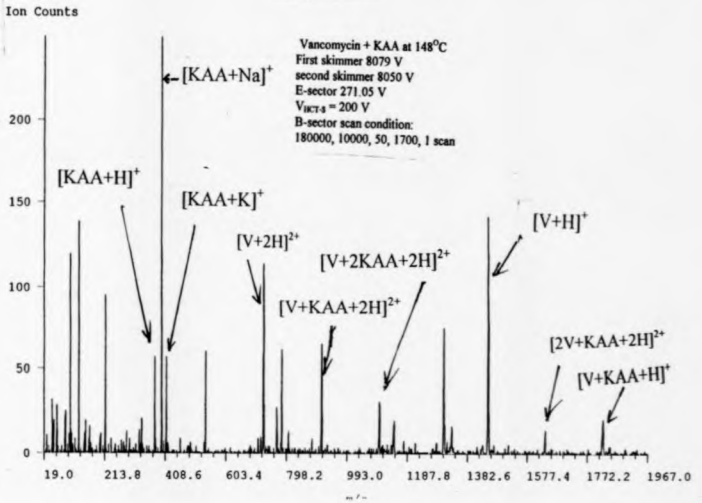
Ion Counts
Vancomycin + KAA at 148°C
First skimmer 8079 V
second skimmer 8050 V
E-sector 271.05 V
V_HCT-8 = 200 V
B-sector scan condition:
180000, 10000, 50, 1700, 1 scan
[KAA+Na]+
[KAA+H]+
[KAA+K]+
[V+2H]2+
[V+2KAA+2H]2+
[V+KAA+2H]2+
[V+H]+
[2V+KAA+2H]2+
[V+KAA+H]+

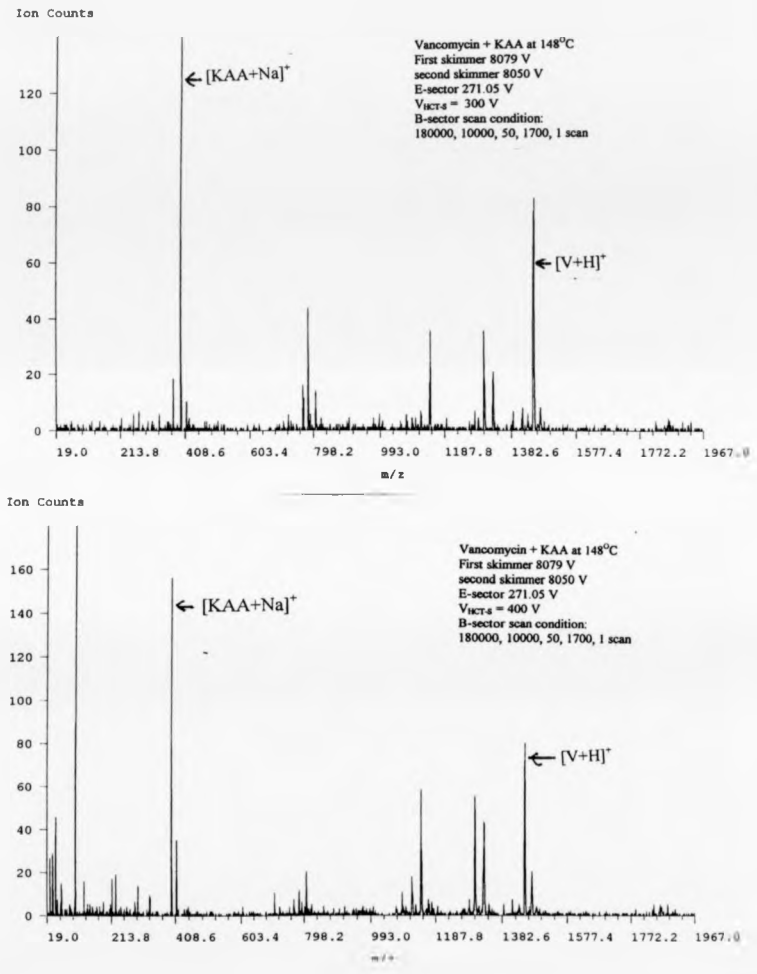

[Figure 5-40] B-sector scan spectra of vancomycin + KAA at 148°C with V_{HCT-S} =1.5 V, 100 V, 160 V, 200 V, 300 V and 400 V

from 198°C to 148°C both optimum $V_{HCT\text{-}S}$ and $V_{HCT\text{-}S}$ range over which the ions were observed shifted to higher voltages. 248°C is the favourite temperature for [V+H]$^+$ and [V+2H]$^{2+}$ ions, in comparison to their non-covalent counterparts [V + KAA + H]$^+$ and [V + KAA + 2H]$^{2+}$. As the thermal-induced dissociation would have been at its highest level, the relative intensities of non-covalent ions were at their lowest. 148°C was the favourite temperature for non-covalent complex ions for the same reason. Comparing [Figure 5-35] and [Figure 5-41], the optimum $V_{HCT\text{-}S}$ values and the peak shapes of the $V_{HCT\text{-}S}$. ranges over which the ions were observed for[V+2H]$^{2+}$ and [V+H]$^+$ ions were the same. The relative intensity differences were larger in [Figure 5-41] than in [Figure 5-35]. It seems doubly charged ions were relatively more stable compared to their singly charged counterparts at 198°C.

[Figure 5-42] shows results due to a phenomenon not fully understood. Normally, when the B-sector current was set to focus a peak, scanning the E-sector over a narrow region was sufficient to give the E-sector setting used in later B-sector scans or other experiments. But sometimes, this narrow E-sector scan showed a peak with a shoulder or a peak split at the top. [Figure 5-42] was acquired at 8068 V on the first skimmer and 8050 V on the second skimmer with the B-sector setting unchanged compared with [Figure 5-35] (8077 V on the first skimmer and 8050 V on the second skimmer). In [Figure 5-42], the first two experiments used 270.63 V on the E-sector and the second two experiments used 270.68 V. As the [V+2H]$^{2+}$ ion mass is 724 m/z, a 0.05 V setting difference represented 0.134 m/z (Da), i.e. less than 0.5 Da. So the result was not caused by the isotopic peak. But this small difference in E-sector setting caused a big difference in ion intensity vs. the voltage $V_{HCT\text{-}S}$. An E-sector setting of 270.68 V

gave results similar to that for $[V+KAA+2H]^{2+}$ in [Figure 5-37]; 270.63 V setting gave a lower optimum $V_{HCT\text{-}S}$ value and stronger signal.

Figure 5-42 vancomycin +KAA. [V+2H]2+ (724m/z) signal intensities vs. the $V_{HCT\ S}$ voltage between the HCT and the first skimmer at 148°C, 5.00-mm HCT-skimmer distance, first skimmer 8068 V, second skimmer 8050 V, (0.134m/z = 0.05V on E), no change in B

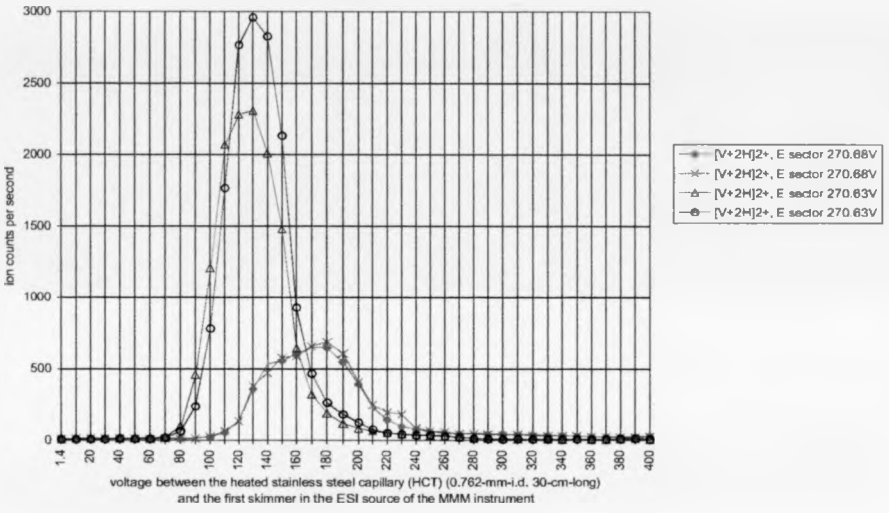

5.3.5 Polyethylene glycol (PEG) 800 and PEG 1500

Narrow-molecular-weight PEG standards (Mn 800 and 1500) have a repeating unit of 44 Da. Their concentrations were 1×10^{-4}M in $(CH_3)_2CO$:H_2O=90:10 (by volume) (with 1.2 mM CH_3COONa) solvent or 5×10^{-5}M in H_2O (5 mM CH_3COONH_4): CH_3OH: CH_3COOH = 49.5 : 49.5 :1 (by volume). For PEG 1500 sample, the singly charged ions were observed in the m/z 900-2000 region with peak spacing of 44 m/z, doubly charged ions were apparent at 22 m/z intervals in m/z 500-1000 region and triply charged ions were observed from 400 to 700 at m/z 14.7 intervals.

$(CH_3)_2CO:H_2O$=90:10 (by volume) (with 1.2 mM CH_3COONa) solvent was used for PEG 800 samples. [Figure 5-43], [Figure 5-44], [Figure 5-45] and [Figure 5-46] give experiment results of PEG 800 at 248°C and 148°C. [Figure 5-47] and [Figure 5-48] give the relevant B-sector scan spectra where only singly charged ions were observed. The PEG 800 results showed that for ions with the same charge but different masses: lower-mass ions (lower m/z) had lower optimum V_{HCT-S} and higher-mass ion had higher optimum V_{HCT-S}. A lower HCT temperature moved both the optimum V_{HCT-S} and V_{HCT-S} range for ion observation towards higher voltages. The effect of a 6 V potential increase on the first skimmer (8071 V for [Figure 5-43] and [Figure 5-44], 8077 V for [Figure 5-45] and [Figure 5-46] and keeping 8050 V on the second skimmer) was too small to be observed compared to the opposite effect of the HCT temperature dropping. These results confirmed what had already been found with substance P, insulin, ubiquitin and vancomycin and KAA experiments. Because all the ions were already in the singly charged state and each ion was one monomer unit different from its neighbour, it could not be established whether or not there was a fragmentation process from the B-sector spectra.

H_2O (with 5 mM CH_3COONH_4): CH_3OH: CH_3COOH = 49.5 : 49.5 :1 (by volume) solvent was used for the PEG 1500 sample. [Figure 5-49] and [Figure 5-50] show the very limited results for PEG 1500 at 248°C and 148°C. [Figure 5-51] and [Figure 5-52] show corresponding B-sector scan spectra. Comparing [Figure 5-49] with [Figure 5-2], as the HCT temperatures were the same and the ions m/z values were relatively similar (triply charged ions were 753 and 675 m/z, doubly charged ions were 538 and 450 m/z respectively). The optimum V_{HCT-S} values were equal, or very nearly so, and the shapes of V_{HCT-S} ranges were similar. In [Figure 5-49], triply and doubly

charged PEG 1500 ions have nearly the same highest intensities as each other, though the intensities of the doubly charged ions were still little higher. B-sector scan spectra [Figure 5-51] supported the results in [Figure 5-49]. These also showed that singly charged ions had the highest intensities among the three charge states and that intensities did not change much in the whole V_{HCT-S} test region. In [Figure 5-50], though all the ions were measured only once, the results matched well with the spectra in [Figure 5-52]. Triply charged ions were the strongest from 1.5 V to ~ 145 V, and doubly charged at higher V_{HCT-S} were stronger than singly charged ions. Doubly charged ions were the strongest in [Figure 5-52] when V_{HCT-S} = 200.0 V. Comparing [Figure 5-50] and [Figure 5-9] (148°C), though at low V_{HCT-S} voltage all intensities of the PEG 1500 ions were quite high, at a higher V_{HCT-S} voltage the intensities of triply and doubly charged ions in both graphs fell at similar V_{HCT-S} values. It seems that lower HCT temperature favoured the multiply charged PEG ions and that the HCT temperature determined ions could show up at low V_{HCT-S} potential. The much stronger effect, however, was ion optical focusing which was determined by $V_{HCT-S,}$ and had the final say in deciding which ions were allowed to pass the system. Comparing [Figure 5-52] with [Figure 5-53] , [Figure 5-54] and [Figure 5-55], the solvent effect is manifested so that the lower organic solvent percentage favoured the multiply charged PEG ions.

[Figure 5-53] , [Figure 5-54] and [Figure 5-55] give the B-sector scan spectra of the PEG 1500 sample in $(CH_3)_2CO$: H_2O (90:10 (by volume)) with 1.2 mM CH_3COONa at 148°C when first skimmer potential was 8068 V, 8078 V and 8088 V respectively. From [Figure 5-53], it shows the same pattern as in [Figure 5-9]. Only one thing is different which is that the intensities of the singly charged ions dropped when V_{HCT-S} was increased from 300 V to 400 V. [Figure 5-54] and [Figure 5-55]

show the same pattern. In [Figure 5-55] the triply charged ions were relatively strong compared with the doubly and singly charged ions. The absolute intensities of all ions in [Figure 5-55] were lower than those in [Figure 5-54] and [Figure 5-53]. For [Figure 5-54] , as the narrow E-sector scanning spectra showed the main ion peak split at the peak top when $V_{HCT\text{-}S}$ = 100, 200 and 300 V, both of the split peak values were used to acquired B-sector spectra. The spectra show that the lower E-sector voltage setting favoured multiply charged ions appearing at lower $V_{HCT\text{-}S}$ values, as what was shown in [Figure 5-42].

Figure 5-43 PEG 800 [M+Na]+ singly charged ions signal intensities vs the $V_{HCT\text{-}S}$ voltage between the HCT and the first skimmer at 248°C, 5.00-mm HCT-skimmer distance, first skimmer 8071 V, second skimmer 8050V

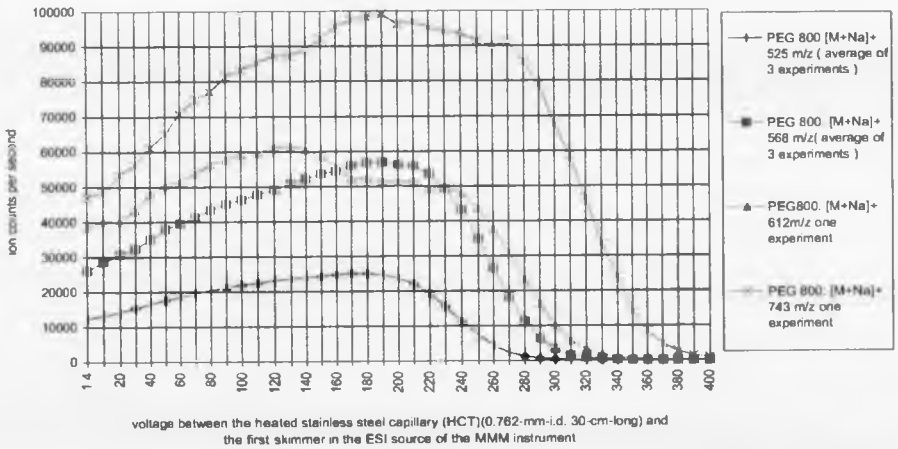

Figure 5-44 PEG 800 [M+Na]+ singly charged ions signal intensities vs. the V_{HCT-S} voltage between the HCT and the first skimmer at 248°C, 5.00-mm HCT-skimmer distance,first skimmer 8071 V, second skimmer 8050V

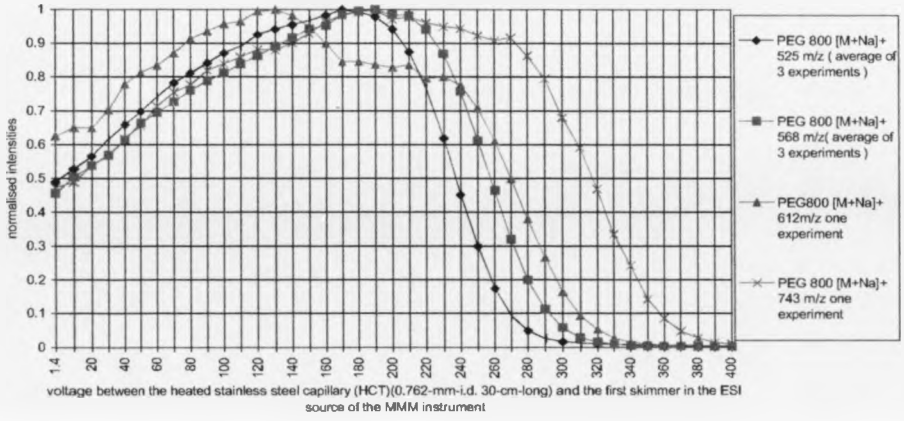

Figure 5-45 PEG 800 [M+Na]+ singly charged ions signal intensities vs. the VHCT-S voltage between the HCT and the first skimmer at 148°C, 5.00-mm HCT-skimmer distance, first skimmer 8073 V, second skimmer 8050V

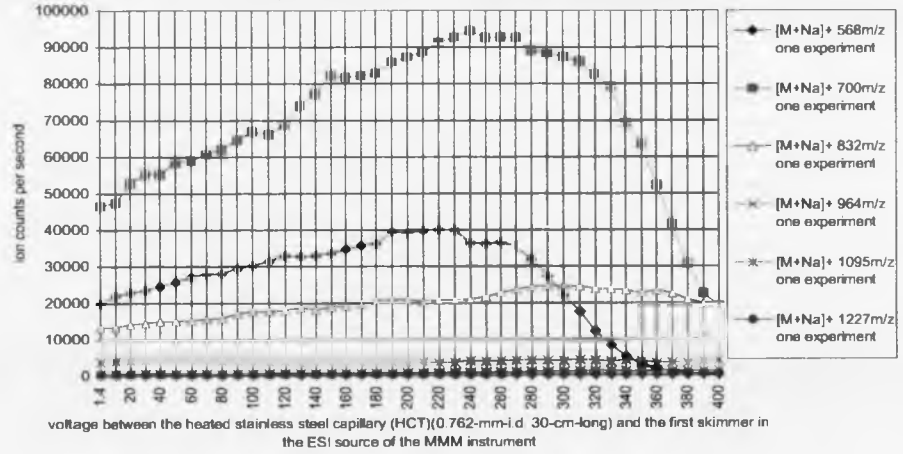

Figure 5-46 PEG 800 [M+Na]+ singly charged ions signal intensities vs. the VHCT-S voltage between the HCT and the first skimmer at 148°C, 5.00-mm HCT-skimmer, distance first skimmer 8073 V, second skimmer 8050V

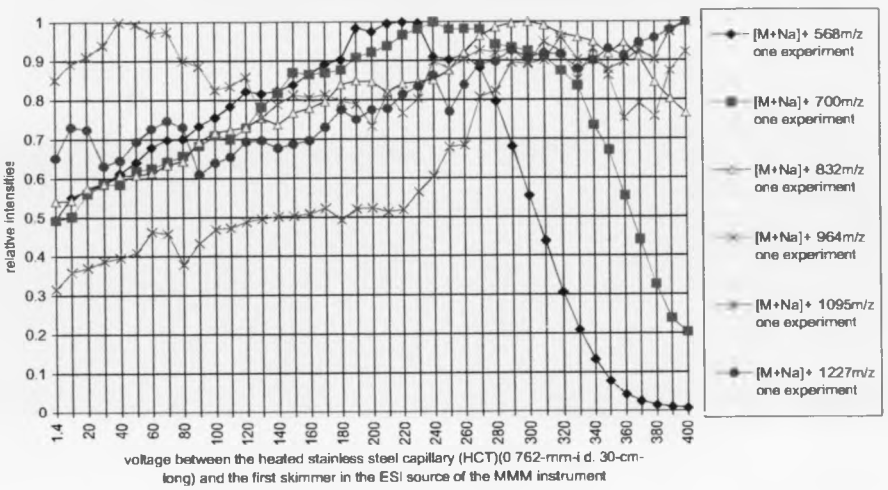

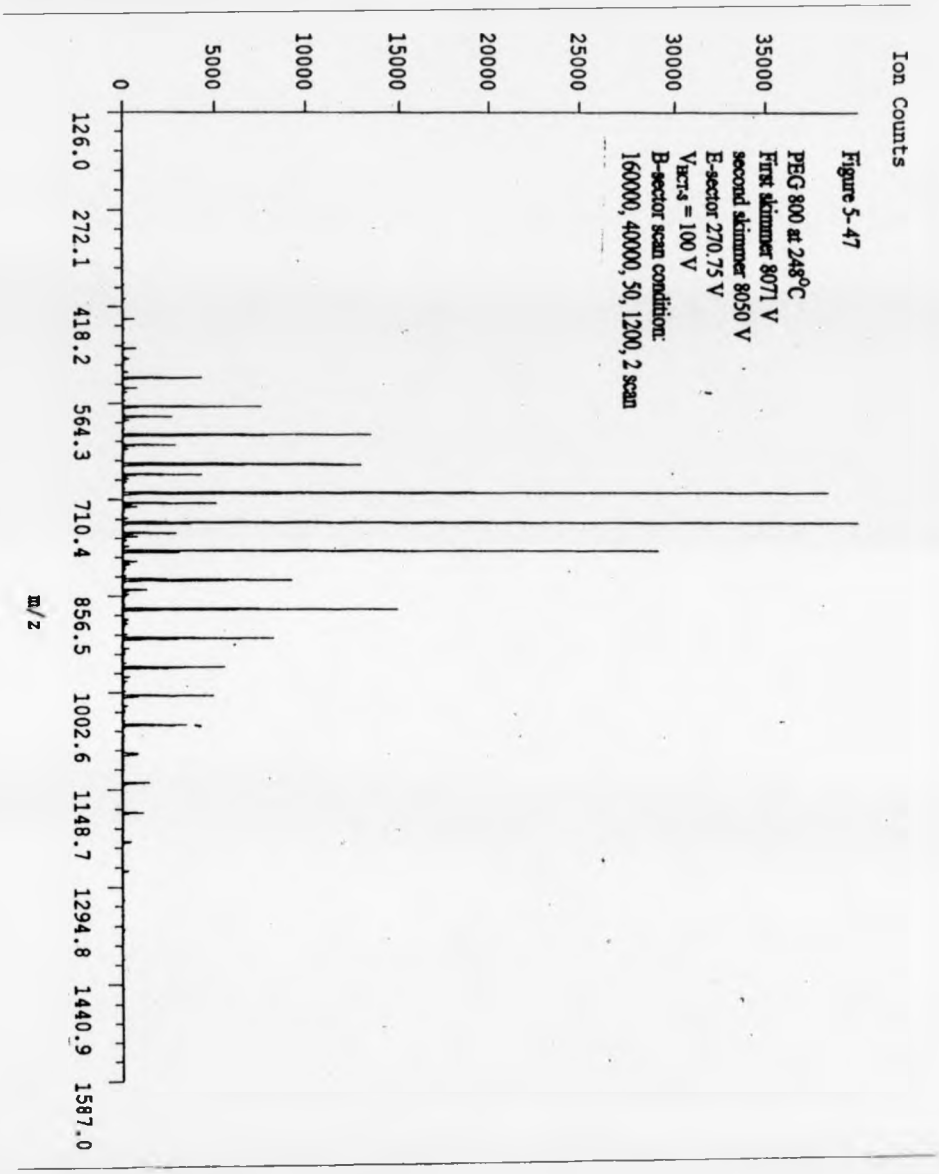

[Figure 5-47] B-sector scan spectrum of PEG 800 in $(CH_3)_2CO$:H_2O=90:10 (by volume) (with 1.2 mM CH_3COONa) solvent at 248°C with $V_{HCT\text{-}S}$ =100 V.

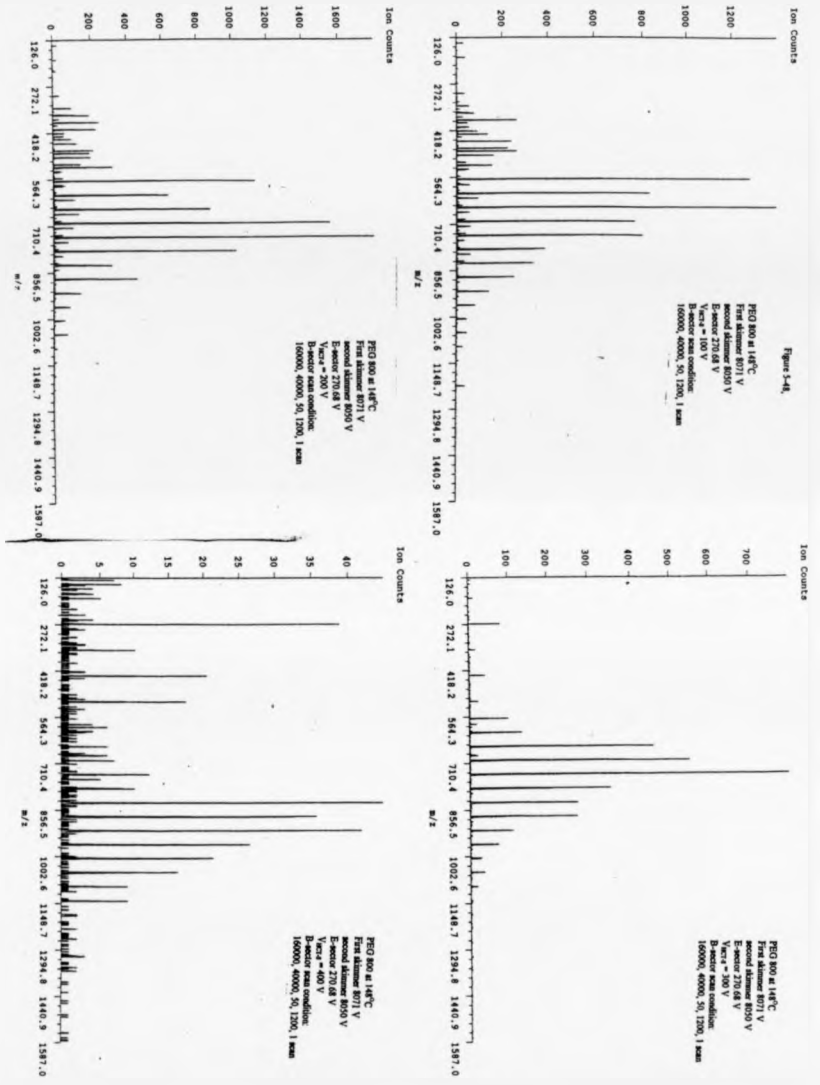

[Figure 5-48] B-sector scan spectra of PEG 800 in $(CH_3)_2CO$:H_2O=90:10 (by volume) (with 1.2 mM CH_3COONa) solvent at 148°C with $V_{HCT\text{-}S}$ =100 V, 200 V, 300 V and 400 V.

Figure 5-49 PEG 1500 [M+3H]3+ and [M+2H]2+ ions signal intensities vs. the VHCT-S voltage between the HCT and the first skimmer at 248°C, 5.00-mm HCT-skimmer distance, first skimmer 8071 V, second skimmer 8050V

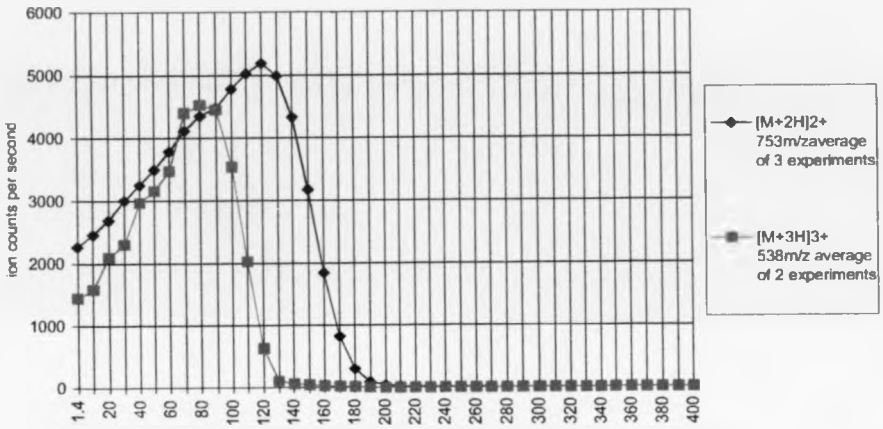

Figure 5-50 PEG1500 [M+H]+(1446;1402 m/z);[M+2H]2+(752;730 m/z);[M+3H]3+(537;522m/z) ions signal intensities vs. the voltage V_{HCT-S} between the HCT & the first skimmer at 148°C, 5.00-mm-HCT-skimmer distance, first skimmer 8073V, second skimmer 8050V

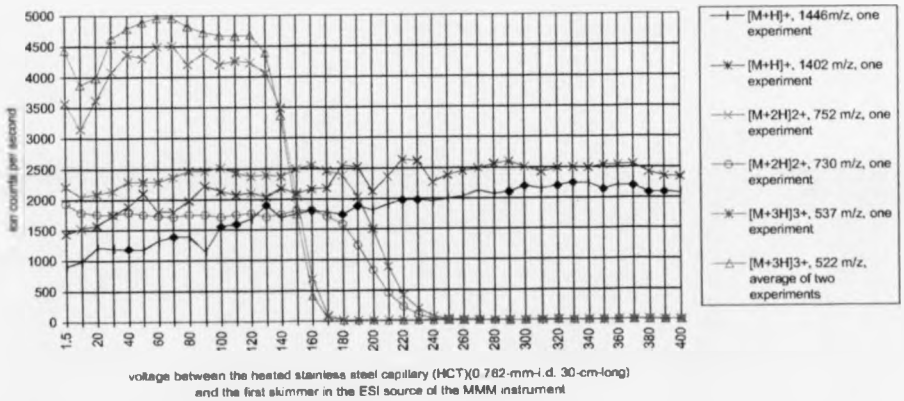

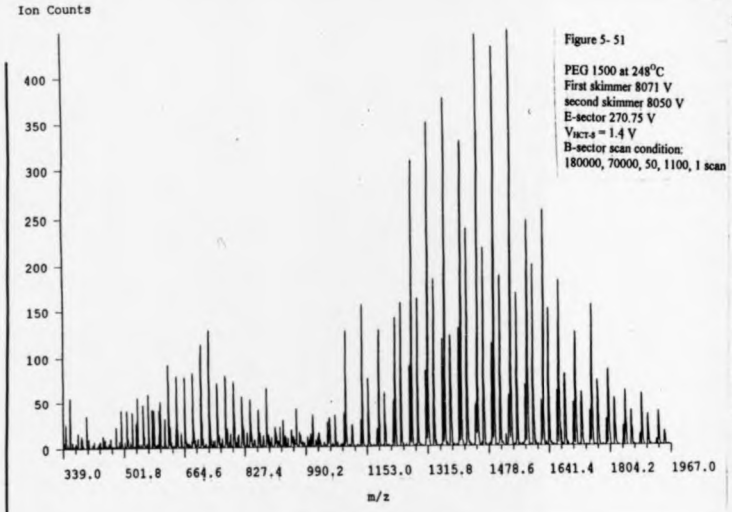

Figure 5- 51

PEG 1500 at 248°C
First skimmer 8071 V
second skimmer 8050 V
E-sector 270.75 V
V_{HCT-S} = 1.4 V
B-sector scan condition:
180000, 70000, 50, 1100, 1 scan

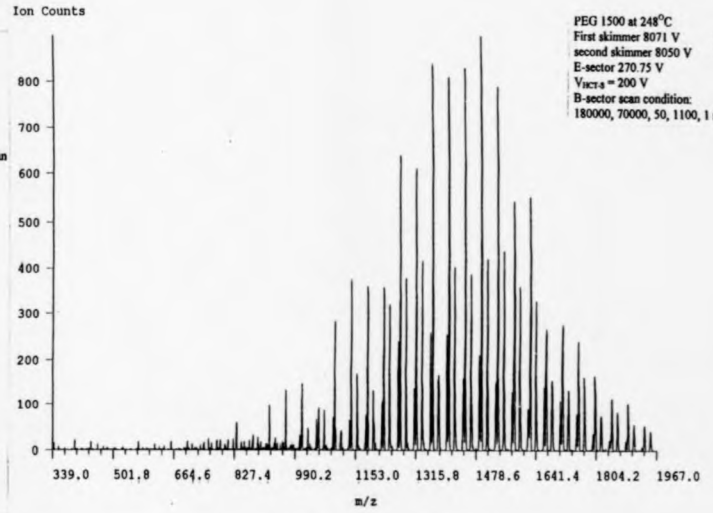

PEG 1500 at 248°C
First skimmer 8071 V
second skimmer 8050 V
E-sector 270.75 V
V_{HCT-S} = 200 V
B-sector scan condition:
180000, 70000, 50, 1100, 1 scan

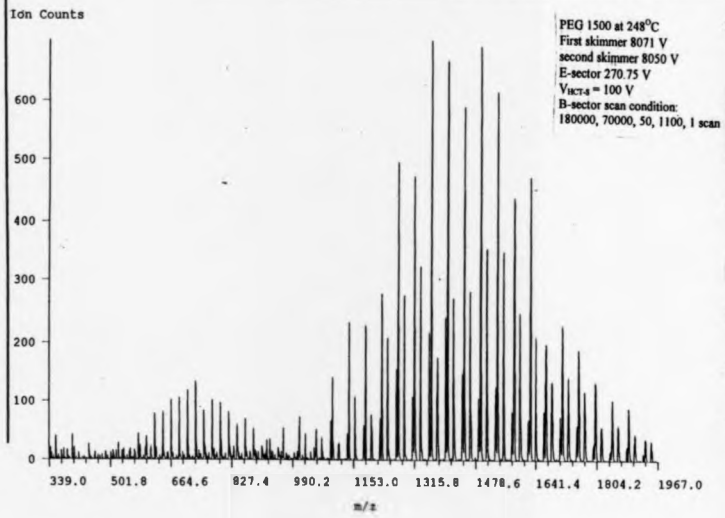

PEG 1500 at 248°C
First skimmer 8071 V
second skimmer 8050 V
E-sector 270.75 V
V_{HCT-S} = 100 V
B-sector scan condition:
180000, 70000, 50, 1100, 1 scan

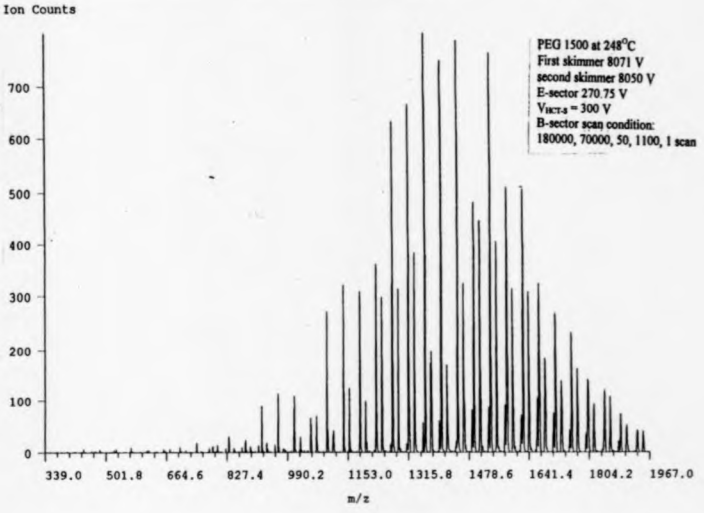

PEG 1500 at 248°C
First skimmer 8071 V
second skimmer 8050 V
E-sector 270.75 V
V_{HCT-S} = 300 V
B-sector scan condition:
180000, 70000, 50, 1100, 1 scan

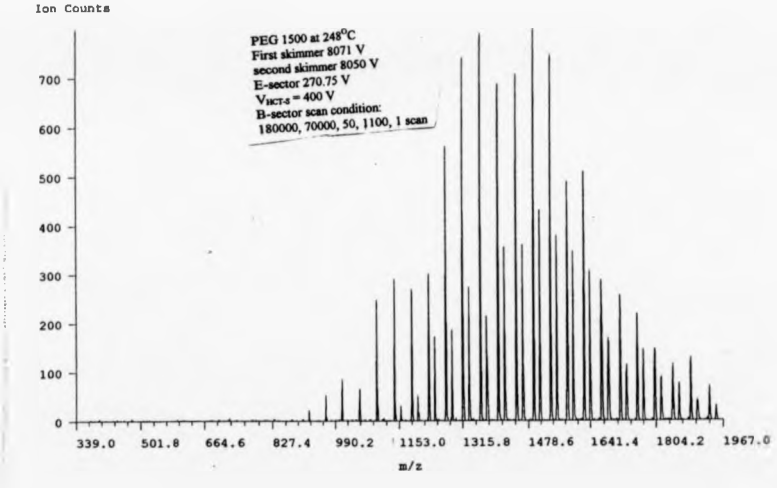

[Figure 5-51] B-sector scan spectra of PEG 1500 in H_2O (with 5 mM CH_3COONH_4): CH_3OH: CH_3COOH = 49.5 : 49.5 :1 (by volume) solvent at 248°C with V_{HCT-S} =1.4 V, 100 V, 200 V, 300 V and 400 V.

Ion Counts
m/z
339.0 501.8 664.6 827.4 990.2 1153.0 1315.8 1478.6 1641.4 1804.2 1967.0
PEG 1500 at 148°C
First skimmer 8078 V
second skimmer 8050 V
E-sector 270 85 V
V(CE)4 = 1.5 V
B-sector scan condition:
180000, 70000, 50, 1100, 1 scan
Figure 5- 52
PEG 1500 at 148°C
First skimmer 8078 V
second skimmer 8050 V
E-sector 270 85 V
V(CE)4 = 100 V
B-sector scan condition:
180000, 70000, 50, 1100, 1 scan
PEG 1500 at 148°C
First skimmer 8078 V
second skimmer 8050 V
E-sector 270 85 V
V(CE)4 = 200 V
B-sector scan condition:
180000, 70000, 50, 1100, 1 scan
PEG 1500 at 148°C
First skimmer 8078 V
second skimmer 8050 V
E-sector 270 85 V
V(CE)4 = 300 V
B-sector scan condition:
180000, 70000, 50, 1100, 1 scan

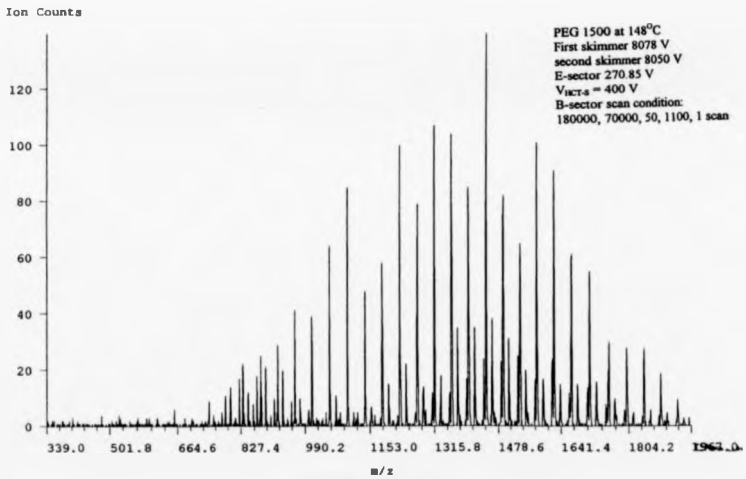

[Figure 5-52] B-sector scan spectra of PEG 1500 in H_2O (with 5 mM CH_3COONH_4): CH_3OH: CH_3COOH = 49.5 : 49.5 :1 (by volume) solvent at 148°C with V_{HCT-S} =1.5 V, 100 V, 200 V, 300 V and 400 V.

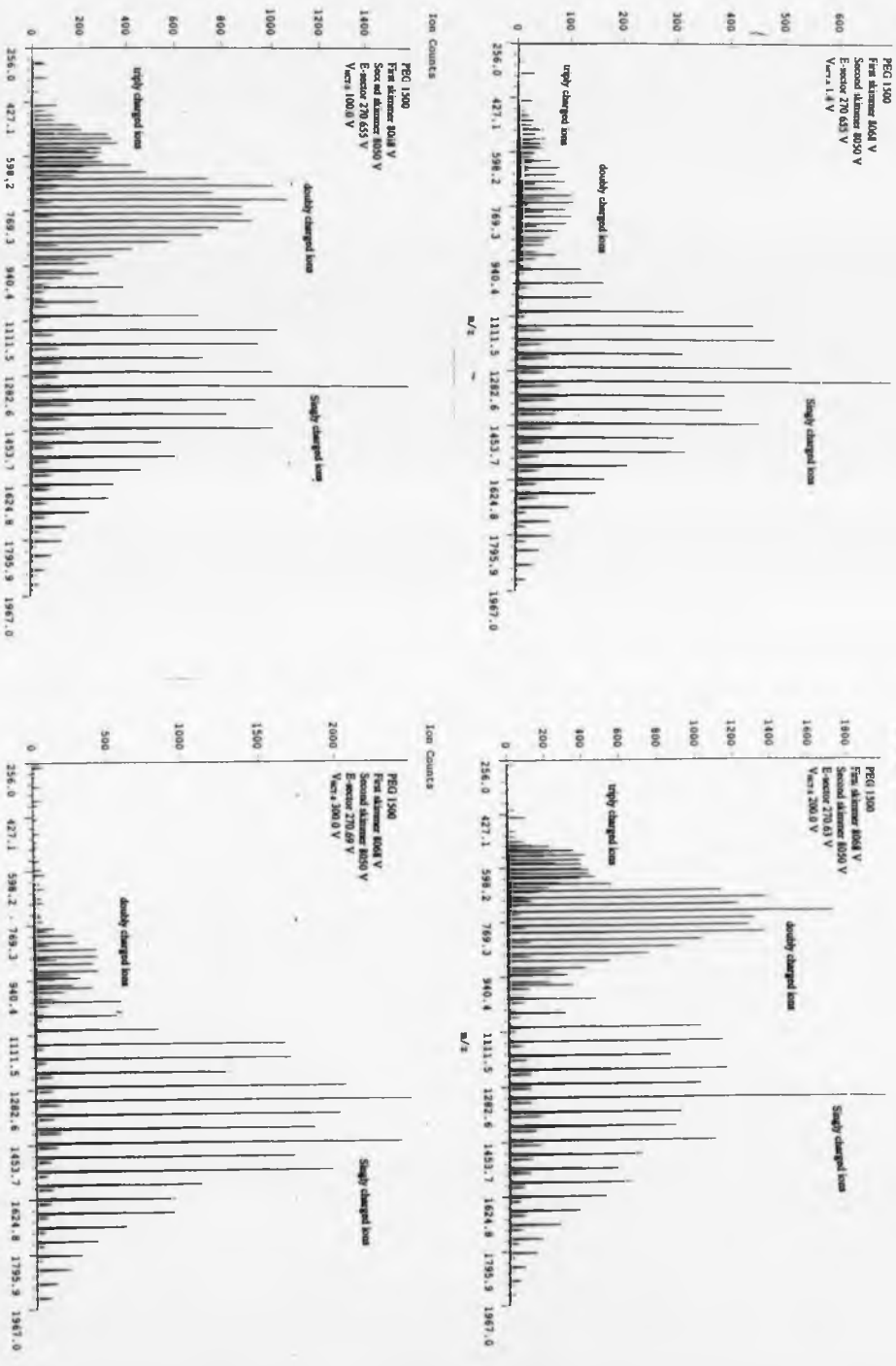
Ion Counts
PEG 1500
First skimmer 8044 V
Second skimmer 8050 V
E-sector 270.653 V
Vacc x 1.4 V
triply charged ions
doubly charged ions
Singly charged ions
m/z
Ion Counts
PEG 1500
First skimmer 8044 V
Second skimmer 8050 V
E-sector 270.653 V
Vacc x 100.0 V
triply charged ions
doubly charged ions
Singly charged ions
Ion Counts
PEG 1500
First skimmer 8044 V
Second skimmer 8050 V
E-sector 270.69 V
Vacc x 200.0 V
triply charged ions
doubly charged ions
Singly charged ions
m/z
Ion Counts
PEG 1500
First skimmer 8044 V
Second skimmer 8050 V
E-sector 270.69 V
Vacc x 300.0 V
triply charged ions
doubly charged ions
Singly charged ions

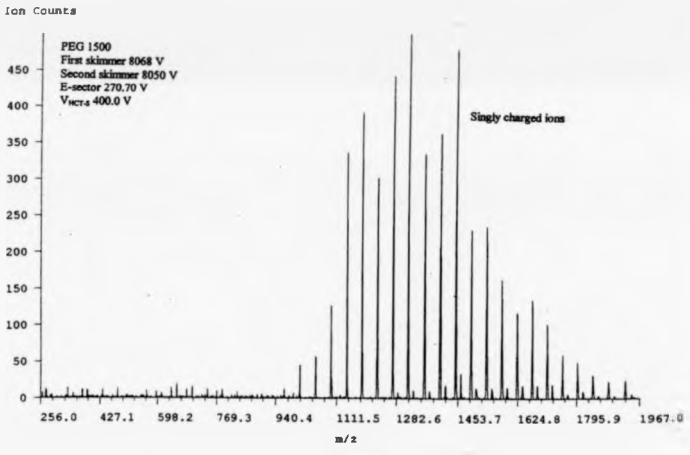

[Figure 5-53] B-sector scan spectra of PEG 1500 sample in solvent ($(CH_3)_2CO$: H_2O = 90:10 (by volume) with 1.2 mM CH_3COONa) at 148°C with first skimmer 8068 V, second skimmer 8050 V and V_{HCT-S} =1.4 V, 100 V, 200 V, 300 V and 400 V.

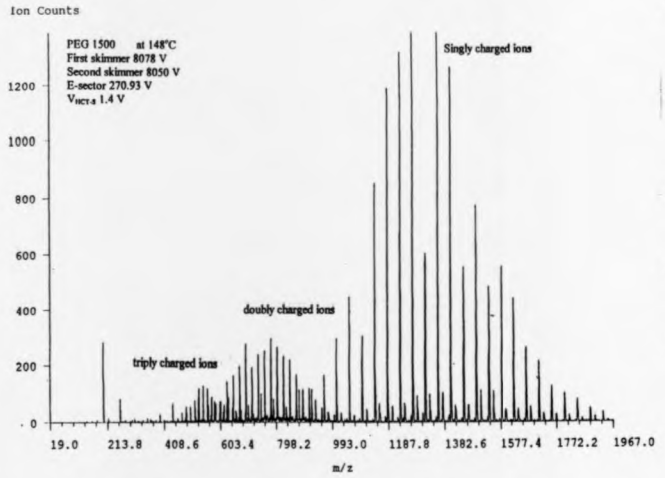
Ion Counts
PEG 1500 at 148°C
First skimmer 8078 V
Second skimmer 8050 V
E-sector 270.93 V
V_HCT-8 1.4 V
Singly charged ions
doubly charged ions
triply charged ions
1200
1000
800
600
400
200
0
19.0
213.8
408.6
603.4
798.2
993.0
1187.8
1382.6
1577.4
1772.2
1967.0
m/z

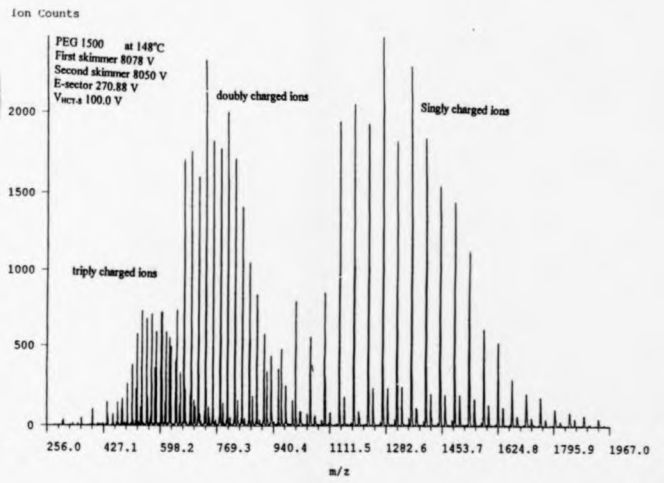
Ion Counts
PEG 1500 at 148°C
First skimmer 8078 V
Second skimmer 8050 V
E-sector 270.88 V
V_HCT-8 100.0 V
doubly charged ions
Singly charged ions
triply charged ions
2000
1500
1000
500
0
256.0
427.1
598.2
769.3
940.4
1111.5
1282.6
1453.7
1624.8
1795.9
1967.0
m/z

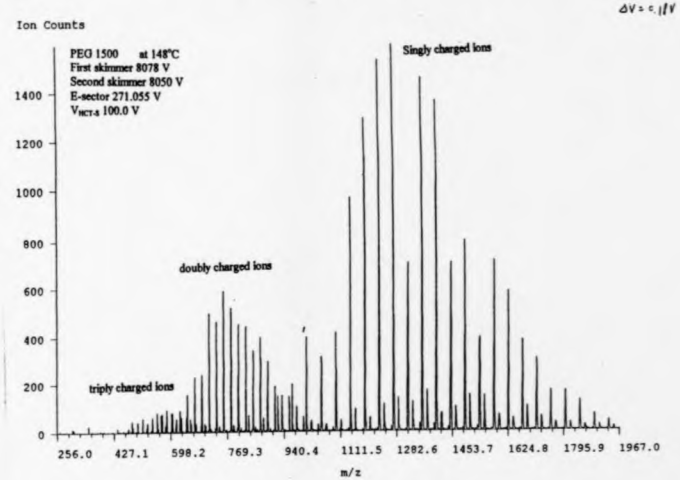
Ion Counts
PEG 1500 at 148°C
First skimmer 8078 V
Second skimmer 8050 V
E-sector 271.055 V
V_HCT-8 100.0 V
Singly charged ions
doubly charged ions
triply charged ions
1400
1200
1000
800
600
400
200
0
256.0
427.1
598.2
769.3
940.4
1111.5
1282.6
1453.7
1624.8
1795.9
1967.0
m/z

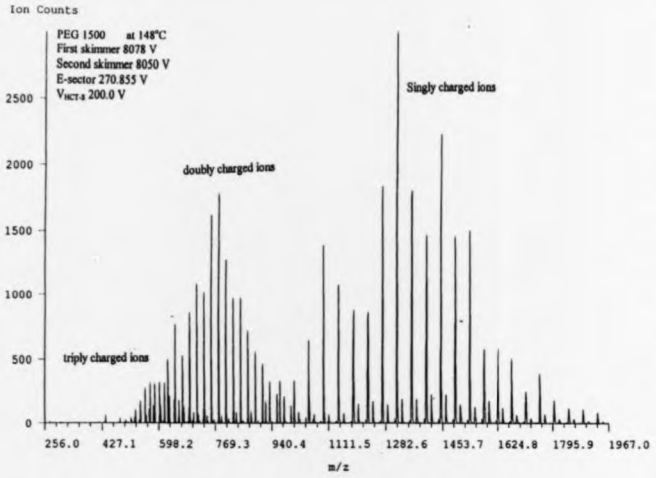
Ion Counts
PEG 1500 at 148°C
First skimmer 8078 V
Second skimmer 8050 V
E-sector 270.855 V
V_HCT-s 200.0 V
Singly charged ions
doubly charged ions
triply charged ions
2500
2000
1500
1000
500
0
256.0 427.1 598.2 769.3 940.4 1111.5 1282.6 1453.7 1624.8 1795.9 1967.0
m/z

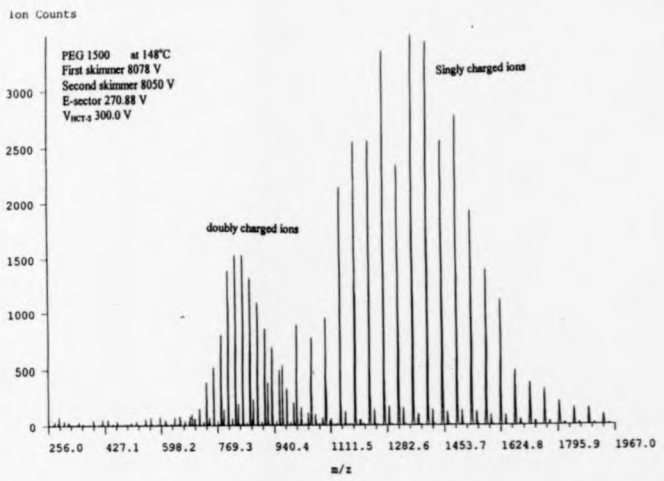
Ion Counts
PEG 1500 at 148°C
First skimmer 8078 V
Second skimmer 8050 V
E-sector 270.88 V
V_HCT-s 300.0 V
Singly charged ions
doubly charged ions
3000
2500
2000
1500
1000
500
0
256.0 427.1 598.2 769.3 940.4 1111.5 1282.6 1453.7 1624.8 1795.9 1967.0
m/z

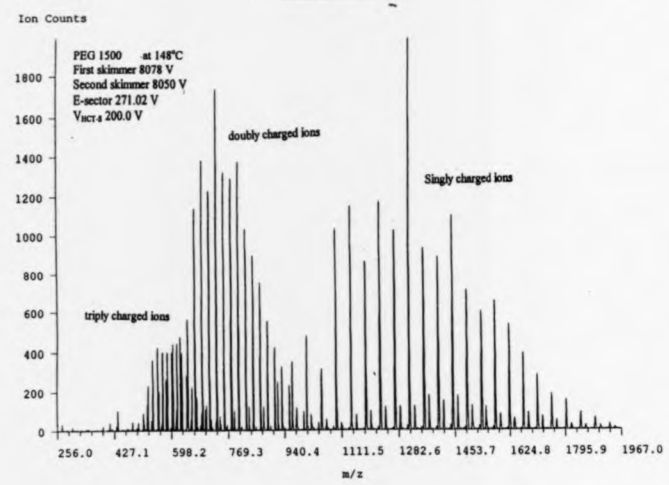
Ion Counts
PEG 1500 at 148°C
First skimmer 8078 V
Second skimmer 8050 V
E-sector 271.02 V
V_HCT-s 200.0 V
doubly charged ions
Singly charged ions
triply charged ions
1800
1600
1400
1200
1000
800
600
400
200
0
256.0 427.1 598.2 769.3 940.4 1111.5 1282.6 1453.7 1624.8 1795.9 1967.0
m/z

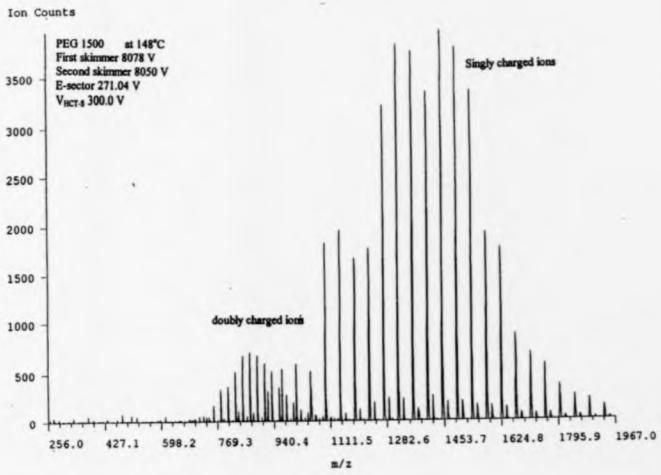
Ion Counts
PEG 1500 at 148°C
First skimmer 8078 V
Second skimmer 8050 V
E-sector 271.04 V
V_HCT-s 300.0 V
Singly charged ions
doubly charged ions
3500
3000
2500
2000
1500
1000
500
0
256.0 427.1 598.2 769.3 940.4 1111.5 1282.6 1453.7 1624.8 1795.9 1967.0
m/z

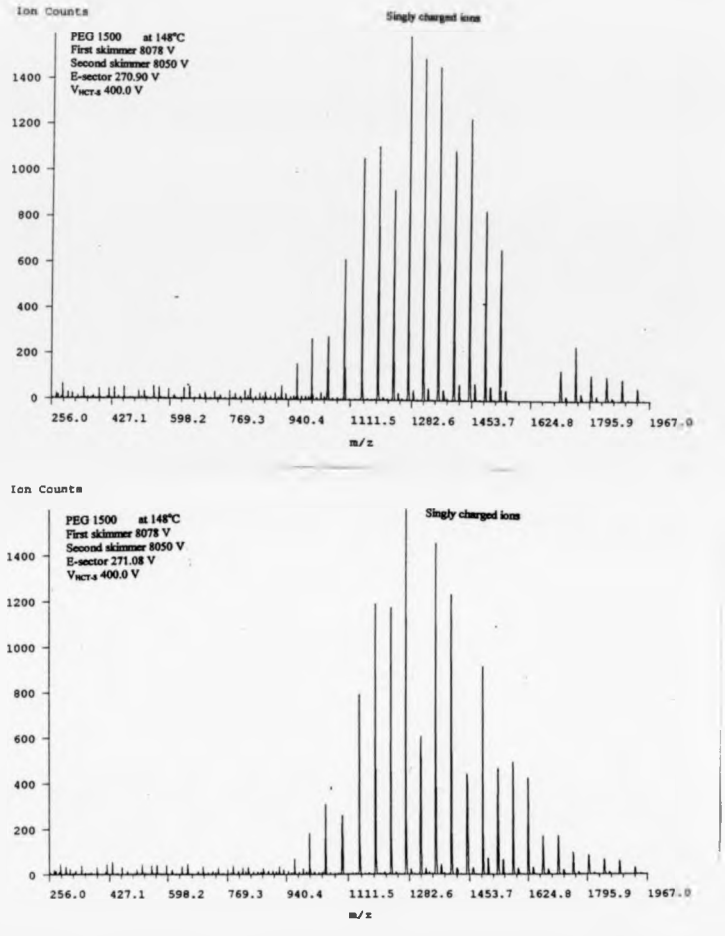

Figure 5-54: B-sector scan spectra of PEG 1500 sample in solvent ($(CH_3)_2CO$: H_2O = 90:10 (by volume) with 1.2 mM CH_3COONa) at 148°C with first skimmer 8078 V, second skimmer 8050 V and V_{HCT-S} =1.5 V, 100 V, 200 V, 300 V and 400 V. As at V_{HCT-S} = 100 V, 200 V and 300 V, the parent ion E-sector scan peaks split at top, two E-sector values were used for parent ion peak setting

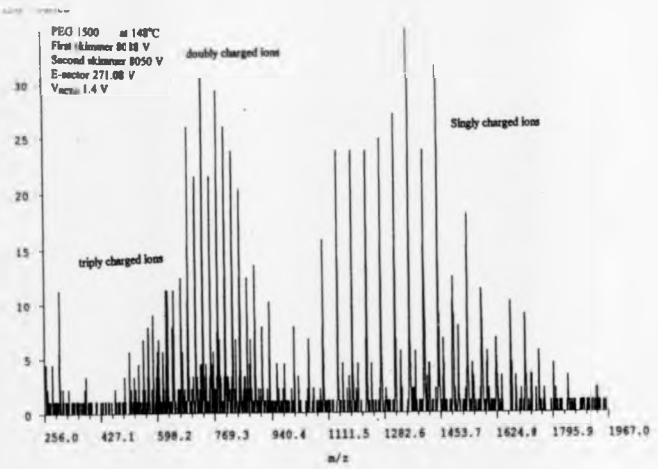
PEG 1500 at 148°C
First skimmer 8088 V
Second skimmer 8050 V
E-sector 271.08 V
doubly charged ions
Singly charged ions
triply charged ions
m/z

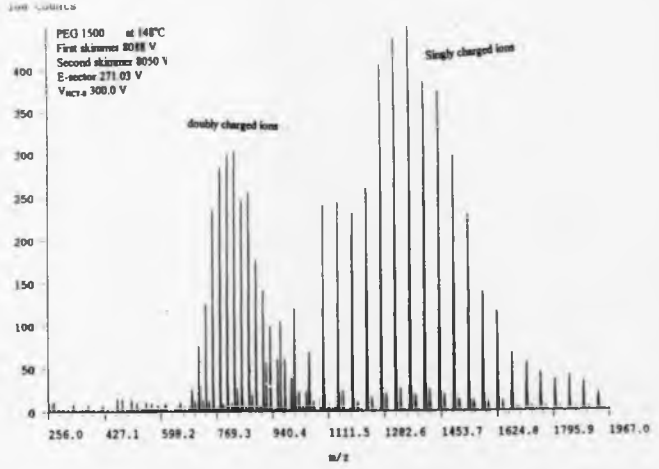
PEG 1500 at 148°C
First skimmer 8088 V
Second skimmer 8050 V
E-sector 271.03 V
doubly charged ions
Singly charged ions
m/z

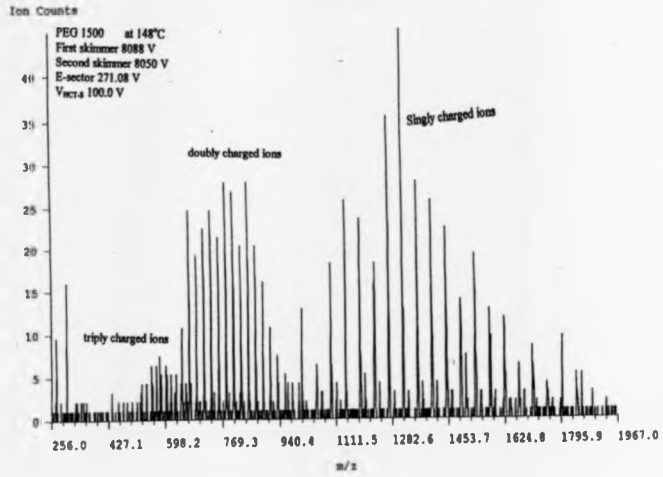
Ion Counts
PEG 1500 at 148°C
First skimmer 8088 V
Second skimmer 8050 V
E-sector 271.08 V
doubly charged ions
Singly charged ions
triply charged ions
m/z

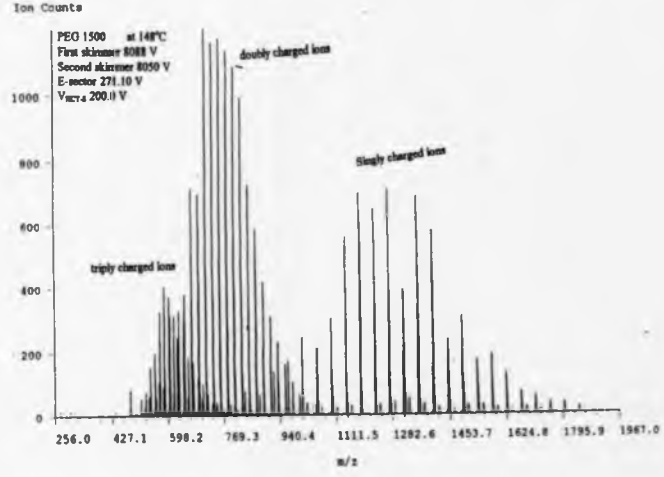
Ion Counts
PEG 1500 at 148°C
First skimmer 8088 V
Second skimmer 8050 V
E-sector 271.10 V
doubly charged ions
Singly charged ions
triply charged ions
m/z

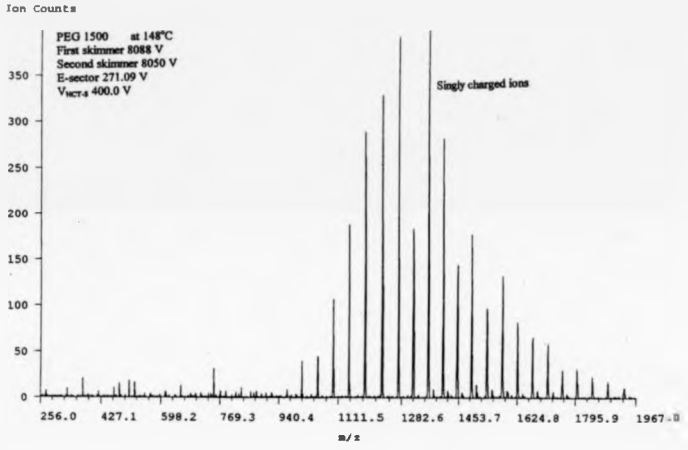

[Figure 5-55] B-sector scan spectra of PEG 1500 sample in solvent ($(CH_3)_2CO$: H_2O = 90:10 (by volume) with 1.2 mM CH_3COONa) at 148°C with first skimmer 8088 V, second skimmer 8050 V and $V_{HCT\text{-}S}$ =1.4 V, 100 V, 200 V, 300 V and 400 V.

5.4 Conclusion

5.4 Conclusion

In the electrospray ionization (ESI) source, the potential difference (V_{HCT-S}) between the capillary-skimmer in the so-called intermediate-pressure region affected the final ions' charge distribution heavily. The main effect was the ion optical focusing effect which guided the ions through the ion optical system to reach the detector of the mass spectrometer. Improperly focused ions would have been lost on the way and could not have been detected as they did not match the ion optical system's requirements. Changing the potential difference between the first skimmer and the second skimmer in the ESI source (which is the next stage behind the intermediate region), changed the ion optical requirements. Two processes influenced the sample ions' states before they were affected by V_{HCT-S} : one was the desolvation process of charged droplets to form the ions needed. This was assisted by the heat of the heated capillary tube (HCT). The other process was the resolvation process facilitated by the free jet expansion, which was caused by the large pressure difference between atmosphere in the spraying stage and high vacuum in the mass spectrometer. At high HCT temperature, the desolvation rate would have been high and the speed of the resolvation process could have been quite low, if the temperature of the carrier gas remained above the saturation value during free jet expansion. In this situation, the suprathermal desolvating collisions between ions and ambient neutral gas molecules in the free jet expansion which caused by the accelerating effect of the V_{HCT-S} would not have been needed. Increasing the V_{HCT-S} potential caused some collisional-induced dissociation (CID) at certain voltage levels but the CID process would have been overpowered by the optical effect and the fragments from CID would have been lost when V_{HCT-S} increased further. At low HCT temperature, the suprathermal desolvation process became more important. As part of

the $V_{HCT\text{-}S}$ potential was consumed by this desolvation process, the $V_{HCT\text{-}S}$ value needed in order for the ions to match the ion optical requirements had to be increased. This caused the optimum $V_{HCT\text{-}S}$ and $V_{HCT\text{-}S}$ range to shift to higher potential, while at the same time an ion's $V_{HCT\text{-}S}$ range became narrower for the same reason. As highly charged ions were affected more by the same electric field strength, considering ions of different charges but the same mass, ions of higher charge states were focused at lower $V_{HCT\text{-}S}$ and the $V_{HCT\text{-}S}$ region over which ions were observed was narrower than those of their low-charge counterparts. For ions of the same charge but different masses, the optimum $V_{HCT\text{-}S}$ value increased as the mass increased.

5.5 References:

[5-1] M. Yamashita and J. B. Fenn

J. Phys. Chem., **88**, 4451 (1984)

[5-2] J. B. Fenn, M. Mann, C. K. Meng, F. Wong and C. M. Whitehouse

Science **24**, 64 (1989)

[5-3] M. Dole, L. L. Mack, R. L. Hines, R. C. Mobley, L. D. Ferguson and M. B. Alice,

J. Chem. Phys., **49**, 2240 (1968)

[5-4] L. L. Mack, P. Kralik, A. Rheude and M. Dole

J. Chem. Phys., **52**, 4977 (1970)

[5-5] G. Wang and R. B. Cole, *Chapter 4: Solution, Gas-Phase, and Instrumental Parameter Influence on Charge-State Distributions in Electrospray Ionization Mass Spectrometry* in the book: *Electrospray Ionization Mass Spectrometry: Fundamentals, Instrumentation, and Applications*, Edited by R. B. Cole, A Wiley-interscience Publication JOHN WILEY & SONS, INC. (1997).

[5-6] J. L. Jones, A. R. DongrĖ, A. Somogyiand V. H. Wysocki,

J. Am. Chem. Soc. **116**, 8368, (1994)

[5-7] J. V. Iribarne and B. A. Thompson

J. Chem. Phys. **64**, 2287 (1976)

[5-8] B. A. Thompson and J. V. Iribarne

J. Chem. Phys. **71**, 4451 (1979)

[5-9] J. B. Fenn, M. Mann, C. K. Meng, S. K. Wong and C. Whitehouse

Mass Spectrom. Rev. **9**, 37 (1990)

[5-10] J. B. Fenn *J. Am. Soc. Mass Spectrom.* **4**, 524 (1993)

[5-11] J. A. Loo, H. R. Udseth, and R. D. Smith

Biomed. Environ. Mass Spectrom. **17**, 411 (1988)

[5-12] T. R. Covey, R. F. Bonner, B. I. Shushan and J. Henion

Rapid Commun. Mass Spectrom. **2**, 249 (1988)

[5-13] J. A. Loo, C. G. Edmonds, H. R. Udseth, and R. D. Smith

Anal. Chem. **62**, 693 (1990)

[5-14] S. K. Chowdhury, V. Katta, and B. T. Chait

J. Am. Chem. Soc. 112, 9012 (1990)

[5-15] J. A. Loo, R. R. O. Loo, H. R. Udseth, C. G. Edmonds, and R. D. Smith

Rapid Commun. Mass Spectrom. **5**, 101 (1991)

[5-16] J. Li, J. A. Taraszka, A. E. Counterman and D. E. Clemmer

Int. J. Mass Spectrom. 185/186/187, 37 (1999)

[5-17] J. C. Y. Le Blanc, D. Beuchemin, K. W. M. Siu, R. Guevremont, and S. S. Berman

Org. Mass Spectrom. **26**, 831 (1991)

[5-18] U. A. Mirza, S. L. Cohen, B. T. Chait

Anal. Chem. 65, 1 (1993)

[5-19] O. Vorm, B. T. Chait and P. Roepstorff

Proceedings of the 41st ASMS Conference on Mass Spectrometry and Allied Topics, San Francisco, CA, 621a (1993)

[5-20] G. J. Van Berkel, F. Zhou and J. T. Aronson

Int. J. Mass Spectro. Ion Proc. **162**, 55 (1997)

[5-21] B. E. Winger, K. J. Light-Wahl, R. D. Smith

J. Am. Soc. Mass Spectrom., **3** , 624 (1992)

[5-22] B. A. Thomson *J. Am. Soc. Mass Spectrom.* **8**, 1053 (1997)

[5-23] S. H. Hunt and M. M. Sheil, M. Belov and P. J. Derrick

Anal. Chem. **70**, 1812 (1998)

[5-24] B. B. Schneider and D. D. Y. Chen *Anal. Chem. 72, 791 (2000)*

[5-25] F. He, J. Ramirez, B. A. Garcia, C. B. Lebrilla

Inter. J. Mass Spectrom., **182/183**, 261 (1999)

[5-26] R. K. Boyd, E. E. Kingston, A. G. Brenton and J. H. Beynon

Proc. R. Soc. London, A 39, 89 (1984)

[5-27] (or [3-13]) J.B. Fenn *Inter. J. Mass Spectro.* **200**, 459 (2000)

[5-28] (or [3-14])D. J. Creasey, D. E. Heard, M. J. Pilling, B. J. Whitaker,

M. Berzins, R. Fairlie

Applied Physics B Lasers and Optics, **65**, 375, (1997)

[5-29] J. C. Barna and D. H. Williams

Ann. Rev. Chem. Soc., **38**, 339 (1984)

[5-30] A. van de Kerk-van Hoof and A. J. R. Heck

Journal of Anitimicrobial Chemotherapy **44**, 593 (1999)

[5-31] T. Staroske, D. P. O'Brien, T. J. D. Jorgensen, P. Roepstorff, D. H. Williams,

and A. J. R. Heck

Chem. Eur. J. **6**, 504 (2000)

[5-32] T. J. D. Jorgensen, P. Roepstorff and A. J. R. Heck

Anal. Chem. **70**, 4427 (1998)

Chapter 6: Conclusion and future work

6.1 The development of the electrospray ionization (ESI) source on the MMM sector mass spectrometer

An improvement of one or two orders of magnitude in the strength of the ion signal intensities at the final detector of the MMM mass spectrometer has been achieved as a result of the developments made to the ESI source. In addition, the ESI source was made easier to operate through these developments and the ion signals were made more stable. The important changes made to the source are listed here.

1) A very thin stainless steel capillary has been used as the electrospray needle to replace the original glass capillary sheathed in a hypodermic needle. The replacement solved the ion current oscillation problem of the ESI source, which had been a consequence of an unstable spray jet. The instability had been caused by the insulation property of the glass capillary. The need to adjust the tip position of the electrospray needle depending on the conductivity and the flow rate of the analyte solution was reduced by the replacement.

2) Simply putting a collar on the entrance end of the heated stainless steel capillary (HCT), to smooth the equipotential lines in the electric field between the end of the HCT and the electrospray needle tip and lessen the defocusing effect, has greatly reduced the need for precise alignment between the electrospray needle tip and the HCT entrance. This simple modification was equivalent to installing an atmospheric pressure ion lens[3-6] and had the same effect of improving ion current.

3) The use of a larger inside-diameter heated stainless steel capillary (HCT) in the final ESI source has increased the ion transmission efficiency still further and has helped avoid possible discrimination against low-mass ions [3-9].

4) The large capacity of a new pre-pumping rotary pump overcame the extra pumping load of the larger HCT and opened up possibilities for other improvements made to the ESI source.

5) Dual insulating pumping pipes[3-1] between the ESI source and the pre-pumping rotary pump have restrained the pressure in the capillary-skimmer region, so that region of the Pachen curve[3-6] in which the source was most vulnerable to vacuum discharging has been avoided. Another advantage is that the length of the gas discharge path has been increased. This simple method solved the unique gas-breakdown problem, faced with any ESI source on a sector instrument, and helped to suppress discharging and allow the rotary pump to be run at earth potential.

6) Adjusting the HCT-first skimmer distance appropriately[3-13] and with the right pressure, the first skimmer has been set to sample the undisturbed low-temperature ion beam[3-13, 3-14] (and carrier gas) from the "zone-of-silence" of the free-expansion jet.

7) Using a proper skimmer-shape (in place of the restraining tube) for a second skimmer has greatly increased the ion transmission through the region.

8) A large-aperture cylindrical extracting-electrode (first lens after the second skimmer) and a grounded lens with the same aperture and eight extra same-size pumping holes (second lens after the second skimmer) have worked well in this vacuum region (immediately after the second skimmer) where not only the ion optics, but also the gas dynamics, still influence the ion beam movement. The new ion optics system has been much simpler to operate than that of the prototype source.

6.2 Mass-analyzed ion kinetic energy spectroscopy (MIKES) on the MMM instrument with an ESI source

The larger parent ion currents with the improved ESI source, compared to the prototype, has allowed mass-analyzed ion kinetic energy spectroscopy (MIKES) to be performed reproducibly with ESI. Results have tended to confirm conclusions reached in earlier study on MMM using field desorption.

1) The doubly charged ions have given more fragment ion peaks than their singly charged counterparts in the mass-analyzed ion kinetic energy spectroscopy (MIKES) experiments on MMM instrument with the ESI source. The fact that doubly charged parent ions have given both doubly and singly charged fragment ions, whereas the singly charged parent ions have given only singly charged fragment ions, might be one reason. The difference in the center-of-mass collision energies of singly and doubly charged parent ions in CID process could be a second reason.

2) The collision-induced dissociation (CID) and metastable dissociation spectra of doubly charged substance P have demonstrated the translational energy losses associated with peaks from CID. Future study on translational energy losses of different charge states (such as triply charged substance P, doubly to hexa charged insulin ions) of different masses (1,000 ~ 5,000 Da) under different collision conditions could be very interesting with the MMM instrument and the developed ESI source.

3) Nearly identical spectra have been obtained with He, Ar and Kr-CID from doubly charged bradykinin under conditions close to that of the prototype ESI source (smaller inside-diameter HCT, high pressure in intermediate capillary/skimmer region, first skimmer out of Mach disc of the free-expansion jet and high HCT temperature). The reason why the extra collision energy introduced by changing to heavier collision gases (from He to Ar and Kr) have not shown any effect is not clear.

3) Strong fragment peaks from the CID of ubiquitin ions might be seen in the future, if still stronger parent ion signals could be achieved and the appropriate potential differences, between the HCT and first skimmer and the first skimmer and the second skimmer, were used.

6.3 Effects of ESI source conditions on the charge-state distributions of mass spectra

The conclusion from this study is that the charge state distribution of the ESI spectra is largely been determined by ion optical effects, as determined by the potential difference ($V_{HCT\text{-}S}$) between capillary and skimmer in the intermediate vacuum region of the ESI source and the potential difference between the first skimmer and the second skimmer in the following region.

The ESI spectra acquired at different $V_{HCT\text{-}S}$ values have shown different charge-state distributions. For each charge state of a particular sample, there exists a specific optimum $V_{HCT\text{-}S}$ value and certain $V_{HCT\text{-}S}$ voltage regions over which the ions could be detected (detected $V_{HCT\text{-}S}$ region).

For the different charge states of ions of the same mass, their optimum $V_{HCT\text{-}S}$ values have decreased with increased charge and the widths of the detected $V_{HCT\text{-}S}$ regions have narrowed as well. As a result the higher-charged ions of the same mass have had lower $V_{HCT\text{-}S}$ values and narrower detected $V_{HCT\text{-}S}$ regions.

For the same charge state with ions of different masses, the lower-mass ions have had lower optimum $V_{HCT\text{-}S}$ values and smaller detected $V_{HCT\text{-}S}$ regions. It is obvious that high charge-state ions would have felt stronger electrostatic forces than lower charge-state ions of the same mass, and on one level it seems reasonable that the high charge-state ions have had the lower optimum $V_{HCT\text{-}S}$ values. This argument does,

however, assume that the ions' kinetic energies are charge-independent. With ions of a given charge, the electrostatic forces felt would have been the same for small or large masses but the effects (i.e. in terms of acceleration) would have been greater for the low-mass ions. Thus, again on one level, it is reasonable that the low-mass ions have required lower $V_{HCT\text{-}S}$ values, and again there is an assumption of mass-independent kinetic energy.

An effect of the temperature of the HCT upon the $V_{HCT\text{-}S}$ required for efficient transmission has been discovered. Lowering the temperature of the HCT has moved all ions' optimum $V_{HCT\text{-}S}$ values to higher voltages and the detected $V_{HCT\text{-}S}$ regions have been narrowed. Adjusting the potential difference between the first and second skimmers of the ESI source has also shifted the ions' optimum $V_{HCT\text{-}S}$ values and their detected $V_{HCT\text{-}S}$ regions. An increase in this potential difference has led to higher $V_{HCT\text{-}S}$ values being required to match the requirements of changed ion optical system between the skimmers.

The so-called capillary-skimmer dissociation effect has been found to be relatively small with the ESI source used here. Possibly this is because the first skimmer has been inserted through the Mach disk of the free jet expansion and the undisturbed, low-temperature ions from the " zone of the silence " of the jet have been sampled. The fragment ions (with suitable charge states and mass values) from capillary-skimmer dissociation have been detected with the samples used (Chapter 5). Relatively strong fragment ion peaks have been seen in the magnetic-sector scan spectra, when $V_{HCT\text{-}S}$ has been around 200 V. On further increasing $V_{HCT\text{-}S}$, the fragment ion peaks have diminished, presumably having been over-focused and lost by the ion optical system.

The basic reasons behind the above phenomena lie with the inter-relationship of effects concerning ion formation and transport. These effects are the ESI droplets' desolvation by heat from the HCT, the condensation or re-solvation in the free jet expansion (adiabatic free expansion), the suprathermal desolvating collisions between ions and ambient gas molecules introduced by the potential difference between the HCT and first skimmer (V_{HCT-S}) in this intermediate pressure region and most significantly the ion optical effect of V_{HCT-S}.

The conclusion from this study is that, at high HCT temperature, desolvated ions would have been formed in the HCT and carried out of the HCT by the gas flow. The desolvation effect of the heat would have been strong and the condensation effect of the free jet expansion relatively low. Quite large portions of ions could have overcome the condensation effect and passed through this intermediate vacuum region even under very low V_{HCT-S} values. Increasing the V_{HCT-S} voltage value would helped the suprathermal desolvating effect to form more ions and would have increased the ion focusing effect. The conclusion is that increasing V_{HCT-S} would have caused over-focusing . Over-focused ions are those which could not match the requirements of the ion optical system and were lost on the way to the final detector of the mass spectrometer. It is concluded that lowering the temperature weakened the desolvation effect and enhanced condensation in the free jet expansion. More and more of the applied V_{HCT-S} potential drop would have been used on the suprathermal desolvation to overcome the re-solvation effect of the free jet expansion and to desolvate the un-desolvated droplets to make ions available. The free ions would have experienced only part of the potential drop due to V_{HCT-S}. The optimum V_{HCT-S} values of all the ions and their detected V_{HCT-S} regions would have been raised to keep the match to the fixed ion

optical requirements. When the HCT temperature dropped further, the desolvation effect of the HCT would have been so low and condensation effect of the free jet expansion would have been so high, that suprathermal desolvation would have been ineffective. The total ion output of the ESI source would then have been too low to acquire a usable spectra.

All the ions' optimum $V_{HCT\text{-}S}$ values and detected $V_{HCT\text{-}S}$ regions would move in the high-voltage direction when the potential difference between the two skimmers was increased. This experimental result is strong evidence that the charge-state distributions of the ESI spectra were largely decided by the ion optical effect. As the second skimmer potential was fixed during the experiments and the virtual object for the mass spectrometer was located between the first and second skimmers, increasing the potential on the first skimmer would have increased the accelerating voltage of the ions produced by the ESI source which accordingly required changing the settings of the magnetic and electric sectors. Because $V_{HCT\text{-}S}$ always used the first skimmer as the potential reference point, changing the potential difference between the two skimmers could not have affected the ions' behavior before the first skimmer. The shift of the optimum $V_{HCT\text{-}S}$ values and detected $V_{HCT\text{-}S}$ regions reflected altered ion optical requirements, caused by the potential difference changing between the two skimmers. Under the altered ion optical requirements, ions were detected at high $V_{HCT\text{-}S}$ values whereas previously at these $V_{HCT\text{-}S}$ the ions were over-focused. Retrieving signal at high $V_{HCT\text{-}S}$ values in this way establishes that the capillary-skimmer dissociation effect was relatively small in the ESI source in comparison to the ion optical effect and that the disappearance of ions at high $V_{HCT\text{-}S}$ was not a consequence of loss by capillary-skimmer dissociation. Further study of the interdependence of skimmer-skimmer

potential difference and $V_{HCT\text{-}S}$ could be beneficial in promoting deeper understanding of the ESI process. The effects of HCT temperature upon the relationship between skimmer-skimmer potential and $V_{HCT\text{-}S}$ merit further investigation.

The study of ESI has been negative in one sense in that results concerning fragmentation of the small protein (ubiquitin) as a result of collisional activation have not been reproduced. The positive implication of the conclusions of the study are, however, considerable. The study points strongly to an importance of ion optical effects in determining much of the apparent variability in changing encountered in ESI. In principle, ion optical effects can be understood and controlled. There is no evidence from this study of charge transfer processes contributing significantly in the ESI source. Collision-induced dissociation (CID) did occur in the ESI source, but could be suppressed. CID became important only because the potentials required to create the required ion optical conditions for ions of interest inadvertently happened to produce conditions conducive to CID. The final conclusion from this study is that dissociation even of weak non-covalent complexes can be wholly avoided in ESI source, and that practical difficulties experienced in present-day sources arise from the need to satisfy ion optical conditions.

5

DX

221016